



3 1176 00163 9997

NASA-CR-162857

NASA-CR-162857
19800012877

The Deep Space Network Progress Report 42-56

January and February 1980

LIBRARY copy

APR 21 1980

LIBRARY USE AND RETURN
LIBRARY OF
BUREAU OF INVESTIGATION

April 15, 1980

National Aeronautics and
Space Administration

Jet Propulsion Laboratory
California Institute of Technology
Pasadena, California

NF02046

The Deep Space Network Progress Report 42-56

January and February 1980

April 15, 1980

National Aeronautics and
Space Administration

Jet Propulsion Laboratory
California Institute of Technology
Pasadena, California

80N2B62*

The research described in this publication was carried out by the Jet Propulsion Laboratory, California Institute of Technology, under NASA Contract No NAS7-100

Preface

This report presents DSN progress in flight project support, tracking and data acquisition (TDA) research and technology, network engineering, hardware and software implementation, and operations. Each issue presents material in some, but not all, of the following categories in the order indicated:

Description of the DSN

Mission Support

- Ongoing Planetary/Interplanetary Flight Projects
- Advanced Flight Projects

Radio Astronomy

Special Projects

Supporting Research and Technology

- Tracking and Ground-Based Navigation
- Communications-Spacecraft/Ground
- Station Control and Operations Technology
- Network Control and Data Processing

Network and Facility Engineering and Implementation

- Network
- Network Operations Control Center
- Ground Communications
- Deep Space Stations
- Quality Assurance

Operations

- Network Operations
- Network Operations Control Center
- Ground Communications
- Deep Space Stations

Program Planning

TDA Planning

In each issue, the part entitled "Description of the DSN" describes the functions and facilities of the DSN and may report the current configuration of one of the seven DSN systems (Tracking, Telemetry, Command, Monitor & Control, Test & Training, Radio Science, and Very Long Baseline Interferometry)

The work described in this report series is either performed or managed by the Tracking and Data Acquisition organization of JPL for NASA.

This Page Intentionally Left Blank

Contents

DESCRIPTION OF THE DSN

Network Functions and Facilities	1
N A Renzetti	
DSN Telemetry System: Design for Megabit Telemetry	4
E C Gatz	
NASA Code 311-03-43-10	
DSN Tracking System, Mark III-1979	7
G L Spradlin	
NASA Code 311-04-31-01	
DSN VLBI System MK 1-80	26
W D Chaney and N C Ham	
NASA Code 311-04-31-01	

MISSION SUPPORT

Ongoing Planetary/Interplanetary Flight Projects

DSN Load Forecasting for Proposed Future	
NASA Mission Sets	35
W A Webb	
NASA Code 311-03-25-00	
Viking Orbiter Completion Mission and	
Viking Lander Monitor Mission	42
R L Gillette	
NASA Code 311-03-22-50	

RADIO ASTRONOMY

Radio Astronomy	46
R M Taylor	
NASA Code 311-03-21-00	

SUPPORTING RESEARCH AND TECHNOLOGY

Tracking and Ground-Based Navigation

X-Band Uplink Ground Systems Development	48
R Hartop, C Johns, and R Kolbly	
NASA Code 310-10-64-10	

**VLBI Detection of Crustal Plate Motion Using DSN
Antennas as Base Stations** 59

D D Morabito, E S Claflin, and C J Steinberg
NASA Code 310-10-61-10

Communications — Spacecraft/Ground

**A Bent Pipe Design for Relaying Signals Received by
an Orbiting Deep Space Relay Station to a Ground Station** 76

M A Koerner
NASA Code 310-20-65-03

**Arithmetic Techniques Used in the High-Speed Front End
of the Multimegabit Telemetry Modem** 85

E R Wechsler
NASA Code 310-20-67-16

**Sensitivity of Reflector Backup Structure Weight to
Variable Wind Speed Loadings** 90

R Levy and D Strain
NASA Code 310-20-65-07

Station Control and Operations Technology

**Analysis of a Class of Totally Self-Checking Circuits
Implemented in an NMOS Custom LSI Structure** 100

M W Sievers
NASA Code 310-30-70-15

**Pulse-Position-Modulation Coding as Near-Optimum Utilization
of Photon Counting Channel with Bandwidth and Power
Constraints** 108

R G Lipes
NASA Code 310-30-70-14

**NETWORK AND FACILITY ENGINEERING
AND IMPLEMENTATION**

Network

**Deep Space Network Control Room Noise and
Vibration Study** 114

J C Rayburn
NASA Code 311-03-13-32

A Fast Algorithm for Encoding the (255, 223) Reed-Solomon Code Over GF (2⁸)	120
---	-----

R L Miller, T K Truong, and I S Reed
NASA Code 311-03-43-20

Ground Communications

Maximum CW RFI Power Levels for Linear Operation of the DSN Block IV Receiver at S-Band Frequencies	122
--	-----

D R Hersey and M K Sue
NASA Code 311-06-50-00

Deep Space Stations

General Sensitivity Analysis of Solar Thermal-Electric Plants	130
--	-----

F L Lansing, E W Hayes, and C S Yung
NASA Code 311-03-41-08

Experimental Investigation of the Effects of Antenna Pointing Errors on Range Delays (Part II)	143
---	-----

T Y Otoshi
NASA Code 311-03-42-55

OPERATIONS

Network Operations Control Center

Network Operations Control Center (NOCC) Implementation Status Report	147
--	-----

E A Garcia
NASA Code 311-03-12-00

Network Functions and Facilities

N A Renzetti

Office of Tracking and Data Acquisition

The objectives, functions, and organization of the Deep Space Network are summarized, deep space station, ground communication, and network operations control capabilities are described

The Deep Space Network was established by the National Aeronautics and Space Administration (NASA) Office of Space Tracking and Data Systems and is under the system management and technical direction of the Jet Propulsion Laboratory (JPL). The network is designed for two-way communications with unmanned spacecraft traveling approximately 16,000 km (10,000 miles) from Earth to the farthest planets and to the edge of our solar system. It has provided tracking and data acquisition support for the following NASA deep space exploration projects: Ranger, Surveyor, Mariner Venus 1962, Mariner Mars 1964, Mariner Venus 1967, Mariner Mars 1969, Mariner Mars 1971, and Mariner Venus-Mercury 1973, for which JPL has been responsible for the project management, the development of the spacecraft, and the conduct of mission operations; Lunar Orbiter, for which the Langley Research Center carried out the project management, spacecraft development, and conduct of mission operations; Pioneer, for which Ames Research Center carried out the

project management, spacecraft development, and conduct of mission operations; and Apollo, for which the Lyndon B Johnson Space Center was the project center and the Deep Space Network supplemented the Manned Space Flight Network, which was managed by the Goddard Space Flight Center. The network is currently providing tracking and data acquisition support for Helios, a joint U.S./West German project; Viking, for which Langley Research Center provided the Lander spacecraft and project management until May, 1978, at which time project management and mission operations were transferred to JPL, and for which JPL provided the Orbiter spacecraft; Voyager, for which JPL provides project management, spacecraft development, and is conducting mission operations; and Pioneers, for which the Ames Research Center provides project management, spacecraft development, and conduct of mission operations. The network is adding new capability to meet the requirements of the Galileo mission to Jupiter, for which JPL is providing the Orbiter spacecraft, and

the Ames Research Center the probe In addition, JPL will carry out the project management and the conduct of mission operations

The Deep Space Network (DSN) is one of two NASA networks The other, the Spaceflight Tracking and Data Network (STDN), is under the system management and technical direction of the Goddard Space Flight Center (GSFC) Its function is to support manned and unmanned Earth-orbiting satellites The Deep Space Network supports lunar, planetary, and interplanetary flight projects

From its inception, NASA has had the objective of conducting scientific investigations throughout the solar system It was recognized that in order to meet this objective, significant supporting research and advanced technology development must be conducted in order to provide deep space telecommunications for science data return in a cost effective manner Therefore, the Network is continually evolved to keep pace with the state of the art of telecommunications and data handling It was also recognized early that close coordination would be needed between the requirements of the flight projects for data return and the capabilities needed in the Network This close collaboration was effected by the appointment of a Tracking and Data Systems Manager as part of the flight project team from the initiation of the project to the end of the mission By this process, requirements were identified early enough to provide funding and implementation in time for use by the flight project in its flight phase

As of July 1972, NASA undertook a change in the interface between the Network and the flight projects Prior to that time, since 1 January 1964, in addition to consisting of the Deep Space Stations and the Ground Communications Facility, the Network had also included the mission control and computing facilities and provided the equipment in the mission support areas for the conduct of mission operations The latter facilities were housed in a building at JPL known as the Space Flight Operations Facility (SFOF) The interface change was to accommodate a hardware interface between the support of the network operations control functions and those of the mission control and computing functions This resulted in the flight projects assuming the cognizance of the large general-purpose digital computers which were used for both network processing and mission data processing They also assumed cognizance of all of the equipment in the flight operations facility for display and communications necessary for the conduct of mission operations The Network then undertook the development of hardware and computer software necessary to do its network operations control and monitor functions in separate computers A characteristic of the new interface is that the Network provides direct data flow to and from the stations, namely, metric data, science and engi-

neering telemetry, and such network monitor data as are useful to the flight project This is done via appropriate ground communication equipment to mission operations centers, wherever they may be

The principal deliveries to the users of the Network are carried out by data system configurations as follows

- (1) The DSN Tracking System generates radio metric data *i.e.*, angles, one- and two-way doppler and range, and transmits raw data to Mission Control
- (2) The DSN Telemetry System receives, decodes, records, and retransmits engineering and scientific data generated in the spacecraft to Mission Control
- (3) The DSN Command System accepts spacecraft commands from Mission Control and transmits the commands via the Ground Communications Facility to a Deep Space Station The commands are then radiated to the spacecraft in order to initiate spacecraft functions in flight
- (4) The DSN Radio Science System generates radio science data, *i.e.*, the frequency and amplitude of spacecraft transmitted signals affected by passage through media such as the solar corona, planetary atmospheres, and planetary rings, and transmits these data to Mission Control
- (5) The DSN Very Long Baseline Interferometry System generates time and frequency data to synchronize the clocks among the three Deep Space Communications complexes It will generate universal time and polar motion and relative Deep Space Station locations as by-products of the primary data delivery function

The data system configurations supporting testing, training, and network operations control functions are as follows

- (1) The DSN Monitor and Control System instruments, transmits, records, and displays those parameters of the DSN necessary to verify configuration and validate the Network It provides the tools necessary for Network Operations personnel to control and monitor the Network and interface with flight project mission control personnel
- (2) The DSN Test and Training System generates and controls simulated data to support development test, training and fault isolation within the DSN It participates in mission simulation with flight projects

The capabilities needed to carry out the above functions have evolved in the following technical areas

- (1) The Deep Space Stations, which are distributed around Earth and which, prior to 1964, formed part of the Deep Space Instrumentation Facility. The technology involved in equipping these stations is strongly related to the state of the art of telecommunications and flight-ground design considerations, and is almost completely multimission in character
- (2) The Ground Communications Facility provides the capability required for the transmission, reception, and monitoring of Earth-based, point-to-point communications between the stations and the Network Operations Control Center at JPL, Pasadena, and to the JPL Mission Operations Centers. Four communications disciplines are provided teletype, voice, high-speed, and wideband. The Ground Communications Facility uses the capabilities provided by common carriers throughout the world, engineered into an integrated system by Goddard Space Flight Center, and controlled from the communications Center located in the Space Flight Operations Facility (Building 230) at JPL

The Network Operations Control Center is the functional entity for centralized operational control of the Network and interfaces with the users. It has two separable functional elements, namely, Network Operations Control and Network Data Processing. The functions of the Network Operations Control are

- (1) Control and coordination of Network support to meet commitments to Network users

(2) Utilization of the Network data processing computing capability to generate all standards and limits required for Network operations

(3) Utilization of Network data processing computing capability to analyze and validate the performance of all Network systems

The personnel who carry out the above functions are located in the Space Flight Operations Facility, where mission operations functions are carried out by certain flight projects. Network personnel are directed by an Operations Control Chief. The functions of the Network Data Processing are

- (1) Processing of data used by Network Operations Control for control and analysis of the Network
- (2) Display in the Network Operations Control Area of data processed in the Network Data Processing Area
- (3) Interface with communications circuits for input to and output from the Network Data Processing Area
- (4) Data logging and production of the intermediate data records

The personnel who carry out these functions are located approximately 200 meters from the Space Flight Operations Facility. The equipment consists of minicomputers for real-time data system monitoring, two XDS Sigma 5s, display, magnetic tape recorders, and appropriate interface equipment with the ground data communications

DSN Telemetry System: Design for Megabit Telemetry

E C Gatz
TDA Engineering

A description is presented of the functional design of the additions to the DSN Telemetry System to handle increased data rates up to 30 megasymbols per second. The new system design includes a new demodulator, additional digital recording and formatting, and augmented monitor and control capability.

I. Introduction

The Deep Space Network Telemetry System has been described in Ref 1. The current configuration, Mark III-77, performs three main functions

- (1) Telemetry data acquisition
- (2) Telemetry data conditioning and transmission
- (3) Telemetry System validation

Telemetry data acquisition consists of those functions necessary to extract the telemetry information modulated on the downlink carrier(s) from the spacecraft. Telemetry data conditioning and transmission consist of those functions necessary to decode, format, record, and transmit the data to users. Telemetry system validation consists of those functions necessary to verify the performance of the Network in the acquisition, conditioning, and transmission of telemetry data.

This article describes the system design to handle data at rates up to 30 megasymbols per second. This addition is planned as a multimission capability, initially to support the proposed Venus Orbiter Imaging Radar (VOIR) Mission.

II. Key Characteristics

The key characteristics of the megabit addition to the DSN Telemetry System consist of

- (1) Extension of telemetry data rate capability from a maximum of 250 kilosymbols per second to 30 megasymbols per second
- (2) Maximum-likelihood decoding of short-constraint convolutional codes at the increased symbol rate
- (3) Accommodate data modulated directly on the carrier, i.e., with no subcarrier
- (4) Accommodate either suppressed or residual carrier
- (5) Central station control of all functions via the Monitor and Control Subsystem
- (6) Real-time monitoring of the system performance at the Network Operations Control Center (NOCC)
- (7) On-site recording of detected, decoded data for delivery to project user
- (8) Quick-look delivery, in near-real-time, of a limited sample of data

III. Functional Description

A simplified block diagram of the megabit system is shown in Fig 1. The megabit stream is handled by the antenna, antenna microwave and receiver in the conventional manner. A new megabit demodulator-detector, now under development, will be interfaced with the receiver to extract and detect the telemetry symbols. A new high-rate decoder is also being developed.

The decoded data are then formatted for interface to a digital recorder. This formatting includes the interlacing with the data of the following status information:

- (1) Receiver, demodulator, and decoder lock status
- (2) Received signal level
- (3) Signal-to-noise ratio (SNR)
- (4) Configuration
- (5) Data rate

The read-after-write output from the recorder is formatted to allow real-time monitoring of the system performance. The performance monitor is to search for, and verify, the telemetry frame sync pattern in the recorded data. This frame sync status, together with the interlaced status data, are displayed

for local operators, and continuously sent to NOCC via GCF high-speed data lines for central network monitoring.

The standard plan for data delivery is to deliver the digital record itself to the project user. A record validation capability will be installed in the GCF Central Communications Terminal to facilitate this delivery. However, additional capability is planned to replay the record at the DSS for transmission to the project via the GCF. Depending on the quantity of data, this playback could occur from 224 kbits per second up to 40 Mbit/s. The GCF is considering a "burst-mode" 40-megabit channel, which could be scheduled periodically to accommodate this replay.

To provide flight projects with a timely sample of the megabit data, a "quick-look" sample is planned for near-real-time delivery. The "quick-look" allows for selecting and buffering up to 30 seconds of data, or about 5×10^8 bits. This buffer can then be replayed over a conventional GCF wideband channel, currently 56 kbit/s.

The megabit capability, as described here, is added in parallel to the current Mark III-77 telemetry capability. The performance will be monitored in the NOCC by the Telemetry Real-Time Monitor (RTM), just as in the current operation. The RTM will be modified to monitor the megabit status indicators, and the quick-look data stream.

Reference

- 1 Gatz, E C, "DSN Telemetry System Mark III-77," *The Deep Space Network Progress Report 42-49*, pp 4-7, Jet Propulsion Laboratory, Pasadena California, February 15, 1979

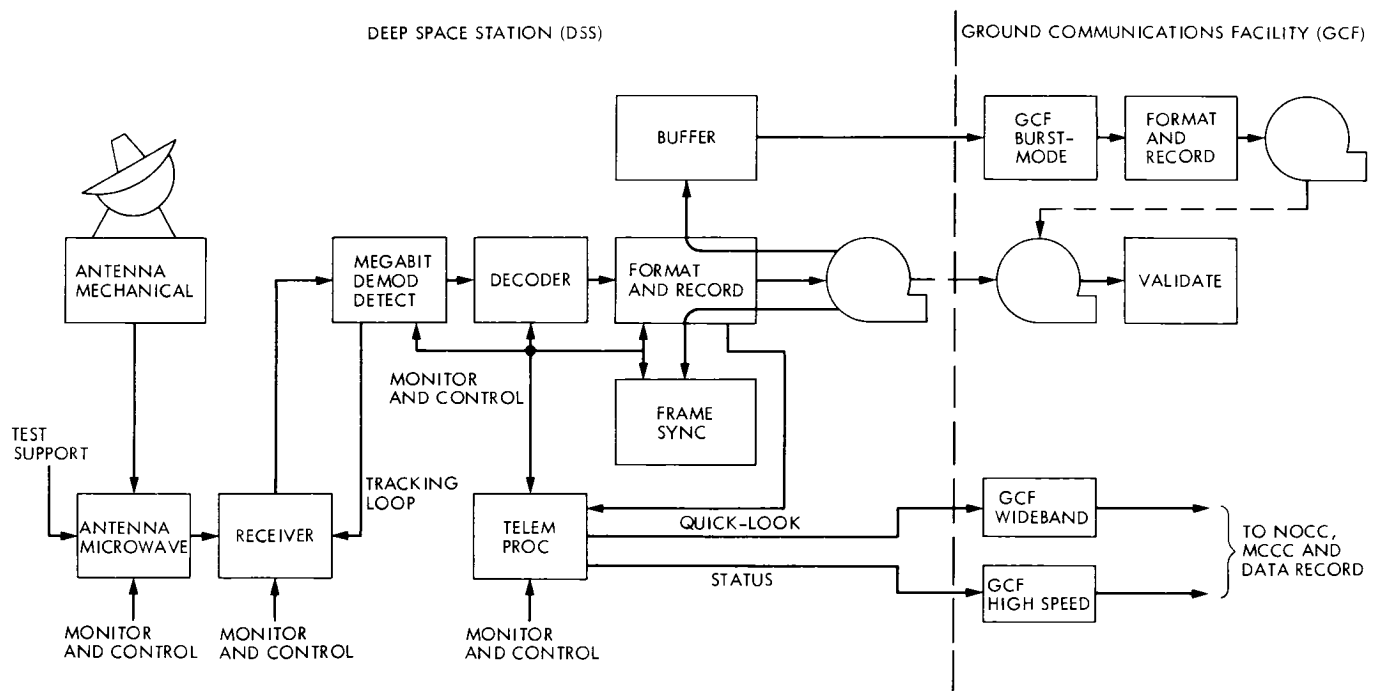


Fig. 1 Megabit telemetry system block diagram

DSN Tracking System, Mark III-1979

G L Spradlin

TDA Engineering

The Tracking System is one of eight generic DSN systems. This article describes, in functional terms, how the Tracking System performs its primary functions of signal acquisition, radio metric data generation, data transmission, and performance validation. Included are the system's functional requirements and required performance based upon identified user and DSN needs. Block diagrams of the 26-, 34-, and 64-meter DSS implementations are provided to indicate subsystem relationships and data flow paths.

I. Introduction

A. Definition

The DSN Tracking System, one of eight generic DSN systems, consists of hardware, software, personnel, and procedures necessary to perform its four primary functions in support of flight project and other radio metric data users. These four primary functions are

- (1) Perform spacecraft (source) signal acquisition (uplink and/or downlink)
- (2) Generate radio metric data
- (3) Transmit radio metric data to users
- (4) Perform radio metric data validation to assure user requirements are satisfied

Radio metric data are defined as range, range rate, and antenna pointing data, and are used by flight project navigation teams for spacecraft orbit determination, platform parameter determination, and ephemeris development, radio metric data are also used by radio science experimenters for interplanetary media investigations, relativity investigations, planetary

atmosphere probes, among other experiments. In addition to the observables mentioned above, system status, configuration, data mode, and calibration (including local atmospheric and ionospheric) data are also provided to the user.

The following sections provide a functional description of the DSN Tracking System, a description of its operation, and its performance parameters through the 1983 era.

B. Key Characteristics

The key characteristics of the DSN Tracking System are

- (1) End-to-end prediction capability to efficiently and reliably generate and provide data necessary to establish and sustain spacecraft communications and for system performance validation
- (2) Automated receiver-exciter control for spacecraft acquisition and tracking from frequency profile predictions
- (3) Simultaneous dual-frequency band (S-X) doppler and near simultaneous range and DRVID (differenced range versus integrated doppler) data at 34-m and 64-m DSSs

- (4) Improved doppler quality resulting from increased automated controls, improved data reporting, improved frequency standards
- (5) Improved ranging performance at increased planetary distances through use of higher frequency range codes and improved reliability
- (6) Radio metric data time-tagged to microseconds accuracy relative to the DSN master clock
- (7) Real-time reporting of DSN Tracking System status to the Network Operations Control Center (NOCC)
- (8) Generation of tracking standards and limits and performance validation by DSN Network Operations

Each of the 26-meter DSS (Fig 1) has the capability of generating one-way, two-way, or three-way S-band doppler and angles from a single spacecraft carrier. Each 34- and 64-meter DSS (Figs 2 and 3) has the capability of generating one-way, two-way, or three-way S- and X-band doppler, S- and X-band range, and S- and X-band DRVID and angles. Table 1 summarizes the planned capability for doppler, range, and DRVID generation, as well as, angle drive capability.

C. Functional Breakdown

The primary functions of the DSN Tracking System are distributed among and performed by the three elements of the DSN: the Deep Space Stations (DSSs), the Ground Communications Facility (GCF), and the Network Operations Control Center (NOCC). Section II of this article and, in particular, Figs 4, 5, and 6 delineate this distribution and provide the relevant functional performance specifications.

D. Functional Operation

Simplified block diagrams of the DSN 26-m, 34-m and 64-m DSSs for Mark III-79 are shown in Figs 1, 2, and 3, respectively. Functional operation is as follows:

A spacecraft ephemeris is received from the project, together with standards and limits consisting of spacecraft frequencies, tuning rates, tuning range, data types and rates. DSN tracking predictions are generated from the spacecraft (S/C) ephemeris by the Network Operations Control Center (NOCC) Tracking Subsystem. After validation, the predictions are transmitted from the NOCC to the DSS via high-speed data lines (HSDLs) for use in acquiring the S/C carrier(s) and for frequency control. The predictions are also used in DSN Tracking System performance validation.

Data mode and system configuration messages are generated by NOCC and transmitted to the DSS by HSDL or voice,

and are used to select the radio metric data mode and system configuration.

Radio metric data, consisting of angles, range, DRVID, and doppler, together with associated data (i.e., time, frequencies, system configuration, data mode, and status) are measured and sampled by the DSS Tracking Subsystem and are formatted for transmission via HSDL. Performance validation data consisting of doppler, range, and angle residuals, and other analytic data, in addition to calibration data consisting of ground weather data and ionosphere data, are also formatted for transmission via HSDL. An Original Data Record (ODR) is generated for post-pass recall if necessary.

The radio metric data received from the DSS by the GCF are routed to the NOCC. A log containing all data received either in real time or by recall is generated by the GCF Central Communications Terminal, and is used to generate the project-dependent Intermediate Data Record (IDR) for delivery to radio metric data users.

The radio metric data received by the NOCC are formatted for digital television (DTV) and hard copy displays to be used in performance validation, fault isolation, and analysis by the Network Operations Control Team (NOCT). A System Performance Record (SPR) is generated which includes all received radio metric and calibration data, as well as analytic data generated from comparison of received data with predictions (residuals and data noise estimates). The SPR is used for nonreal-time detailed analysis of the systems performance.

II. System Functional Requirements and Performance

A. General

The following defines specific DSN Tracking System functional requirements for the Deep Space Stations (DSSs), Ground Communications Facility (GCF) and the Network Operations Control Center (NOCC). Figures 4, 5, and 6 present the functional requirements, subsystems, and interfaces for the Deep Space Stations, Ground Communications, and NOCC Tracking Subsystem, respectively.

Availability requirements for the DSN Tracking System during noncritical periods is 96 percent, based upon utilization of a single station. Availability is increased to 98 percent if redundancy is introduced through use of multiple stations. During critical periods availability is 98 percent with single station support and 99 percent with two or more stations supporting.

B. Deep Space Station Requirements

The Tracking System functional requirements assigned to the Deep Space Stations and the subsystems which perform these functions are shown in Fig 4. The following paragraphs further define these requirements.

1 Prediction data The DSS shall receive predictions transmitted via HSDL. The prediction HSD blocks shall be tested for errors and for data outages. If a block error or outage is detected, automatic recall shall be initiated.

The DSS shall store up to 12 sets of tracking predictions, 2 sets of uplink frequency control predictions, 2 sets of receiver control predictions, and 2 sets of receiver control predictions for DSS Operations Control and for DSS radio metric data validation. A set of tracking predictions is defined as predictions for up to 8 consecutive passes with a maximum of 200 lines per pass (2 lines per HSD block) for a DSS-spacecraft combination, or in the case of uplink frequency control and receiver control predicts, the predicts shall consist of frequency/time pairs with up to 28 pairs per predicts set. The system design shall attempt to minimize the number of predicts transmissions necessary to support tracking operations. The DSS will acknowledge receipt of predicts to the NOCC by transmission of an acknowledge message.

The DSS shall display all predictions received upon demand on a centrally located hard copy device.

2 System configuration and data mode messages The DSS shall receive and display system configuration and data mode messages transmitted via HSDL. The HSD blocks shall be tested for errors or outages at the DSS, and automatic recall shall be initiated if outages or errors are detected. The DSS will acknowledge receipt of configuration and data mode messages to the NOCC by transmission of an acknowledge message.

The DSS shall store and display on hard copy up to 12 system configuration and data mode messages.

3 System configuration and data mode control The DSS shall configure the Tracking Subsystem and select the data mode based on the system configuration and data mode messages. The configuration and data mode selection shall be under control of software in response to system configuration and data mode messages.

4 Antenna pointing control The DSS shall provide the following modes of antenna pointing control:

- (1) Autotrack mode (26 m)

- (2) Computer-aided mode with conical scan (34-m and 64-m DSSs) and without conical scan (26-m DSS)
- (3) Computer aided from
 - (a) Predictions
 - (b) Three-point right ascension-declination pairs
 - (c) Sidereal drive
- (4) Manual-aided mode

The antenna pointing control shall continuously point the DSS (assuming conscan in use at 34-m and 64-m DSSs) antenna to within $\pm 0.004^\circ$ (-0.05 dB from peak at X-band) of the center of the beam for 64-m DSSs, and $\pm 0.010^\circ$ (-0.1 dB from peak at X-band) for 34-m DSSs, and $\pm 0.050^\circ$ for 26-m DSSs. The control must be able to point the antenna under the following conditions

Angle motion about axis	HA $\pm 90^\circ$ from local meridian 26- and 34-m DSSs
	Dec 270° plus local latitude to 88° for northern hemisphere 26- and 34-m DSSs
	Dec 270° to 90° minus local latitude for southern hemisphere 26- and 34-m DSSs
	Az $\pm 265^\circ$ and E1 6° to 89° for 64-m DSSs
Angle rates	0 001° to 0 25° per second for 64-m DSSs
	0 001° to 0 4° per second for 34-m DSSs
	0 001° to 0 8° per second for 26-m DSSs
Wind conditions	0-48 km/h (nondegraded performance)

5 Frequency and timing The DSN Frequency and Timing System shall support the DSN Tracking System by providing interstation and intercomplex epoch time synchronization and relative clock frequency data. Data relating each station to a complex master, and the DSN master to the National Bureau of Standards (NBS) shall be provided. Required performance is as follows:

- (1) Provide time and frequency synchronization to the DSN master clock. Time synchronization to better than 10 microseconds, and knowledge of frequency synchronization between 26-m DSSs and the complex master clock to less than 3 parts in 10^{13} and between the

34-m and 64-m DSSs and the DSN master clock to less than 3 parts in 10^{13} required, and less than 1 part in 10^{13} as a design goal

- (2) Knowledge of time synchronization between the DSN master clock and NBS shall be less than 5 microseconds

6 Receiver and exciter assembly frequency control The DSS shall provide software control of the receiver and exciter assembly frequencies for S/C acquisition and tracking. The frequencies shall be referenced to predictions. The receiver-exciter programmed oscillator frequency control shall be $< 3^\circ$ phase at S-band (60-second average). Frequency control resolution shall be $\leq 2^{-12}$ Hz per second at S-band. Exciter and receiver reference frequencies shall be reported in the radio metric data block so that reconstruction of the uplink by the project orbit determination group is accurate to 3° phase at S-band. The capability for simultaneously supporting an uplink and downlink on noncoincident frequency channels shall be provided. A monitor of receiver performance (actual receiver frequency) shall be provided.

7 Doppler extraction and counting The DSS shall extract and count doppler from one S-band carrier and one X-band carrier simultaneously at the 64-m stations, one S-band and one X-band carrier from the 34-m stations, and one S-band carrier at 26-m stations

One-, two-, and three-way doppler shall be extracted under the following conditions

Doppler shift ± 79 km/s (mission life time)

35 km/s (single pass)

Doppler rate near Earth 500 m/s 2

Doppler rate planetary encounter or orbit 10 m/s 2

Integrated doppler resolution shall be < 0.005 cycle. Accuracy requirements for round-trip light time (RTLT) of 1000 seconds for 26-m stations, 2000 seconds for 34-m stations, and 10,000 seconds for 64-m stations are listed in Table 2

Integrated three-way doppler shall conform to the same accuracy as two-way doppler except for the offset in frequency standards between the transmitting and receiving DSS S/X-band integrated doppler, when differenced, shall be accurate to 0.1 meter per 15 minutes and 0.2 meter per 12 hours. Doppler sample rates shall be selectable at 10 per second, 1 per 10 seconds, 1 per 20 seconds, 1 per 30 seconds, 1 per minute, 1 per 2 minutes and 1 per 10 minutes. Capability shall be provided to demonstrate the required system performance

8 Range and DRVID generation, acquisition, and measurement The DSS shall extract and measure S- and X-band range and DRVID for one spacecraft using the discrete spectrum code. Code length, probability of good acquisition, DRVID, and range integration times shall be selectable under software control. Operator control inputs shall be minimized. DRVID data shall be available after an acquisition has been completed. The DSS shall provide a capability of automatically measuring and reporting the DSS ranging calibration. Ranging calibration shall be included in the radio metric data stream, along with pertinent configuration information.

Range ambiguity shall be selectable between 150 m and 150,000 km. Range and DRVID high-frequency noise errors are a function of received ranging signal power and integration time and may be reduced to < 1 m RMS by selection of longer integration times. For all other ground error sources, range is required to be accurate to $< 4.5\sqrt{2}$ m, the design goal is < 3 m. Range and DRVID resolution shall be ≤ 1 nanosecond. DRVID stability shall be < 1.0 m per 15 minutes and < 1 m per 12 hours.

DRVID and range data shall be output to the HSDL for each DRVID and range acquisition. Multiple range acquisitions shall be possible within the round-trip light time to the spacecraft. DRVID data between range acquisitions shall be possible.

9 Angle readout The DSS shall provide the antenna axis position readout in the HA/Dec* coordinate system. Angle data shall be read out to a resolution $\leq 0.001^\circ$ and have an accuracy (boresight) of $< 0.05^\circ$ for 26-m DSSs, $< 0.01^\circ$ for 34-m DSSs, and $< 0.004^\circ$ for 64-m DSSs. Angle sample rates shall be 1 per second, 1 per 10 seconds, 1 per 20 seconds, 1 per 30 seconds, 1 per minute, 1 per 2 minutes, and 1 per 10 minutes.

10 Calibration data ground weather and ionosphere Ground weather data, consisting of pressure, temperature, and relative humidity, shall be provided at each DSS complex with the capability of digital sampling at rates of one per minute, one per 5 minutes, one per 10 minutes, and one per 15 minutes. Ionosphere data in the form of Faraday rotation data from polarimeter tracking of a stationary Earth satellite shall be digitized and sampled at rates of one per minute, or one per five minutes. Information to determine satellite line of sight shall be provided with the Faraday rotation data.

The calibration data (ground weather and ionosphere) shall be formatted into a calibration data block and interlaced with

*DSS 44 angle readout will be in X/Y coordinates

radio metric data for transmission to the NOCC Continuous recording of these data shall be provided to support scheduled recall for user IDR generation

Ground weather data shall be provided to the following accuracies

Pressure ≤ 10 millibar ($\leq 100 \text{ N/m}^2$)

Temperature $\leq 10^\circ\text{C}$

Relative humidity ≤ 5 percent

Ionosphere data shall have an accuracy of $\leq 10.0^\circ$ polarization angle. Continuous recording of ionospheric data shall be provided with no outage < 5 minutes unless so scheduled. The user shall be provided 99 percent of the recorded ionospheric data.

11 Radio metric data handling control and formatting
The DSS shall provide identification by DSS and spacecraft for data stream control; and for selective sampling of doppler, range, DRVID, angle data, and calibration data. Data sampling shall be selectable as stated above. The radio metric data with interlaced exciter and receiver reference frequencies, system status, and system configuration and data mode shall be formatted in HSD blocks for output to the GCF High-Speed Data Subsystem. Also, calibration data (ground weather and ionosphere) shall be formatted in HSD blocks, separately from radio metric data, for output to the GCF High-Speed Data Subsystem.

12 Partial status interface with radio metric data The DSS shall include the partial status parameters listed in Table 3 with the radio metric data. In addition to Table 3 parameters, each DSS shall also have the capability to provide the following status parameters

- (1) Doppler residual
- (2) Doppler phase jitter
- (3) Estimate of doppler slipped cycles
- (4) Receiver signal level (AGC) and receiver frequency
- (5) Static phase error (SPE)
- (6) Range residual
- (7) Range and DRVID noise
- (8) Ranging signal power to noise ratio (Pr/No)

Estimate of doppler slipped cycles, doppler noise, range noise, and DRVID noise shall conform to the following accuracies

Slipped cycles	≤ 1 cycle	Carrier signal level	≤ 1 dB
Doppler	≤ 0.002 Hz	Static phase error	$\leq 3^\circ$
Range	≤ 1 nanosecond	Pr/No	≤ 1 dB
DRVID	≤ 1 nanosecond		

13 Radio metric and calibration data output to HSDL

Radio metric and calibration data shall be sampled and transmitted as requested. A capability shall be provided to retransmit an HSD block or blocks during an active pass in response to a replay request from the NOCC at any sample rate up to 10 samples per second.

14 DSS tracking high rate data record A High Rate Data (HRD) Record containing all data available for replay transmission shall be made by the DSS. The HRD record shall reliably contain 99.5 percent of all data recorded within the most recent 14 hours or more and shall be available for replay within 10 minutes of a request. The radio metric data on the HRD record shall be available for replay by time span and will constitute a new data stream.

15 Station location and universal time calibrations The DSN VLBI System shall support the DSN Tracking System by providing determination of DSS locations (longitude, distance normal to the spin axis, Z-height) and UT1 (Universal Time relative to Atomic Time) to the accuracies indicated in the various Project System Instrumentation Requirements Documents (SIRDs). Baseline parameters (length, longitude, relative Z-height, and polar motion) used in the VLBI System shall be conveyed to the flight projects by the DSN Tracking System. The capability to determine DSS location and UT1 calibrations using radio metric (two-way doppler) data shall be retained until the VLBI System capability is fully implemented and verified.

C. Ground Communications Requirements

The Ground Communications Facility HSD Subsystem transmits DSN Tracking System data between the DSS and the NOCC via HSD lines. NOCC communications between the NOCC Tracking Real-Time Monitor and the NOCC Display Subsystem is via the Wideband Data Subsystem.

The functional requirements assigned to the Ground Communications Facility and the subsystems used to perform these functions are shown in Fig. 5. The following paragraphs further define these requirements.

1 Radio metric and calibration data transmission Ground communications shall have the capability to transmit DSS radio metric and calibration data from the DSS to the NOCC

via high-speed data lines Routing of the high-speed data blocks shall be based on destination code and UDT

The maximum data transmission outage shall be < 15 minutes The maximum data transmission loss due to outages or blocks in error shall be ≤ 2 percent per 12 hours and < 1 percent per 10 days

2 Tracking predictions transmission Ground communications shall have the capability to transmit DSS tracking predictions from the Network Support Controller to the DSS via high-speed data circuits Routing of the high-speed data blocks shall be based on the destination code and UDT

3 System configuration and data mode message transmission Ground communications shall have the capability to transmit system configuration and data mode messages from the NOCC to the DSS Routing of the high-speed data blocks shall be based on destination code and UDT

4 Error detection and correction Ground Communications Facility HSD block errors or outages shall be detected and corrected by automatic recall from the transmitting source An alarm shall be generated if reception is not achieved in five or less attempts to recall the desired data

5 Tracking ODR generation The GCF shall generate an Original Data Record (ODR) that contains > 99 percent of all data received from the DSS Tracking Subsystem Capability for recall of radio metric data from the ODR shall be supplied

6 Selective recall from GCF log (IDR generation) The GCF Central Communications shall generate an Intermediate Data Record (IDR) for radio metric data and calibration data Data shall be selectable as project dependent and DSS independent It shall be possible to merge in a time ordered sequence data from more than one IDR to provide up to seven days of radio metric data on a single IDR IDR data content shall be as follows ≥ 95 percent of noncritical phase radio metric data, and ≥ 95 percent of critical phase data available within 30 minutes of receipt of request and 98 percent within 24 hours Percent of data on an IDR is relative to data available on Original Data Record at transmitting source

D. Network Operations Control Center Requirements

The NOCC generates predictions from project-supplied ephemeris and generates data mode and system configuration messages that are transmitted via HSDL for use by the DSS in the acquisition of the S/C signal and the generation of radio metric data The NOCC Tracking Subsystem shall generate a System Performance Record

The functional requirements assigned to the NOCC Tracking Subsystem and the assemblies used to perform these functions are presented in Fig 6 The following paragraphs further define these requirements

1 DSS predictions The NOCC Tracking Subsystem shall have the capability to generate DSS predictions from project-supplied ephemeris data, S/C frequencies, and S/C standards and limits consisting of uplink tuning rates and ranges DSS predictions consist of the following parameters

- (1) GMT
- (2) Angles and angle rates (HA/dec, az/el or X/Y)
- (3) One-way S-band doppler and doppler rate
- (4) One-way X-band doppler and doppler rate
- (5) Two-way S-band doppler and doppler rate
- (6) Two-way X-band doppler and doppler rate
- (7) Three-way S-band doppler for up to six transmitting stations
- (8) Three-way X-band doppler for up to six transmitting stations
- (9) Two-way range
- (10) Uplink frequency and frequency rate
- (11) Receiver-exciter digital-controlled oscillator predictions
- (12) Spacecraft rise-spacecraft set
- (13) Round-trip light time
- (14) Subcarrier Demodulator Assembly frequencies

The accuracy of predictions computed from project-supplied ephemeris is as follows

Angles $< 0.0035^\circ$

Doppler ≤ 0.1 meter per second (cruise phase)

≤ 0.2 meter per second (launch phase or orbital phase)

Range ≤ 5 meters (cruise phase)

≤ 45 meters (launch phase or orbital phase)

S/C rise/set ≤ 5 minutes (approximately 1 degree), cruise or orbital phase

≤ 30 seconds (approximately 2 degrees), launch phase

Occultation events ≤ 0.1 second

Differenced range minus integrated doppler 2 meters in 4 hours

Prediction point-to-point relative accuracy and precision shall be as follows

Angles $\leq 0.001^\circ$

Doppler ≤ 0.07 millimeter per second

Range ≤ 0.2 meter

2 System configuration, data mode messages The NOCC Tracking Subsystem shall generate system configuration and data mode messages for use by the DSS in generating radio metric data and validation of DSN Tracking System performance

3 Tracking predictions, system configuration, and data mode messages The NOCC Tracking Subsystem shall format predictions, system configuration, and data mode messages The NOCC Tracking Subsystem shall output these messages for transmission to the appropriate DSS via HSDL

4 System configuration and data mode verification The NOCC Tracking Subsystem shall verify the system configuration and data mode by comparison of system configuration and data mode parameters against standards and limits Alarms and/or changes in system status and configuration shall be reported to DSN Operations Control within 10 seconds after detection

5 Radio metric data/prediction data comparisons The NOCC Tracking Subsystem shall compare doppler data with predictions for two data streams Two station range validation shall be accomplished to verify ranging performance

6 System performance and status detection The NOCC Tracking Subsystem shall detect system performance and status by the analysis of system status parameters and alarms A capability shall be provided to isolate the alarm to the subsystem level

7 Status and alarms transmission to DSN Monitor and Control All alarms and changes in system status shall be reported to DSN Monitor and Control System

8 Display data transmission to Network Operations Control Area System status, configuration, modes, and performance parameters such as data residuals and noise estimates, HSDL status, NOCC Tracking Subsystem status, and prediction status shall be reported to the Network Operations Control Area for DTV and hardcopy display A graphics capability shall provide plotted displays of selected radio metric parameters

9 Tracking system performance record A record for system performance, status, and alarms shall be generated for nonreal-time analysis

10 Control messages from Network Operations Control Area The NOCC Tracking Subsystem shall receive and respond to control messages transmitted from the Network Operations Control Area

11 DSN time synchronization performance monitor and reporting The DSN Frequency and Timing System shall provide interstation time synchronization to better than 10 microseconds between DSS and the DSN master clock, and to better than 5 microseconds between the DSN master clock and National Bureau of Standards A capability shall be provided to monitor performance to this level with clock synchronization data provided to radio metric users on a regular basis

12 Replay requests Requests for replay data from the HRD record at the DSS shall be generated at the NOCC Replay request shall be by time span and may be at any data sample interval up to 10 samples per second Replay data shall appear as a new data stream, and may be received along with other radio metric data streams from a single DSS

III. Summary

This article, composed primarily of excerpts from the recently released Deep Space Network Systems Requirements Document (821-9), DSN Tracking System (1979 through 1983), is intended to provide an overview of the DSN Tracking System and its functional requirements and performance characteristics For a more detailed description including the allocation of requirements to subsystems, testing philosophy and requirements, and implementation priorities, the reader is referred to the aforementioned document Also, for a detailed description of a major and new capability implemented in response to the failure of the Voyager 2 spacecraft receiver, Reference 1 is suggested

Reference

- 1 Spradlin, G L , "DSN Tracking System Uplink Frequency Control," *DSN Progress Report 42-53*, pp 108-112, Jet Propulsion Laboratory, Pasadena, California, October 15, 1979

Table 1 Planned DSS radio metric data capability

Data type	26-m DSS	34-m DSS	64-m DSS
Doppler	1 S-band	1 S-band or 1 S- and X-band	1 S-band or 1 S- and X-band
Range	N/A	1 S-band or 1 S- and X-band	1 S-band or 1 S- and X-band
DRVID	N/A	1 S-band or 1 S- and X-band	1 S-band or 1 S- and X-band
Angles	Auto track or computer aided	Computer aided with conical scan	Computer aided with conical scan

Table 2 Integrated two-way doppler accuracy

Averaging times	Accuracy
1 s	≤0 003 m per second
60 s	≤0 045 m per 60 seconds
1000 s	≤0 10 m per 1000 seconds
12 h	≤0 50 m per 12 hours

Table 3 Partical status parameters

Status	Configuration	Data mode
Doppler good-bad	Block III or Block IV doppler extractor	Sample rate
Receiver lock	Doppler receiver reference	Doppler type
Transmitter frequency lock	Doppler bias	Angle mode
Frequency standard	Exciter in use (Block III – Block IV)	Conscan mode
Timing standard	Transmitter on-off	Range code length (first component, last component)
Angle autotrack	Transmpter (klystron) in use	Range inte- gration times
Range acquisition	Transmitter power level	
Range validity	Maser type and number	
DRVID acquisition	Angle type	
DRVID validity	FTS frequency standard	
DTK hardware/ software (self- diagnostic test)	Predicts set in use	
	Range Modulation on-off	
	Carrier suppression for ranging	
	Chopper frequency on-off	
	Pipelined acquisitions on-off	
	Prime range channel S-X	

This Page Intentionally Left Blank

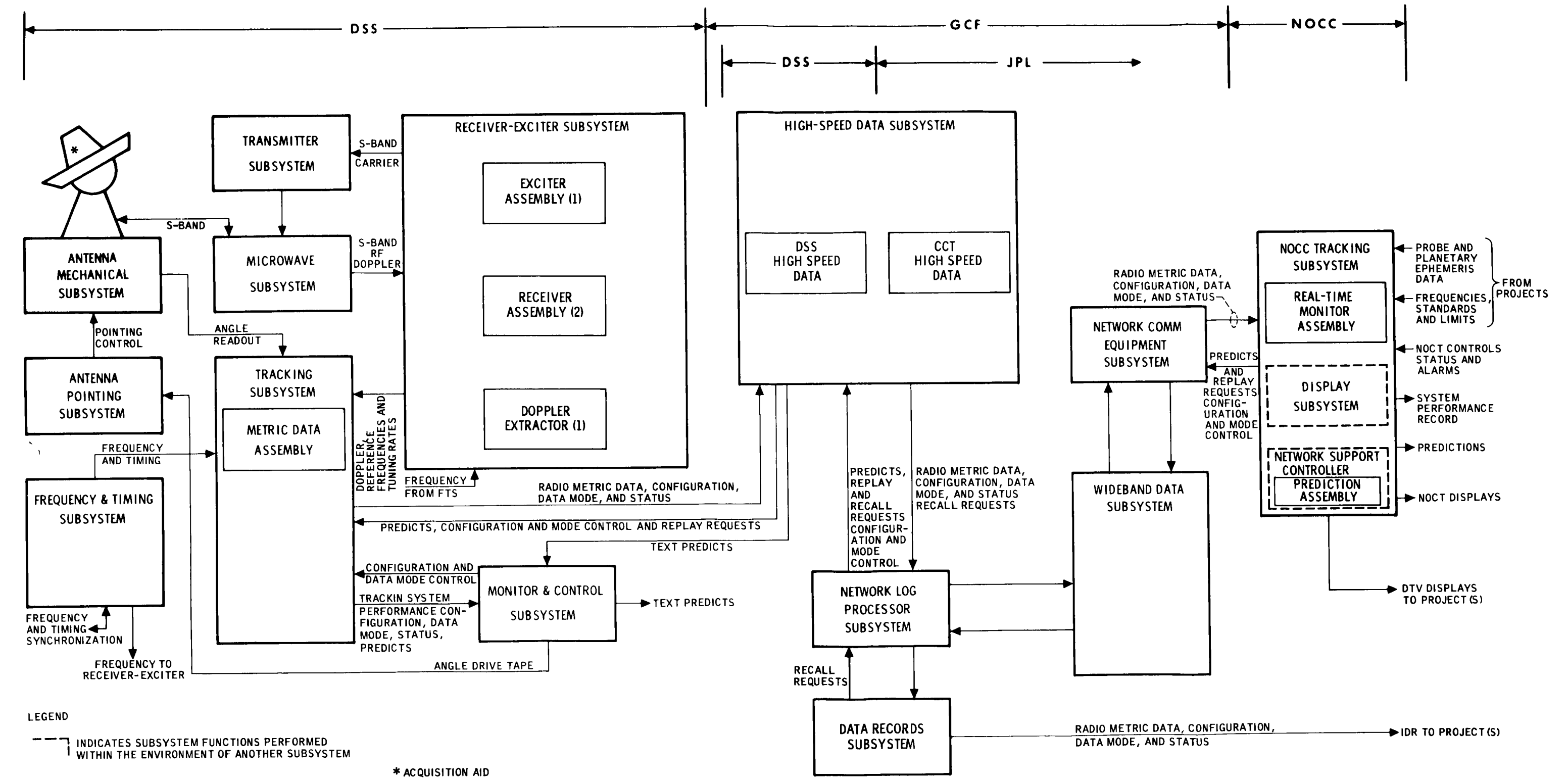


Fig 1 DSN Tracking System 26-m DSS simplified block diagram, Mark III-1979 configuration

This Page Intentionally Left Blank

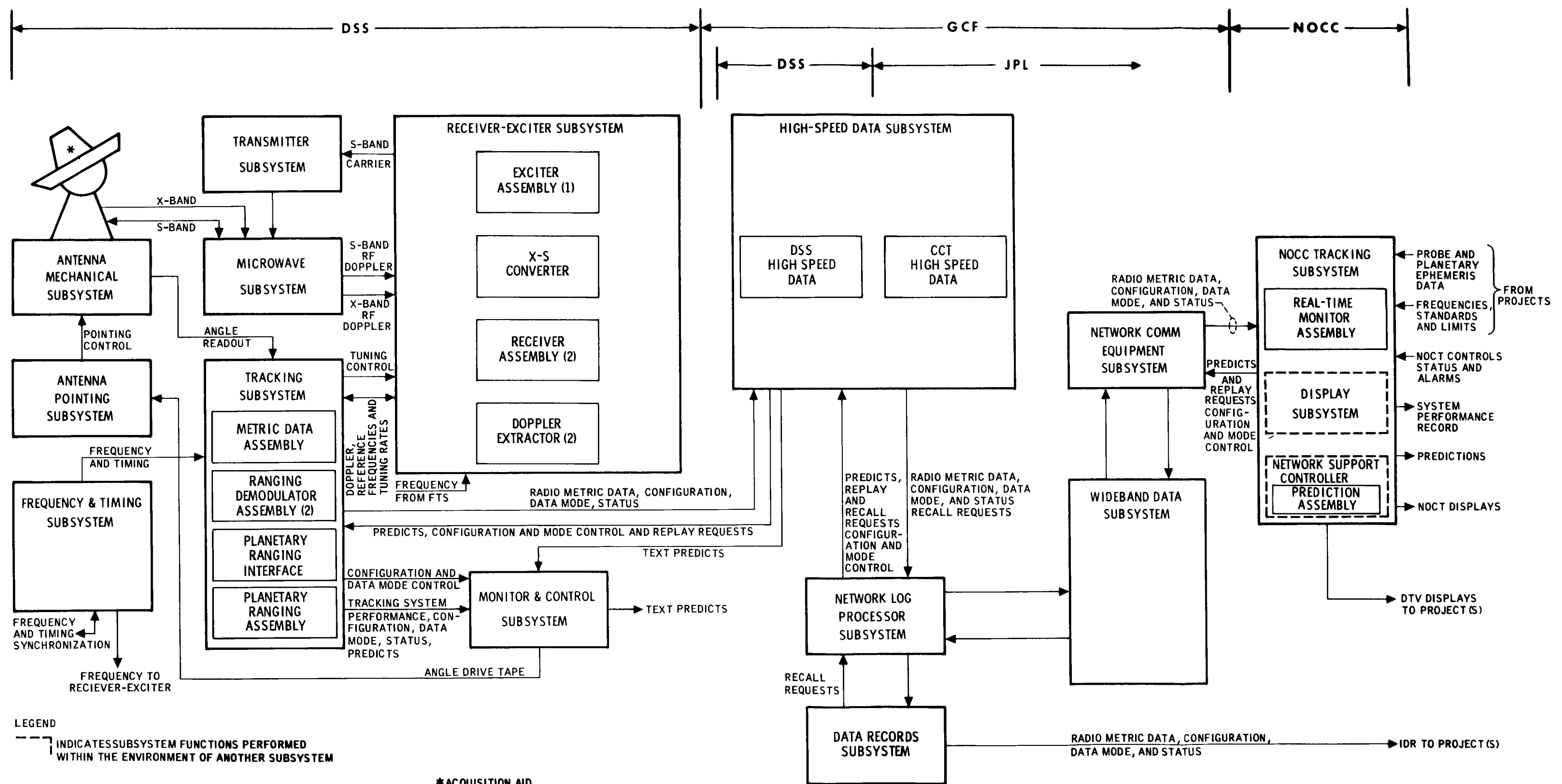


Fig 2 DSN Tracking System 34-m DSS simplified block diagram, Mark III-1979 configuration

This Page Intentionally Left Blank

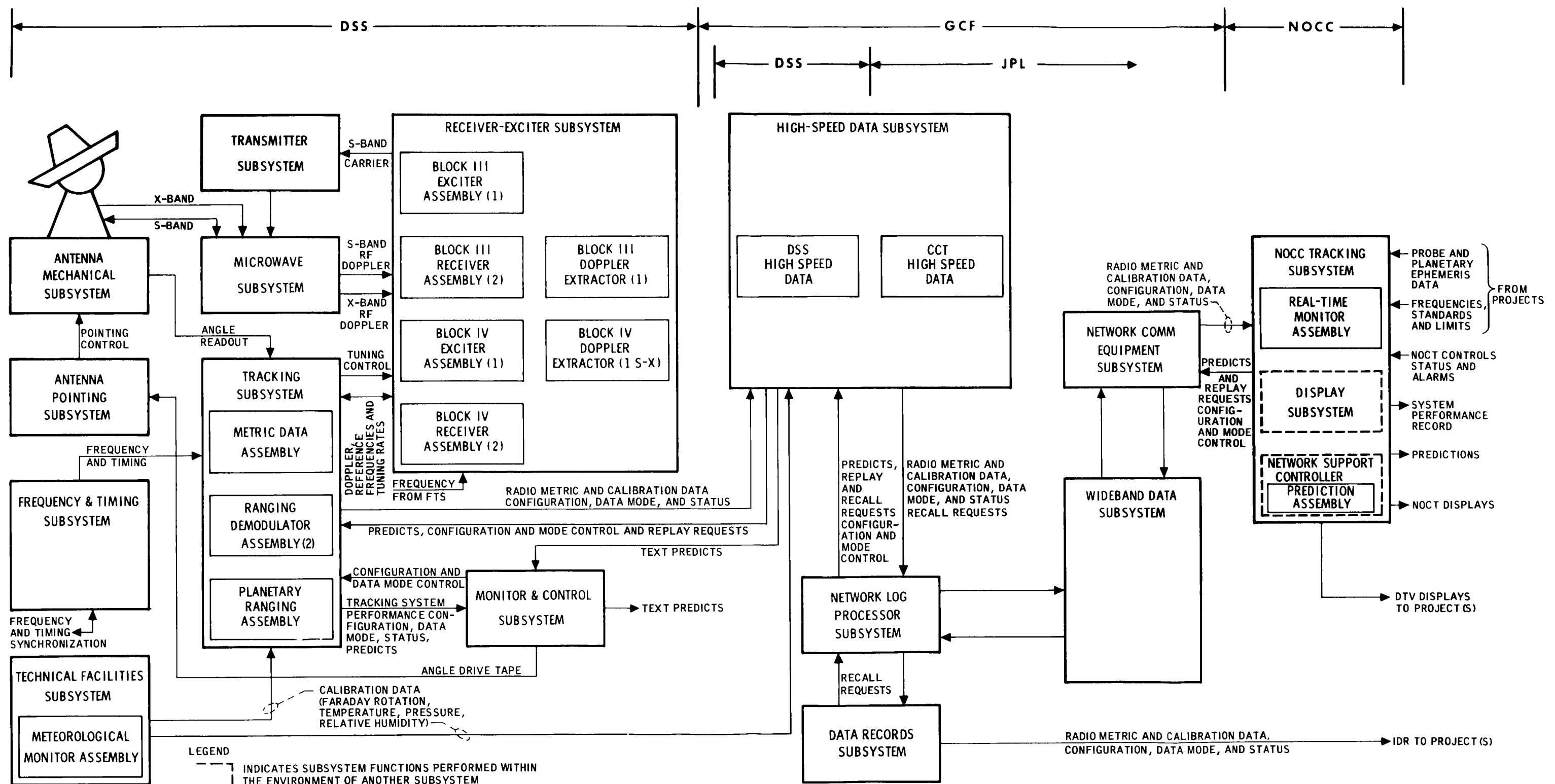


Fig 3 DSN Tracking System 64-m DSS simplified block diagram, Mark III-1979 configuration

This Page Intentionally Left Blank

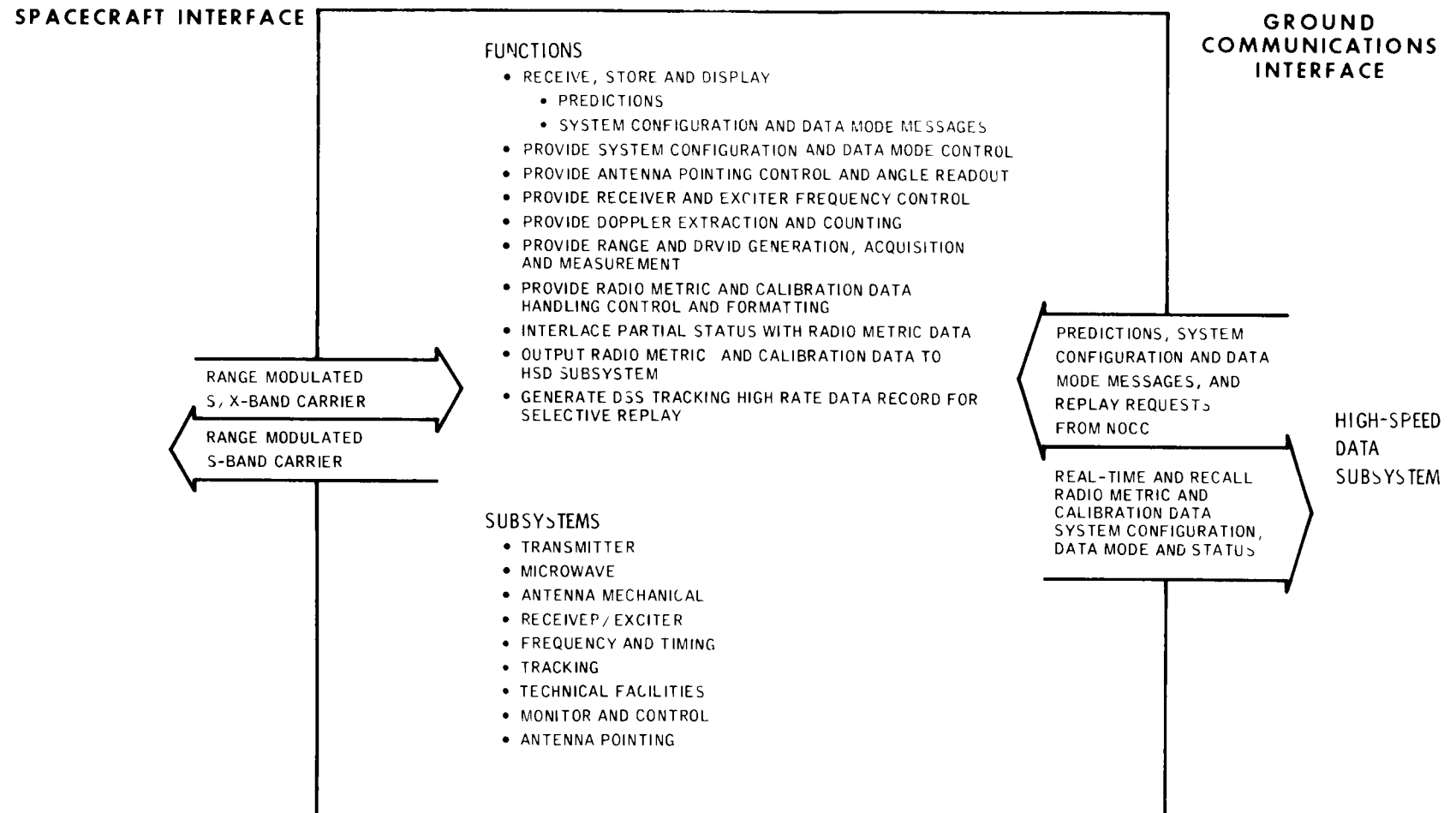


Fig 4 DSS tracking functional requirements and interfaces for spacecraft acquisition and radio metric data generation

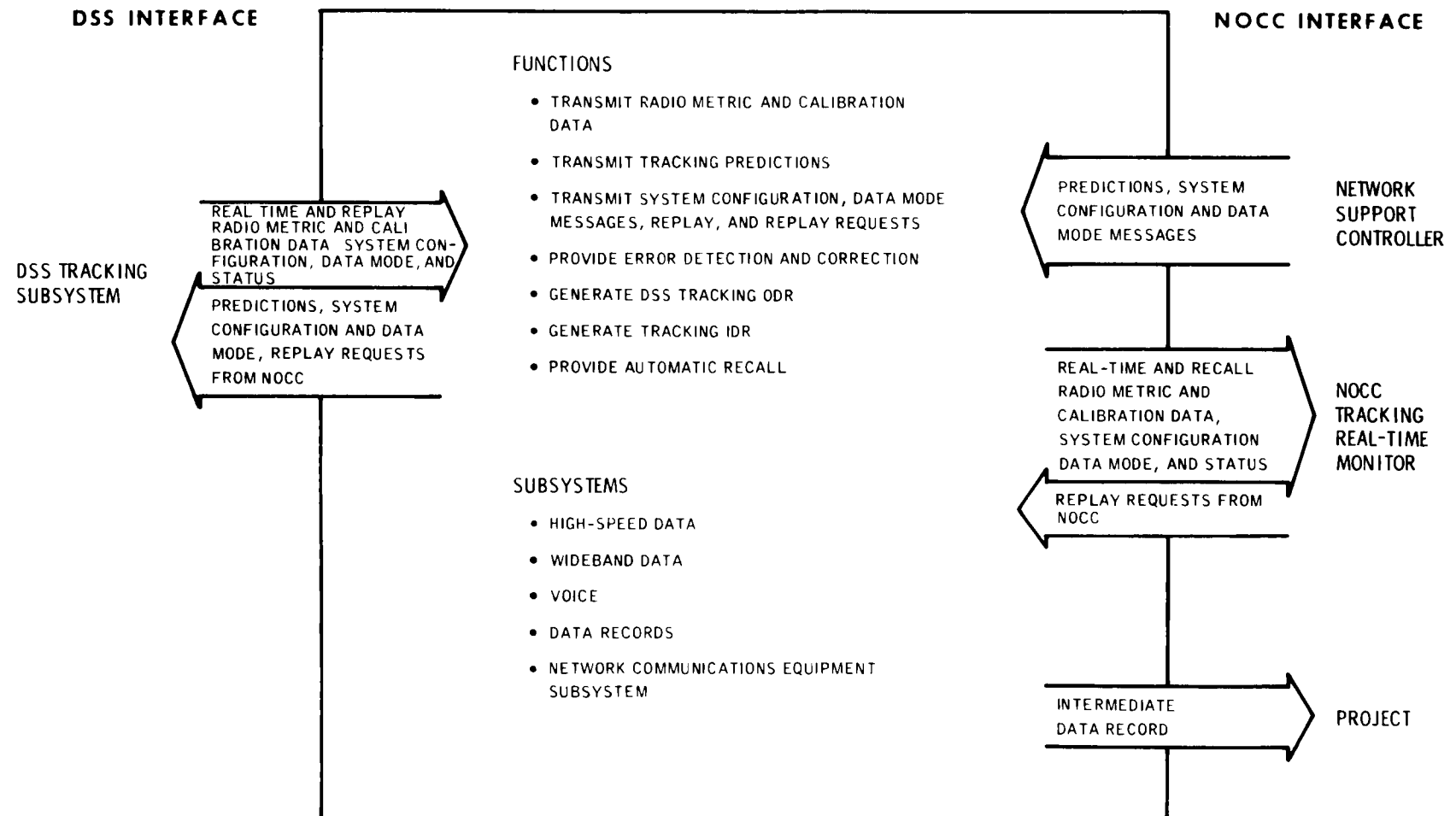


Fig 5 Ground Communications Facility functional requirements and interfaces

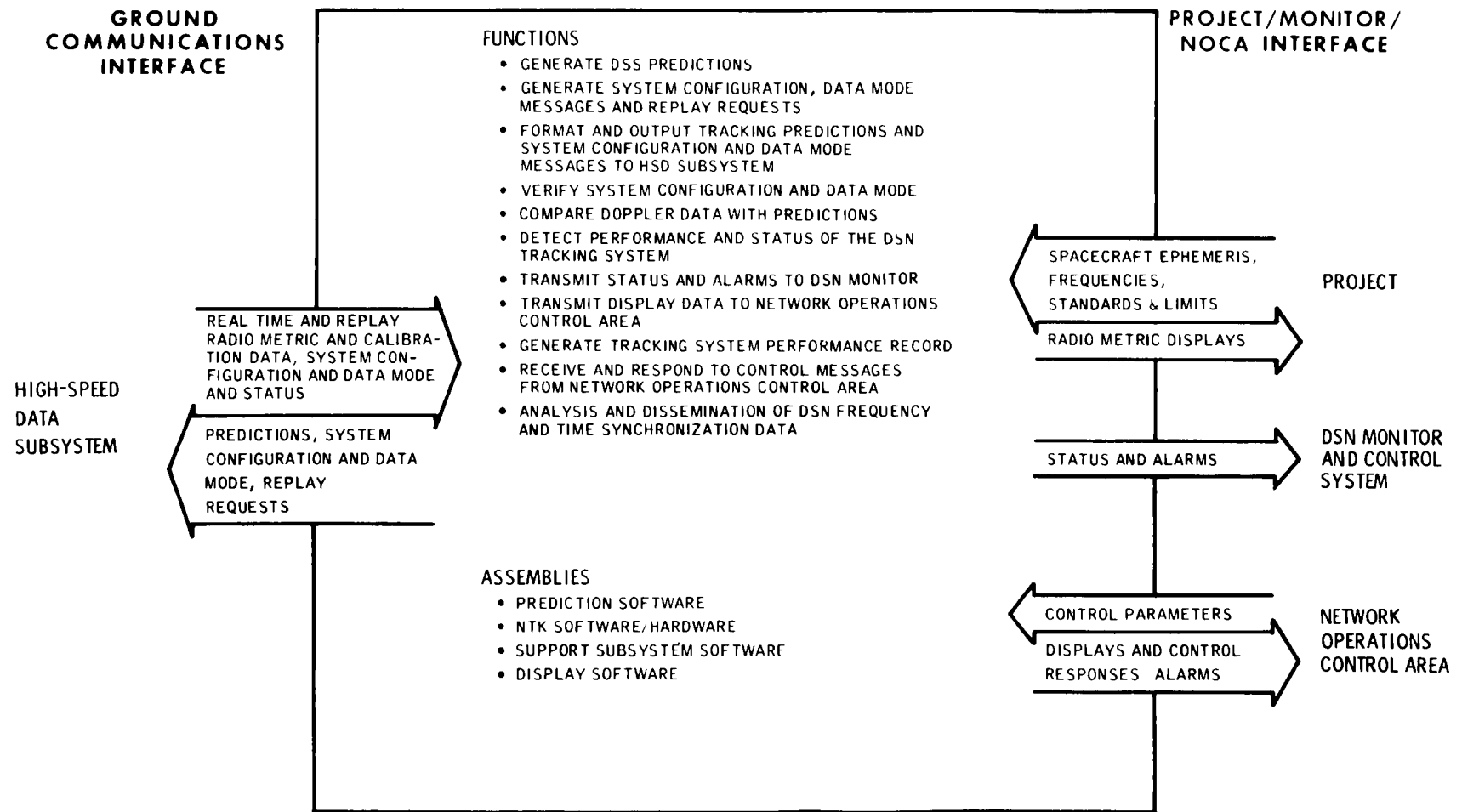


Fig 6 NOCC Tracking Subsystem functional requirements and interfaces

DSN VLBI System MK 1-80

W D Chaney

TDA Engineering Office

N C Ham

Telecommunications Science and Engineering Division

This article describes the DSN VLBI System MK 1-80 that is being implemented to provide navigation support to the Voyager Project. It describes the system requirements, description and the implementation plan.

I. Introduction

The DSN VLBI System MK 1-80 is being implemented to provide navigation support to the Voyager Project. The measurements made by Very Long Baseline Interferometry (VLBI) will provide precision time and time interval between the 64-m Deep Space Stations located at Goldstone, California, Canberra, Australia, and Madrid, Spain. In addition, measurements of interstation baseline, Earth rotation (Universal Time One) and polar motion will be made.

The Voyager project navigation requirements for Saturn encounter are $< 10 \mu\text{sec}$ interstation time synchronization and < 3 parts in 10^{13} for intercomplex time interval measurements. In addition, it is desired to measure Universal Time One to < 1 millisecond and polar motion to < 0.7 meters.

A functional description, estimated accuracies and implementation phasing are discussed in this article.

II. System Description

A. Definition

The Deep Space Station (DSS) VLBI System is the assemblage of various subsystems at a specific DSS which form an instrument for receiving and obtaining necessary VLBI data in conjunction with other similar DSSs and, together with

elements involved with the monitoring and control and data processing functions, comprise the DSN VLBI System.

Elements external to the DSSs receive the data via the Ground Communication Facility (GCF) and through further data processing provide information in a form for user application. These elements are located at JPL, as portions of the Network Operational Control Center.

The DSS system, when used for VLBI application, is defined as the mode when observation of only extragalactic radio source (EGRS) is being performed by two DSSs. From the measurements of difference in time of arrival of the EGRS signal between stations, the position of the radio sources can be determined, together with several other parameters of the problem solution. These other parameters include Universal Time One (UTI), Earth polar motion, the relative position of the observing stations, as well as the time offset and rate of change between station clocks.

B. Description

Functionally the VLBI system (Fig. 1) is comprised of the DSSs, which individually receive the RF signal and down-convert segment bandwidths of the RF spectrum to video-band frequencies which are then digitized and formatted by

digital equipment The digital data is then transmitted via the GCF to the NOCC and to the VLBI processing area for signal processing with data from other observing stations

The DSS Antenna Subsystem is pointed to the appropriate signal source at the proper time by the Antenna Pointing Subsystem, which obtains pointing information (predicts) from the Network Data Processing Area (NOPA) of the NOCC via the GCF and DSS Tracking Subsystem (DTS)

The Antenna Microwave Subsystem (UWV) receives the signal flux gathered by the antenna After amplification by the Traveling Wave Maser (TWM) the signal is sent to the Receiver-Exciter Subsystem, which heterodynes this signal to an intermediate frequency (IF) The IF signal is down-converted to video-band frequencies which are then digitized and formatted by the DSS Radio Science Subsystem (DRS)

The Frequency and Timing Subsystem (FTS) provides the station local clock, using a very stable hydrogen maser as the primary standard Reference frequencies and timing signals are derived from the clock for distribution to other subsystems Similarly, a reference signal from the coherent reference generator (CRG), which distributes the reference signals, will drive coherent comb generators located within the Microwave Subsystem via a coaxial-cable, phase-stabilization assembly which effectively translates the station's clock frequency stability to the comb generators The comb generator provides comblike, phase-stable, line spectra S- and X-band microwave frequencies, which are injected into the respective Microwave Subsystems prior to the input circuitry of the TWMs

These phase-stable reference signals are amplified by the receiver and are down-converted simultaneously with the received signals These reference signals will be used to calibrate out phase variations (which occur within the receiver, down converter, and digital subsystems) later during the cross-correlation and data processing procedure Since the comb signal encounters the received signal for the first time at the injection point, this point is established as the instrument's RF reference point for the DSS VLBI System This is the point at which the cross-correlation and postcorrelation estimation calculations refer the resultant Earth parameters, station location and clock offset and rate information relative to the other instruments

The reference is used to relate other station references such as the station's location reference point (intersection of antenna axes or equivalent) and the Epoch reference point at the FTS CRG output located within the control room The cable stabilizer effectively translates these points with a known time delay for interstation clock synchronization purposes The clock Epoch reference point in turn will function as the

reference for all subsystems and assemblies within the respective stations

The DRS records the VLBI data for a real-time record and, in near-real-time, sends the data to the NOCC and the VLBI processing area This subsystem controls the various DSS subsystems for proper configuration during the operational sequence It also receives ancillary data from the DSS subsystems which is forwarded to NOCC for monitoring information and to the processing area as processing information

The DSS Monitor and Control Subsystem (DMC) sends control and configuration information to the DRS from data received from NOCC via the GCF It also collects various calibration and configuration data which is provided to the DRS for logging and transmission, via the GCF, with the VLBI data or separately for monitoring purposes

At NOCC (Fig 2), the Network Data Processing Terminal (NDPT) uses the data for monitoring-display functions in the Network Operations Control Area (NOCA) The NOCA also provides the control information to the DSSs, via the GCF, to the DMC The NDPA uses the data for real-time monitor functions

The VLBI Processor Subsystem performs the cross-correlation of the data from the observing stations and, with further postcorrelation and estimation processing, VLBI information is made available to the user in the proper form

III. Implementation

A. General Description

Implementation of the DSN VLBI System MK 1-80 will be in four phases as described below

Phases 1, 2, and 3 configurations (Fig 3) at the DSS remain essentially unchanged, with the changes occurring in the NOCC and VLBI processing area The Phase 4 configuration change occurs largely within the DSS portion where the Receiver-Exciter and Radio Science Subsystems are involved The DSN VLBI System MK 1-80 configuration will exist at the 64-m DSSs with the VLBI processor in NOCC

B. Phase 1 Configuration

The Phase I configuration (Fig 3) will utilize the existing DSS BLK IV receivers for a simultaneous S- and X-band reception capability The wide-band capability is achieved by providing a separate wide-band output from the antenna mounted assemblies and a separate coaxial cable to the control room equipment

The receiver outputs are input to the Advanced Equipment Subsystem (AES), which can select any receiver IF signal. The receiver IF signal is input to the IF to video down-converter for bandwidth synthesis (BWS) function. The outputs of the down converter channels are sent to the DRS, via an interface assembly, where the VLBI Converter Assembly and Occultation Data Assembly (ODA) digitizes and formats the data for transmission to NOCC. The ODA also provides a Real Time Record of the data and control to the AES via the interface assembly.

Station weather data, which is obtained by the Meteorological Monitoring Assembly (MMA) of the Technical Facility Subsystem (FAC), is sent to the DSS Tracking Subsystem (DTS). This information, together with the antenna angles sent from the Antenna Mechanical Subsystem (ANT), is also sent to the ODA and is included with the VLBI data which is forwarded to the station wideband data assembly of the GCF.

The antenna pointing predicts are generated by the Predict Program within the Network Control Support Subsystem (NCSS) of the NOCC, from the Radio Source Catalog, and are received by the DTS via the GCF HSDL and CMF. These predicts are then used to direct the Antenna Pointing Subsystem (APS) from a drive tape prepared via the DSS Monitor and Control Subsystem (DMC).

The DMC obtains various monitor input information which is sent to the DRS as control and configuration data for transmission to NOCC. Sequence-of-Events (SOE) and status information is also sent between the DMC and NOCC via the HSDL. The NOCC NDPT displays the configuration and status information at the Network Display Subsystem, with display to and control from the Network Operations Area (NOA).

The VLBI data from the ODA is received by the Network Log Processor Assembly (Fig 4) of the GCF, which generates a network data log. This data is used to generate an Intermediate Data Record (IDR), which is then sent to the NOCC NDPA as a precorrelation record, with similar records from the other observing stations for cross-correlation within the VLBI Processor Subsystem. A postcorrelation record is obtained from the correlation program of the processor and, with the postcorrelation program and estimation program, the information related to station clock synchronization, UTI and Earth polar motion is made available to the user.

C. Phase 2 Configuration

The DSS portion of this phase remains the same as Phase I. The main change occurs in the VLBI data transmission and the VLBI Processor Subsystem (Fig 5). The VLBI data from the DRS is sent via the GCF over wide-band data lines (WBDL) to the VLBI Processor Subsystem, located in the VLBI Processor

Subsystem, which cross-correlates the similar precorrelation record from the other observing station.

The postcorrelation record is obtained from the VLBI Processor Subsystem and, in addition, the VLBI correlator status information is sent from this processor to the DMC via the GCF HSDL. The postcorrelation record is then used by the postcorrelation and estimation program of the interim VLBI Post Correlation Processor (360/75), which is remotely located from the VLBI Processing Room. The resulting computed information on clock synchronization, UTI and polar motion is obtained from the processor for user application.

D. Phase 3 Configuration

The primary change of this phase occurs in the VLBI Processor Subsystem. This subsystem replaces the interim postcorrelation (360/75) function (Fig 2) and performs all the normal functions of cross-correlation and postcorrelation and estimation within the VLBI Processor Subsystem.

E. Phase 4 Configuration

This phase has the major change within the DSS, particularly within the Receiver-Exciter and Radio Science Subsystems (Fig 1). The receivers operating at both S- and X-band replace the DSS Block IV receivers previously used. These new receivers are phase stable and possess a wide instantaneous bandwidth (span bandwidth of approximately 400 MHz centered at 300 MHz).

The IF signals terminate in their individual IF to video converter assembly, which replaces the BWS channels of the AES. The video converters each provide two down-converted video band spectrum signals, in quadrature phase, which are sent to the DRS for further operation. The local oscillator which down-converts the wide-band IF spectrum into individual channels is comprised of 8 (for X-band) separate frequency-set digital controlled oscillators (DCO), which are sequentially selected to provide the narrow segment bandwidth channels. This scheme permits the independent frequency setting and continuous operations of the individual channel oscillators to maintain the phase continuity as they are sequentially selected.

The DRS receives the two quadrature signals from the converters and, after digitization and further processing, rejects the image noise "foldover" of the video spectrum and then low-pass filters this spectrum to reduce the harmonics by using digital techniques. The signal is then formatted and transmitted to the VLBI Processor Subsystem via the GCF WBDL. The DRS also provides the control signals to the receiver subsystem for DCO frequency control and channel selection.

The S-band receiver IF video converter contains only four channels instead of the eight channels

IV. Summary

The DSN VLBI System MK 1-80 Phases 1 and 2 will be operational to support Voyager Project navigation and will

meet or exceed the accuracy requirements. It is expected that the Galileo project will have the same accuracy requirements. The design of the DSN VLBI System MK 1-80 anticipated a future requirement of Δ VLBI (angular measurement of a spacecraft relative to a known radio source). The DSN VLBI System MK 1-80 can support Δ VLBI, with some software additions to the VLBI Processor Subsystem.

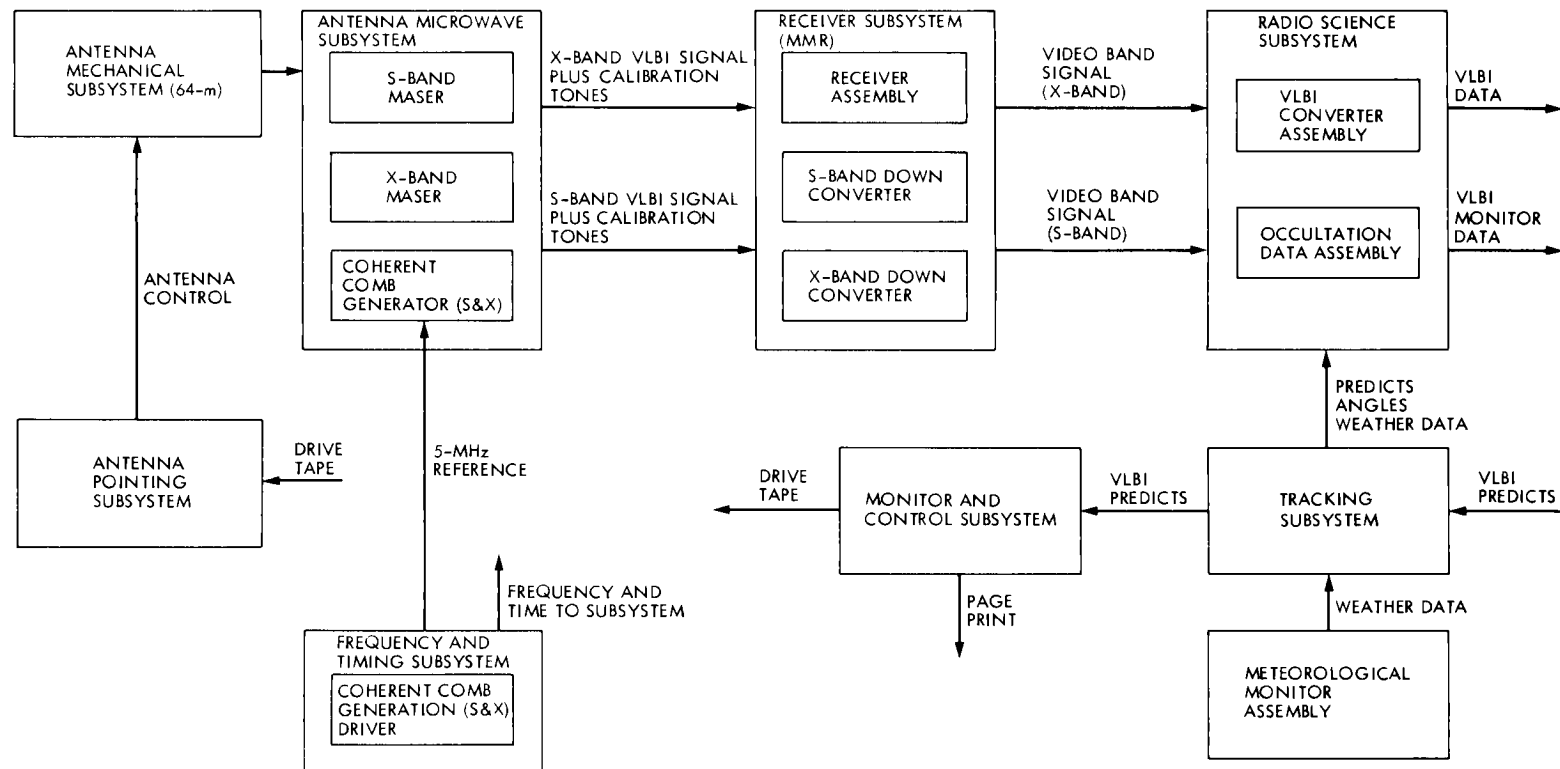


Fig 1 DSS VLBI functional block diagram

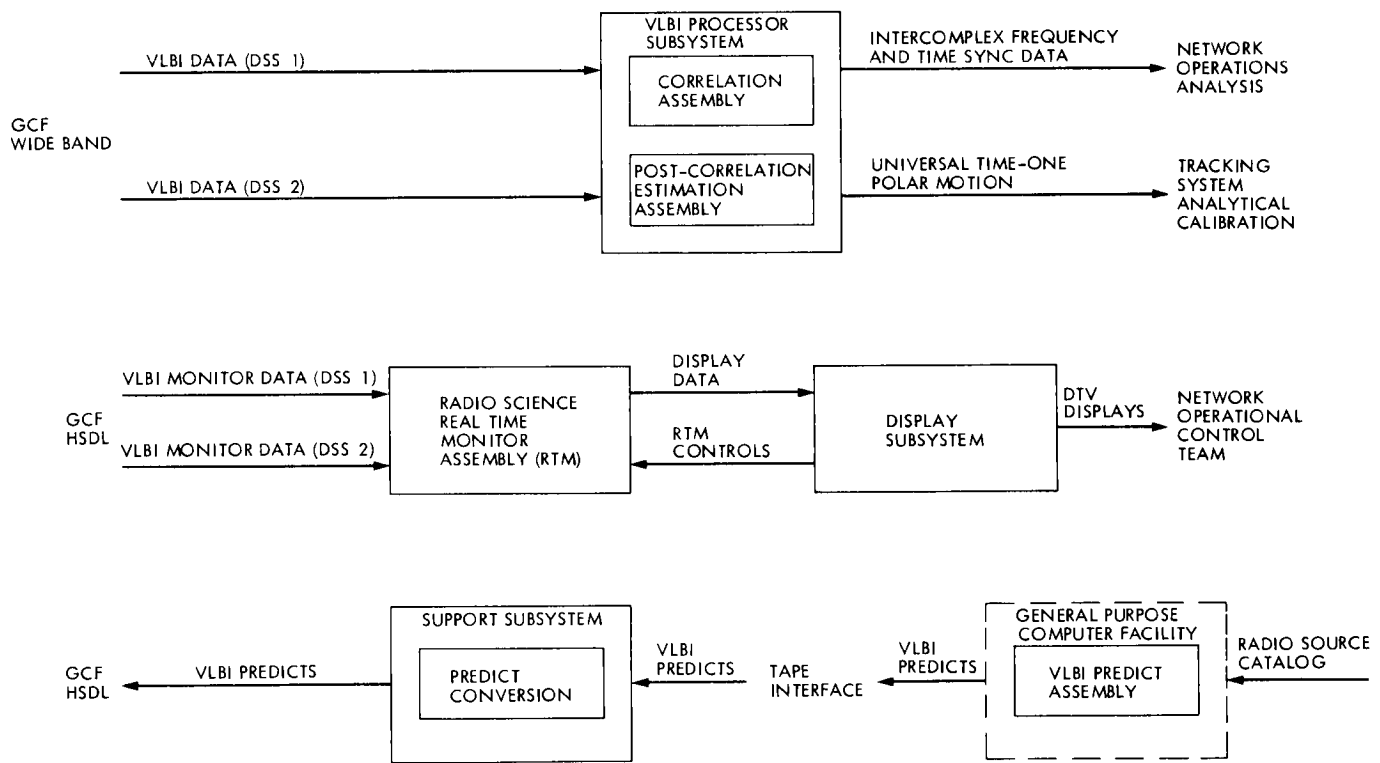


Fig 2 NOCC VLBI functional block diagram, Block I, VLBI Phases 3 and 4

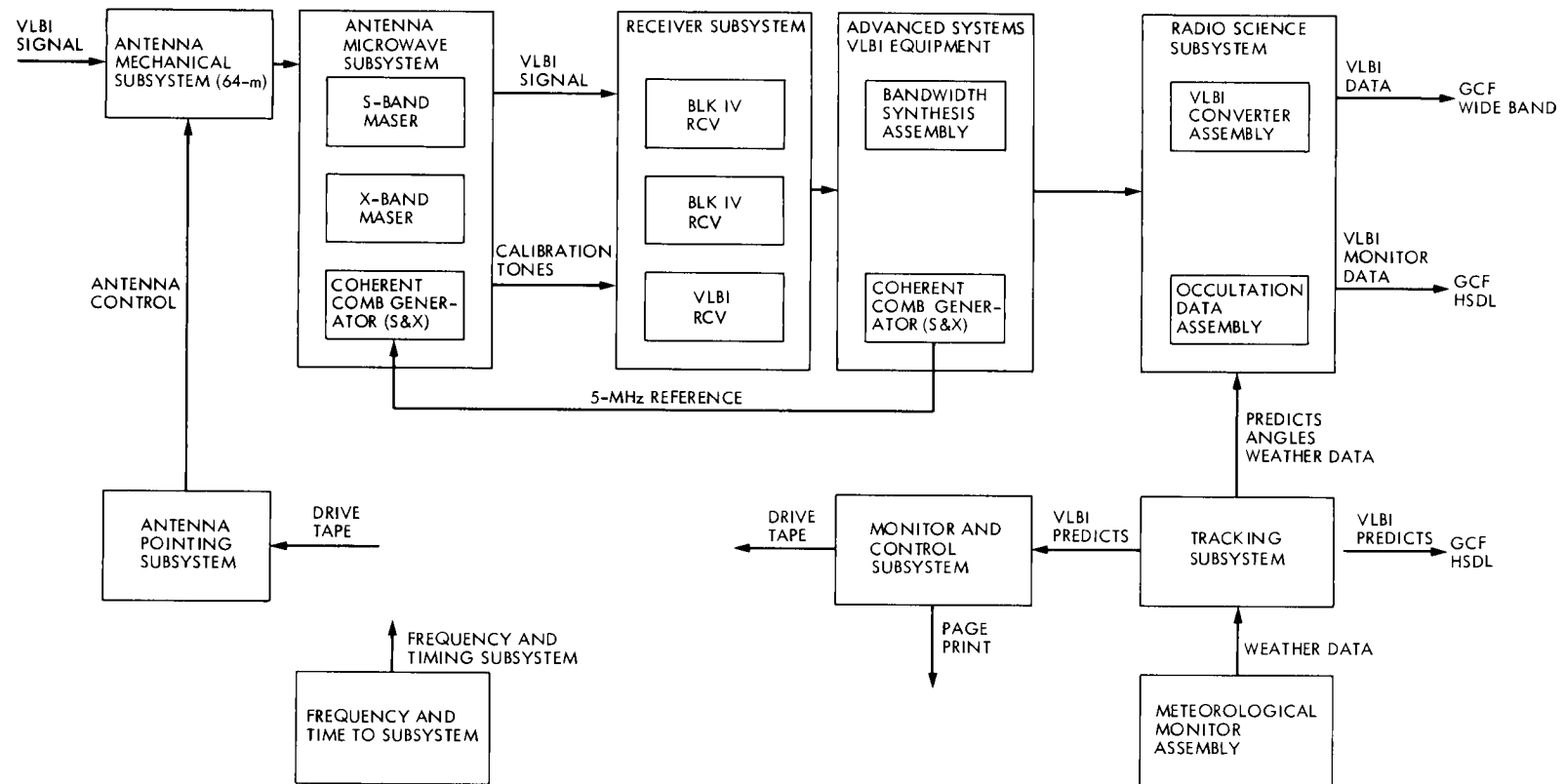


Fig 3 DSS VLBI functional block diagram, Block I, VLBI Phases 1, 2, and 3

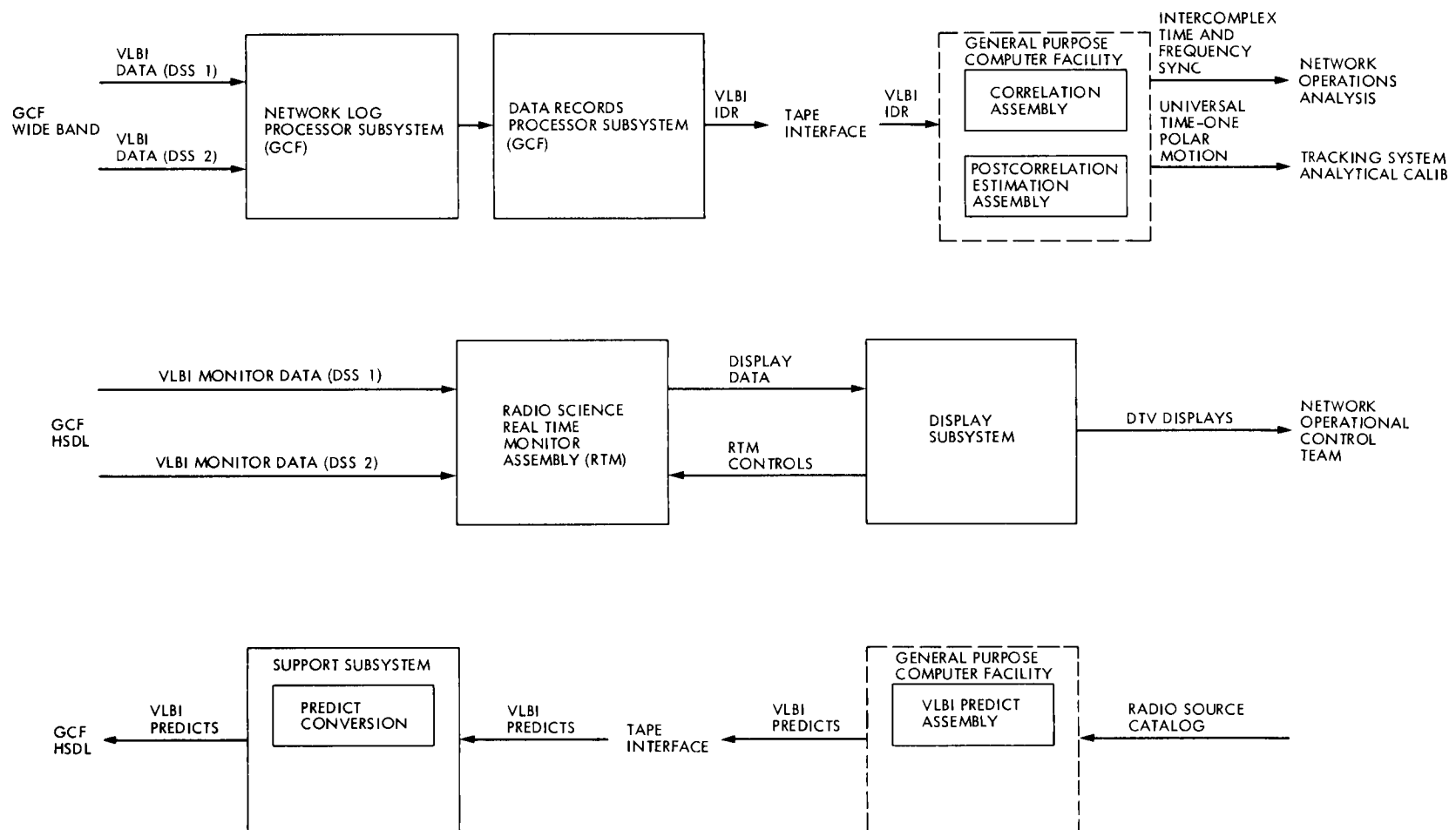


Fig. 4 NOCC VLBI functional block diagram, Block I, VLBI Phase 1

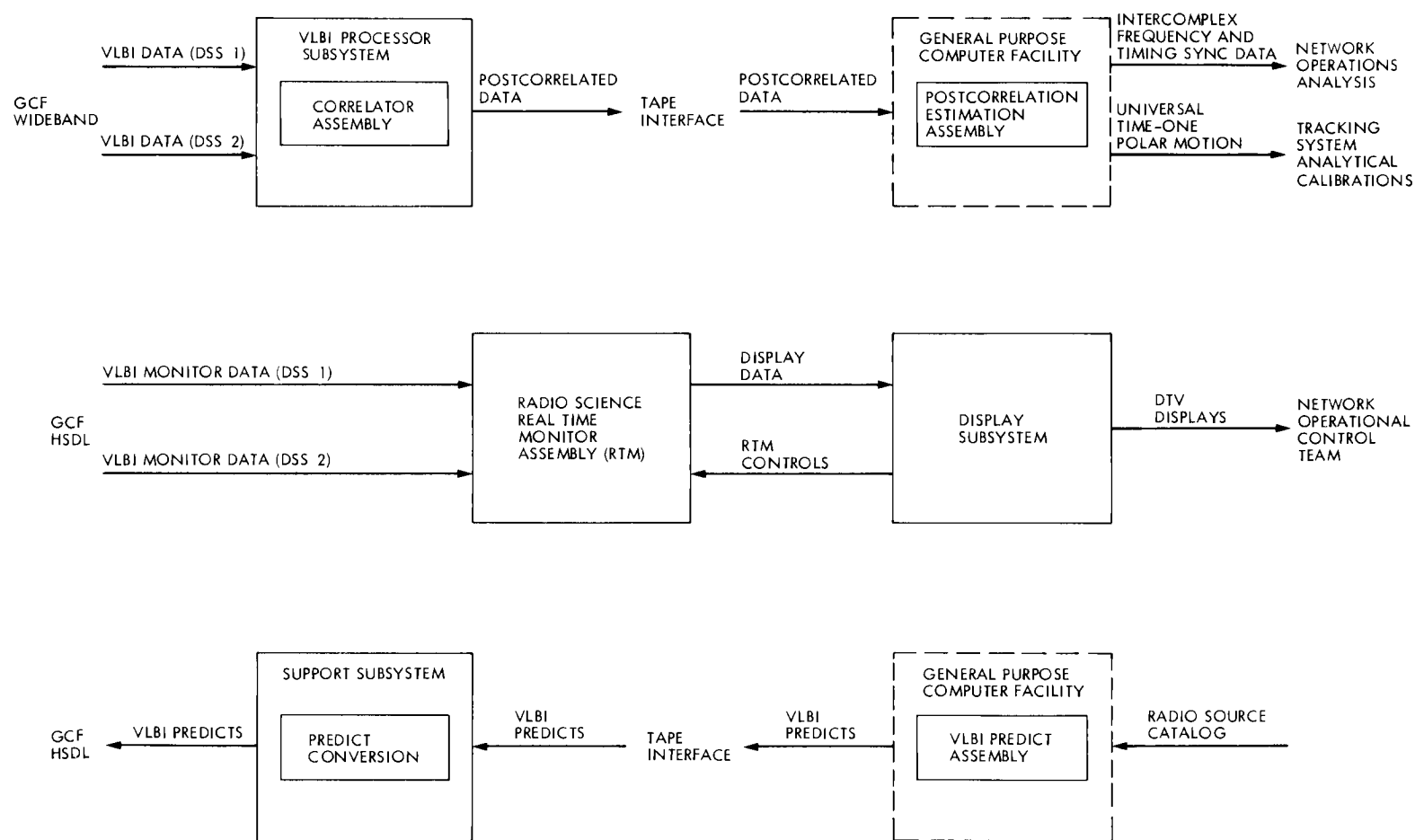


Fig 5 NOCC VLBI functional block diagram, Block 1, VLBI Phase 2

DSN Load Forecasting for Proposed Future NASA Mission Sets

W A Webb
Mission Design Section

This article describes a computer program, DSNLOAD, which provides load forecasting information given a DSN configuration and mission requirements for a set of proposed future NASA missions

I. Introduction

As proposed future NASA interplanetary mission sets are considered, it is necessary to assess the load on the DSN given the individual tracking requirements for each of the proposed missions. A computer program, DSNLOAD, is described which provides DSN load forecasting information given a proposed future NASA mission set. In DSNLOAD, the DSN is analytically modeled so that spacecraft (S/C) tracking schedules are determined periodically throughout the future period of interest. These schedules are determined from the view periods or available tracking times for each mission on one sample day each month and reflect a typical or average tracking situation for the month. These typical tracking schedules are then transformed into data which shows the load or "how busy" each DSN station is "on the average" at different times of the day. The DSNLOAD model includes required pre- and postcalibration periods and station "overhead" such as maintenance or "down" time. Also included in the model is the option of "off-loading" some of the tracking load of a station which is overloaded onto another station.

DSNLOAD provides data which assists in identifying time periods in the future where the DSN may be overloaded and tracking requirements may not be satisfied for one or more missions. It also helps to identify tracking conflicts between

missions, particularly at critical periods such as launch or encounter when intensive tracking is required. This information may influence the mission design or a decision to alter the capabilities of the DSN.

II. DSN Load Candidate Mission File

A flowchart of the procedure of selecting a possible future mission, determining a representative heliocentric orbit for the mission, generating view period schedules, and converting these schedules into Basic Loading Data for each mission at each station is shown in Fig 1. The Basic Loading Data represents the percentage of available tracking time in different time slots during the monthly sample day. The Basic Loading Data for all possible missions is stored in a file called the Candidate Mission File for access by DSNLOAD. Given a proposed mission set, DSNLOAD reads the Basic Loading Data for the proposed missions from this file.

The missions which are included in a typical load forecasting study are either active or in-flight missions, missions which are funded as "projects" and scheduled for future launch, or missions which are being studied and considered as becoming possible "funded" projects in the future. Research is currently

being carried out for possible interplanetary missions with launch dates throughout the rest of the century

Early in the advanced studies process, a mission reference trajectory is generated. The reference trajectory is used to study and analyze mission characteristics. In this process, basic mission design parameters are determined such as launch date, arrival date, geocentric injection energy (C_3) required, and the direction of the geocentric injection vector. From these mission design parameters, a heliocentric geometric conic is determined which intersects the Earth at launch and the arrival planet (or other body such as a comet) at arrival for ballistic trajectories or a polynomial fit which approximates the trajectory for low-thrust trajectories. For planet orbiter missions, the heliocentric orbit of the planet is used during the orbital phase of the mission. For missions which are "in-flight," the actual launch and arrival date are used to determine the trajectory.

The reference trajectories are used to determine geocentric direction vectors as a function of time. From these direction vectors, the DSN station locations, and knowledge of the Earth's rotation, the view period schedules are generated. The view period schedules are generated for the 15th day of each month for the mission duration. For deep space missions, the configuration of view periods from station to station varies slowly from month to month and a sample rate of one day per month is adequate for generating future loading information.

The current DSNLOAD Candidate Mission File includes Basic Loading Data for 60 missions which are either currently in-flight or have been proposed for launch at some future date. Also included are Basic Loading Data for each of the nine planets, which may be used to study DSN loading for prospective planetary orbiter missions.

III. Tracking Schedule Model

The DSNLOAD tracking schedule model considers the tracking schedule to be represented by tracking passes which are of a maximum required length and centered within the view period or available tracking time for each mission. If view periods overlap for a station, no attempt is made to sequence tracking for the station or to distribute tracking over the entire available tracking period.

The assumption that each tracking pass is centered in the middle of the view period provides a model which is computationally simple, is easily understood by upper level technical management which use the results in decision making, and which identifies potential tracking requirement conflicts or time periods where view periods for two or more missions overlap and tracking requirements cannot be satisfied.

In a sense, the model provides a "reasonable" upper bound on the potential overload for a given tracking situation. Since in actual tracking, overlap is not possible (a station cannot normally track more than one spacecraft at a time), a sequencing scheme is worked out as a result of human decision-making reflecting compromises between conflicting requirements by representatives of the active missions at that time. The DSNLOAD tracking schedule model provides a reasonable upper bound on maximum loading or a "worst case" situation. This serves to identify time periods and times during the day when there may be potential overloading problems and tracking requirements cannot be met. Monthly view period charts which are printed by the program throughout the period of interest assist in determining and understanding where potential conflicts may occur.

The basic assumptions of the DSNLOAD tracking schedule model are now stated as follows:

- (1) The view period schedule for each mission for each month is represented by the schedule for the 24-hr day on the 15th of the month.
- (2) The tracking pass for a given mission at a station is assumed to be of a required maximum length and centered in the middle of the view period.
- (3) The tracking requirements (i.e., number of tracking passes/month required for a mission) are handled by weighting multipliers.
- (4) For each tracking pass, pre- and postcalibration periods are added which are represented as an extension, at the beginning and end, of the tracking pass.
- (5) The loading due to station overhead (maintenance or "down" time) is added after the tracking schedule for the mission set has been determined.

The first assumption is based on the premise that for interplanetary missions the view period configuration at each station varies slowly from day to day and that a sample rate of once per month is adequate for generating future loading information. Monthly loading data is then averaged into quarterly data to provide an overall picture of the loading situation over the time period of interest, usually 10 or more years in a typical loading study.

The tracking requirements are provided by representatives of each mission and are specified as the number of tracking passes desired during each month at each station. For each mission, the average loading contribution is determined by breaking up the sample day (the 15th of the month) into six 4-hour time slots, computing the tracking load in each time slot and then multiplying each of these loading percentages by

a weighting multiplier which reflects the tracking requirements

Load contributions for each mission and each of the six 4-hour time slots are computed in the same manner and the load summed over all missions to get the total average load contribution at the station for the month due to spacecraft tracking. The "overhead" is then added for the station to get the total load for the month. Monthly loading data is then averaged into quarterly data and printed by the program in the form of "loading matrices".

A schematic for computing the average load for one month, for a set of missions at one station, is presented in Fig 2. The load contribution for each mission is computed at each station and the load is summed over all missions to get the total load at each station. Maintenance or station "overhead" time is then added to obtain the total load contribution for the mission set at each station.

The station maintenance model is designed to reflect the load contribution which is due to the necessary time when the station is not actually tracking, but is being repaired or maintained. The DSN maintenance shifts are typically 4 to 8 hours long and performed on as regular a basis as possible at times when a station is least busy with spacecraft tracking. The basic strategy of the DSNLOAD maintenance algorithm is to assign the maintenance load for each station, each month, to the time slots in ascending order of load percentage and in proportion to the relative amount of tracking time available in each time slot. The maintenance load is almost always distributed over at least two time slots. If there is not enough available time for the required maintenance load, the time slots with available time are filled to 100% and the remaining maintenance load distributed evenly throughout the day. The maintenance time is input into DSNLOAD as the average number of hours of maintenance time required per month for each station. The maintenance load in hours/month is converted to loading percentage in a 4-hour time slot by the program.

IV. Calculation of DSN Loading Matrices

After the total average load contribution, in each time slot, is determined at each station for each month of the period of interest, the monthly loading data are averaged into loading matrices which show the average quarterly loading for a year. The loading matrices give an "overall picture" of the loading situation, as a function of time, for each quarter at each station.

A loading matrix is a 6×4 array of numbers,

$$Q = \begin{bmatrix} q_{11} & q_{12} & q_{13} & q_{14} \\ q_{21} & & & \cdot \\ \cdot & & & \cdot \\ \cdot & & & \cdot \\ \cdot & & & \cdot \\ q_{61} & \cdot & \cdot & q_{64} \end{bmatrix}$$

where each q_{kl} is the average percentage of time that the station is busy, due to tracking and overhead, for the k th 4-hour time slot and the l th quarter of the year. An element, q_{kl} , of the loading matrix whose value is greater than 100%, indicates that the station is overloaded "on the average" for the k th time slot and l th quarter of that year.

In assessing loading, two subnets of the DSN are usually considered, each consisting of three stations located at Goldstone, California, Australia and Spain. The subnets are designated the "34-meter net" and the "64-meter net". In terms of loading assessment, the 64-meter subnet generally has more capability than the 34-meter subnet so that an overload on the 34-meter subnet may be "off-loaded" onto the 64-meter subnet but not vice-versa.

The DSNLOAD off-loading model considers the Q matrices for stations in the same location of each subnet on an element by element basis. Let q_{kl}^{34} represent the loading percentage for the k th time slot and l th quarter of the year for the 34-meter station and q_{kl}^{64} represent the loading percentage for the k th time slot and l th quarter of the year for the 64-meter station. The assumptions of the DSNLOAD off-loading model are as follows:

- (1) If $q_{kl}^{34} \leq 100$, no off-loading is necessary.
- (2) If $q_{kl}^{34} > 100$ and $q_{kl}^{64} \geq 100$, off-loading from the 34-meter station to the 64-meter station is not permitted since the 64-meter station is already overloaded.
- (3) If $q_{kl}^{34} > 100$ and $q_{kl}^{64} < 100$ then,
 - (a) If $q_{kl}^{34} + q_{kl}^{64} \leq 200$, split the load equally between the 34-meter station and the 64-meter station.
 - (b) If $q_{kl}^{34} + q_{kl}^{64} > 200$, load the 64-meter station up to 100% and assign the remaining load to the 34-meter station. (Note, in this case the 34-meter station is still overloaded for this time slot and quarter.)

In the DSNLOAD output, for a typical loading study, the loading matrices for the three stations for each subnet are

computed and printed, as well as the "off-loaded" loading matrix for each station

Two other types of loading matrices are computed and printed for each subnet for each year which summarize the results over each subnet, a Maximum Loading Matrix and an Average Loading Matrix. A Maximum Loading Matrix is a 6×4 array of numbers,

$$Q^m = \begin{bmatrix} q_{11}^m & q_{12}^m & q_{13}^m & q_{14}^m \\ q_{21}^m & & & \cdot \\ \cdot & & & \cdot \\ q_{61}^m & \cdot & \cdot & q_{64}^m \end{bmatrix},$$

where each q_{kl}^m is the maximum percentage of time that the subnet is busy, due to tracking and overhead, or the maximum value of q_{kl} taken over the three stations of the subnet for the k th time slot for the 1th quarter of the year. The Maximum Loading Matrix shows peak loading on the subnet and identifies time periods when the DSN as a whole is overloaded.

An Average Loading Matrix is a 6×4 array of numbers,

$$Q^a = \begin{bmatrix} q_{11}^a & q_{12}^a & q_{13}^a & q_{14}^a \\ q_{21}^a & & & \cdot \\ \cdot & & & \cdot \\ q_{61}^a & \cdot & & q_{64}^a \end{bmatrix},$$

where each q_{kl}^a is the average percentage of time that the subnet is busy, or the average value of q_{kl} taken over the three stations of the subnet for the k th time slot for the 1th quarter

of the year. The Average Loading Matrix provides an "overall picture" of what the loading situation on the DSN will be for each quarter of the year.

For each type of loading matrix, the quarterly average is computed and printed. This is the average of the six elements of each column of the loading matrices. This provides an "overall picture" of what the load is for each quarter and allows comparison of the average load between quarters.

V. Further Development

The DSNLOAD program, using the view period tracking model described in this paper, is currently operational at JPL and is used to assess future DSN capability and mission feasibility by JPL and NASA management. This data provides a reasonable "upper bound" on what future loading might be and assists in identifying time periods where DSN overloads may occur. Detailed examination of view period charts printed out by DSNLOAD provides further insight into potential overloading problems.

A second DSN tracking model, which is now being developed by the author, will attempt to determine an optimal or "ideal" tracking schedule for a given mission set. This optimal tracking model will utilize mathematical programming techniques to periodically determine a tracking schedule which is optimal in the sense of maximizing the tracking capability of the DSN with respect to the tracking requirements of the mission. In actual experience, tracking schedules are determined by human decision making, reflecting compromises of conflicting requirements by representatives of the missions and are not necessarily optimal by any "predictable" performance measure. So it is intended that the optimal tracking model provide a "lower bound" on the predicted tracking situation and that the two models provide "best" and "worst" case limits on what the actual loading situation might be. This lower bound information, along with current DSNLOAD results, will advance further the technology of using a computer model of the DSN to forecast future DSN loading.

Acknowledgment

The author wishes to acknowledge W L Martin of the TDA Technology Development Section of JPL for his support and contribution to the DSNLOAD development effort

References

- 1 Webb, W A , "Scheduling of Tracking Times for Interplanetary Spacecraft on the Deep Space Network," Joint National Meeting of the Institute of Management Sciences and Operations Research Society of America, New York, N Y , May 1978
- 2 Webb, W A , "Forecasting of Loading on the Deep Space Network for Proposed Future NASA Mission Sets," AAS/AIAA Astrodynamics Specialist Conference, Provincetown, Mass , June 25-27, 1979

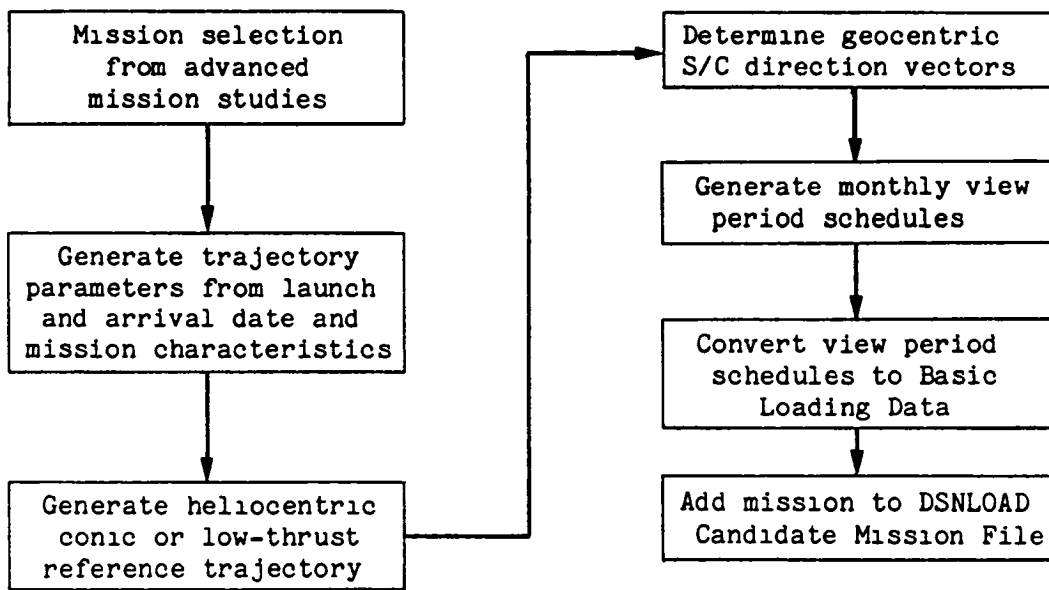


Fig 1 Procedure for determining Basic Loading Data for a proposed future mission

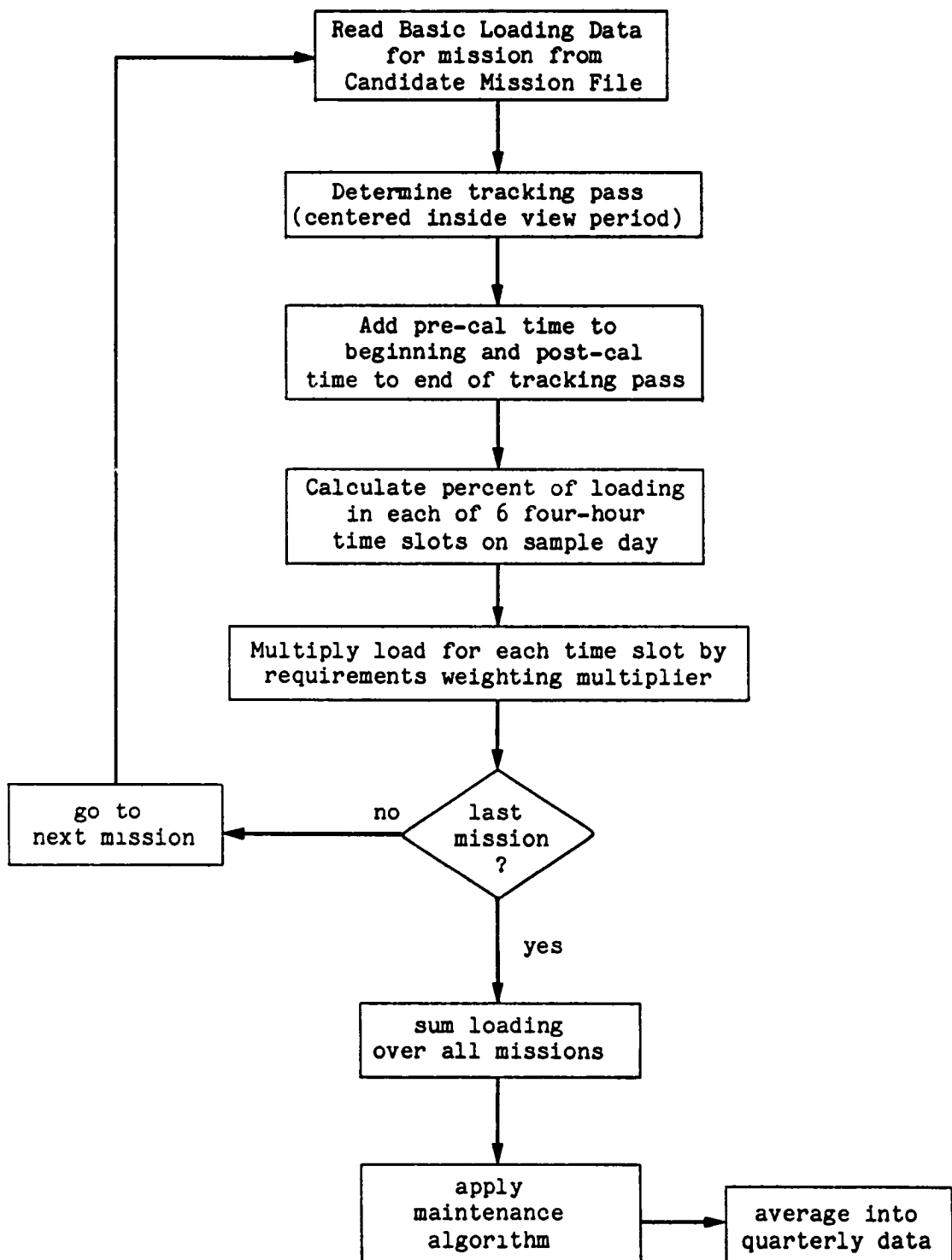


Fig 2 Procedure for computing the average load for a month, at one station,
for a set of missions

Viking Orbiter Completion Mission and Viking Lander Monitor Mission

R L Gillette

Deep Space Network Operations Section

This report covers from 1 December 1979 through 31 January 1980 and continues reporting on DSN Viking Tracking Support for the same period

I. Viking Operations

A. Orbiter Completion Mission

On 6 November 1979, a Viking Mars Orbit Trim Maneuver officially terminated the Viking Survey Mission and moved the Project into a new phase of the Viking Mission termed the Viking Orbiter Completion Mission. The Viking Orbiter Completion Mission (VOCM) is the fifth phase of the Viking Mission and is currently scheduled to terminate on 30 June 1980.

1 Mission objective The objective of the Orbiter Completion Mission is to obtain moderate resolution photographic coverage of Martian surface areas not previously photographed or inadequately covered during the earlier survey mission.

2 Status During this reporting period the Orbiter 1 spacecraft continued to operate normally, collecting and returning weather data and moderate resolution Mars surface photos to Earth as well as relaying data from the Lander 2 (VL-2) spacecraft.

B. Lander Monitor Mission

On 6 November 1979, along with the start of the Orbiter Completion Mission, the Lander-1 spacecraft became a separate mission of its own, termed the Lander Monitor Mission

(LMM). Throughout the Lander Monitor Mission, the Lander-1 spacecraft will be in an automatic-mission mode, operating autonomously on the programs that have previously been stored in the on-board computers.

1 Mission objectives The objectives of the Lander Monitor Mission are to obtain S-band ranging data from the surface of Mars periodically over a long time span for the conduct of radio science, and, obtain meteorology and imaging data from the surface of Mars periodically over a long time span to monitor and disseminate information relative to any significant changes with time.

2 Status The Viking Landers continued to operate as expected during this reporting period. All Lander-1 essential subsystems are healthy as the spacecraft collects imaging and meteorology data for weekly transmission to Earth whenever a Deep Space Station (DSS) is available. All Lander 2 essential subsystems are healthy, except for the transmitter which supports transmission of telemetry data directly to Earth. All data from Lander-2 are transmitted to Orbiter-1, and then relayed to Earth using the Orbiter transmitter.

II. Radio Science

During this reporting period the only radio science activity has been the near-simultaneous Lander-Orbiter Ranging Experiment.

III. Ground Communication Facility Reconfiguration

Throughout the Viking Mission the low rate telemetry, command and radio metric data, collected at a DSS has been transmitted to the JPL Viking Mission Control and Computing Center over the Ground Communications Facility (GCF) 7.2 kb/s High-Speed Data Line encoded with an Error Polynomial Code (EPC) of 33 bits

The Error Polynomial Code (EPC) is encoded into each 1200-bit high-speed data block as it leaves a DSS, and is then decoded upon receipt at JPL to verify that all data bits have been received correctly. As the GCF equipment was upgraded to support new projects, the EPC was changed to 22 bits. Older GCF equipment was maintained to continue supporting Viking with an EPC of 33 bits.

With the new extension of the Viking Mission out to 1 July 1980, and the need for additional space for new GCF equip-

ment, a plan has been developed to convert the Viking Project over to the newer GCF equipment using an EPC of 22 bits. This requires a new cable interface between the Viking computers and the GCF equipment along with software changes in the Viking telemetry and command computers. Figure 1 shows the new GCF configuration scheduled to support Viking, starting on 3 March 1980.

IV. Network Support

Table 1 shows the DSN tracking support for the Viking Mission from August 1979 through January 1980. Since August, there has been a continual decrease in the requirements for tracking support. This is due to the reduction in overall tracking time required to return science data to Earth at the higher telemetry data rate made possible as Mars approaches opposition on 26 February 1980.

Bibliography

- 1 Gillette, R. L., "Viking Extended Mission Support," in *The Deep Space Network Progress Report 42-46*, pp 29-32, Jet Propulsion Laboratory, Pasadena, California, August 15, 1978
- 2 Gillette, R. L., "Viking Extended Mission Support," in *The Deep Space Network Progress Report 42-47*, pp 15-20, Jet Propulsion Laboratory, Pasadena, California, October 15, 1978
- 3 Gillette, R. L., "Viking Continuation Mission Support," in *The Deep Space Network Progress Report 42-48*, pp 7-11, Jet Propulsion Laboratory, Pasadena, California, December 15, 1978
- 4 Gillette, R. L., "Viking Continuation Mission Support," in *The Deep Space Network Progress Report 42-51*, pp 14-18, Jet Propulsion Laboratory, Pasadena, California, June 15, 1979
- 5 Gillette, R. L., "Viking Orbiter Completion Mission," in *The Deep Space Network Progress Report 42-55*, pp 4-6, Jet Propulsion Laboratory, Pasadena, California, February 15, 1980

Table 1. DSN Viking Mission tracking support

DSS	1979 - 1980					
	Aug	Sept	Oct	Nov	Dec	Jan
11	<i>a</i> - <i>b</i>	1 6	1 3	2 11	-	2 15
12	-	-	-	-	-	-
14	22 91	15 65	12 62	8 64	6 52	2
42	1 5	2 10	-	-	-	-
43	1 5	1 1	1 6	-	2 13	2 8
44	4 18	-	3 12	-	-	-
61	-	-	-	-	-	-
62	2 2	1 4	-	-	-	6 41
63	29 131	27 105	19 104	15 119	16 142	2 14
Total	59 252	47 191	36 187	25 194	24 207	14 78

*a*Total number of Viking tracks

*b*Total Viking station support in hours

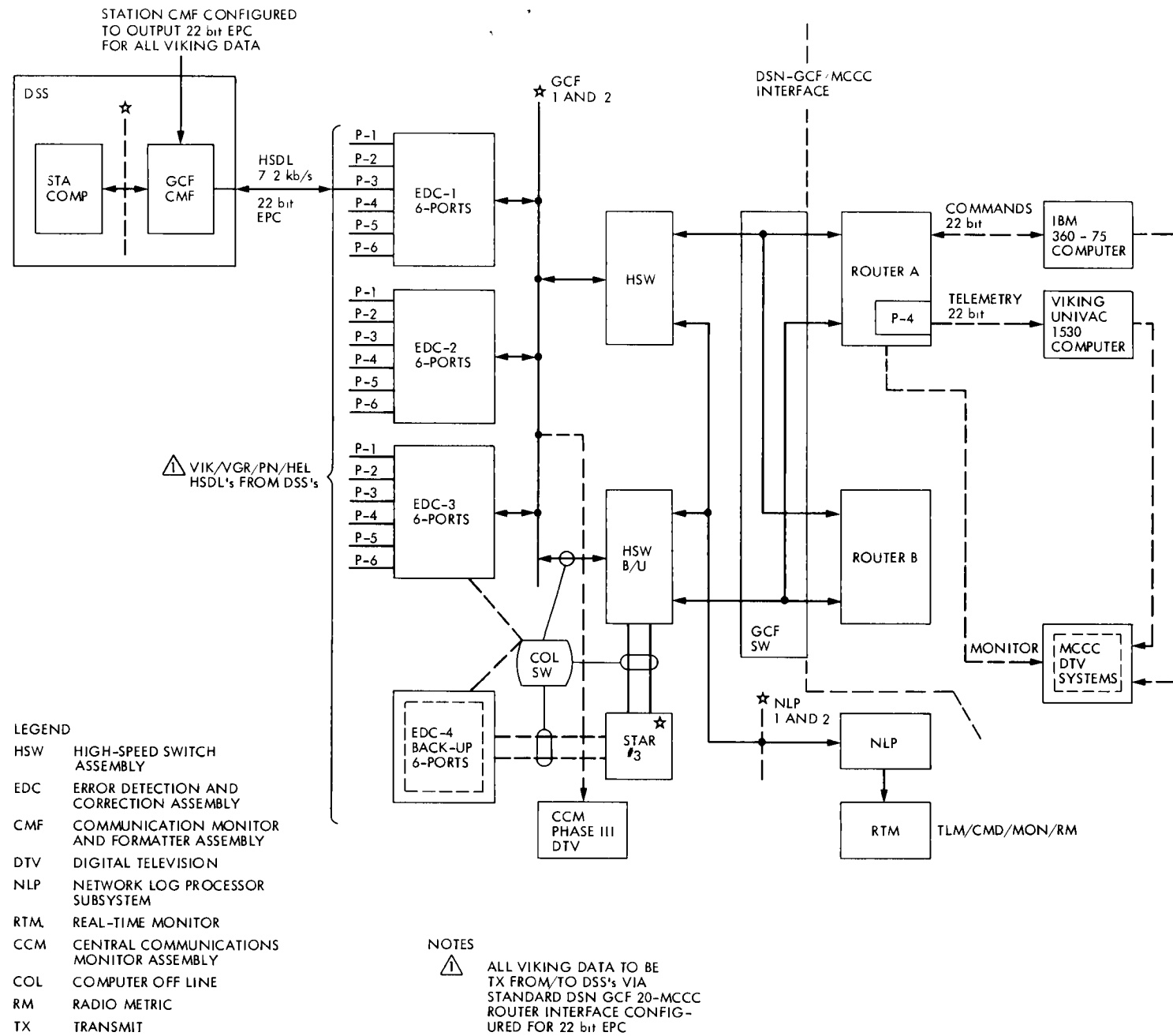


Fig. 1 Viking Orbiter Completion Mission and Viking Lander Monitor Mission

Radio Astronomy

R M Taylor

Deep Space Network Operations Section

This article reports on the activities of the Deep Space Network in support of Radio and Radar Astronomy operations during January and February 1980. It also reports on the objectives, results, and implications of the Pulsar Rotation Constancy Experiment sponsored by OSS.

I. Introduction

Deep Space Network 26-meter, 34-meter, and 64-meter antenna stations are utilized in support of experiments in four categories NASA OSS, NASA OSTDS, Radio Astronomy Experiment Selection (RAES), and Host Country

One unexpected benefit of being able to measure the average observed pulse shape at Deep Space Network frequencies (particularly 13 cm) allows measurement of fluctuations in pulse energy on intermediate time scales, possibly due to interstellar inhomogeneities

II. Radio Astronomy Operations

A. NASA OSS Category

On 17 February, the Goldstone 26-meter station and the Tidbinbilla 64-meter station supported for five hours the first in the resumed series of Alsep/Quasar VLBI observations. Support for the Jupiter Patrol observations of Planetary Radio Astronomy has continued at prior levels at the Goldstone and Madrid 26-meter antenna stations. Similarly, the Pulsar Rotation Constancy experiment has enjoyed a consistent level of support. The following is a brief summary of the status of this activity.

Pulsar Rotation Constancy (OSS 188-41-52-09-55)

1 Observational objectives To measure the phase of the pulse train from these naturally occurring radio sources at regular intervals, e.g., intervals which are short compared with the time scale of known changes in the pulse train

2 Observed results

- (1) Known pulse periods vary from the 33 milliseconds of the Crab nebula pulsar to as long as 4 seconds
- (2) Period of the pulse is slowly growing in time, i.e., P of the "ripple" is always positive. No radio pulsars have been observed with a significant negative first derivative
- (3) There have been observed steps in the period, where the period suddenly decreases slightly by parts in 10^6 (Vela pulsar) and parts in 10^8 (Crab pulsar)
- (4) There is another level of observed activity consisting of short term positive and negative changes in pulse period of the order of parts in 10^{10} . This is known as "timing noise."
- (5) If the pulsar model is well maintained, then model parameters (e.g., proper motion) can be resolved over appropriate time periods

3 Implications The range of periods observed is best explained by remnants of earlier Super Nova Explosions One of the phenomena observed, i.e., the consistent slowing down of the pulsar, may indicate some measure of drag on the object and may be linked with the pulse generation process

Current thinking is that a pulsar object is a neutron star, but is a neutron star really solid neutron? Or is it a composite structure and, if so, what are the components? It is currently hypothesized that there are at least two components a crust, composed mostly of iron, and a neutron interior This is predicated by the steps exhibited in the epoch These components may be weakly coupled, may have different spin rates, and at the "step" time it could be that the crust speeds up because it collapses slightly while the inner core takes time to catch up Question Is there yet another component? The interaction between the two or more components is more complex than was previously thought and requires a lot more work Of particular interest is the possibility of being able to predict the next epoch step of the Vela pulsar, say, to within two months

The long-term tracking requirements of these objects are similar to spacecraft requirements so that stability of equipment and personnel expertise and the availability of time itself all contribute significantly to a successful observing program

B. NASA OSTDS Category

Support for activity in this category is limited to Planetary Radar Imaging, and during the period of this report support has been at a very high level Approximately 10 hours every 4 days has been provided at the Goldstone 64-meter antenna station, utilizing the 400-kW 13-cm transmitter and advanced systems receivers and radar correlator in observations of the planet Mars through its current opposition (26 February) On 29 January, with very short notice, the Goldstone 64-meter facility was made available to attempt radar imaging of the comet Bradfield, 1979L, a singular, exciting opportunity Almost one hour of data was gathered from a 4-hour pass

C. RAES Category

1 RA 169 On 1 February, the Goldstone and Tidbinbilla 64-meter stations supported VLBI observations of the compact radio nuclei of normal and extended galaxies and quasars for five hours

This experiment was the first in a series of observations designed to traverse the celestial sphere over a period totalling 25 hours, with the object of observing previously detected

sources at 3.8 cm and searching for hitherto undetected sources at 13 cm

At 3.8 cm the resolution obtainable from this baseline is about three times greater and the sensitivity about four times greater than on US baselines At 13 cm the resolution is comparable with that of US baselines at 3.8 cm, but the sensitivity is an order of magnitude better

2 RA 171 On 2 and 3 February, for a total of 16 hours, several observatories, including Owens Valley Radio Observatory, Jodrell Bank Radio Observatory, and the Goldstone and Madrid 64-meter antennas, supported VLBI observations of M87 and NGC 6251

These observations fulfill the requirements as described in the experimenters' proposal, which is now transferred to the completed file Publication of the results will be forthcoming after the data are analyzed

3 RA 176 On 26 and 27 February, the Goldstone and Madrid 64-meter antenna stations combined with the Max Planck Institute, Bonn Observatory, for a total of 23 hours to observe the Twin QSO 0957, +56 A, B This experiment was first supported in November 1979, and, at first, it was thought to have been unsuccessful due to a precessed position error in the source coordinates However, good science data were obtained at 13 cm on the Bonn-Goldstone baseline, and this latest observation was designed to replicate this with the increased sensitivity available with the Mark III Data Acquisition System

The Deep Space Network does not yet have the Mark III available on a regular basis, but a loan to the Goldstone facility from Owens Valley Radio Observatory was arranged, enabling both Mark II and Mark III data to be recorded at the California station, supported with Mark II data in Spain and Mark III data in Germany Also, on this occasion during the last 90 minutes of the observation, the stations were reconfigured to provide some data at 3.8 cm The data reduction and analysis and results publication are eagerly awaited

D. Host Country Category

1 Australia During this period host country activity in Australia has been, almost exclusively, pulsar observations at Orroral Valley at the rate of approximately 10 hours support per week

2 Spain There has been no host country activity in Spain during this period

X-Band Uplink Ground Systems Development

R Hartop, C Johns, and R Kolbly
Radio Frequency and Microwave Subsystems Section

The development of new ground equipment for an X-band uplink to supplement the present S-band uplink is underway. The exciter and doppler extractor developments, and the high-power transmitter development with some early test results are presented.

I. Introduction

The requirements for increased accuracies of spacecraft navigation as well as charged particle calibrations has prompted the development of an uplink in the X-band region with much improved short- and long-term frequency stabilities.

To provide this stable X-band uplink signal, a new exciter design concept is being used. In addition, an X-band phase modulator is being incorporated to provide broad instantaneous bandwidth to accommodate higher clock frequencies with consequent improved resolution.

The exciter design is discussed in Part II, covering such aspects as the block diagram, expected oscillator frequency stability, effect of instability of the cables between the control room and the antenna, improvement in uplink stability obtained with the transmitter phase control loop, expected frequency stability of exciter references for the doppler extractors, expected performance of the X-band range modulator and the frequency stability improvement to be obtained with temperature control of the hardware environment.

In addition to the exciter and doppler extractor, a 20-kW transmitter is being designed and built for installation at DSS 13, where it will be evaluated for application in the Deep

Space Network. A major portion of any transmitter design is the system for protection, monitor, and control of the various subsystems associated with the transmitter. Also, the Monitor and Control System is a major part of overall system reliability. Part III of this article will describe the control system to be used in the transmitter. Also, further evaluation of the VA-876 klystron will be described and the results presented.

II. Exciter

A simplified block diagram of the exciter is shown in Fig. 1. To generate the 7.2-GHz exciter signal, the 100 MHz from the hydrogen maser frequency standard is multiplied up to 6500 MHz and summed with 700 MHz generated by multiplying the exciter's digitally-controlled oscillator (DCO) by 16. Sixteen is the minimum multiplying factor possible that permits an X-band operating range from 7145 MHz to 7235 MHz. The limitation is the DCO frequency range of 40 to 51 MHz. This method of generating the exciter signal reduces the DCO contribution to the exciter signal stability. To illustrate this, assuming an X-band frequency of 7200 MHz, the input frequencies to the summing junction are 700 MHz and 6500 MHz. Relative to the X-band frequency, the frequency ratios are 700/7200 and 6500/7200. In this configuration, the exciter DCO contributes less than 10 percent of its instability.

to the X-band signal. Since the stability of the hydrogen maser is considerably better than the exciter DCO, the total exciter stability is improved

A. Exciter Oscillator Stability

To establish stability estimates for the X-band exciter, three Dana synthesizers (DCOs) were measured using the same techniques that are used for measuring maser stability (Ref 1). Figure 2 is a graph showing the stability of the synthesizers for integration periods in excess of 1000 seconds. For comparison, a hydrogen maser stability curve is included.

Figure 3 is a stability curve computed from the data in Fig 2. The curve shows the resultant X-band stability (σ_{exc}) when synthesizer B is algebraically added to the maser as shown

$$\sigma_{exc} = 700/7200 \sigma_{DCO} + 6500/7200 \sigma_{maser}, \text{ worst case}$$

where the ratios 700/7200 and 6500/7200 are the weighting constants for the contribution of the synthesizer and hydrogen maser to the X-band instability

B. 100-MHz Cable Stabilizer

Figure 4 is a simplified block diagram of the complete exciter. The stability of the cable used to transmit the 100-MHz reference frequency from the control room to the antenna is critical. Environmental conditions, such as temperature and mechanical stress, will cause a cable to change electrical length. For the type cable used between the control room and antenna, measurements made at DSS 14 (Ref 2) showed that the frequency stability ($\Delta f/f$) is approximately 6.6×10^{-15} .

To improve the stability of the 100-MHz reference signal transmitted through the cable from the control room to the antenna, a cable stabilizer will be used. Lab measurements made on a prototype cable stabilizer indicate a reduction of phase delay change of a factor of 50 can be achieved.

C Transmitter Phase Control Loop

The 20-kW X-band klystron proposed for use in the X-band uplink is undergoing evaluation tests (Part III) including the measurement of the amplifier's phase sensitivity to coolant temperature, drive power, beam voltage, etc. To stabilize the phase of the X-band uplink signal, a phase control loop has been incorporated that will reduce the phase perturbations due to the klystron by a factor of 100.

The phase control loop compares the exciter and transmitter outputs in a phase detector, and the error voltage is

filtered, amplified, and applied to the control port of an X-band voltage-controlled phase shifter. The signal phase delay through the phase shifter is automatically shifted in the opposite sense of the transmitter variations, thus maintaining a nearly constant transmitter output phase.

The loop parameters were selected for a 3-dB frequency response of 2 Hz to eliminate any possibility of reducing (tracking out) low-frequency command modulation signals. To accommodate future science experiments, a multibandwidth loop can be incorporated.

D. X-X Doppler Reference Generator

The frequency of the exciter reference required for the doppler extractor must be

$$a/b f_{Tx}$$

where a/b is the coherent DOWN/UP ratio and equals

$$240/749 \text{ for X up and S down}$$

$$880/749 \text{ for X up and X down}$$

It is not practical to generate these frequencies entirely from the X-band output signal due to hardware limitations. An output from the exciter at a lower frequency is required. However, at no point in the exciter mechanization does f_{Tx}/n (where n is a whole number) exist. Therefore, this frequency must be generated in some manner.

To accomplish this, the output of the exciter DCO was selected as the reference frequency for generating the doppler reference signal (Fig 4). Due to the mechanization of the exciter, the DCO output inherently contains a portion of the 6500-MHz reference signal (i.e., $f_{DCO} = f_{Tx}/16 - 6500/16$). To eliminate the 6500/16 term, the DCO output is divided by five to yield a frequency of $f_{Tx}/80 - 1300/16$ and then summed (mixed) with a 1300/16 signal resulting in an output frequency of $f_{Tx}/80$. This frequency is subsequently multiplied by 2096/749 and then again by five to yield 131/749 f_{Tx} , which is added to the exciter output frequency to derive the 880/749 f_{Tx} doppler reference.

The stability of the doppler reference, like the exciter, is a weighted combination of the exciter DCO and the 100-MHz maser signals. The worse case exciter stability was shown to be

$$\sigma_{EXCIT} = 700/7200 \sigma_{DCO} + 6500/7200 \sigma_{MASER} \quad (1)$$

and the X-X band doppler reference stability is

$$\sigma_{X-X} = 131/749 \sigma_{EXC} + \sigma_{EXC} \quad (2)$$

Substituting Eq (1) into Eq (2), the doppler reference stability is found to be

$$\sigma_{X-X} = 0.114 \sigma_{DCO} + 1.061 \sigma_{MASER}$$

E. X-S Band Doppler Reference

The doppler reference for the X-S band doppler extractor is generated in a similar manner as the X-X band reference (Fig 4) The $f_{Tx}/80$ signal is multiplied by 8144/749 and then by 5 to obtain a frequency of 509/749 f_{Tx} . This frequency is subtracted from the exciter output to yield the 240/749 f_{Tx} doppler reference. The S-X doppler reference stability is determined by

$$\sigma_{X-S} = \sigma_{EXC} - 509/749 \sigma_{EXC} \quad (3)$$

Again, by substituting Eq (1) into Eq (3), the X-S band doppler stability is

$$\sigma_{X-S} = 0.03115 \sigma_{DCO} + 0.2893 \sigma_{MASER} \quad (4)$$

F. X-Band Phase Modulator

To accommodate higher ranging clock frequencies for improved navigation, an X-band phase modulator is being utilized in the exciter. The instantaneous bandwidth is 90 MHz, established by a bandpass filter. The modulator can be modulated with frequencies up to 10 MHz. Two modulation ports are available to allow range and command signal inputs.

G. Coherent Test Signals

Coherent receiver test signals are generated in the same manner as the X-X and X-S doppler reference signals, with the exception that the test signals can be phase modulated by means of the X-band phase modulator. To accomplish this, the modulated X-band signal is summed with the 131/749 f_{Tx} and the 509/749 f_{Tx} outputs. The levels of the test signals can be varied, by means of programmable step attenuators (not shown in Fig 4), to facilitate receiver calibration and testing.

H. Equipment Temperature Stabilization

To assure long-term stability of the antenna-mounted exciter equipment, all of the RF hardware will be packaged in temperature-stable enclosures. Based on stability measurements made on Block IV R/E RF modules, it is conservatively

estimated that the temperature-controlled exciter equipment will contribute 0.26×10^{-15} to the total exciter instability.

III. High-Power Transmitter

A DSN transmitter generally consists of four major components separated by considerable distances. These components are the Power Amplifier Assembly, the Heat Exchanger, the Power Supply, and the Control Panel. It is a requirement that the Power Amplifier Assembly be mounted near the antenna feed, while the Heat Exchanger and Power Supply are mounted on the ground. The Control Panel is mounted near the operator position in the control room. A further requirement of the X-band uplink transmitter is that it be compatible with unattended operation and DSN Station automation. Figure 5 illustrates a typical Transmitter System.

A major problem with high-power circuits distributed over a large area is induced noise in the form of ground loops and inductive pick-up of extraneous signals, while well-shielded multiconductor cables are bulky and expensive.

A Control System

The planned Control System for the X-band uplink transmitter will incorporate the following features:

- (1) Each component will respond to high-level commands and contain sufficient control and protective circuitry to prevent damage to that component.
- (2) Communications between components will be by means of a single serial data circuit.
- (3) Control hierarchy will minimize communications between components.
- (4) Protection of hardware and personnel will not rely on Control System software.
- (5) Commercially-available equipment will be used in the Control System to the maximum extent possible.

Figure 6 is a block diagram of the Control System for the X-band uplink transmitter. By using a serial data stream and minimizing communications between transmitter components, it will be possible to economically use techniques for noise reduction such as error-checking and error-correcting codes, filtering, low data rates, and isolation schemes such as fiber-optic communications. To meet the protection requirements (item 4), a hard-wired safety interlock between transmitter components will be incorporated. Since sufficient fast protection circuitry will be incorporated in each component, this intercomponent interlock will not be required to operate at high speed (ten millisecond response will be adequate).

There is at present a wide variety of commercially-available Control System hardware that is compatible with other manufacturers, so that it will be economical to utilize this type of hardware. In particular, there are industrial-grade control modules designed to interface to high-power parts, such as contactors, meters, relays, etc with a minimum of mechanical and electrical design. Figures 7 and 8 show an example of this type of industrial control equipment that will be incorporated in the design.

B. Klystron Evaluation

The signal source for driving the klystron at the Microwave Test Facility had poor short-term phase stability (Ref. 3), so a Hewlett-Packard Model 5065A Rubidium Frequency Standard, a Hewlett-Packard Model 5100A Frequency Synthesizer, and a modified California Microwave, Inc., Model PE84PL-109 X75 Frequency Multiplier was installed as a new signal source (Fig. 9), replacing the HP Model 620A Signal Generator described in the reference. Figure 10 illustrates the short-term stability improvement of the X-band drive chain.

Using the test configuration of Fig. 9, 500-s stability tests were conducted (Fig. 11). Since the klystron phase delay is most sensitive to beam voltage, this parameter is also recorded on the chart.

The VA-876P klystron has been tuned to operate over the full transmitter design range (7145-7235 MHz) with no degradation in performance. The klystron has shown no instabilities or erratic performance during these tests. Figures 12 and 13

show the passband response at both high and low limits of the DSN frequency band.

Figure 14 shows the phase change across the klystron as a function of frequency. This parameter is sometimes referred to as "Group Delay" and is used as a measure of the electrical length of the klystron. Using the values from Fig. 14, the group delay of the VA-876P klystron at mudband is 44 ns. The period of the center frequency (7190 MHz) is 0.139 ns, giving an electrical length of the klystron of 1.14×10^5 electrical degrees.

As of this reporting, Varian Klystron Model VA-876P S/N 344 has operated 692 filament hours and 545 beam hours. The test bed transmitter has operated the klystron through a total of 155 on/off cycles.

IV. Conclusions

The design of the X-band exciter and the transmitter control system have been presented. Techniques were incorporated into the exciter design to assure good short- and long-term frequency stability. From data and conservative estimates, the overall exciter and doppler reference stabilities will be approximately 2.5×10^{-15} for 1000-s integration periods. The 20-kW X-band klystron tube continues to operate satisfactorily and data is being obtained that will permit analysis and prediction of overall system performance.

A future article will describe the complete X-band uplink scheme including the receiver and doppler extractor mechanization and their expected stability factors.

References

- 1 Kuhnle, P. F., "Hydrogen Maser Implementation in the Deep Space Network at the Jet Propulsion Laboratory," to be published.
- 2 Clements, P. A., "Electrical Length Stability of Coaxial Cable in a Field Environment," Technical Report 32-1526, Vol. VII, pp. 97-100, Jet Propulsion Laboratory, Pasadena, Calif.
- 3 Kolbly, R. B., "Evaluation of the VA-876P Klystron for the 20-kW X-Band Uplink Transmitter," *The Deep Space Progress Report 42-54*, pp. 41-50, Jet Propulsion Laboratory, Pasadena, Calif., Dec. 1979.

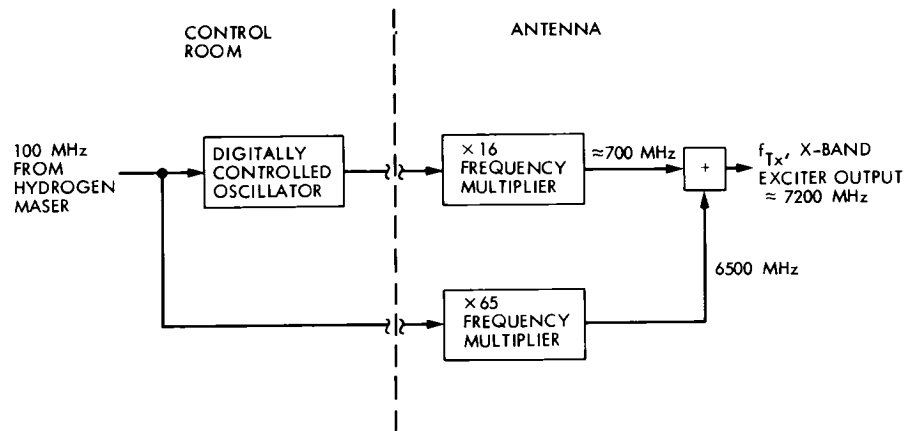


Fig. 1 Simplified block diagram of the basic exciter mechanization

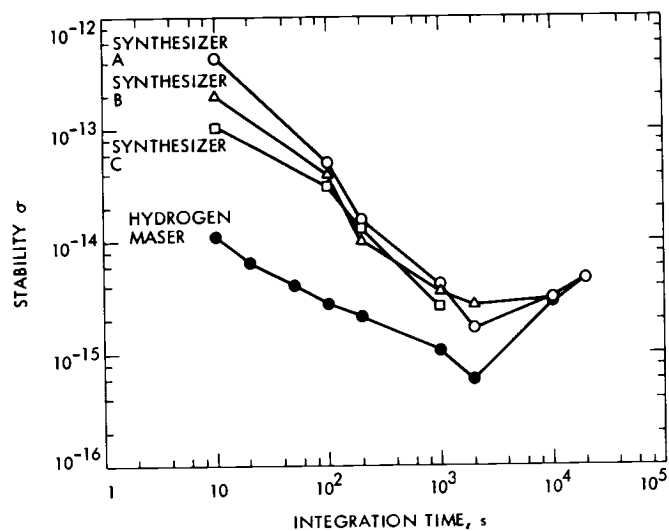


Fig. 2 Measured frequency stability of Dana synthesizers and hydrogen maser

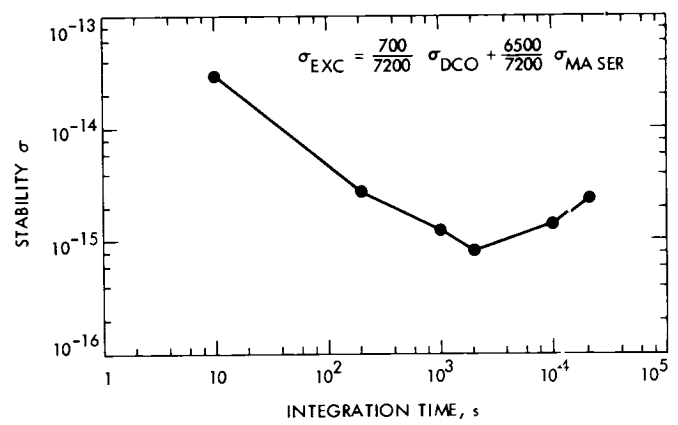


Fig. 3 Combined frequency stability of a Dana synthesizer and hydrogen maser

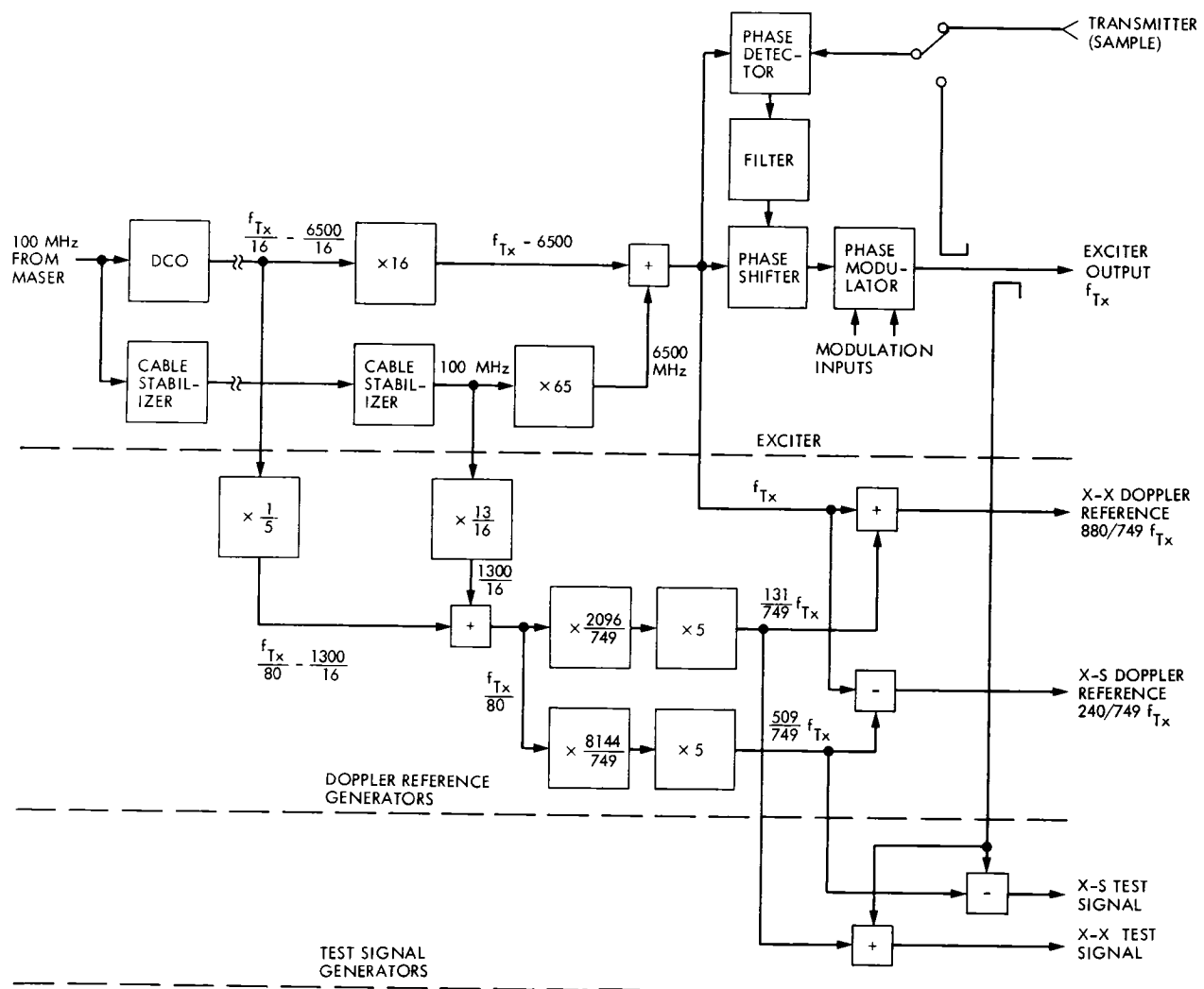


Fig 4 Block diagram of the complete exciter

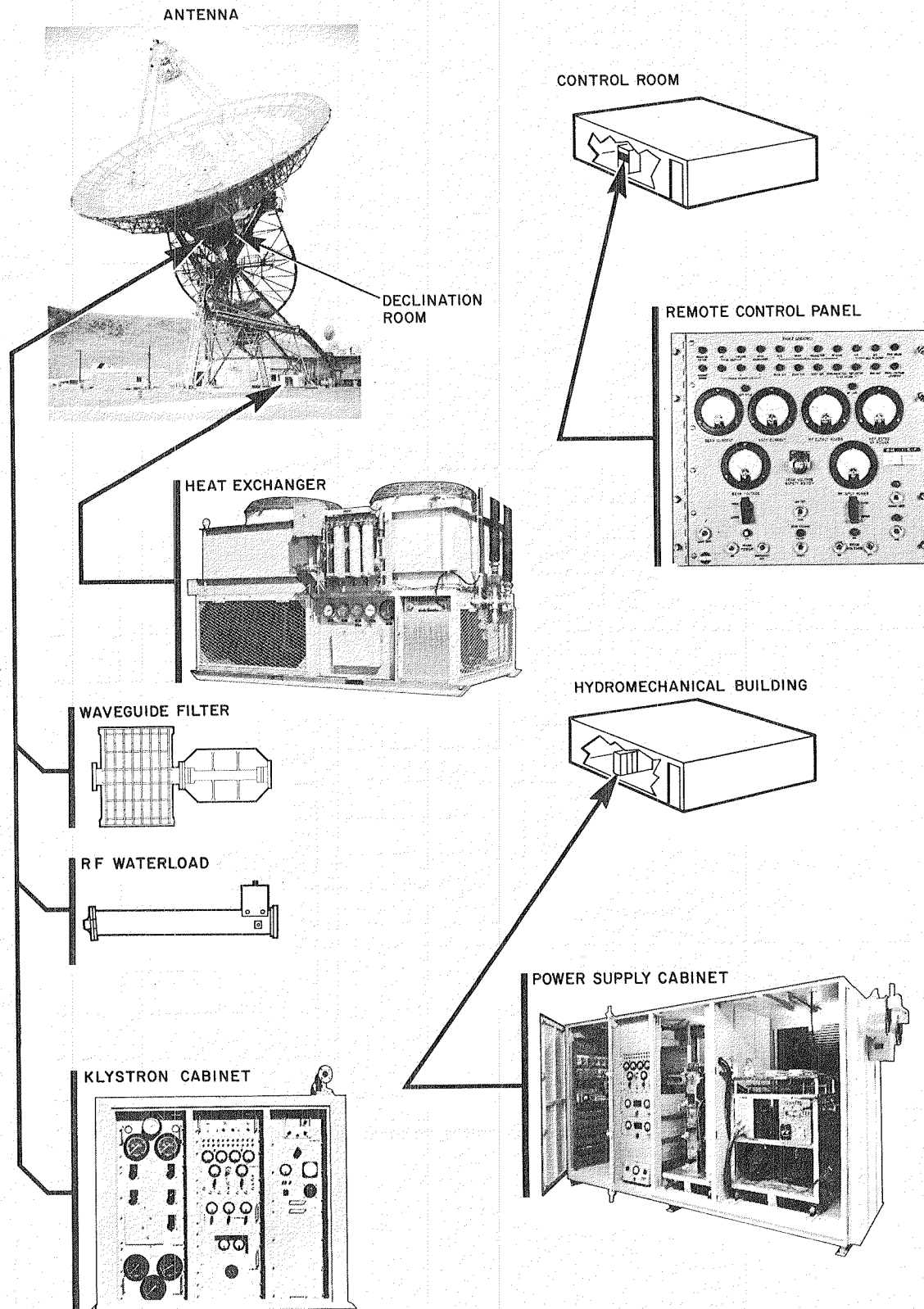


Fig. 5. Typical DSN transmitter subsystem

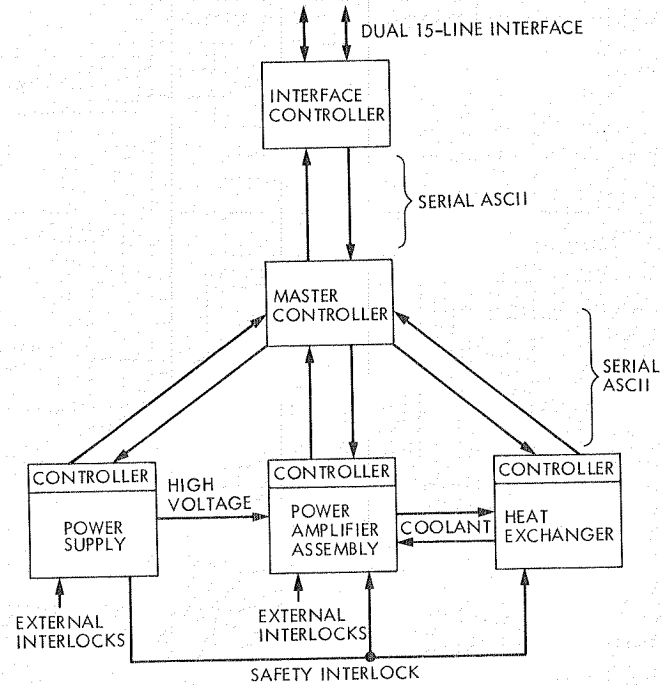


Fig. 6. Block diagram of transmitter control system

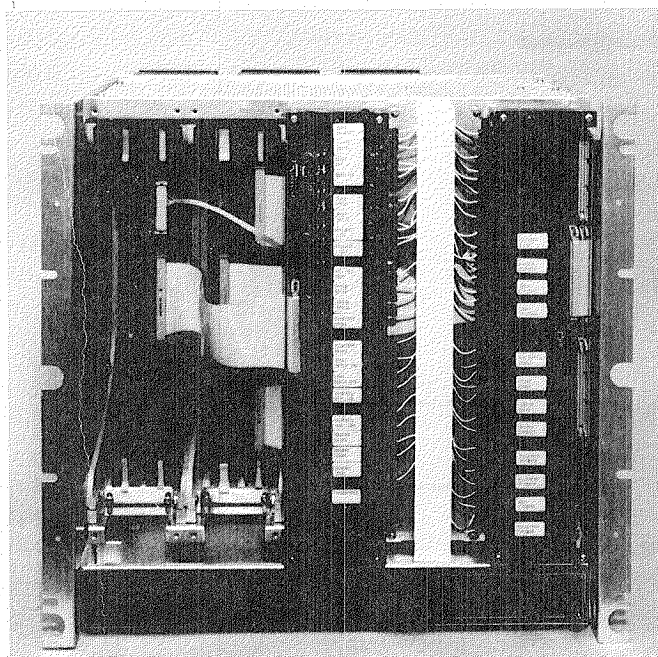


Fig. 7. ICS-80 chassis, front view

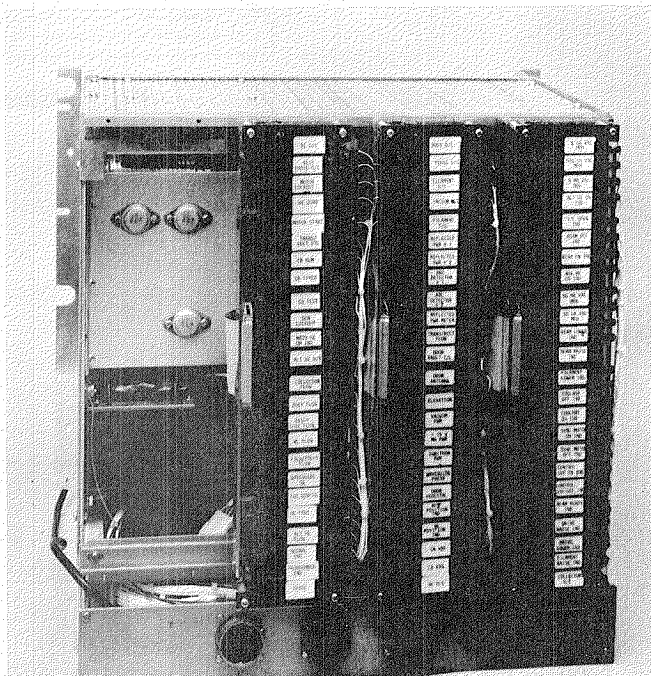


Fig. 8. ICS-80 chassis, rear view

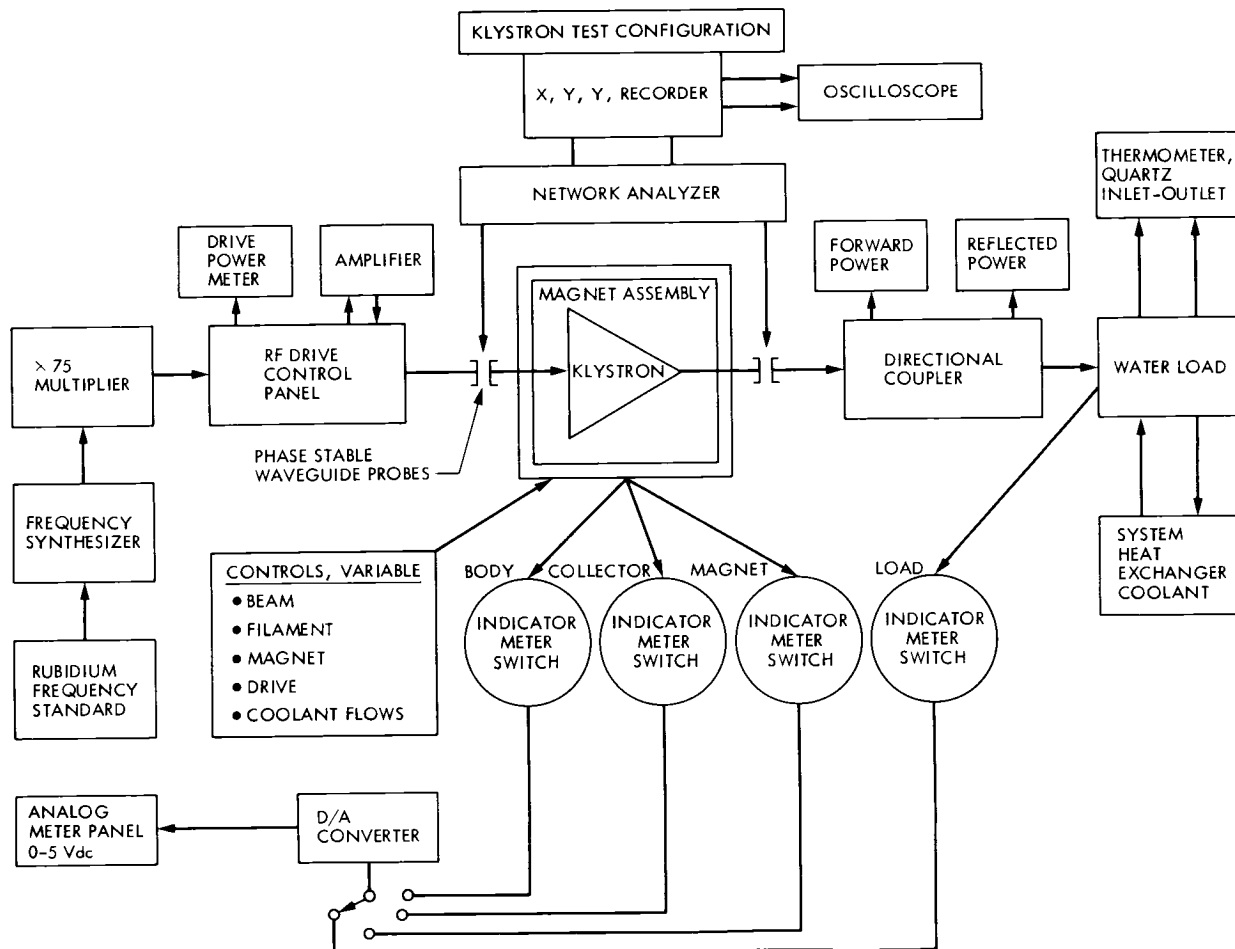


Fig 9 Klystron test configuration

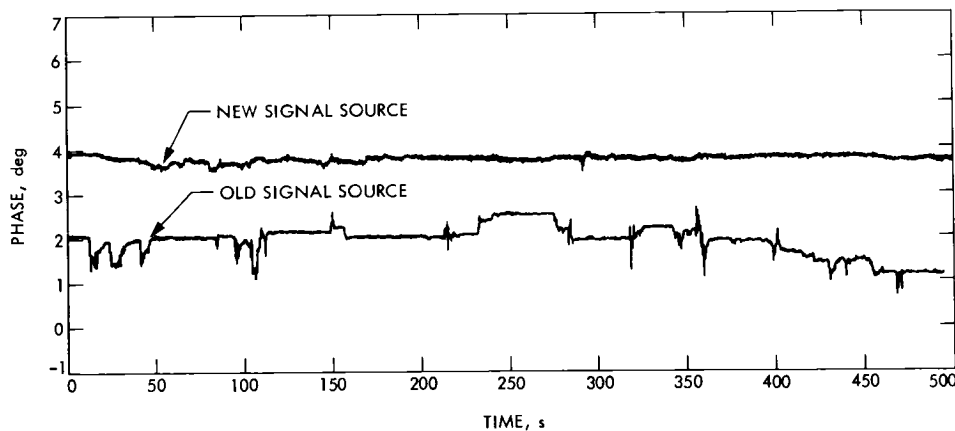


Fig 10. Stability comparison of old and new signal sources

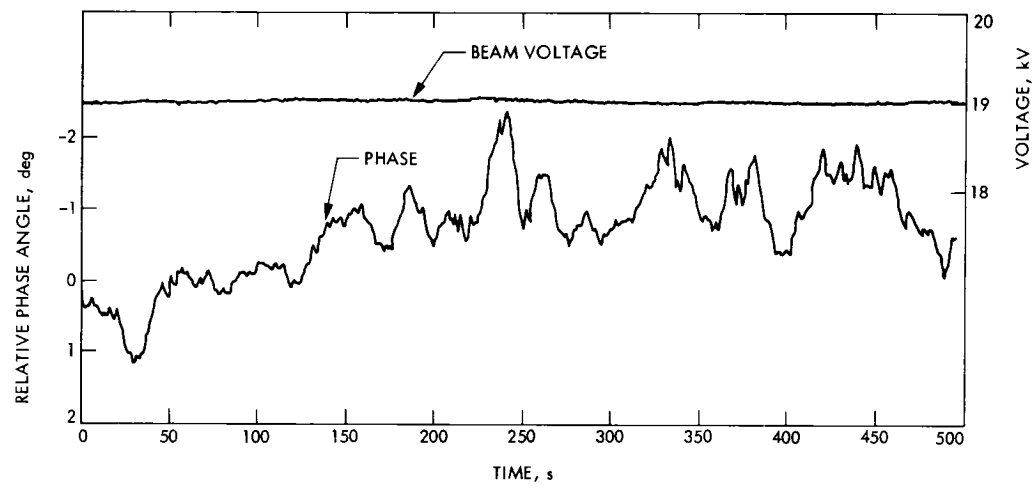


Fig 11 Klystron stability test

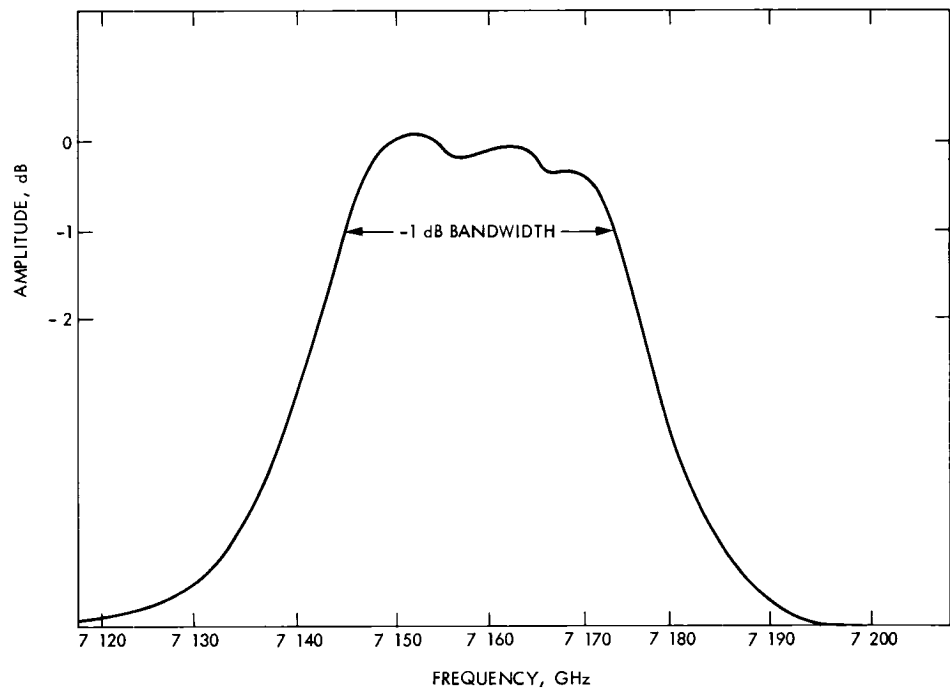


Fig 12 Klystron bandwidth, tuned for lower band

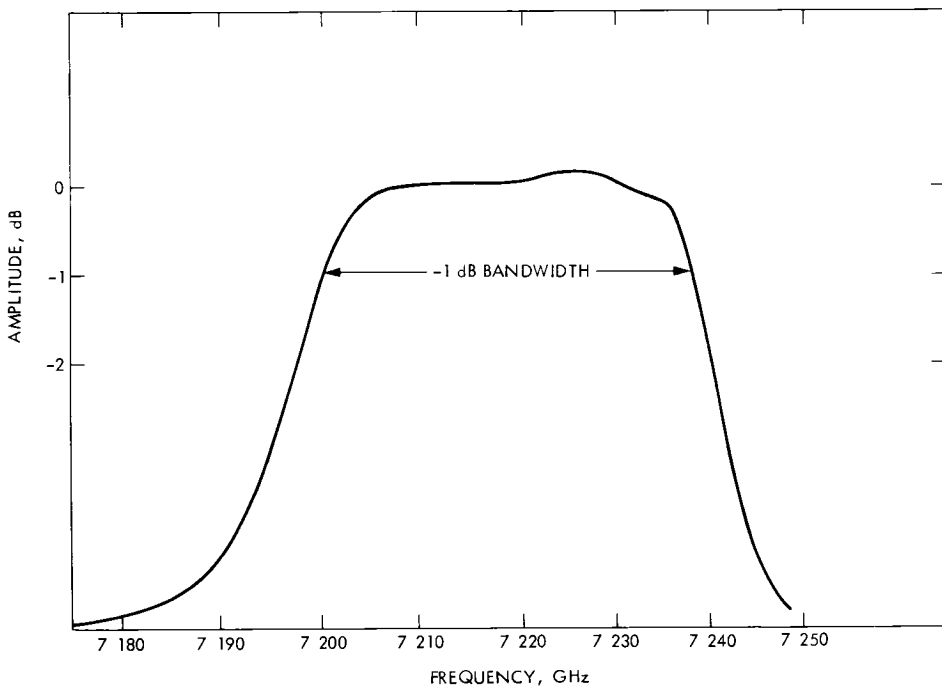


Fig. 13 Klystron bandwidth, tuned for upper band

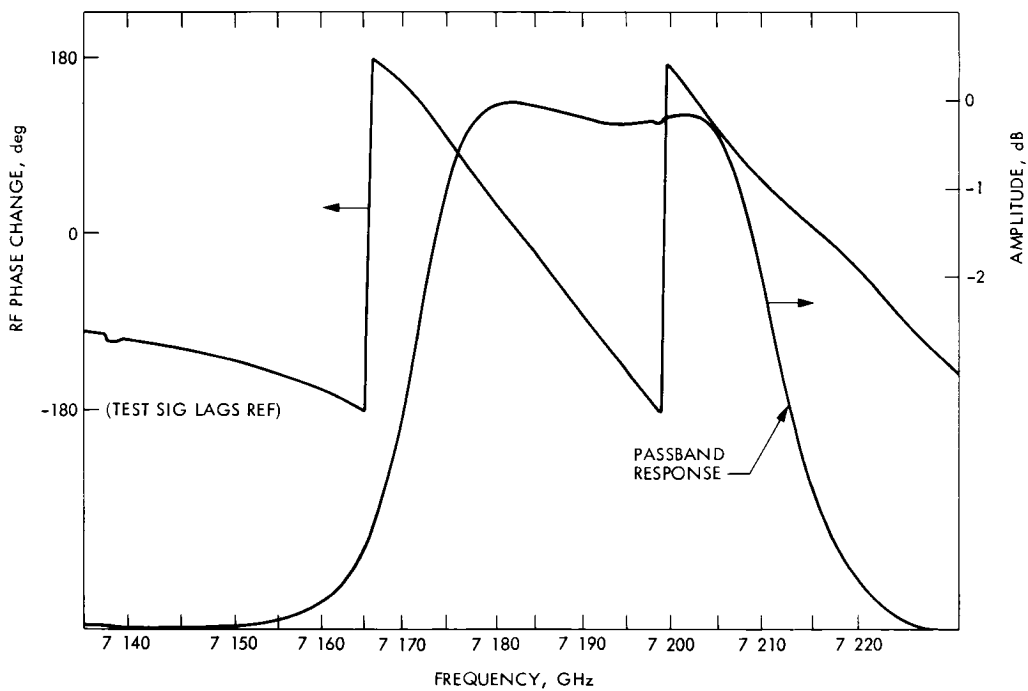


Fig. 14. Klystron RF phase change vs frequency

VLBI Detection of Crustal Plate Motion Using DSN Antennas as Base Stations

D D Morabito, E S Claflin, and C J Steinberg

Tracking Systems and Applications Section

Estimated crustal plate motion is presented with respect to each of the three Deep Space Network (DSN) sites, Goldstone, Madrid and Canberra, based on a plate motion model by Minster et al. The technique of Very Long Baseline Interferometry (VLBI) is capable of measuring crustal movements of a few centimeters per year. The estimated crustal movement predicted by the model is compared with apparent movement measured by the ARIES VLBI group at JPL across a plate boundary in Southern California.

I. Introduction

The Earth's crust consists of six or seven major plates and several minor plates. Indirect evidence of various types indicates that these plates are moving with respect to each other with speeds (based on long term data averages) on the order of several centimeters per year. It was only in the last few decades that geologists realized that the Earth's crust is not rigid (Ref 1), and that the surface features of the Earth are mostly due to the interactions of these plates.

The relative movement between 11 of these plates has been numerically modeled by Minster et al (Refs 2 and 3). Minster assumed the plates to be internally rigid, and used existing indirect geological data types consisting of ocean ridge spreading rates, fracture zone trends and earthquake slip vectors to obtain a self-consistent model of instantaneous relative motions. The plate motion model developed yields a parameter known as the rotation rate vector, which describes the rotation of each plate with respect to another reference plate. Using a DSN station as one component of a VLBI (Very Long Baseline Interferometry) interferometer on a

reference plate, Minster's model can be applied to predict how much relative movement with respect to the DSN station will be detected using a second station at any point on any other plate. The model predictions are valuable for choosing potential new antenna sites where significant continental drift may be detected and measured.

The VLBI measurement technique has been developed in recent years with applications to geodesy, astronomy, and spacecraft navigation. As a geodetic tool, VLBI has the potential to measure crustal movement with high accuracies, yielding errors as low as a few centimeters on baselines measuring up to several hundred kilometers, and possibly up to intercontinental distances.

Thus, VLBI possesses the potential to make direct measurements of relative crustal plate motion which may be compared with the motions inferred from indirect geological data. Such measurements would allow important geophysical questions to be studied and perhaps answered. One such question asks whether the motion between plates is episodic or relatively continuous. Another important question of concern addresses

the relationship between the observed motion and earthquakes. Finally, how do such phenomena as warping and cracking along plate boundaries modify the large scale picture of rigid plate motion? VLBI would be a useful tool in helping to resolve such questions.

Project ARIES (Astronomical Radio Interferometric Earth Surveying) is currently performing geodetic measurements in California (Refs 4-6). The base stations include the DSN antennas at Goldstone and the Caltech Owens Valley Radio Observatory, both of which reside on the North American plate. The San Andreas fault separates the North American plate from its western neighbor the Pacific plate, which includes much of coastal Southern California. The ARIES 9-meter portable dish antenna has occupied several sites in this coastal region, and hence may be able to directly measure the relative motion of these two plates.

This article discusses the prospects of the VLBI technique for detection and measurement of crustal drift using DSN stations. Potential sites for other, fixed or portable stations are suggested by applying the model developed by Minster. Current measurements from Project ARIES are compared with the crustal model predictions.

II. The Rigid Plate Model

The description of the displacement of a rigid plate on the surface of a sphere may be understood in terms of rigid body motion. The correspondence becomes clear if one imagines that the moving plate contains an embedded set of body axes and the Earth (or another plate) contains the reference axes. The two coordinate systems have common origins at the center of the sphere (Earth). A basic theorem of rigid body motion then assures us that any translation and/or rotation of the plate is describable as purely a rotation about some axis fixed in the reference system and passing through the Earth's center. Simplicity ends here, however, because the sum of two rotation vectors does not, in general, give a displacement equal to the successive application of the individual rotations. However, by writing the coordinate transformation equations in linear approximation, it can be shown that the rotation vectors for small displacements are additive.

The important implications of these results for plate motion are that instantaneous relative motion of two plates can be described completely by a single rotation rate vector and that the relative rotation rates of plates are additive. Thus the Minster et al data was easily applied to predict plate motion with respect to the DSN antennas for six major plates.

The magnetic anomalies used by Minster to compute spreading rates are as old as several million years. Changes in

the instantaneous rotation rate vectors become significant after approximately 10 million years. We will assume that this model is valid for current geological time.

III. Crustal Drift Rates With Respect to DSN Stations

Plate motion has been determined using the rotation rate vectors given by Minster et al (Ref 2), using the DSN sites as base stations. Figures 1-3, 4-6, and 7-9 display the plate motions to be expected for reference stations at Goldstone (North American plate), Australia (Indian plate), and Madrid (Eurasian plate), respectively. Displayed for each DSN station is a contour map of constant total velocity magnitude, constant baseline extension rate (movement along the baseline), and constant transverse velocity magnitude (movement perpendicular to the baseline). Each map displays motion with respect to five other plates. The six major plates included on the maps are the North American, Pacific, Indian, Eurasian, African and South American plates. The DSN site is marked on each map with a plus sign. Plate boundaries displayed are not necessarily definitive, but are believed to be accurate enough for the purposes of these maps.

IV. VLBI as a Geodetic Tool

The technique of VLBI may be applied to detect and measure crustal plate drift. The VLBI system consists of two or more radio telescopes widely separated, each residing on different tectonic plates. A VLBI experiment consists of having both antennas of a particular baseline simultaneously observe a sequence of extragalactic radio sources well distributed across the sky. Each experiment usually lasts several hours and each observation of a radio source lasts several minutes. The measured baseline is obtained from a fit using the measurements of the differential time of arrival of the wavefronts from each radio source at the two antennas. The overall theoretical development and data reduction technique is quite involved and will not be discussed here. The reader is referred to the papers by Thomas (Refs 7 and 8) for more detailed discussions.

By performing VLBI experiments over a period of many years, we have the capability of measuring variations of the baseline vector and hopefully refining current plate motion models significantly. In particular, small scale deformations (deviations from rigid plate theory) may be determined using this technique. Deviations from the rigid plate theory are certain to exist. Plate boundaries are diffuse, small plates do exist, and motion along plate boundaries is not continuous, as exhibited by the existence of earthquakes. Movement along

plate boundaries involves slippage to relieve stress. Accumulation of stress can cause a wide zone of deformation across plate boundaries which can go deep within a plate. Also, the motion computed from the rigid plate model is averaged from data which spans millions of years and may vary over shorter time scales.

The two principal components measured by VLBI are the baseline extension component and the transverse velocity component. The baseline extension rate is easily computed by fitting a slope through the solved-for baseline lengths from several VLBI experiments on the same baseline. The baseline length has a very low error since it is a direct consequence of measured delay and does not depend on coordinate orientations. The baseline transverse component may have a higher error since it is dependent on baseline orientations. Therefore, VLBI may measure baseline extension rates more accurately, and this should be taken into consideration when examining these maps for detection opportunities.

The maps indicate some excellent short baseline opportunities in Australia. Short baseline measurements have the advantage over long baseline (intercontinental) measurements of having lower errors and decreased cross-coupling between estimates of baseline components. Using the DSN sites in Canberra, Australia as a base station, some nearby sites where significant baseline extension may be detected and measured are New Zealand, Southeast Asia, and some nearby islands on the Pacific Plate. Movement here is on the 5 cm/year level. Measurements of total velocities will yield larger numbers (~10 cm/year), thus detection is perhaps possible after only a couple of years of observing.

The maps also indicate many long baseline opportunities for detecting crustal movement using Canberra as a base station. In every other crustal plate displayed, total velocities run about 5 cm/year or greater. The Hawaiian islands as a portable site have total velocities with respect to Canberra running about 8 cm/year, with the corresponding extension rate being about -5.5 cm/year. The Goldstone/Canberra baseline has a predicted -3.5 cm/year baseline extension rate. Some islands east of Japan may yield total velocity measurements of about 11 cm/year.

Short baseline opportunities using Madrid as a base station are obviously not as good since the rates in the local area are relatively smaller. Subcentimeter accuracies may become a reality as the VLBI technique matures, thus allowing the less dramatic crustal motions to be detected in time periods of a few years. Using Madrid as an intercontinental site shows some interesting opportunities with respect to total velocities on the Indian plate (~5 cm/year in Australia) and Pacific plate (~8 cm/year in Hawaii). Using a Madrid/Goldstone interferometer

may yield baseline extension rate measurements on the order of 2 cm/year.

Goldstone as a base station has interesting opportunities for measurement of crustal plate drift using portable stations on various islands on the Pacific plate, and the Indian plate (Australia and vicinity). Here movement is on the order of 6 to 9 cm/year. A Goldstone/Hawaiian interferometer may measure a 2.5-cm/year extension rate.

Short baseline opportunities using Goldstone as a base station are excellent owing to the close proximity of the Pacific plate. Short baseline experiments using Goldstone as a base station have actually been carried out. The next section describes the results.

V. Present Measurements (Project ARIES)

Project ARIES currently operates the only sophisticated transportable VLBI system in the world, monitoring various baselines in California. The idea of using portable antennas to monitor a tectonically active and complex region such as California has been presented by Shapiro and Knight (Ref 9). Project ARIES has been taking data since 1973, occupying various sites on the western side of the San Andreas fault (Pacific Plate) while the DSN stations at Goldstone and the Owens Valley Radio Observatory (OVRO) served as the larger fixed base stations on the North American plate side.

California is a tectonically complex region where the San Andreas fault serves as the principal plate boundary. Near the boundary each plate actually consists of many blocks, each behaving differently, hence the need for occupying many different sites in order to understand the tectonics of the region.

The current accuracy with which an ARIES vector baseline can be determined is at the 6- to 10-cm level (one sigma) in each of three orthogonal components. The accuracy of the baseline length is at the 3-cm level. Since plate motion per year is at approximately the same magnitude as the error level, detection of continuous movement is possible after a few years of data taking. The number of years of data taking for detection of plate drift depends on frequency of measurement and individual measurement error. The only site (baseline) occupied by the ARIES portable 9-meter antenna in which enough data has been taken and movement apparently detected is the JPL site (DSS 14/JPL baseline).

Figures 10-12 show the local California area displaying the Minster model results, using DSS 14 at Goldstone as a base station. The ARIES JPL location is also shown. The model predicts that the DSS 14/JPL interferometer should detect a

5 5-cm/year total velocity magnitude, a -1 0-cm/year baseline extension rate, (or +1 0-cm/year baseline compression rate) and a 5 4-cm/year transverse velocity magnitude, all consistent with the right lateral strike slip motion along the San Andreas fault, which separates the North American and Pacific plates. Transforming the model results to the usual geographic directions, one then predicts that JPL should move 3 6 cm/year west and 4 1 cm/year north, with respect to Goldstone. To date the only component of movement detected from VLBI that is statistically significant is a 5.6 ± 1.9 -cm/year westward movement of JPL relative to Goldstone (DSS 14) (Ref 6). This rate was measured by the ARIES group utilizing data from VLBI experiments performed during the period 1974-1977. The measured rate is in reasonable agreement with the predicted 3.6 cm/year westward rate, but it is cautioned that it is not necessary for local measurements to match the general plate motion model, due to the complexities of plate tectonics previously discussed.

Project ARIES is a current research and development VLBI project. The operational version of ARIES, now in the design stages, is project ORION (Operational Radio Interferometry Observing Network), which will utilize a network of many portable stations. In addition to extragalactic radio sources, satellites may prove to be a valuable emitter of radio signals for application to VLBI. A future variation of the ARIES

technique is the newly initiated project SERIES (Satellite Emission Radio Interferometric Earth Surveying). This technique will make use of military satellites as sources instead of natural radio sources. Because the artificial satellites have higher received signal-to-noise ratios than natural radio sources, this technique has the advantage of utilizing less sophisticated ground equipment.

VI. Conclusion

VLBI provides an excellent tool for measuring crustal movements and deformation by judicious placement of antennas on various sites within plates and across plate boundaries. Measurement of crustal movement will confirm the theory of plate tectonics, and measurement of deformations may yield valuable information regarding the structure of the plates. Thus, we will be able to get an improved picture of local deformations, and be able to see what type of behavior is occurring as a function of time. Many measurements over the course of a year can give us increased time resolution. Important geodetic information can be obtained by combining results from both short (local) and long (intercontinental) baselines. As the VLBI technique is perfected, the accuracy in measuring baselines has the potential of reaching the subcentimeter level.

Acknowledgments

We would like to thank R A Preston, D W Trask, and M A Slade for their valuable comments and the ARIES group for the use of their data

References

- 1 Hurley, Patrick M "The Confirmation of Continental Drift," *Scientific American*, April 1968
- 2 Minster, J B , Jordan, T H , Molnar, P , and Haines, E , "Numerical Modeling of Instantaneous Plate Tectonics," *Geophys J Royal Astron Soc* (1974) 36, pp 541-576
- 3 Minster, J B , and Jordan, T H , "Present-Day Plate Motions," *J Geophys Res* (November 10, 1978), Vol 83, No B 11, pp 5331-5354
- 4 Niell, A E , Ong, K M , MacDoran, P F , Resch, G M , Morabito, D D , Claflin, E S , and Dracup, J F , "Comparison of a Radio Interferometric Differential Baseline Measurement With Conventional Geodesy," *Tectonophysics*, 52 (1979) 49-58
- 5 Ong, K M , MacDoran, P F , Niell, A E , Resch, G M , and Morabito, D D , "Radio Interferometric Geodetic Monitoring in Southern California," *EOS-Trans , Amer Geophys Union*, Vol 58, No 12, p 1121 (Nov 1977)
- 6 Niell, A E , "Further Monitoring of the Pasadena, Goldstone, Owens Valley Baselines by VLBI Geodesy," *EOS-Trans , Amer Geophys Union*, V 60, No 46, p 810 (Nov 1979)
- 7 Thomas, J B , "An Analysis of Long Baseline Radio Interferometry," Technical Report 32-1526, Vol VII, p 37, Jet Propulsion Laboratory, Pasadena, Calif (1972)
- 8 Thomas, J B , "An Analysis of Long Baseline Interferometry, Part III," Technical Report 32-1526, Vol XVI, p 47, Jet Propulsion Laboratory, Pasadena, Calif (1973)
- 9 Shapiro, I I , and Knight, C A , "Geophysical Applications of Long Baseline Radio Interferometry," in *Earthquake Displacement Fields and the Rotation of the Earth*, edited by L Mansinha, D E Smylie and A E Beck, p 284, Springer, New York (1970)

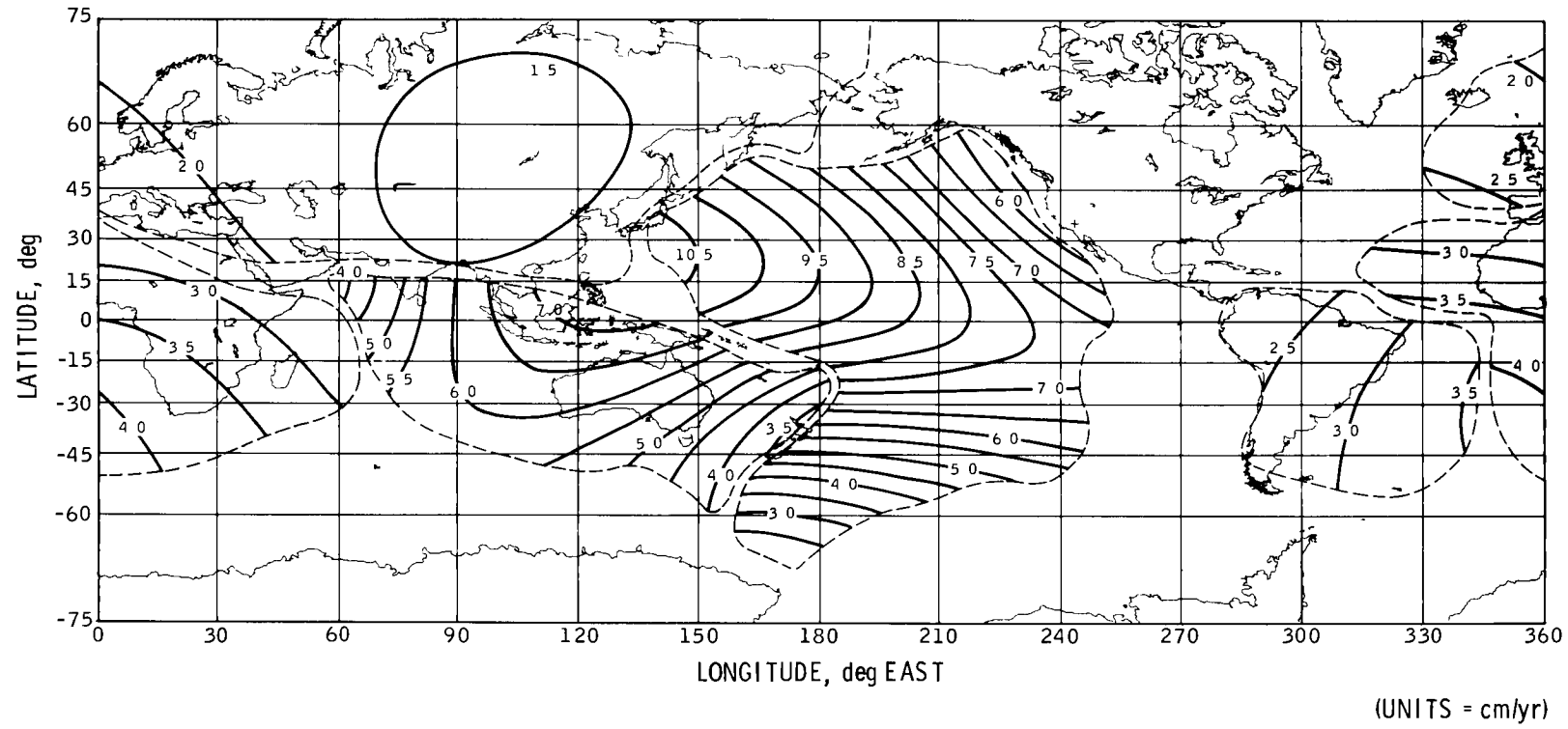


Fig 1 Tectonic plate total velocities with respect to Goldstone

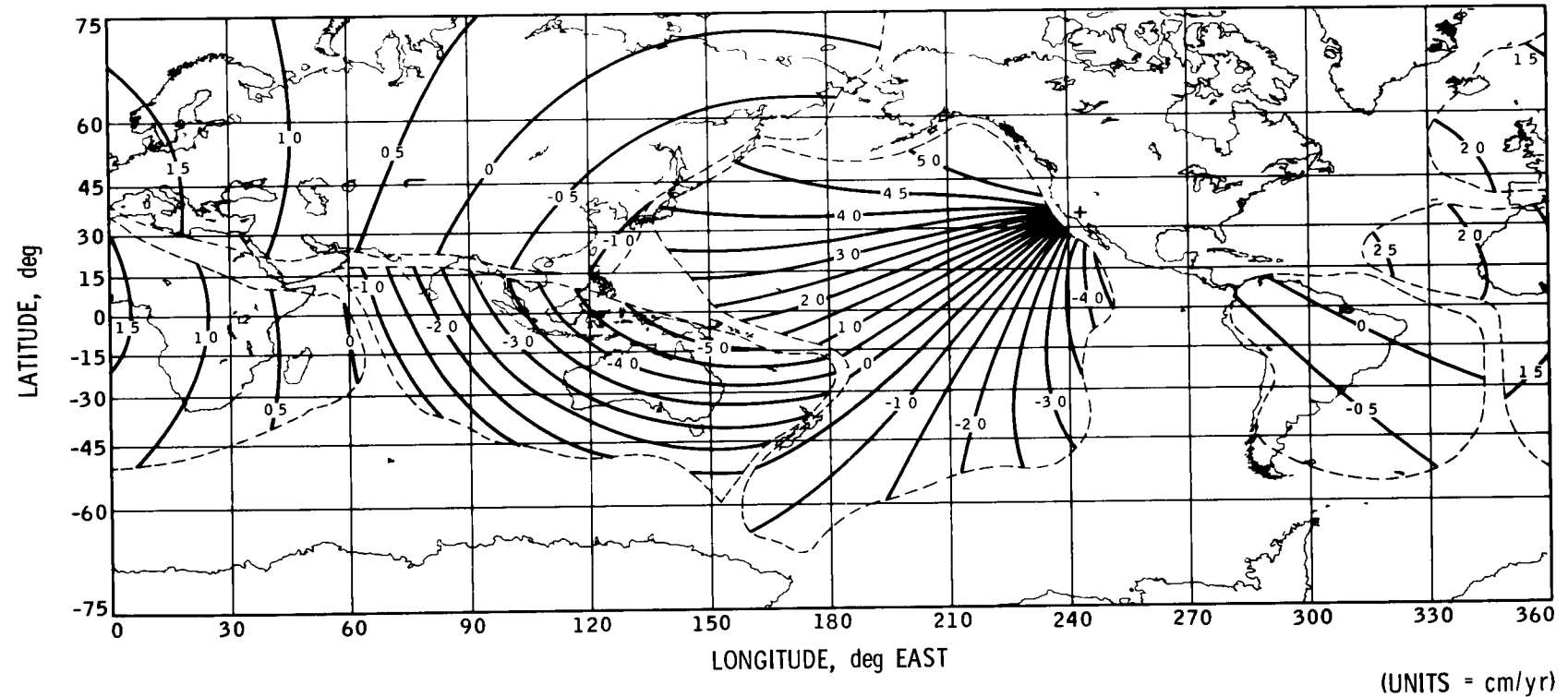


Fig 2 Tectonic plate extension rates with respect to Goldstone

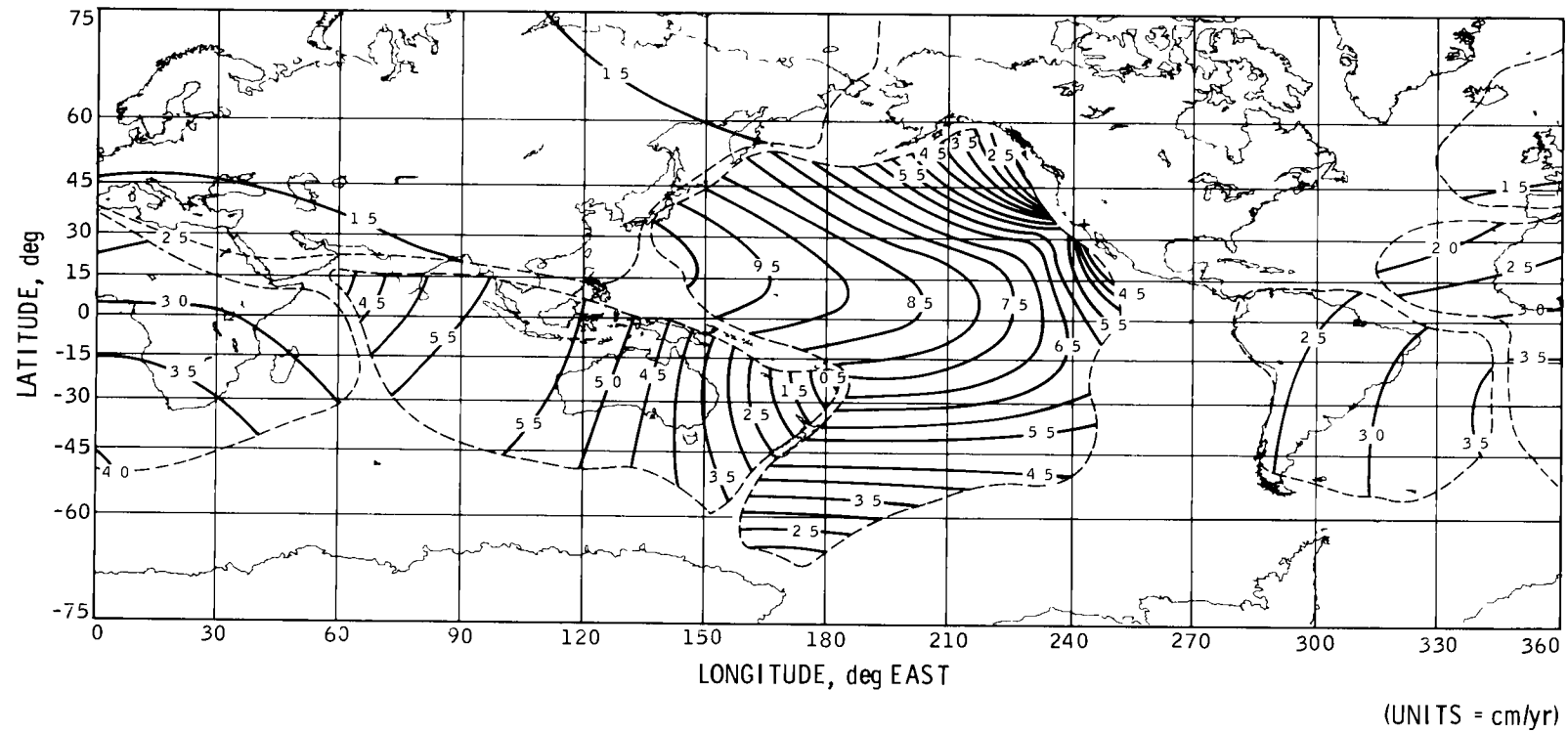


Fig. 3 Tectonic plate transverse velocities with respect to Goldstone

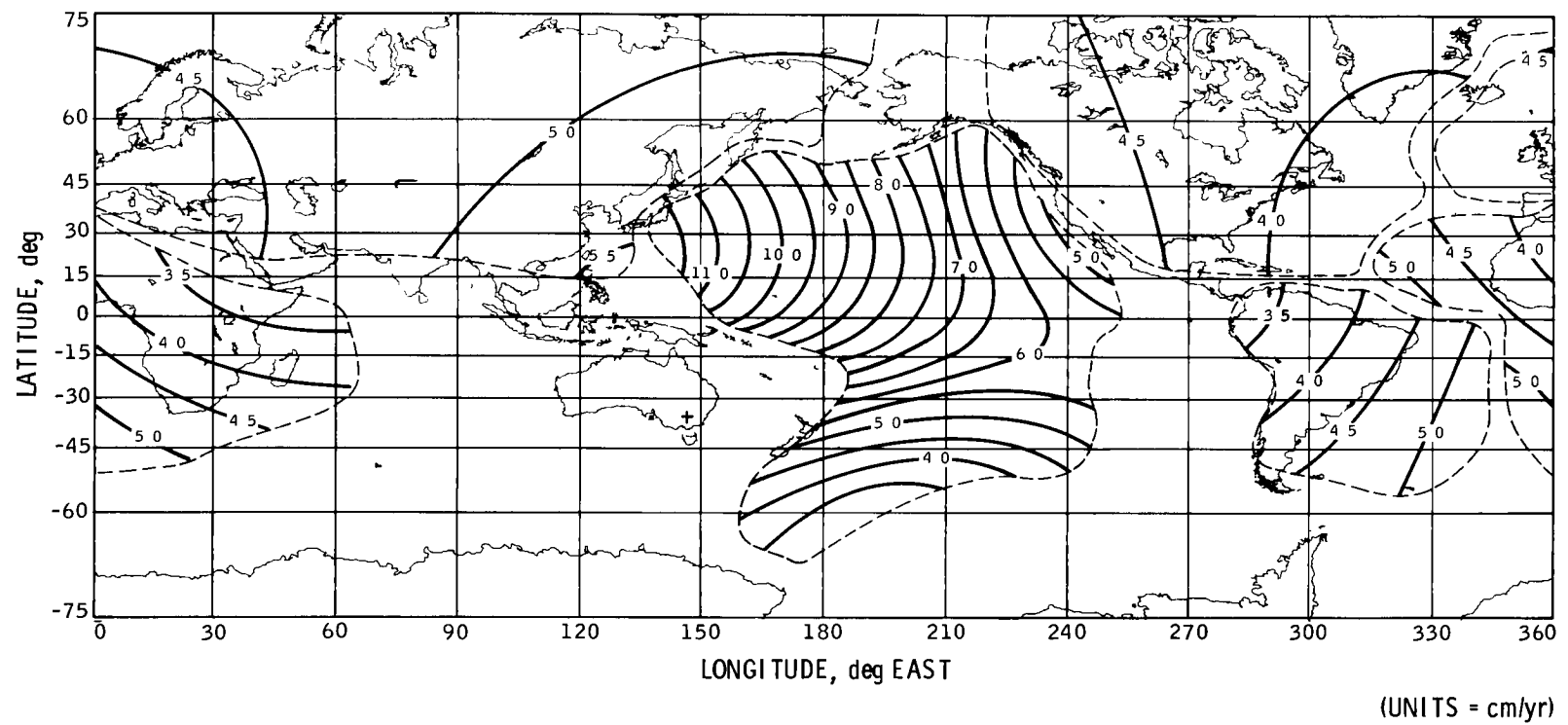


Fig. 4 Tectonic plate total velocities with respect to Canberra

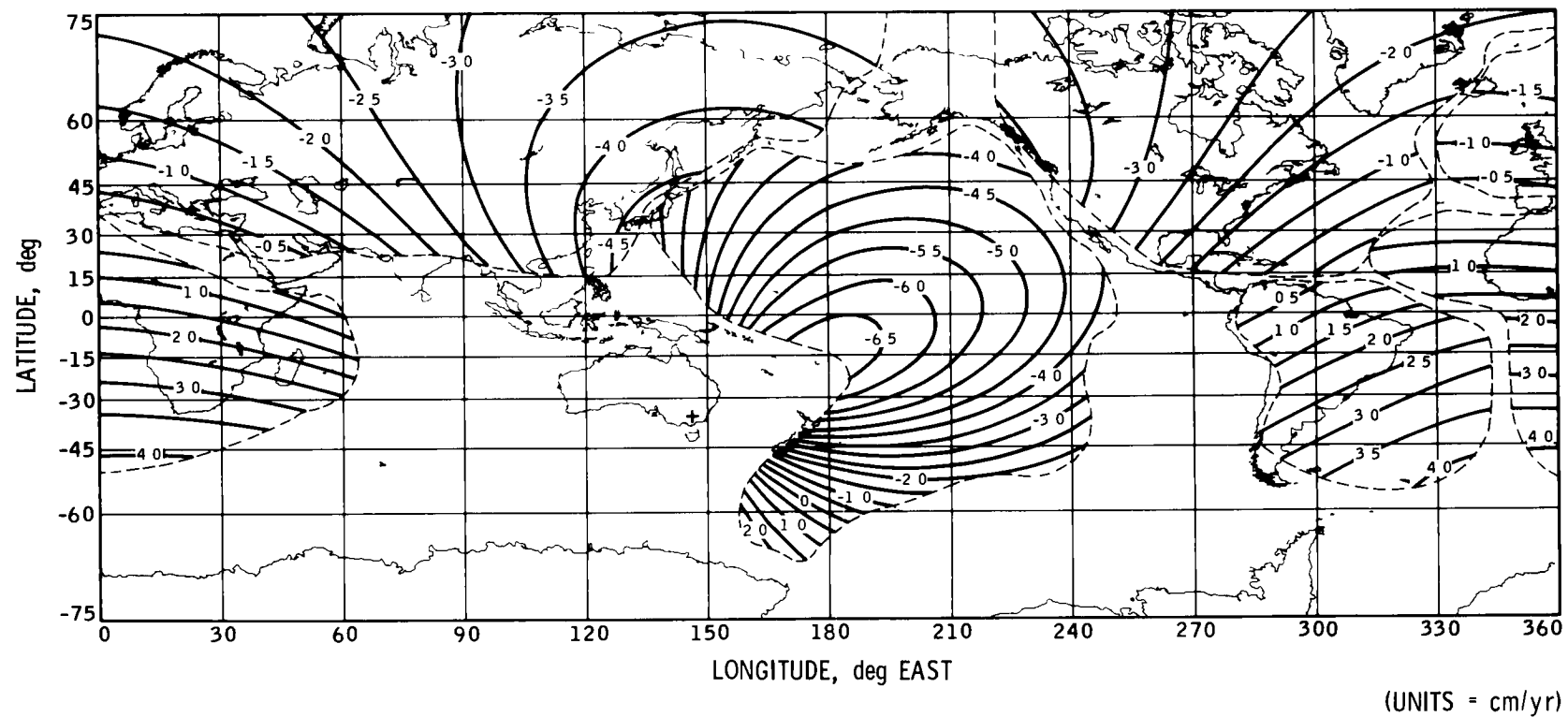


Fig. 5 Tectonic plate extension rates with respect to Canberra

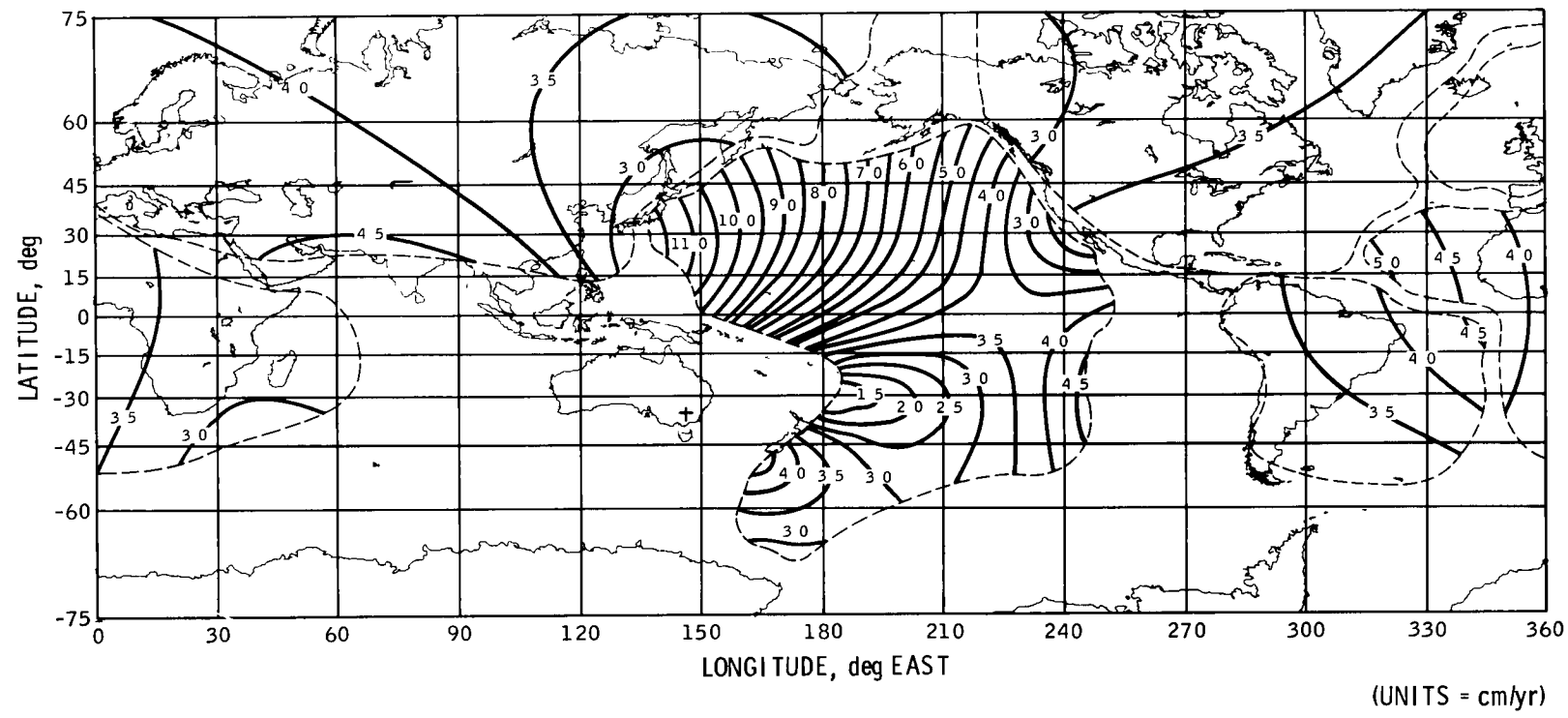


Fig 6 Tectonic plate transverse velocities with respect to Canberra

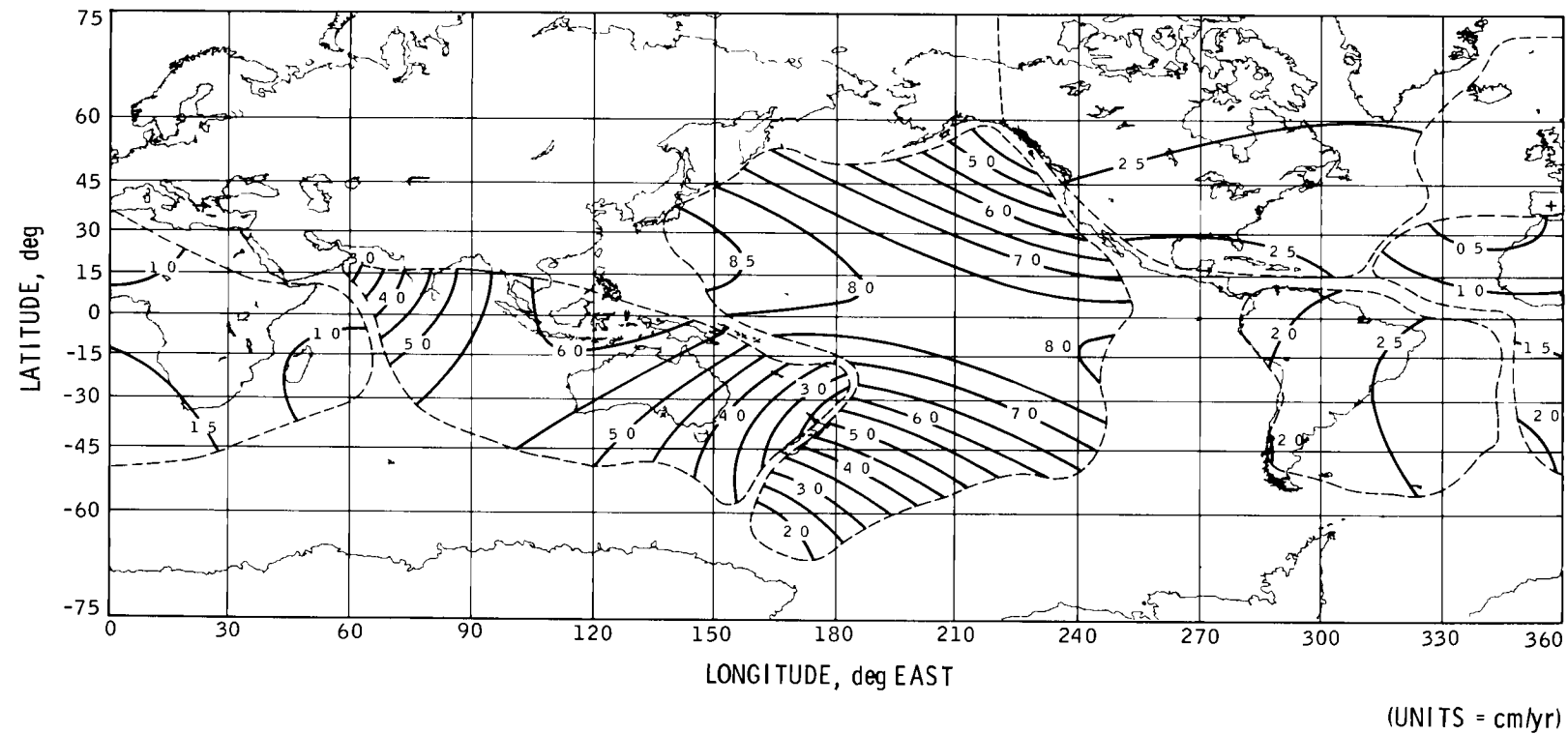


Fig 7 Tectonic plate total velocities with respect to Madrid

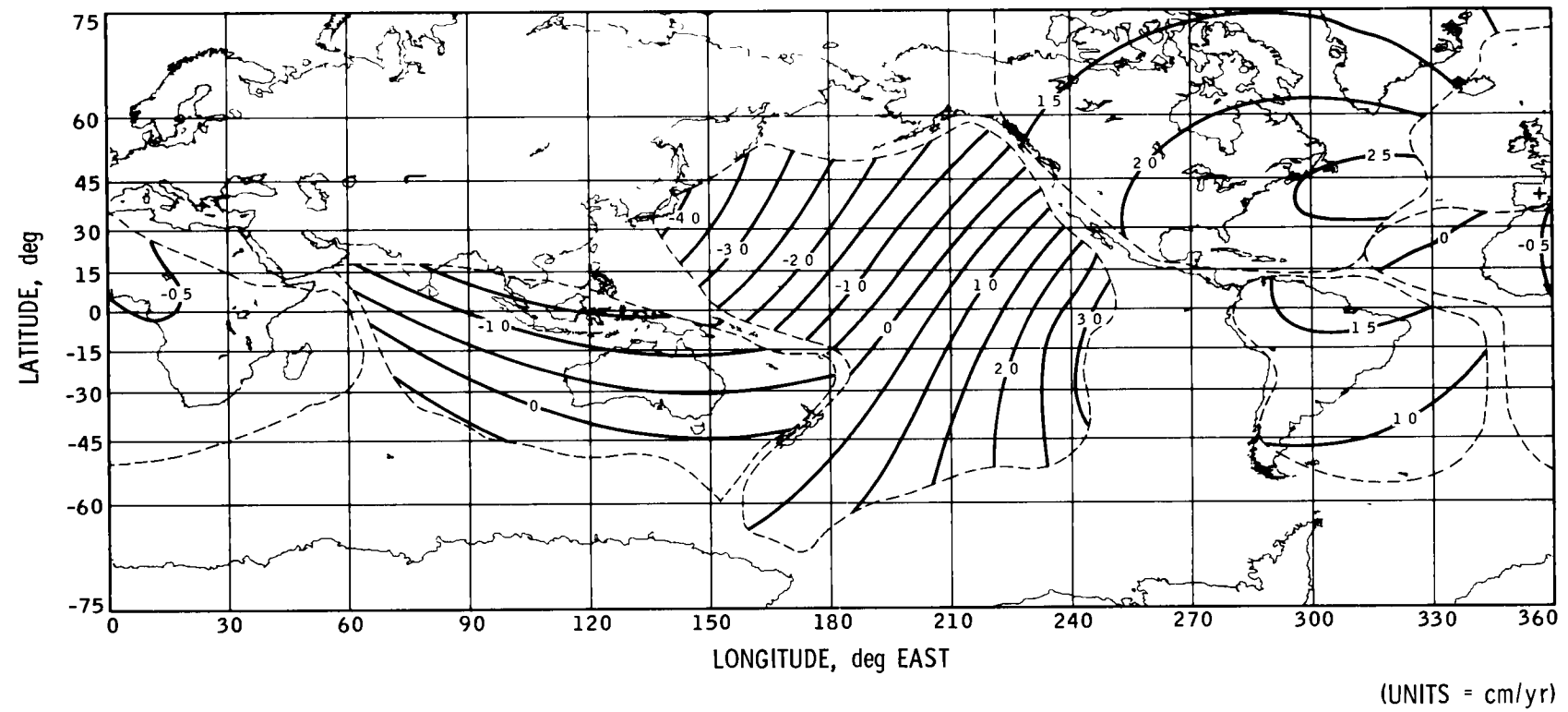


Fig 8 Tectonic plate extension rates with respect to Madrid

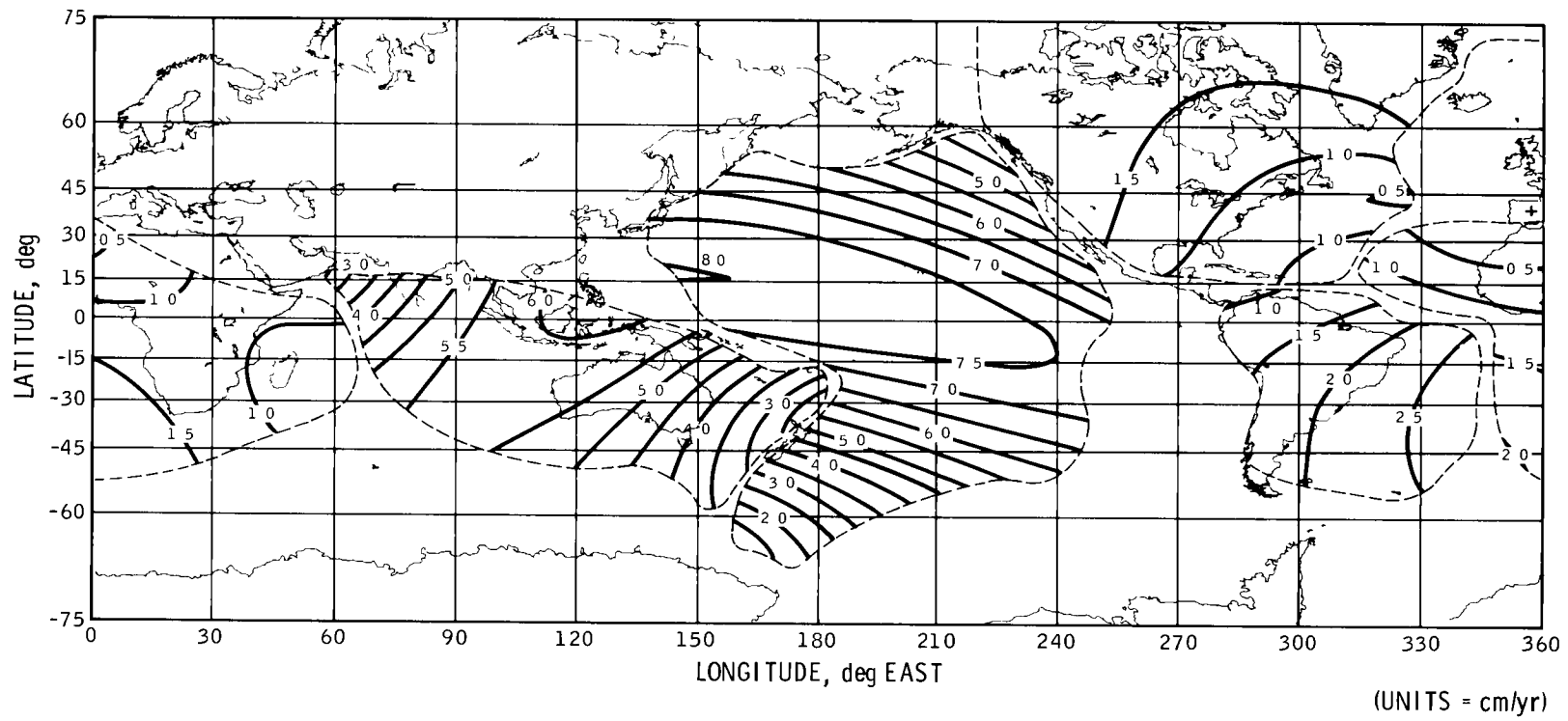


Fig. 9 Tectonic plate transverse velocities with respect to Madrid

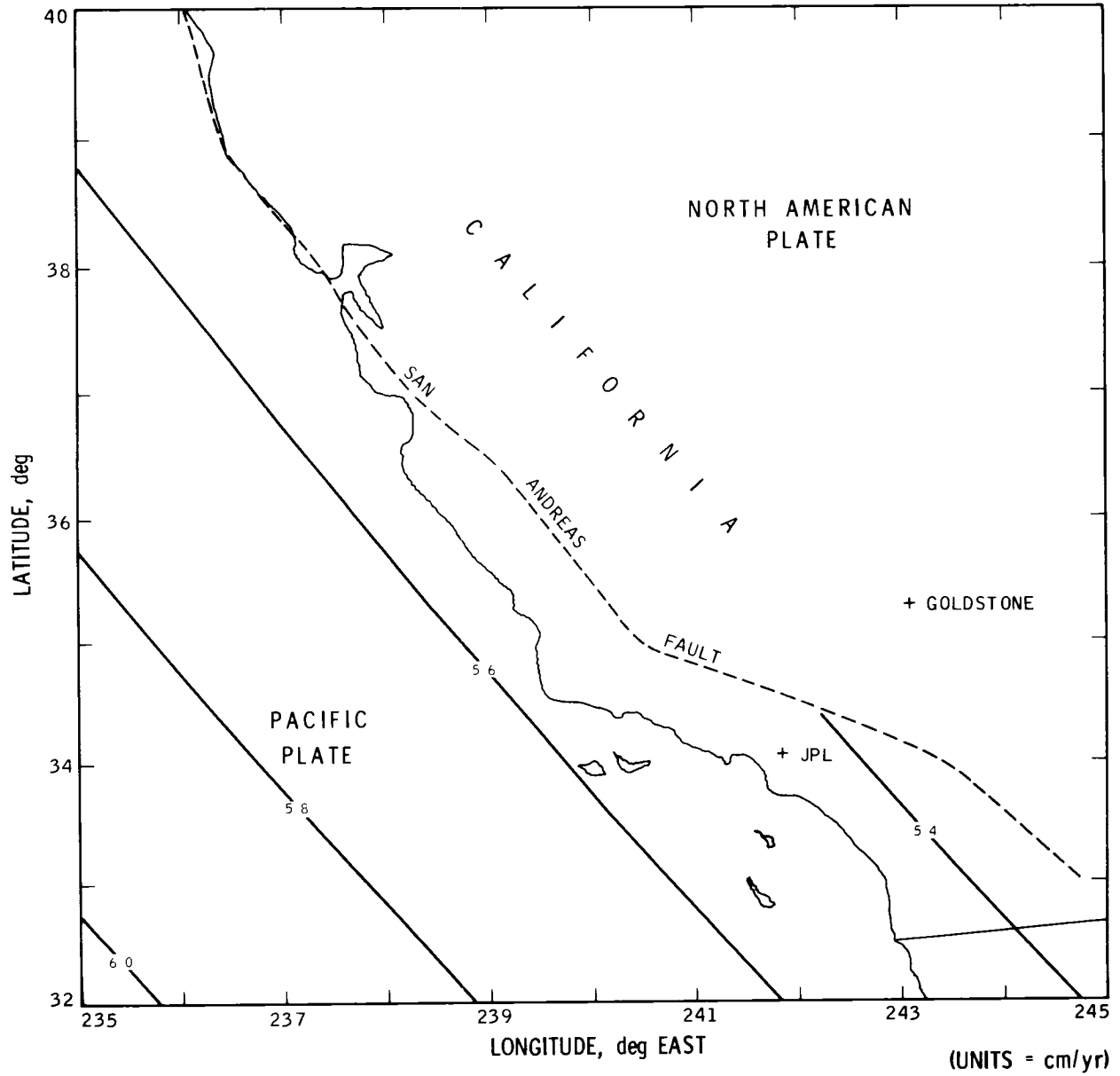


Fig. 10 Local plate total velocities with respect to Goldstone

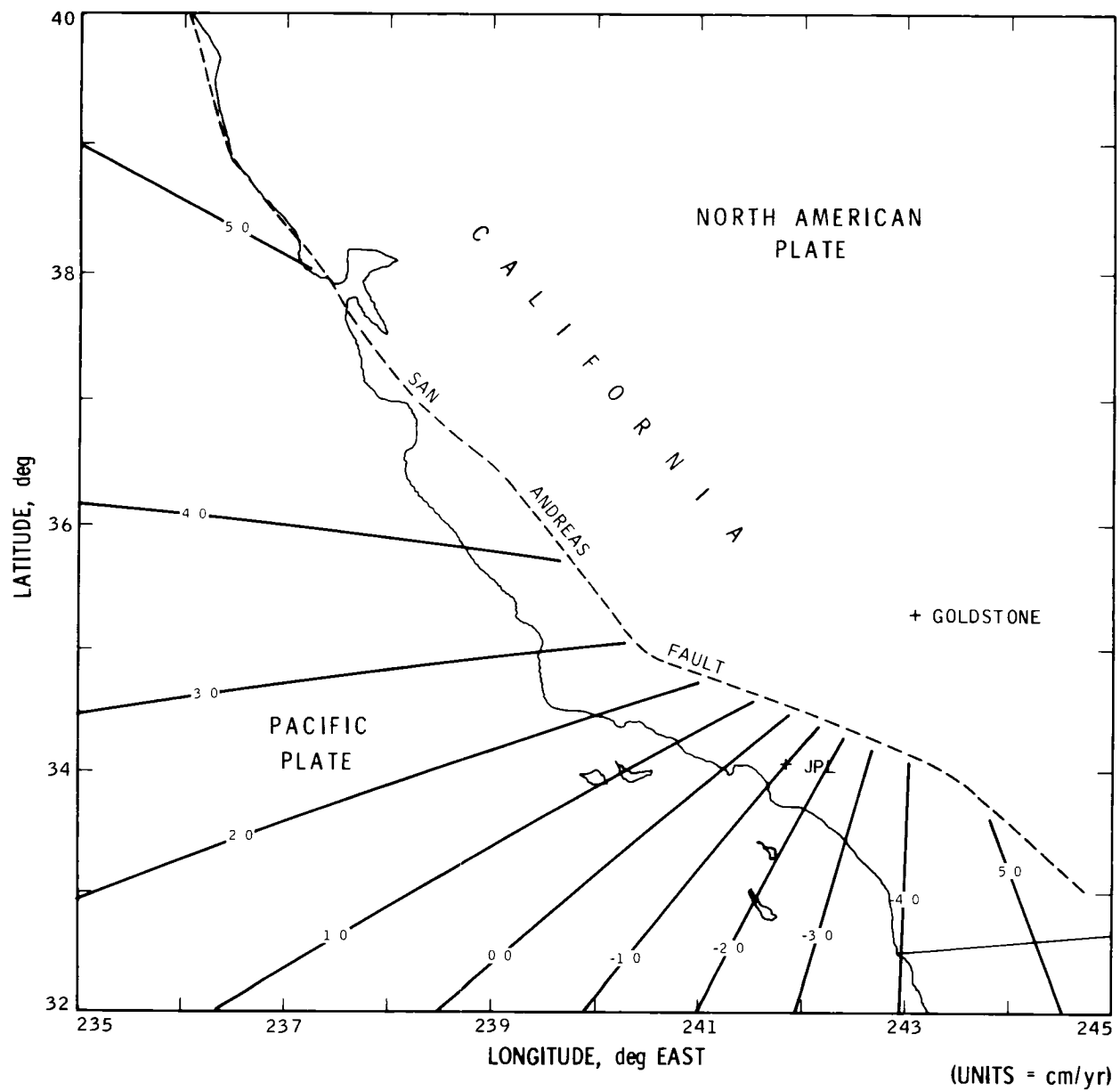


Fig 11 Local plate extension rates with respect to Goldstone

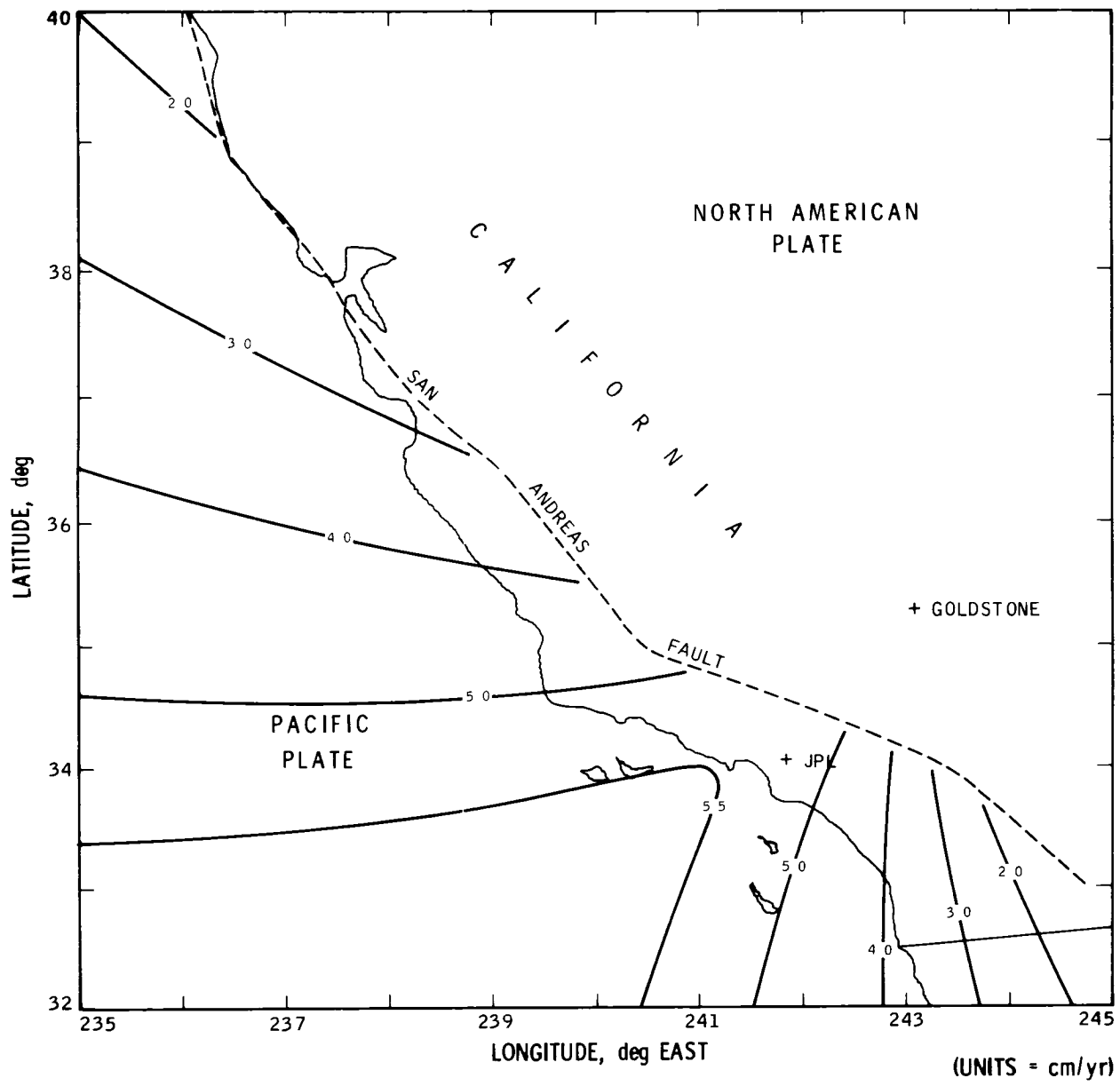


Fig. 12 Local plate transverse velocities with respect to Goldstone

A Bent Pipe Design for Relaying Signals Received by an Orbiting Deep Space Relay Station to a Ground Station

M A Koerner

Telecommunications Systems Section

The ODSRS (Orbiting Deep Space Relay Station) would be a geostationary or geosynchronous earth satellite designed to receive signals from spacecraft at lunar or planetary distances. A communication link will be required to transfer the data received by the ODSRS to a ground station. This article examines the feasibility of using a "bent-pipe" type system to relay the entire RF signal received by the ODSRS together with its receiving system noise to the ground station.

The analysis and numerical results presented herein should provide an acceptable basis for selecting an ODSRS/ground link design. The use of a "bent-pipe" channel appears feasible for each of the three ODSRS applications considered herein. Of the three applications considered, the maximum ODSRS transmitter RF power output required was 5.3 watts for a 25 Mbps, uncoded, suppressed-carrier telemetry channel. This calculation assumed that the ODSRS/ground link frequency is 14 GHz, the ODSRS antenna diameter is 2 m, the ground antenna diameter is 5 m, and the ground receiving system uses an uncooled parametric amplifier. The results presented herein also indicate that ground adjustment of the ODSRS transmitter RF power output for different spacecraft, different spacecraft modes of operation, and changes in spacecraft/ODSRS range will normally be necessary to avoid violation of CCIR power flux density limitations.

I. Introduction

The ODSRS (Orbiting Deep Space Relay Station) would be a geostationary or geosynchronous earth satellite designed to receive signals from spacecraft at lunar or planetary distances and relay these signals to a ground station. The ODSRS antenna for the spacecraft/ODSRS link would be a large (about 30-m) parabolic dish capable of efficient operation at S-band, X-band, and K-band. A maser amplifier would be provided at each of these frequencies. The K-band receiving capability of the ODSRS would be at least 6 dB greater than

the current X-band receiving capability of a DSN 64-m station in clear weather. The S-band and X-band receiving capability of the ODSRS would be significantly less than that of the DSN 64-m stations and would primarily be used for those radio metric measurements which require dual-frequency operation.

An important part of the ODSRS system design is the method used to relay to Earth either the signal received by the ODSRS from a spacecraft or the information carried by the signal. One method would be to extract the information

carried by the signal and remodulate this information on the ODSRS/ground link. However, signal processing on the ODSRS would increase the complexity of the ODSRS and decrease its reliability and flexibility. Since the anticipated ODSRS lifetime is at least 10 years, such ODSRS equipment could become obsolete. An alternative, which will be the method considered in this article, is the use of a "bent-pipe" channel. In this method, the signal received at the ODSRS, together with the ODSRS receiving system noise, is translated in frequency, amplified and retransmitted. The method minimizes on-ODSRS equipment and maximizes ODSRS reliability and flexibility. However, the "bent-pipe" method will require a more powerful ODSRS/ground link transmitter and will have more difficulty meeting international restrictions on the power flux density that may be received from earth satellites than a method employing on-ODSRS signal processing.

One consideration which is important to the ODSRS/ground link design is the CCIR limitation on the power flux density that can be received from a satellite at any point on the earth's surface. Power flux density is the maximum received signal power per unit area in some specified bandwidth. In this article this bandwidth is assumed to be 4 kHz. When the ODSRS/ground link transmitter power is fixed, it may not be possible to meet international restrictions on the power flux density which may be received *from the ODSRS* over the range of signal levels which may be received *at the ODSRS*. Hence, this article also examines the impact of varying the ODSRS/ground link transmitter RF power output to always use only that power level necessary to achieve the required spacecraft/ODSRS/ground link performance.

Two other limitations impact the ODSRS/ground link design. First, as the ODSRS must be maneuvered to point its main antenna toward the spacecraft, the antennas for the ODSRS/ground link must be steerable in two axes. To minimize pointing problems, it would be desirable to make the diameter of this antenna about 2 meters. Second, one objective of the ODSRS system design is to locate the earth receiving station for the ODSRS/ground link at the site where the data is to be processed. Possible antenna locations might be the roof of the spaceflight operations center at JPL, Goddard, or Houston. Hence, ground receiving antennas with diameters much greater than 5 meters should be avoided.

The objective of this analysis is to determine, given the limitations on antenna size discussed previously, the feasibility of using a bent-pipe design for relaying signals received by the ODSRS to the ground. For the purposes of this article, a feasible ODSRS/ground link design is one for which the received power flux density at the ground does not exceed the CCIR limitation. In addition, to minimize the impact on the ODSRS power system, the RF power amplifier for the

ODSRS/ground link should not require more than 100 to 200 watts of raw power. Since the power amplifier must be a linear amplifier, its efficiency may be as little as 5 percent. Thus, 100 to 200 watts of raw power corresponds to an RF power output of 5 to 10 watts.

The ODSRS/ground telemetry link should be capable of supporting a wide variety of applications. In this article three such applications, chosen to be limiting cases, are examined in detail.

It is expected that a suppressed carrier system will be used when the telemetry bit rate exceeds 250 kbps. As 25 Mbps appears to be the highest data rate that might be required, the first application considered is a 25-Mbps, suppressed carrier telemetry link. Of the three applications considered herein, this one should require the greatest ODSRS/ground link transmitter RF power output. The results obtained herein show that the CCIR limitations can be met for this application with a fixed 2.6 watt ODSRS/ground link transmitter RF power output if the allowable spacecraft/ODSRS/ground link degradation caused by the ODSRS/ground link is 0.2 dB or greater.

The second application considered herein is a 250-kbps, discrete carrier telemetry system with 1-dB carrier suppression by ranging. The ODSRS feed-through channel noise bandwidth was assumed to be 5 MHz for this application. This is sufficiently wide to pass most of the harmonics of the 500-kHz square wave ranging modulation. The results obtained herein show that the *maximum* ODSRS/ground link transmitter RF power output required for this application is 0.093 watts if the allowable degradation of the spacecraft/ODSRS/ground link performance by the ODSRS/ground link is 0.2 dB. If the allowable spacecraft/ODSRS/ground link degradation caused by the ODSRS/ground link is less than about 0.7 dB, the actual RF power output must be adjusted to use only the minimum value required. By making this adjustment, the CCIR restrictions on power flux density can be met whenever the allowable degradation of the spacecraft/ODSRS/ground link by the ODSRS/ground link is 0.2 dB or greater.

The third application considered herein is a 250-kbps discrete carrier telemetry channel with 1 dB carrier suppression by DOR (differential, one-way ranging) modulation. Because of the bandwidth of the DOR modulation, the ODSRS feed-through channel noise bandwidth for this application must be about 50 MHz, about 10 times that used in the preceding example. The results obtained in this report show that the maximum ODSRS/ground link transmitter RF power output for this application is 0.84 watts if the allowable spacecraft/ODSRS/ground link degradation by the ODSRS/ground link is 0.2 dB. By adjusting the ODSRS/ground link

transmitter RF power output to use only the minimum value required, the CCIR power flux density limitations can be met whenever the allowable spacecraft/ODSRS/ground link degradation by the ODSRS/ground link is 0.2 dB or greater

II. Analysis

A functional block diagram of the ODSRS "bent pipe" feed-through channel is shown in Fig 1. The receiver, which follows the maser amplifier, consists of a bandpass filter, linear amplifier, and frequency translator. A power-controlled AGC system adjusts the gain of the linear amplifier to hold the power level at the receiver output at some constant value. The transmitter consists of a linear power amplifier whose input power level, in those applications which require a variable ODSRS/ground link transmitter RF power output, can be controlled by a variable attenuator.

The required performance of the spacecraft/ODSRS/ground link can be measured in terms of the required signal-power-to-noise spectral density ratio $(P/\Phi)_{REQ}$ at the ground receiver. Let P_1 be the total power received at the ODSRS from the spacecraft and let Φ_1 be the one-sided noise spectral density of the ODSRS receiving system. Let P_2 be the total power received at the ground from the ODSRS and let Φ_2 be the one-sided noise spectral density of the ground receiving system. Then, if B is the one-sided noise bandwidth of the ODSRS feed-through channel and

$$\delta = \frac{\frac{P_1}{\Phi_1}}{\left(\frac{P}{\Phi}\right)_{REQ}} \quad (1)$$

$$\left(\frac{P_2}{\Phi_2}\right)_{REQ} = \frac{B + \delta \left(\frac{P}{\Phi}\right)_{REQ}}{\delta - 1} \quad (2)$$

Note that $(P_2/\Phi_2)_{REQ}$ becomes infinite as δ decreases to one. Thus, delta must always be greater than one to achieve the required overall link performance.

$(P_2/\Phi_2)_{REQ}$ decreases monotonically as δ increases. Since $(P_2/\Phi_2)_{REQ}$ becomes infinite as δ decreases to one, the ODSRS/ground link must be designed for some acceptable minimum value of δ . Let δ_M be the minimum value of δ . Then

$$\left(\frac{P_2}{\Phi_2}\right)_{MAXREQ} = \frac{B + \delta_M \left(\frac{P}{\Phi}\right)_{REQ}}{\delta_M - 1} \quad (3)$$

is the maximum required ODSRS/ground link signal-power-to-noise spectral density ratio.

International agreements limit the amount of signal power per unit area that can be received from an earth satellite at any ground station in any 4-kHz frequency band. Let PFD be the maximum received signal power at the ODSRS/ground link receiving station in any 4-kHz band, let L_R be the factor by which the received signal power P_2 is reduced by the ODSRS/ground link polarization loss, receiving antenna pointing loss, and receiving system circuit loss, and let A_R be the effective area of the ground antenna for the K-band ODSRS/ground link. Then, if the ODSRS transmitter RF power output is held constant at its maximum required value (for δ equals δ_M), the worst case power flux density will be

$$(PFD)_{MAX} = \frac{\Phi_2}{L_R A_R} \frac{MAX(4000, \eta_s B) + \delta_M \eta_s \left(\frac{P}{\Phi}\right)_{REQ}}{\delta_M - 1} \quad (4)$$

where $MAX(x,y)$ is the greatest of x and y . For all practical applications $\eta_s B$ should be greater than 4000. However, if only the minimum required ODSRS transmitter RF power output is used for each value of δ ,

$$(PFD)_{MAX} = \frac{\Phi_2}{L_R A_R} \frac{4000 + \delta_M \eta_s \left(\frac{P}{\Phi}\right)_{REQ}}{\delta_M - 1} \quad (5)$$

III. CCIR Power Flux Density Limitation

Although the results presented herein somewhat arbitrarily assume that the ODSRS/ground link RF frequency is 14 GHz, the actual RF frequency which will be used for the ODSRS/ground link is unknown. Consequently, the CCIR limitation on power flux density is also unknown. However, the CCIR limitation for RF signals in the 12.5-GHz to 12.75-GHz frequency band appears to be typical of those that might be imposed on the ODSRS/ground link. For this frequency band, the maximum allowable power flux density is -118 dBm/m².

for angles of arrival (δ_A) between 0 and 5 degrees, $-118 + (\delta_A - 5)/2 \text{ dBm/m}^2$ for angles of arrival between 5 and 25 degrees, and -108 dBm/m^2 for angles of arrival greater than 25 degrees. Note that the angle of arrival for any particular ground point is the elevation angle of the ODSRS at that ground point.

The ODSRS/ground link design presented herein will assume that the allowable power flux density which can be received at any point of the earth's surface is -118 dBm/m^2 . The angular separation, as seen from the ODSRS, between a ground station where the ODSRS elevation angle is 30 degrees and a ground point at which the ODSRS angle is 5 degrees is only 1.14 degrees. Thus, a minor operational error in pointing the ODSRS antenna could easily cause it to be pointed at a ground point where the ODSRS elevation angle is 5 degrees or less.

Since the link performance calculations presented in this article will yield, using Eq (4) or (5), estimates of the power flux density at the ODSRS/ground link ground station, it will be convenient to restate the CCIR limitation in terms of the maximum allowable power flux density at the ODSRS ground station. The difference between the power flux density at the ODSRS ground station and other points on the Earth's surface will depend on the differences in space loss (range), ODSRS antenna pointing loss, and atmospheric attenuation for the two signal paths. For the narrow beam (0.67 degree) ODSRS antenna, any increase in power flux density due to reduced range would be more than offset by increased ODSRS antenna pointing error. Hence, neglecting atmospheric attenuation, the maximum power flux density will occur on that point on the Earth's surface where the ODSRS antenna is pointed.

The allowance in Table 1 for ODSRS antenna pointing loss is 0.5 dB. This corresponds to a pointing error of 0.14 degree. Thus, the distance between the ODSRS ground station and the point on the Earth's surface at which the ODSRS antenna is pointed could be as much as 93 km. The combined atmospheric attenuation due to water vapor (0.27 dB) and rain (6.45 dB) could occur on the path from the ODSRS to the ground station, while only that due to water vapor occurs on the path to the point at which the ODSRS antenna boresight is pointed. Thus, the difference in atmospheric attenuation for the two paths could be as much as 6.45 dB. Combining the 6.45-dB possible differential in atmospheric attenuation with the 0.5-dB differential in ODSRS antenna pointing loss, the power flux density at any point on the Earth's surface cannot be more than 6.95 dB greater than that at the ODSRS/ground link ground station. Thus, the maximum allowable power flux density at the ground station is -124.95 dBm/m^2 .

IV. Applications

In this section the results obtained in the previous sections of this article are applied to three ODSRS applications: a 25-Mbps wideband telemetry channel, a 250-kbps telemetry channel with two-way ranging, and a 250-kbps telemetry channel with differential one-way ranging. For each of these three ODSRS applications, the ODSRS/ground RF link parameters, with the exception of the RF transmitter power output, will be those listed in Table 1. Note in Table 1 that, for a transmitter RF power output of 1 watt, P_2/I_2 is 91.07 dB · Hz. Thus the required ODSRS/ground link transmitter RF power output will be

$$(P)_{\substack{\text{MAXIMUM} \\ \text{REQUIRED}}} = \left(\frac{P_2}{\Phi_2} \right) - 91.07 \text{ dBW} \quad (6)$$

where $(P_2/\Phi_2)_{REQ}$ has units dB · Hz.

The results obtained in the preceding sections and Eq (6) can be used to determine the maximum required P_2/Φ_2 , the maximum required ODSRS transmitter RF power output, and the worst case ground station power flux density as a function of δ_M for the three ODSRS applications. Remember δ_M is the amount the spacecraft effective radiated power must be increased to offset the degradation caused by the ODSRS/ground link.

The results of these calculations are tabulated in Tables 2, 3, and 4, which have a common format. Column 1 is the independent variable δ_M . Column 2 is the maximum P_2/Φ_2 required, this was calculated using Eq (3). Column 3 is the maximum ODSRS transmitter RF power output required, this was calculated using Eq (6). Column 4 is the worst case ground station power flux density, assuming that the ODSRS transmitter RF power output remains fixed at the maximum required value for the particular application, this was calculated using Eq (4). Column 5 is the worst case ground station power flux density, assuming that the ODSRS transmitter power is varied to use only the minimum ODSRS transmitter power required to attain the specified spacecraft/ODSRS/ground link performance, this was calculated using Eq (5).

A. 25 Mbps, Uncoded, Suppressed Carrier Telemetry Channel

For a 5×10^{-3} bit error probability, the $(P/\Phi)_{REQ}$ for a 25-Mbps, uncoded, suppressed carrier telemetry channel will be about 80.19 dB · Hz. η_s will be -37.96 dB and $\eta_s(P/\Phi)_{REQ}$ will be 42.23 dB. The maximum P_2/Φ_2 required, the maximum ODSRS transmitter RF power output, and the worst case ground station power flux densities, for constant

and minimum ODSRS transmitted power outputs, are shown in Table 2 as a function of δ_M . The data presented in Table 2 is for a ODSRS feed-through channel with 50-MHz noise bandwidth.

Several aspects of the data presented in Table 2 are of particular interest. First, note the rapid increase in the maximum ODSRS transmitter RF power output required as δ_M decreases. This is typical of "bent pipe" feed-through systems. The transmitter RF power output required is proportional (approximately) to $1/(\delta_M - 1)$ and, hence, increases rapidly as δ_M approaches one. Second, note the relatively small difference between columns 4 and 5 of Table 3. For this application, using only the minimum required ODSRS transmitter RF power output does not substantially reduce the worst case ground station power flux density. Third, note that for the values of δ_M shown in Table 2, the worst case ground station power flux density exceeds the -124.95 dBm/m^2 allowable value only for δ_M as small as 0.1 dB. Assuming it is necessary to make δ_M as small as 0.1 dB, only a relatively small increase in the ground antenna diameter would be required to reduce the power flux density to an acceptable level.

B. 250-kbps Viterbi Coded (Rate 1/2), Discrete Carrier Telemetry Channel and Ranging with 1-dB Carrier Suppression

For a 5×10^{-3} bit error probability, the $(P/\Phi)_{REQ}$ for a 250-kbps Viterbi (rate 1/2) coded telemetry link is 56.62 dB · Hz, η_s is -15.21 dB, and $\eta_s (P/\Phi)_{REQ}$ will be 41.41 dB. If ranging modulation causing 1-dB carrier suppression is added, the $(P/\Phi)_{REQ}$ will increase to 57.62 dB · Hz, η_s will decrease to -16.21, and $\eta_s (P/\Phi)_{REQ}$ will remain unchanged. This assumes, of course, that the increase in the fraction of the spacecraft signal power in a 4000-Hz band centered on the carrier frequency caused by intermodulation products of the telemetry and ranging modulation can be neglected. The maximum P_2/ϕ_2 required, the maximum ODSRS transmitter RF power output, and the worst case ground station power flux densities, for constant and minimum ODSRS transmitter RF power output are shown in Table 3 as a function of δ_M . The data presented in Table 3 is for a ODSRS feed-through channel with 5 MHz noise bandwidth.

Several aspects of the data presented in Table 3 are of particular interest, especially when compared with the results presented in Table 2. First, the maximum required ODSRS transmitter RF power outputs shown in Table 3 are substantially less than those shown in Table 2. The maximum ODSRS transmitter RF power output required increases with both B and $(P/\Phi)_{REQ}$ and both of these parameters are significantly smaller for this application than they are for the application

for which data is presented in Table 2. Second, there is a very significant difference between columns 4 and 5 of Table 3. Thus, for this application, using only the minimum ODSRS transmitter RF power output required does substantially reduce the worst case ground station power flux density. Third, when only the minimum required ODSRS transmitter RF power output is used, the power flux density is less than the -124.95 dBm/m^2 limit for all values of δ_M for which data is shown in Table 4. When the ODSRS transmitter power is held constant at the maximum required value, the worst case ground station power flux density will exceed the -124.95 dBm/m^2 allowed for δ_M less than about 0.7 dB.

C. 250-kbps Viterbi-Coded (Rate 1/2), Discrete Carrier Telemetry Channel and Differential One-Way Ranging with 1-dB Carrier Suppression

This example differs from that in the preceding section only in that the bandwidth of the ODSRS feed-through channel has been increased to 50 MHz to accommodate the high-frequency sidebands created by the 19.125-MHz sinusoidal differential one-way ranging modulation. The $(P/\Phi)_{REQ}$ is 57.62 dB · Hz, η_s is -16.21 dB, and $\eta_s (P/\Phi)_{REQ}$ is 41.41 dB · Hz. The maximum P_2/ϕ_2 required, the maximum ODSRS transmitter RF power output, and the worst case ground station power flux densities, for constant and minimum ODSRS transmitter RF power output, are shown in Table 4 as a function of δ_M .

Several aspects of the data presented in Table 4 are of particular interest, especially when compared to the results presented in Table 3. First, the increase in the ODSRS feed-through channel noise bandwidth, from 5 MHz for the data in Table 3 to 50 MHz for the data in Table 4, has resulted in an almost proportionate increase in the maximum ODSRS transmitter RF power output required and the worst case ground station power flux density that can be expected when the ODSRS transmitter power output is held constant at the maximum value required. Second, the increase in the ODSRS feed-through channel noise bandwidth from 5 MHz to 50 MHz has no effect on the worst case ground station power flux density when only the minimum required ODSRS transmitter RF power output is used. Third, when the ODSRS transmitter RF power output is held constant at the maximum value required, the worst case ground station power flux density exceeds the -124.95 dBm/m^2 allowed for all values of δ_M shown in Table 4.

V. Conclusion

The use of a "bent-pipe" feed-through channel appears feasible for each of the three ODSRS applications considered herein. Assuming the ODSRS/ground link is designed for δ_M

equal 0.2 dB, the maximum ODSRS transmitter RF power output required for any of the three applications considered is 2.6 watts for the 25 Mbps, uncoded, suppressed-carrier telemetry channel. Assuming the efficiency of the linear power amplifier is 5 percent, this RF power output would require 52 watts of raw power. Note that this power level assumes that the ODSRS/ground link RF frequency is 14 GHz, the ODSRS antenna diameter is 2 m, the ground antenna diameter is 5 m, and the ground receiving system uses an uncooled parametric amplifier.

The results shown indicate that, unless the applications of the ODSRS are to be unduly restricted, ground control of the ODSRS transmitter RF power output will be necessary to meet the expected CCIR power flux density limitations. The ODSRS transmitter power output to be used will depend both on the communication functions to be performed, and, in many cases, on the spacecraft/ODSRS link margin above threshold. Thus, the ODSRS transmitter RF power output to be used may be different for different spacecraft, may be different for different operational modes of the same spacecraft, and may vary with the spacecraft/ODSRS range. By using only the minimum ODSRS transmitter RF power output required, the CCIR power flux density limitation can be met for each of the three ODSRS applications considered.

Note that setting the ODSRS transmitter power output to the proper level requires knowledge of P_1/Φ_1 , the ratio of received signal power to receiving system noise spectral density at the ODSRS. An uncertainty in P_1/Φ_1 would reduce the effectiveness of varying the ODSRS transmitter power output,

particularly when the allowable overall link degradation caused by the ODSRS/ground link must be small. Additional work is needed to assess the impact of such uncertainties.

Performance estimates for the spacecraft/ODSRS link can be made by considering only the spacecraft/ODSRS link and using the threshold relationship

$$\left(\frac{P_1}{\Phi_1} \right)_{REQ} = \delta_M \left(\frac{P}{\Phi} \right)_{REQ} \quad (7)$$

where $(P_1/\Phi_1)_{REQ}$ is the spacecraft/ODSRS link threshold. Now note in Tables 2, 3, and 4 that, when δ_M is nearly 0 dB, small changes in δ_M correspond to large changes in $(P_1/\Phi_1)_{MAX REQ}$. Conversely, when the design value of δ_M is nearly 0 dB, large changes in (P_2/Φ_2) , caused by the ODSRS/ground link parameter variations, correspond to only small changes in δ_M . Thus, for example, if the design value of δ_M is 0.2 dB, a ± 3 dB change in (P_2/Φ_2) corresponds to only about a +0.1 dB, -0.2 dB change in δ_M . In most cases this uncertainty in δ_M and the corresponding uncertainty in $(P_1/\Phi_1)_{REQ}$ will be small in comparison with the tolerances on the spacecraft/ODSRS link parameters. Thus, when the design value of δ_M is nearly 0 dB, the ODSRS/ground link transmitter RF power output need be sized only for the required ODSRS/ground link *design value* performance. The effect of favorable or adverse ODSRS/ground link parameter variations will be reflected in only a minor increase in the favorable and adverse tolerances on the spacecraft/ODSRS link performance margin.

Table 1 ODSRS/ground link communication system performance estimate for a one-watt transmitter RF power output

Transmitting system parameters		
(1) RF power output (1W)	30 00 dBm	
(2) Circuit loss	-1 00 dB	
(3) Antenna gain (2-m dia , 70% eff)	47 79 dB	
(4) Antenna pointing loss	-0 50 dB	
Path parameters		
(5) Spaceloss	-207 11 dB	
Frequency = 14 GHz		
Range = 38611 91 km		
(6) Atmospheric attenuation ^a	-6 72 dB	
Receiving system parameters		
(7) Polarization loss	0 00 dB	
(8) Antenna gain (5-m dia , 70% eff)	55 76 dB	
(9) Antenna pointing loss	-0 10 dB	
(10) Circuit loss	0 00 dB	
(11) Noise spectral density	-172 95 dBm/Hz	
System noise temperature = 366K		
30° elevation angle, rain		
(31 mm/hr) ^b		
(12) Received signal power	-81 88 dBm	
(13) Received signal power/receiving system noise spectral density	91 07 dB Hz	

^aThe atmospheric attenuation consists of 0 27 dB due to water vapor and 6 45 dB due to 31 mm/hr rain

^bRain will exceed the 31 mm/hr rate during 0 01% of the year at Goldstone and 0 05% at Goddard and Houston

Table 2 Required ODSRS transmitter RF power output and worst case ground station power flux density for a 25 Mbps, uncoded, suppressed carrier telemetry channel

δM , dB	Maximum P_2/Φ_2 required dB Hz	Maximum required ODSRS transmitter RF power output, W	Ground station worst case power flux density	
			Constant RF power, dBm/m ²	Minimum RF power, dBm/m ²
0 1	98 29	5 3	-123 90	-124 66
0 2	95 29	2 6	-126 90	-127 64
0 3	93 54	1 8	-128 65	-129 37
0 4	92 32	1 3	-129 87	-130 58
0 5	91 37	1 1	-130 82	-131 52
0 7	89 94	0 77	-132 25	-129 92
1 0	88 46	0 55	-133 73	-134 37
1 5	86 81	0 37	-135 38	-135 97
2 0	85 67	0 29	-136 52	-137 06

Table 3 Required ODSRS transmitter RF power output and worst case ground station power flux density for a 0.25 Mbps, Viterbi (rate 1/2) coded, discrete carrier telemetry channel and ranging with 1-dB carrier suppression

δM , dB	Maximum P_2/Φ_2 required, dB Hz	Maximum required ODSRS transmitter RF power output, W	Ground station worst case power flux density	
			Constant RF power, dBm/m ²	Minimum RF power, dBm/m ²
0.1	83.81	0.19	-116.63	-125.31
0.2	80.76	0.093	-119.68	-128.29
0.3	78.95	0.061	-121.49	-130.03
0.4	77.67	0.046	-122.77	-131.24
0.5	76.66	0.036	-123.78	-132.18
0.7	75.11	0.025	-125.33	-133.69
1.0	73.45	0.017	-126.99	-135.05
1.5	71.50	0.011	-128.94	-136.66
2.0	70.05	0.0079	-130.39	-137.76

Note 5 MHz ODSRS feed-through channel noise bandwidth

Table 4 Required ODSRS transmitter RF power output and worse case ground station power flux density for a 0.25 Mbps Viterbi (rate 1/2) coded telemetry channel and downlink one-way ranging with 1-dB carrier suppression

δM , dB	Maximum P_2/Φ_2 required, dB Hz	Maximum required ODSRS transmitter RF power output, W	Ground station worst case power flux density	
			Constant RF power, dBm/m ²	Minimum RF power, dBm/m ²
0.1	93.37	1.7	-107.07	-125.31
0.2	90.31	0.84	-110.13	-128.19
0.3	88.49	0.55	-111.95	-130.03
0.4	87.20	0.41	-113.24	-131.24
0.5	86.19	0.33	-114.25	-132.18
0.7	84.62	0.23	-115.82	-133.59
1.0	82.92	0.15	-117.52	-135.05
1.5	80.91	0.096	-119.53	-136.66
2.0	79.40	0.068	-121.04	-137.76

Note 50 MHz ODSRS feed-through channel noise bandwidth

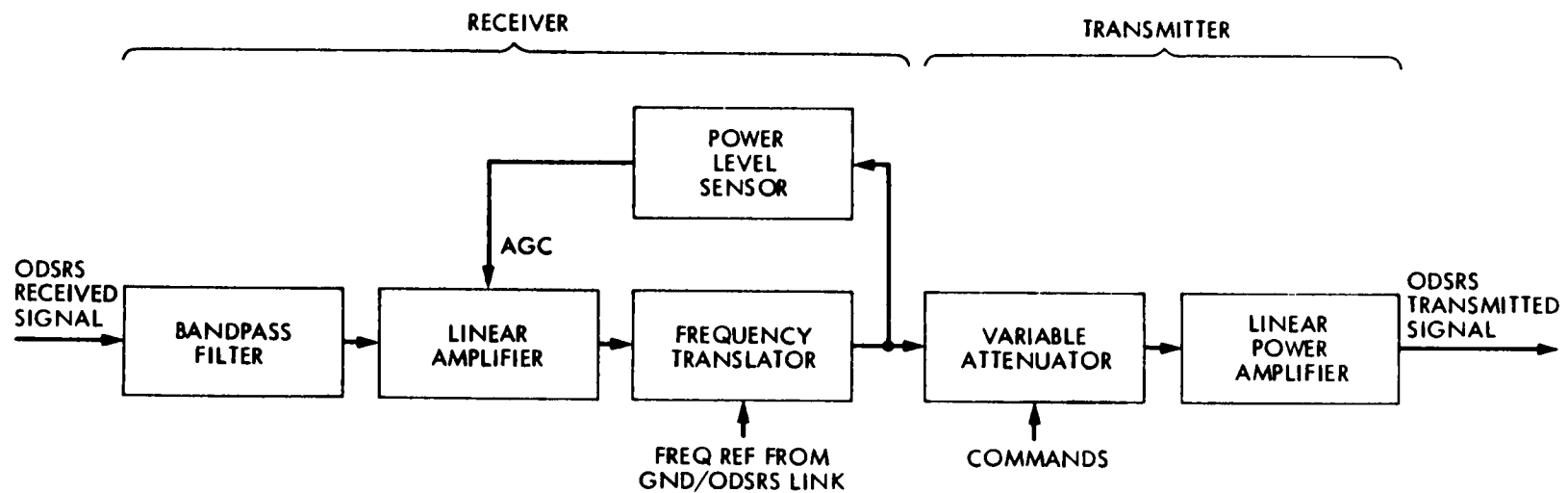


Fig. 1 ODSRS feed-through channel functional block diagram

Arithmetic Techniques Used in the High-Speed Front End of The Multimegabit Telemetry Modem

E R Wechsler

Communications Systems Research Section

Two methods of processing two's complement binary data are presented. They were used in the design of the High-Speed Front End of the Multimegabit Subsystem. The first method is for rounding with zero error in the mean and is useful when large numbers of rounded values are to be accumulated.

The second method consists of attaching a "1" as a least significant bit to the output word of an A-D converter, thus processing it as an odd number with one more bit. This compensates for the negative bias that A-D converters have when their zero is set for symmetrical positive and negative output ranges as is customary.

When used with emitter coupled logic circuits, these methods result in simpler logic design.

I. Introduction

A Multimegabit Subsystem is currently being developed to increase the telemetry data rate of the DSN to 30 megasymbols per second. The high-speed front end (HSFE) is a portion of the Multimegabit Subsystem which converts quadrature analog signals into digital signals for further processing by the detection, estimation, and synchronization assemblies of the subsystem. The incoming analog signals are converted at rates of up to 64 MHz using monolithic 4-bit quantizers newly developed by Advanced Micro Devices, Inc. The following discussion applies to A-D converter output formatting and rounding techniques used in the HSFE which are applicable to any digital system.

II. Selection of the Rounding Technique for Use in the HSFE

Since the data supplied by the HSFE is to be further processed in the Multimegabit System where it is accumulated,

the technique used for rounding must avoid generating unwanted offsets. The assumption is made that all numbers which become equal after rounding are equally probable. A useful observation is that in the two's complement representation, which is used throughout the system, all the bit positions can be considered to have positive weights except for the sign bit which is a negative weight as shown below for an N-bit integer.

Bit label $B_{N-1}, B_{N-2}, \dots, B_k, B_{k-1}, \dots, B_1, B_0$

Bit weight $-2^{N-1}, 2^{N-2}, \dots, 2^k, 2^{k-1}, \dots, 2^1, 2^0$

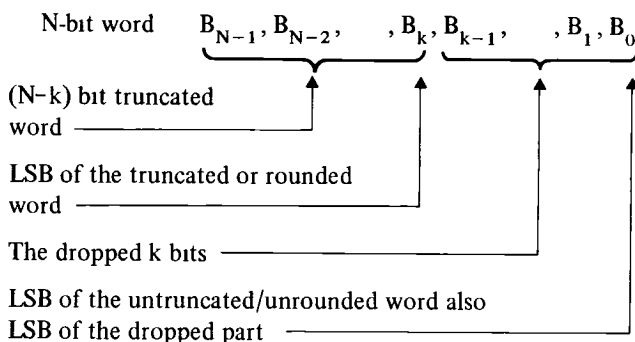
Whenever it is necessary to present a binary number in a shorter format, there are several methods which can be selected, such as truncation, conventional rounding, and rounding with the OR function. In what follows these methods will be compared, and it will be explained why rounding with the OR function was chosen for the HSFE.

A. The Truncation Method

The truncation method consists of dropping the k least significant bits from the binary word without any further correction. As mentioned earlier, in the two's complement representation the bits are considered positive, so the truncated value will always be equal to or less than the original value which will produce a negative mean error as shown in Fig 1. If k bits are truncated, then the mean error $\tilde{\epsilon}$ will be

$$\begin{aligned}\tilde{\epsilon} &= -\frac{0 + 1 + \dots + (2^k - 1)}{2^k} = \left[-2^{-1} + 2^{-(k+1)} \right] 2^k \\ &= \left[-1/2 + 2^{-(k+1)} \right] A\end{aligned}$$

where $A = 2^k$ is the weight of the least significant bit (LSB) of the truncated number as shown below



Assuming infinite resolution for the original number, we get the mean error

$$\tilde{\epsilon} = -\frac{A}{2}$$

The maximum error

$$\epsilon_{\max} = -A$$

The variance

$$\sigma^2 = \frac{A^2}{12}$$

B. The Conventional Rounding Method

This method consists of truncating k least significant bits and then arithmetically adding one LSB (in the new truncated format) to the truncated number when the dropped part is

equal to or larger than one-half of one LSB in the truncated format and leaving it unchanged otherwise

Rounding off k bits will produce a mean error of

$$\begin{aligned}\tilde{\epsilon} &= \frac{-[1 + \dots + (2^{k-1} - 1)] + [1 + \dots + 2^{k-1}]}{2^k} \\ &= 2^{-1}\end{aligned}$$

In this case, the mean error is positive but it is just one-half of one LSB of the dropped part. Since one LSB of the rounded word is $A = 2^k$, the mean error is

$$\tilde{\epsilon} = \frac{A}{2^{k+1}}$$

Rounding requires hardware for adding the LSB. In addition, when the mean error is to be made zero, even more hardware is needed

Assuming infinite resolution for the original number we get for the maximum error

$$\epsilon_{\max} = \pm \frac{A}{2}$$

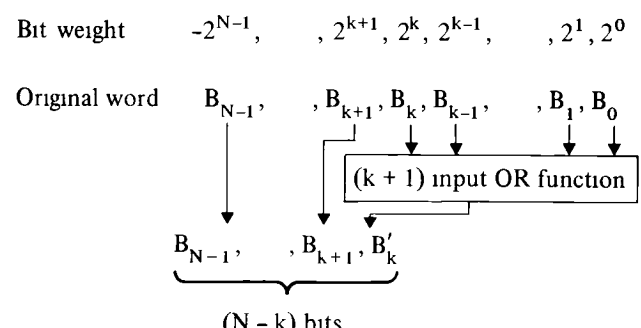
as shown in Fig 2

The variance is

$$\sigma^2 = \frac{A^2}{12}$$

C. Rounding With the OR Function

This method consists of truncating $k + 1$ bits and then attaching a bit in the least significant position, which is an OR function of the bits that were dropped, thus eliminating just k -bit positions as shown below



The mean error due to the truncation of $k + 1$ bits is

$$\tilde{\epsilon}_1 = -(2^{k+1} - 1) 2^{-1}$$

We will attach a "1" as a least significant bit in M cases where M is to be determined as follows

The weight of this bit is 2^k so the average value of this correction bit will be

$$\tilde{\epsilon}_2 = \frac{M \cdot 2^k}{2^{k+1}} = \frac{M}{2}$$

In order to have a zero mean error we must have

$$\tilde{\epsilon}_1 + \tilde{\epsilon}_2 = 0$$

or

$$\frac{2^{k+1} - 1}{2} = \frac{M}{2}$$

Therefore

$$M = 2^{k+1} - 1$$

which means that in all cases but one, the attached LSB will be a "1"

The most convenient logic function of the dropped bits turns out to be the OR because it is "0" when the dropped part is zero and the variance is kept minimum. The mean error is zero by design. Assuming infinite resolution, we get the maximum error

$$\epsilon_{\max} = \pm A$$

as shown in Fig 3

The variance is

$$\sigma^2 = \frac{A^2}{3}$$

In conclusion, this method produces maximum errors as large as those due to truncation and an RMS noise twice as large as that due to truncation or rounding. Its advantages are that no adders are required to round and just one OR function is required thus reducing considerably the time delays which in emitter coupled logic circuits can be implemented by simply wire ORing gate outputs

III. Formatting the Output of the A-D Converter

Aspects of the previous discussion can also be applied to formatting the output of an A-D converter in order to eliminate a residual mean error. We can consider an A-D to be of infinite resolution but supplying a truncated output which has the disadvantage of a negative mean error as shown in Fig 4 for a three-bit converter

Applying the OR rounding to an infinite resolution binary word we get a "1" in the LSB location all the time. This is a method of cancelling the $-1/2$ LSB offset produced by the negative mean error of the A-D and it consists of attaching the "1" all the time on the least significant position, thus increasing the number of bits by one

It is not necessary to actually supply this LSB as long as its effect is accounted for in subsequent operations. For example, if two numbers have to be added, all we have to do is provide a "1" to the carry input of the adder

Another feature is generating the two's complement without using an adder. This is done by keeping the LSB a "1" and making the one's complement of the rest of the word, a great advantage in high-speed circuits required in the HSFE

In addition, the positive and negative ranges of representation are symmetrical as shown in Fig 5 for a three-bit case, with a "1" attached. This eliminates the problem of unequal ranges when compensating for average zero offset by trimming the A-D references as shown in Fig 6. This asymmetry becomes very pronounced for A-D converters with few bits as the case of only 4 bits in the HSFE

An interesting property which results when using odd numbers is that their squares are multiples of eight plus one. For example, let the odd number be $2m + 1$. Its square will be

$$(2m + 1)^2 = 4m^2 + 4m + 1 = 4m(m + 1) + 1$$

The product $m(m + 1)$ has to be even, so the first term is a multiple of eight. The square of an odd number in binary representation always ends in 001 which therefore need not be supplied physically

IV. Conclusion

Two methods of processing binary data in the two's complement were presented, which are used in the High-Speed Front End of the Multimegabit project. The first one is an easy way of rounding, which holds the mean error at zero. The second one allows the easier processing of data from A-D converters while keeping a zero average error (bias) and symmetrical positive and negative ranges

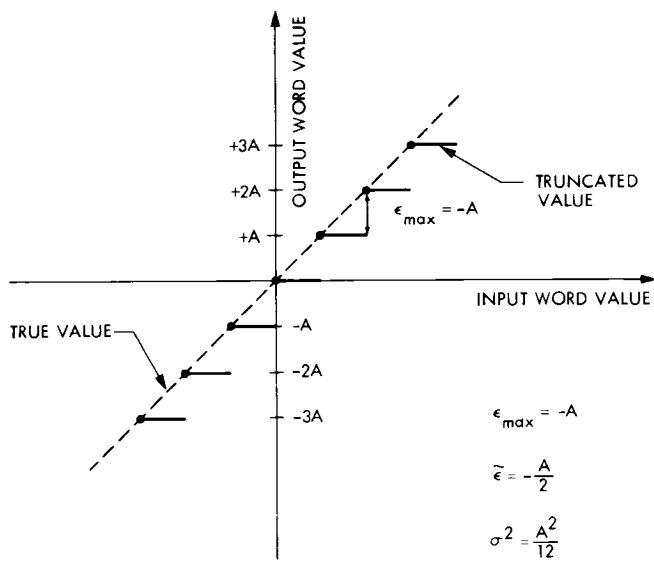


Fig 1 The truncation method

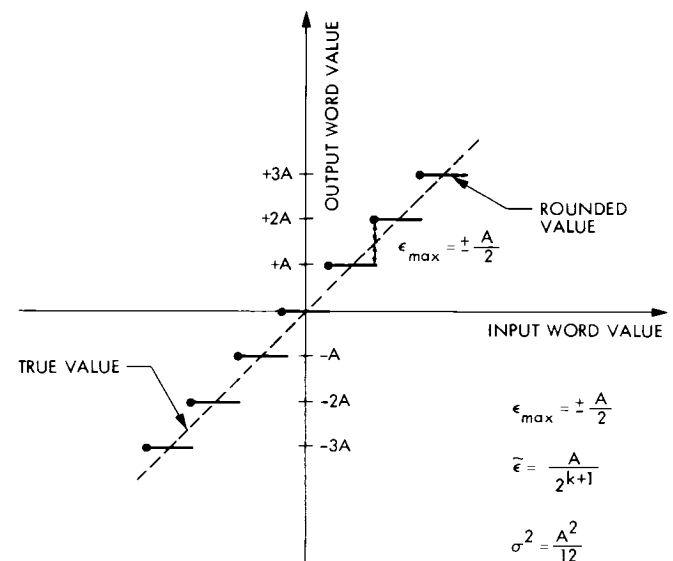


Fig 2 The rounding method

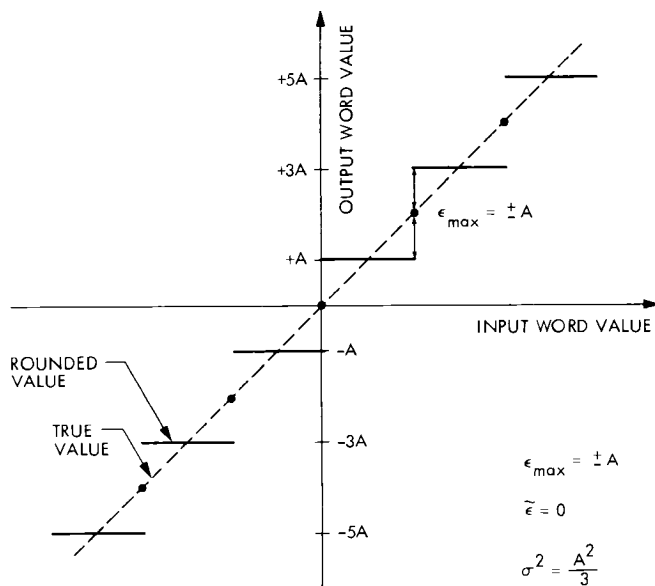


Fig 3 Rounding with the OR function method

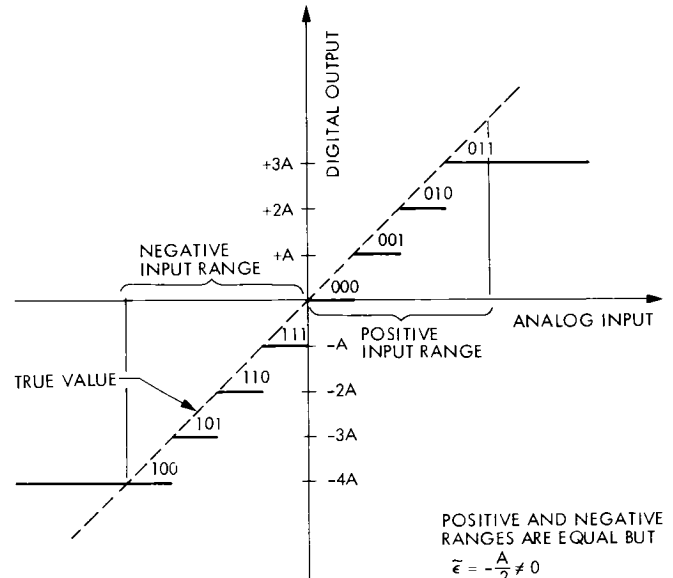


Fig 4 The A-D converter average error

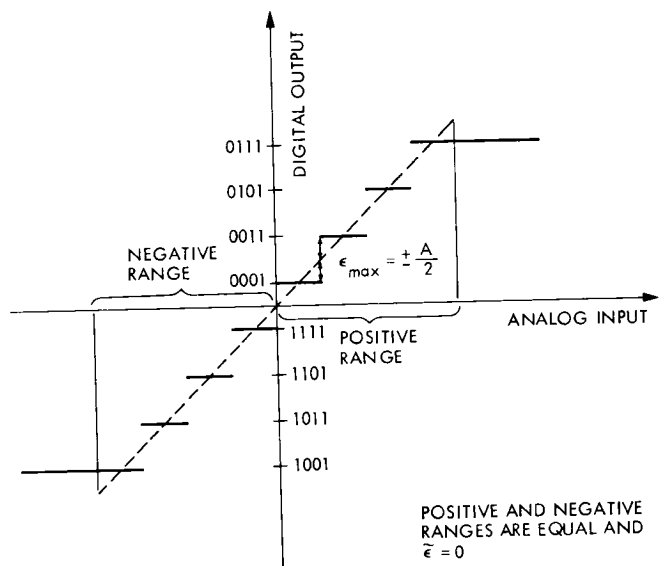


Fig 5 Output of A-D converter when the odd number method is used

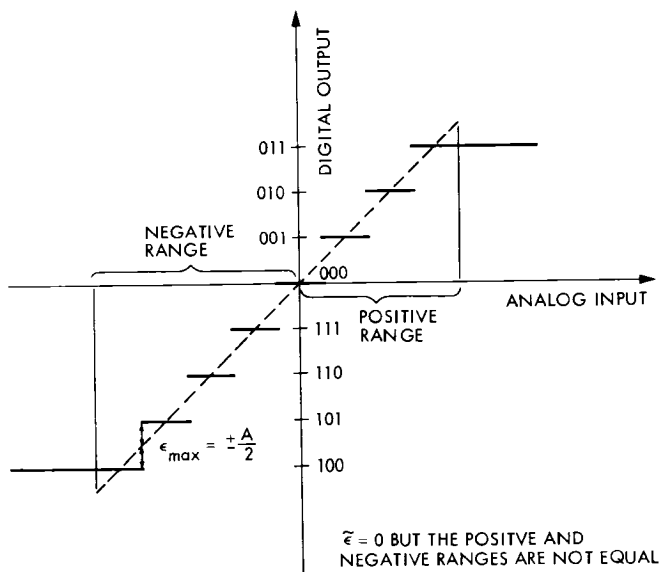


Fig 6 Output of A-D converter when the offset is zeroed by adjusting its references

Sensitivity of Reflector Backup Structure Weight to Variable Wind Speed Loadings

R Levy and D Strain
DSN Engineering Section

Backup structures for paraboloidal reflectors were designed for three diameters to support combinations of gravity, seismic, wind or snow loads. Changes in structure weights were determined as a function of change in wind speed. Low wind speeds were found to have only minor influence on weight, and extremely high hurricane-type wind speeds had only a moderate effect on the weight. One of the backup structure designs was evaluated for performance and judged to be satisfactory for use either as a microwave antenna or solar collector.

I. Introduction

Paraboloidal reflector structures used within microwave antennas or solar collector systems are required to provide structural integrity and suitable performance accuracy at specified operating wind speeds and to maintain structural integrity at specified higher survival wind speeds. Typically, the operating performance requirement for an azimuth-elevation type steerable reflector applies at any elevation angle from horizon to zenith, but the survival wind speed applies with the structure oriented in an advantageous elevation attitude (stow position) that offers the most protection from wind loading.

In view of operating and survival conditions there are three wind speeds to be considered for design:

- (1) The maximum speed at which performance is to be maintained while the structure is at any elevation angle

(2) A slightly higher speed than above that applies during the time the structure is being driven to the stow attitude from any other elevation attitude

(3) A survival wind speed that applies at the stow attitude

The present investigation covered the design and weight of reflector backup structures needed to maintain structural integrity for a spectrum of wind speeds. Performance requirements, which entail examination of the deformation patterns at the operating wind speeds, were not a primary subject for investigation. Consequently, wind speed ranges only for category (2) above, at which the antenna can be at any elevation, and for category (3), at which the structure is stowed, were investigated. To simplify the number of parameters investigated, the survival wind speed was always taken to be twice the maximum drive-to-stow wind speed, which is representative of customary specifications. As the result, we

can characterize any of the wind speed parameters by the survival speed, with the understanding that the structure must withstand one-half of this speed at any arbitrary elevation attitude. Other loadings on the structure included with wind were the gravity loading (which depends upon the elevation attitude), earthquake loading, and snow loading. Details of how specific loading requirements were assembled will be described in conjunction with the description of the design procedure.

II. Backup Structure Configuration

Backup structures were studied for reflector diameters of 15m (50 ft), 26m (85 ft) and 40m (132 ft). Mounts to support the structure were omitted, but the structures were constrained at nodal junctions which were presumed to be logical attachment points to azimuth-elevation (AZ-EL) type mounts. Since gravity loading for a reflector structure supported by an AZ-EL mount is symmetrical about the vertical plane perpendicular to the elevation axis, and since the wind loading here was also assumed to maintain the same symmetry, it was necessary to model and design only one-half of the backup structure.

Backup structure configurations consisted of radial rib trusses with interconnecting circumferential hoop trusses. This is the traditional microwave antenna ring and rib construction that has successfully evolved during the past 20 years. The reflecting surface is provided by individual panels that are assumed to be capable of supporting their own weight plus any additional tributary wind, snow, or earthquake loading. Panel designs, however, were not undertaken. The method of attachment of panels to backup was assumed to transfer mechanical only, and not thermal loading, to the backup and to prevent participation of the panels in the structural response of the backup to its imposed loading.

Figure 1 illustrates details of the backup structure construction. The reflector diameter for this figure is considerably larger than diameters considered here, so that the numbers of rings and ribs exceed those of the reflectors of the current study. The actual layout of the top surface of the three reflectors for this study and their rib profiles are shown on Fig. 2. The rib and ring layout was set for surface panels of approximately 4-m² (45 sq-ft) area. The coordinate system shown on this figure is a local set fixed to the reflector and moves with the reflector as it changes in elevation attitude.

In the schematic layouts of Fig. 1, which, although proposed (Ref. 1) for a 64-m-diameter reflector is typical of the configurations for this study, it can be seen that the backup structure is developed from replicative modules. As shown in Fig. 1d the main rib truss bar members occur in four

categories top, bottom, diagonal, and post. As shown in Fig. 1b and 1c, the hoop truss bar members occur in three categories top, bottom, and diagonal. The intermediate ribs, which consist of a single top bar supported by the hoop trusses occur only at the outer-most rings, and alternative main ribs are omitted at the innermost rings. Three additional categories of interrib bracing are top surface diagonal bracing between adjacent rib tops and bottom surface diagonal bracing between adjacent rib bottoms, and inclined bracing from the top of one rib to the bottom of the next adjacent rib. Consequently, all members of reflector backup structures can be classified within only 10 distinct category types. To emphasize manufacturing economy by means of replication, all members of the same category that occur at the same ring or within the same ring annulus can optionally be assembled into the same design variable group. Each member within a design group is then designed to have the same structural cross section. As an illustration, antenna backup model of Fig. 1, which has over 5000 individual bar members, requires less than 130 detailing variations to manufacture all of the bars.

Because of the great emphasis on symmetry and repetition in this design, data generation is readily automated. Most of the data input required for subsequent design and analysis is generated within a special computer program in less than a minute of 1108 computer central processing unit (CPU) time. For the structure of Fig. 1 there are about 4000 data card images. These are computer-produced on the basis of a relatively small number of input parameters to define key dimensions plus configuration and arrangement options. Another computer program automatically generates data to describe wind loading on the structure by interpolating from our existing wind tunnel pressure data. Loading data that represents the weight of surface panels and additional snow loads is also automated.

Figure 2a shows the projections of the reflector support points, which occur at the bottom chords of main rib trusses. Three support points (at the corners of an equilateral triangle) are provided for the full 15-m-diameter structure, four (at the corners of a square) are provided for the 26-m-diameter structure, and eight (at the corners of an equilateral octagon) are provided for the 40-m-diameter structure. In all cases, the central radius to the support point is 40 percent of the reflector radius. Although these points are unyielding in their support of the backup structure, they are effectively equivalent to simulating an attachment between mount and reflector that has equal stiffness at each of the attachment points.

Computer models of the backup omitted the customary additional structures associated with counterweights or with supporting of subreflectors or receivers. It was assumed that these structures could be attached very closely to the supports so that they would have little, or only local, influence upon

backup structure weight Furthermore, they are customarily open, latticed structures, with only small exposure to wind loading

III. Member Design Specifications¹

All backup structure members were of structural steel, ASTM-A36 quality The design specification adopted for these members was taken from an "ASCE Design Guide" (Ref 2) Compression members are governed by either of two formulas, depending on whether or not they are long or short columns The long column formula for allowable compression stress is

$$Fa = 286,000 / ((KL/r)^2)$$

in which KL/r is the effective slenderness ratio, L is the length of the member, r is the radius of gyration of the cross-sectional area, and Fa is the allowable compression stress in ksi

The short column formula is

$$Fa = (1 - (KL/r)^2 / (2Cc^2))F_y$$

in which $Cc = 126.1$ (for ASTM A-36 Steel) and $F_y = 36.0$ (for ASTM A-36 Steel)

The long column formula applies for KL/r greater than Cc , and the short column formula applies when KL/r is less

For members with normal framing eccentricities, the effective slenderness ratio for L/r less than 120, is given by

$$KL/r = 60 + 0.5L/r$$

For greater L/r , K is taken as 1

The guide recommends that the maximum value of L/r for members carrying calculated compression stress be limited to 200 Our design procedure restricts all members to this value in anticipation of possibilities of stress reversals

For tension members this code recommends the full yield stress on the minimum net cross-section To allow for end connections, we have assumed a 15 percent reduction in

tension member areas, so that we used 30 ksi as the allowable tension stress, rather than the yield stress of 36 ksi These specifications do not include safety factors and members designed accordingly will approach failure by yielding or buckling Consequently, overload factors on the anticipated loading should be used according to designer's judgement

The load factors used here were

Type	Nominal loading	Loading factor
Gravity	1.00 g	1.20
Seismic	0.25 g	1.20
Snow	20 psf	1.00
Wind	Stagnation pressure	1.00

Selection of backup structure member cross-sections for these design specifications is automated within the JPL-IDEAS (Ref 3) computer analysis and design program A loading deflection analysis is performed for a finite element model of the structure from which member forces are computed for a set of environmental loadings The maximum tension and maximum compression force are identified for each member The program then consults one of several self-contained tables of commercially available structural shapes and selects one to meet the specifications An excerpt of the table used in this study is shown in Table 1 In this table, the heading HANDBOOK SHAPE contains a cryptic description of the member For example, shape No 1 is a 75 in nominal standard pipe with 1.05 in outside diameter (OD) and a 1.13 in wall Shape No 2 is a 1 in schedule 10 pipe with 1.315 in OD and a 1.09 in wall The cross-sectional area and radius of gyration are tabulated under the headings AREA and RAD The table is arranged in the order of increasing area Allowable compression loads (kips) are tabulated as a function of span length (inches) These tabulated loads are used in the member selection algorithm to expedite the selection of candidate members The tabulated loads are used to locate trial shapes that are tested for the ability to carry the maximum compression load according to the preceding formulas Zero values of the loads indicate span lengths for which L/r exceeds 200

IV. Design Procedure

The JPL-IDEAS program was constructed to automate optimum design of lattice-type structures for a compliance type of performance criteria At the same time, structural integrity is maintained by selecting only members that have the ability to withstand all the tensile and buckling stresses for a user-supplied set of loading vector cases As an available

¹Design codes, material specifications, and descriptions of commercially available structural members in industrial practice are currently described by traditional English units Consequently, the discussion here will be in terms of the traditional units, rather than SI units These would cause undue confusion by dealing with quantities that are not meaningful in present practice

option, a subset of this design capability examines only loading carrying capability independent of performance. This option is called the "Stress" design mode option and actually is equivalent to the fully stressed design method.

The objective of a fully stressed design is to have each member reach its maximum allowable load in at least one loading condition. The computer approach is to examine member forces for each loading vector and select an appropriate member from the table in accordance with the most critical requirement for each member for any of the loads. However, in a redundant structure, changes in member areas will cause an internal redistribution of loading. As the result, the approach must be performed iteratively, rechecking and correcting the newly sized members at each iteration. However, experience shows that this method will usually converge rapidly and require fewer design iterations for a moderately redundant structure than when performance criteria are also included. In the IDEAS program, the individual members are assembled into design-variable groups and the group member size is set according to the most severely loaded member within the group. By assigning fewer members into the groups and more groups, a lighter weight design could result, but at the expense of increased fabrication complexity.

For each of the three diameters studied, the IDEAS program was executed twice, as follows:

- (1) The first execution loading consisted of four cases to represent the antenna at the horizon and at the zenith elevations with seismic loading from the front and from the rear. The seismic loading was superimposed upon gravity loading, which consisted of the weights of the members plus a reflecting surface weight of 14.6 kg/m^2 (3.0 lb/ft^2) to simulate the effect of reflecting panels. The "Stress" design mode option was used to determine member sizes to support these loads (at a load factor of 1.20). Member group sizes so determined were written into a file for future recovery and reference as the minimums and were not allowed to be reduced during further loading analysis and design.
- (2) The second execution contained nine loading cases that were analyzed to determine the member forces, which were stored on a file for subsequent postprocessing. Two loadings were used to represent gravity loading in the Z-axis direction and in the Y-axis direction (Fig. 2). By forming linear combinations of member forces for these two loadings, it is possible to compute the member forces from gravity at any arbitrary elevation attitude. Six wind loading cases represented wind from the front with the structure at elevations of 0, 60, and 90 deg, and wind from the back at these same elevations for an arbitrary reference speed. The last

loading case was a snow loading of 97.5 kg/m^2 (20 lb/ft^2) of surface area applied in the negative direction of the Z-axis.

Completion of the study of backup structure weight for variable wind speed loading is performed by a postprocessor program written especially for the present study. This program (a) reads in the member forces from the file written during the second execution above, (b) synthesizes the member loading by forming combinations of the Z- and Y-axis loadings gravity appropriate to the particular elevation angle, (c) multiplies the wind loading force read in for this elevation by a factor equal to the square of the ratio of wind speed to be investigated to the reference speed, (d) adds the gravity and factored forces wind loading forces, and (e) finally selects an appropriate member for this loading by using the same table of commercial shapes and design algorithms as the IDEAS program. When snow loading was to be considered, this was added to the wind and gravity loadings for the 90-degree elevation case. In employing this postprocessor, the user supplies the desired factors to be used in the superposition of loadings.

During the selection, no member size is permitted to become smaller than the size determined during the first IDEAS execution. This is the size found necessary for resistance to the seismic loading.

Table 2 shows the wind speeds considered. Gravity loading combined with these wind loads included a load factor of 1.2 applied to the weight of the structure designed in the first IDEAS execution, which also included the mass of reflecting surface panels. There is a small approximation entailed in computing the weight of the backup structure to resist the higher wind speeds, because the added weight of members with increased area is not included in the gravity loading portion of the factored load. Another approximation occurs because the synthesized member loading is subject to redistribution because of internal structural redundancy. The effects of both of these approximations have been verified by additional IDEAS program designs using some of the higher wind speed loadings and starting from member sizes developed within the postprocessor. It was found that although some members were increased, others were reduced, and the total weight of backup structure varied by less than 1 percent from the weight computed in the postprocessor program.

V. Results

Table 3 contains reference data and statistics to describe the three diameters investigated. The focal-length-to-diameter ratio for the 15-m-diameter model can be determined as 0.424, which is typical of antenna requirements. The ratio of 0.6,

which was used for the 26-m and 40-m structures is more nearly in keeping with requirements for solar collectors. However, other investigations performed in the past have shown that the structure weight and performance is not significantly sensitive to much larger changes in focal-length-to-diameter ratios than these. The panel surface weight is typical of the panel weights in current DSN antenna usage and with current proposals for the design of collector panels. The snow loading, when subsequently applied in addition to wind loading, is uniformly distributed over the reflecting surface (not projected) area when the reflector is at the stow-survival (90 deg) elevation. Actual snow loading distribution would presumably be more intense near the center of the aperture than at the rim. The reference weight for the backup structure was determined by the fully stressed design option within the IDEAS program. Gravity and fore-and-aft seismic loadings (0.25 g) were combined for horizon and zenith reflector elevations with a load factor of 1.20 applied to the combined loadings. Note that all physical quantities in Table 3 are for one-half of the backup structure and should be doubled to represent the complete structure.

A Weights of Backup Structure Designs

Table 4 shows the results of the studies of backup structure weight to wind speeds. Figure 3 is a plot of these data. The tabulated percentages of weight increases are based upon the weight of the reference structure as described in the preceding paragraph. All of the wind loading designs also included gravity loading at a load factor of 1.20, but no seismic loading. Smaller weight increases could have been found at some of the lower wind speeds if these designs had not been constrained to prevent reduction of any member below the requirements of the reference design. The percentage increases for snow loading are determined only from the zenith elevation wind and snow requirements. Data in Table 4 were determined from the severest requirements for wind at any of six relative wind orientations (see Table 2).

No increased load factors were applied to the wind to represent gust loading or safety factors for the design. The effect of such factors could be invoked by a downward reinterpretation of the tabulated speeds.

B. Auxiliary Evaluation of Performance

Although the primary objective of this study was to determine the weight of backup structures to support the various loadings, some data were developed to determine sample performance characteristics for the 15-m-diameter reflector structure. The information was based upon the particular design for gravity and wind loading at the 22.3-m/sec (50-mph) operating condition and 44.7-m/sec (100-mph)

survival wind speed conditions. The performance evaluations for this structure were made for wind at 13.4 m/sec (30 mph).

As an X-band microwave antenna operating at the frequency of 8.45 GHz, the efficiency of the backup structure, which is a function of the pathlength length errors caused by structure distortion, was computed to be at least 96 percent for all of the orientations for either wind or gravity loading. The corresponding reduction of antenna gain for this minimum efficiency was 0.15 dB. This gain reduction is expected to be well within error budget allowances that would normally be assigned.

Performance as a solar collector was evaluated by using a computer program that executed the geometric optics calculations and traced the energy reflected from each surface panel to its eventual location on arrival at the receiver plane. The application of this computer program assumes that panels undergo rigid body deformations caused by the displacements of the attachment points at the backup structure. Additional panel distortions caused by the local gravity and wind loading on the panel would have to be applied separately. It can be determined that with a distortion-free reflecting surface, all of the energy would be captured within a 6.4-cm (2.5-in.) receiver radius. The worst case of wind and gravity (simultaneous) loading was found to increase the capture radius required by about 2.5 cm (1 in.). Consequently, a receiver diameter of about 18 cm (7.0 in.) would have a 100 percent intercept factor, assuming no other errors. This would be equivalent to a concentration ratio of about 7300 but of course other errors, such as panel surface deformations, alignment, and pointing, that have not been considered here, would reduce the efficiency and concentration ratio.

VI. Summary and Conclusions

The sensitivity of structure weight to increasing wind speed was considerably smaller than expected at the inception of the study. It can be seen that the lower speeds have only minor effect on the weight, and weight sensitivity does not become pronounced even at the higher speeds. The relative insensitivity of weight to wind speed can possibly be explained as follows:

- (1) The reference design, which included seismic loading, inherently provides sufficient strength to resist the lower wind speed loads.
- (2) The weight of many of the members is set by the maximum permitted L/r ratio of 200. The allowable compression stress for this ratio provides significant load-carrying capability that is sufficient for many of

the lower wind speeds In view of this, structure weight could be reduced by changing the layout to use more, but shorter members This could add to the fabrication costs, since the present number lengths are reasonable with respect to current fabrication, ordering, and handling practice

- (3) The format adopted for the configuration and layout is structurally efficient and has the capability of distributing the effects of and supporting loads of high intensity

The postprocessor program used to develop these designs indicates which of these wind orientations sets the design for

each member group design variable As the result of scanning the lists of critical orientations for the individual member groups, no general conclusion can be developed for which orientations tend to be the most critical However, a tendency observed was that the horizon elevation with wind from the front and the 60-deg elevation with wind from the rear were not often critical

A sample evaluation of the performance for one of the 15-m-diameter backup structures designs indicated that the accuracy of the structure when subjected to representative operating gravity and wind loads would be acceptable when used either in a microwave antenna or solar collector system

References

- 1 Levy R , "Conceptual Studies for New Low-Cost 64-M Antennas," in *The Deep Space Network Progress Report 42-33*, pp 55-67, Jet Propulsion Laboratory, Pasadena, Calif , June 15, 1976
- 2 "Guide for Design of Steel Transmission Towers," ASCE Manual and Report on Engineering Practice, No 52, 1971
- 3 Levy, R , "Computer-Aided Design of Antenna Structures and Components," *Computers and Structures*, Vol 6, Pergamon Press, 1976 pp 419-428

Table 1 Excerpt from commercial member size table

HANDBOOK PROPERTIES FOR PIPES			*****LOAD TABLE*****								
NO.	HANDBOOK SHAPE	AREA	RAD	SPAN LENGTHS							
				25.	50.	75.	100.	125.	150.	175.	200.
1.075STD,1.05X.113	.333	.330	8.4	4.1	.0	.0	.0	.0	.0	.0	.0
2.1.0-10,1.315X.109	.413	.430	11.2	8.3	3.9	.0	.0	.0	.0	.0	.0
3.1.0STD,1.315X.133	.494	.420	13.3	9.8	4.4	.0	.0	.0	.0	.0	.0
4.1.25-10,1.66X.109	.531	.550	15.0	12.4	8.2	4.6	.0	.0	.0	.0	.0
5.1.5-10,1.90X.109	.613	.630	17.7	15.2	12.2	7.0	4.5	.0	.0	.0	.0
6.1.25STD,1.66X.140	.669	.540	18.8	15.5	9.4	5.6	.0	.0	.0	.0	.0
7.2.0-10,2.375X.109	.776	.800	22.9	20.6	17.9	14.2	9.1	6.3	.0	.0	.0
8.1.5STD,1.90X.145	.799	.620	23.0	19.7	15.5	8.8	.0	.0	.0	.0	.0
9.2.5-10,2.875X.120	1.039	.970	31.1	28.7	25.9	22.8	17.9	12.4	9.1	.0	.0
10.2.0STD,2.375X.154	1.075	.790	31.7	28.5	24.6	19.2	12.3	8.5	.0	.0	.0
11.3.0-10,3.50X.120	1.275	1.200	38.7	36.5	33.9	31.0	27.8	23.3	17.1	13.1	
12.3.5-10,4.00X.120	1.463	1.370	44.8	42.5	40.0	37.2	34.2	30.9	25.6	19.6	
13.4.0-10,4.50X.120	1.651	1.550	50.8	48.6	46.2	43.5	40.6	37.5	34.1	28.4	
14.2.5STD,2.875X.203	1.704	.950	51.0	47.0	42.3	36.9	28.1	19.5	14.4	.0	
15.3.0STD,3.50X.216	2.228	1.160	67.6	63.4	58.7	53.4	47.5	38.1	28.0	21.4	
16.5.0-10,5.563X.134	2.285	1.920	70.8	68.5	65.9	63.1	60.1	56.9	53.4	49.8	
17.3.5STD,4.0X.226	2.680	1.340	81.9	77.7	73.0	67.8	62.0	55.7	44.9	34.4	
18.6.0-10,6.625X.134	2.732	2.300	85.1	82.8	80.3	77.7	74.9	71.8	68.6	65.2	
19.4.0STD,4.50X.237	3.174	1.510	97.5	93.2	88.4	83.1	77.3	71.1	64.3	51.7	
20.4.5STD,5.00X.247	3.688	1.680	113.8	109.4	104.5	99.1	93.3	87.1	80.3	73.1	

Table 2 Wind speeds and load factors

Reflector elevation, deg						
Front wind			Rear wind			
0	60	90	90	60	0	
Speeds, m/sec (mph)						
4.5 (10)	4.5 (10)	9.0 (20)	9.0 (20)	4.5 (10)	4.5 (10)	
Load factor = 1						
9.0 (20)	9.0 (20)	17.9 (40)	17.9 (40)	9.0 (20)	9.0 (20)	
Load factor = 4						
13.4 (30)	13.4 (30)	26.8 (60)	26.8 (60)	13.4 (30)	13.4 (30)	
Load factor = 9						
17.9 (40)	17.9 (40)	35.8 (80)	35.8 (80)	17.9 (40)	17.9 (40)	
Load factor = 16						
22.3 (50)	22.3 (50)	44.7 (100)	44.7 (100)	22.3 (50)	22.3 (50)	
Load factor = 25						
26.8 (60)	26.8 (60)	53.6 (120)	53.6 (120)	26.8 (60)	26.8 (60)	
Load factor = 36						
31.3 (70)	31.3 (70)	62.6 (140)	62.6 (140)	31.3 (70)	31.3 (70)	
Load factor = 49						

**Table 3 Backup structure reference data
(half structure models)**

		Diameter, m (ft)	15 (50)	26 (85)	40 (132)
Aperture area	m^2 ft^2	91.2 981.7	263.6 2,837.3	635.7 6,842.4	
Surface area	m^2 ft^2	98.7 1,065.0	274.8 2,958.4	626.7 7,133.0	
Focal length	m ft	6.4 21.2	15.5 51.0	24.1 79.2	
Panel surface load	kg lb	1,449.0 3,195.0	4,025.0 8,875.0	9,704.0 21,399.1	
Reference weight for backup structure	kg lb	989.0 2,181.0	3,039.0 6,701.0	7,333.0 16,169.0	
Snow loading (when applied)	kg lb	9,660.0 21,300.0	26,832.0 59,168.0	103,516.0 228,260.0	

Table 4 Backup structure weight increases for wind loading

Reflector diameter	Survival wind speed, ^b m/sec (mph)						
	9.0 (20.0)	17.9 (40.0)	26.8 (60.0)	35.8 (80.0)	44.7 (100.0)	53.6 (120.0)	62.6 (140.0)
		Weight increase from reference design, ^a percent ph)					
15 m	0.0	0.4	0.4	0.4	6.7	not computed	
With snow load	3.7	3.7	4.6	7.7	9.5		
26 m	0.0	0.7	1.1	3.2	8.9	17.0	23.6
With snow load	6.9	8.1	9.1	10.3	13.0	19.4	27.2
40 m	0.6	0.8	2.3	4.5	11.1	20.7	36.9
With snow load	8.1	8.1	9.2	12.2	17.4	20.7	36.9

^aReference design was for gravity and seismic only^bThese designs are also based upon half the survival speed at elevations other than stow (90° elevation)

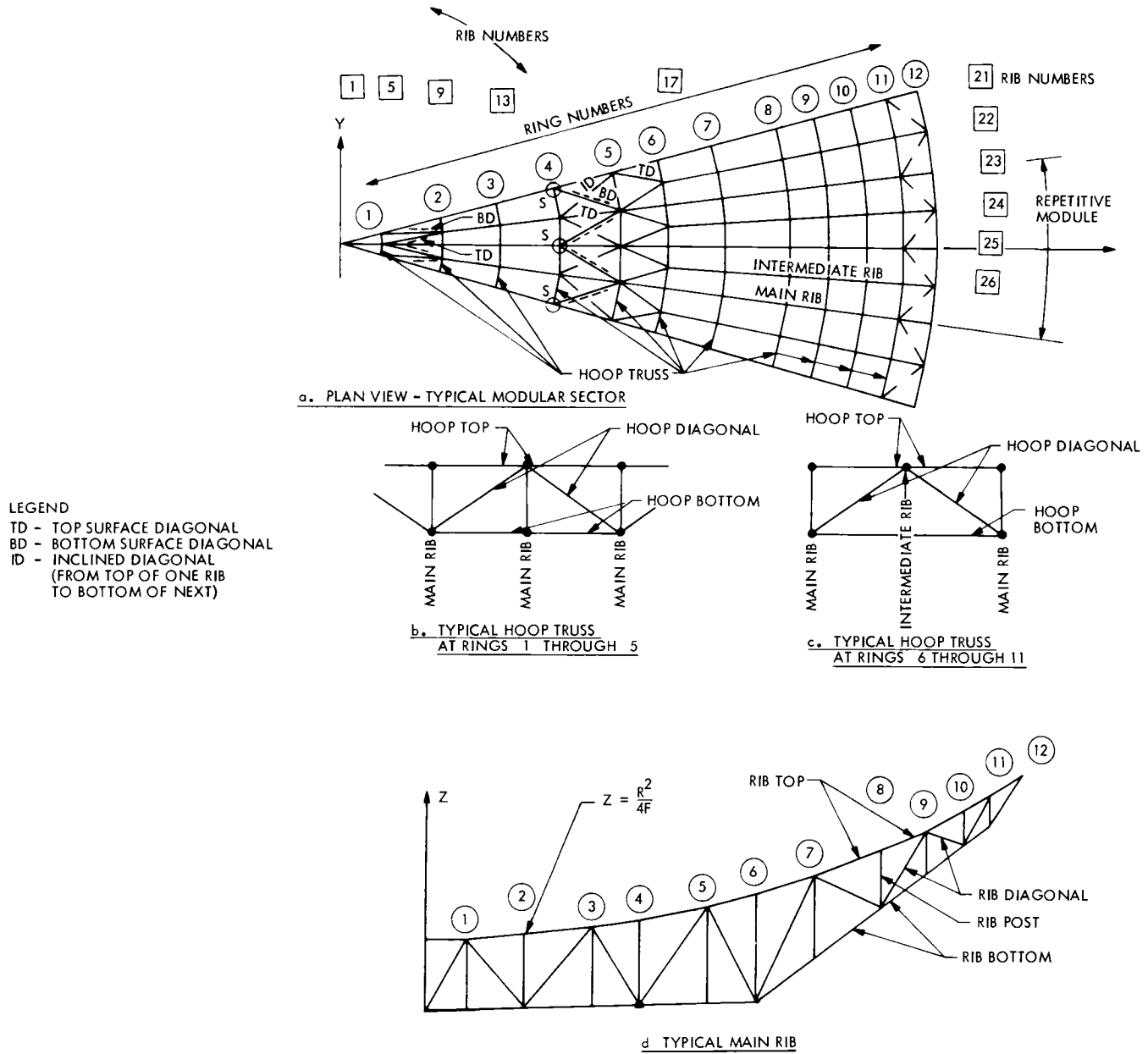
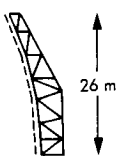
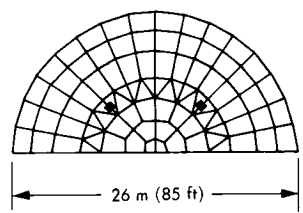
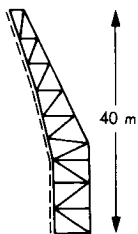
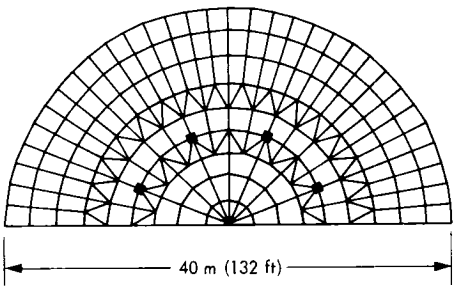
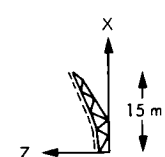
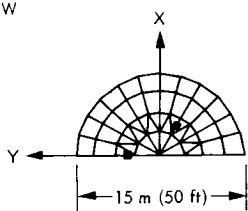


Fig 1 Backup structure framing members



■ SUPPORT POINT
BELOW



(a) PROJECTIONS OF TOP SURFACE

(b) PROFILES OF
MAIN TRUSS RIBS

Fig. 2 Backup structure layouts

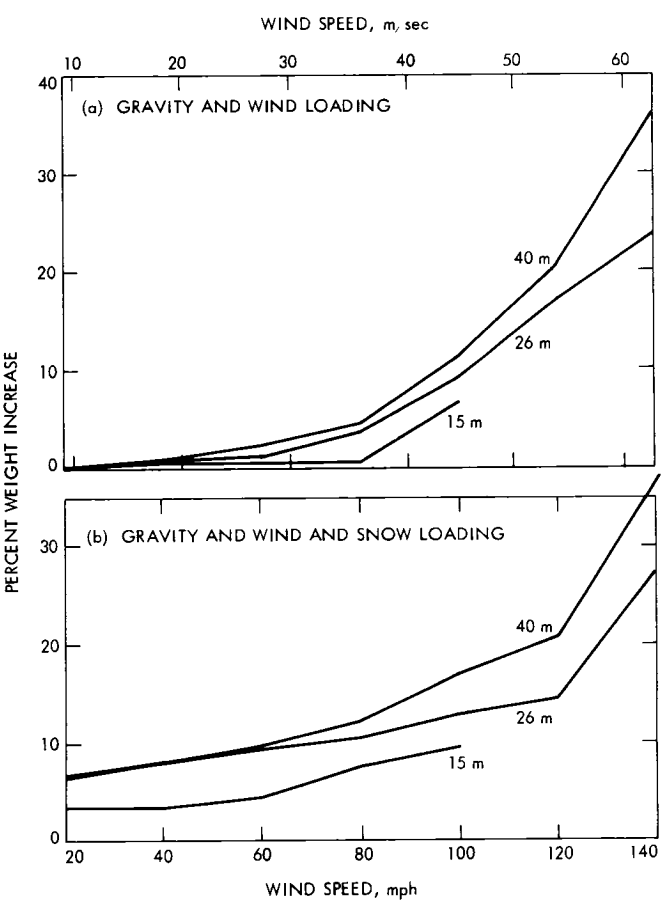


Fig. 3 Backup structure weight increase for varying wind speeds

Analysis of a Class of Totally Self-Checking Circuits Implemented in an NMOS Custom LSI Structure

M W Sievers

Communications Systems Research Section

In the design of ultrareliable computer systems, circuitry must be provided to initiate and execute error control procedures. These procedures include system recovery, data error detection and correction, and handling of singular and exceptional conditions. These procedures are very often implemented by circuitry whose inputs remain constant until an error condition occurs. These circuits, therefore, cannot be fully tested during normal system operation. Lurking faults may be present that will mask the effects of faults in the circuitry being checked.

It is possible to replace constant valued signal lines with a pair of signal lines such that a given logic state has a redundant representation. A class of Boolean algebra called morphic Boolean algebra can then be used to realize totally self-checking circuits to replace semi-passive error handling circuitry. The fault detection properties of these circuits under the assumption of classical stuck-at faults have already been investigated. The purpose of this paper is to specify the expected nonclassical faults in a particular NMOS custom structure and to predict their effect on morphic circuits.

I. Introduction

Fault-tolerant computer systems are made possible only when errors are detected and recovery procedures initiated before permanent data contamination occurs. An error is defined as the corruption of any single line logic state.

Errors may appear anywhere in the implementation of a logic function. A single circuit fault may cause zero, one, or more errors depending on the function, the fault, and the input pattern. A particular line in the implementation of a function is testable if and only if for a given input pattern, a change in the logic state of the line causes a change in the output function.

Lines are termed active if their logic state changes during normal operation. Lines whose state remains constant during normal operation are called semi-passive. The difficulty in detecting errors in active lines is that they are always intermittent. Semi-passive lines are frequently used in error recovery circuitry and do not change state unless an exceptional condition occurs. The error recovery circuitry, therefore, cannot be fully tested. Lurking faults may be present that may mask errors in active lines, causing irreparable data damage.

A means of checking the working condition of error recovery circuitry is to implement them in a totally self-checking scheme. These schemes require that input and output

data be coded so that it is possible to distinguish between valid and invalid codewords. Totally self-checking has been defined by Anderson (Ref 1) as follows

Definition 1

A circuit is termed *self-testing* if for every fault in a given set, the circuit will produce an invalid codeword for at least one valid input codeword

Definition 2

A circuit is *fault secure* if for every fault in a given set, the circuit either generates an invalid output codeword or yields the same codeword as a fault-free circuit

Definition 3

A *totally self-checking* circuit is both self-testing and fault secure

Total self-checking requires that input variables change state in such a way that all paths through the circuit can be sensitized. This requirement is incompatible with semi-passive signal lines. The necessary condition that logic lines change state requires that single semi-passive lines be replaced by a pair of lines, both of which switch state in normal operation. Carter (Refs 2 and 3), has reported on a mapping from semi-passive lines to pairs of lines such that both states have redundant representations. Morphic Boolean algebra operating on these line pairs can realize totally self-checking circuits under the assumption of single stuck-at faults.

The purpose of this article is to investigate the effects of nonclassical faults, predicted for a particular NMOS circuit realization, on the self-checking properties of morphic logic. Faults examined will be those either present at the manufacturing time of a chip or those that appear later due to wear-out.

The next section will present the formalities of morphic logic. Section III offers a failure model for the predicted NMOS failures in a structure for custom LSI. The last section will deal with the expected effect of nonclassical faults on morphic self-checking.

II. Morphic Boolean Algebra

A mapping from single semi-passive signal lines to a pair of lines is defined as follows

$$\begin{aligned} M & [(e_1, e_2), (\bar{e}_1, \bar{e}_2)] \rightarrow 1 \\ & [(\bar{e}_1, e_2), (e_1, \bar{e}_2)] \rightarrow 0 \end{aligned}$$

where $e_1, e_2 \in \{0, 1\}$ (Ref 2). Each wire in the pair can take both values of 0 and 1 without changing the logic state associated with a single line logic. The equivalent single line state is easily determined by the parity of the pair of lines

Two separate problems arise. The first question is one of defining a correspondence between a function g in ordinary Boolean algebra $B = \{0, 1, \{\cdot\}\}$ where $\{\cdot\}$ is the usual set of logic operators, and a function G whose inputs and outputs satisfy the mapping M . It is necessary to define Boolean operators over the pair $\{e_1, e_2\}$. This is done by expanding the mapping M to be a *morphism* between B and

$$\{(e_1, e_2), (\bar{e}_1, \bar{e}_2)\}, \{(\bar{e}_1, e_2), (e_1, \bar{e}_2)\}, \{\cdot^m\}$$

where \cdot^m is defined as the set of morphic Boolean operators

Definition 4

A *morphism* is a general mapping from a set A into a set B that preserves the algebraic structure of A .

Let

$$s_i, s_j \in \{(0,0), (0,1), (1,0), (1,1)\},$$

then

$$M(s_i \cdot^m s_j) = M(s_i) * M(s_j)$$

defines the set of morphic Boolean operators \cdot^m , and

$$B_m = \{(e_1, e_2), (\bar{e}_1, \bar{e}_2), (e_1, \bar{e}_2), (\bar{e}_1, e_2)\}, \{\cdot^m\}$$

forms a Boolean algebra by the definition of morphism M .

It was shown above that semi-passive signal lines could be replaced by a pair of lines and that operators could be defined for the pair. For n input bits in the semi-passive function, there are 2^{2^n} possible morphic Boolean functions. Not all of these will be capable of testing all n input pairs. The second question to be answered is how to determine the self-checking and self-testing properties of the circuit. The following assumes stuck-at faults.

Definition 5

An input A_i of a morphic Boolean function G and an input pattern p is *testable* when a variation in A_i causes a variation in G .

Definition 6

The Boolean difference of a morphic function G with respect to an input A_i is defined as

$$\Delta_{A_i} G(A_1, A_2, \dots, A_i, \dots, A_n) = \\ G(A_1, \dots, A_i, \dots, A_n) \oplus G(A_1, A_2, \dots, \overline{A_i}, \dots, A_n)$$

where \oplus is the EXCLUSIVE OR function

It is easily shown that $\Delta_{A_i} G$ is a function of $A_1, A_2, \dots, A_{i-1}, A_{i+1}, \dots, A_n$ only. These two definitions lead to the following theorem

Theorem 1

An input A_i implemented as (A_{i1}, A_{i2}) of the morphic function $G(A_1, A_2, \dots, A_i, \dots, A_n)$ with a given pattern p in the input space is tested if and only if

$$\Delta_{A_i} G \text{ is TRUE}$$

Proof

The theorem follows immediately from definitions 5 and 6

The next theorem shows a simple method for determining the testability of an input to a morphic function solely as a function of the semi-passive input pattern and the functional specification

Theorem 2

Let a semi-passive input pattern p be such that A_i is FALSE for $i = 0, 1, 2, \dots, k$ inputs and A_i is TRUE for the remaining inputs. A term A_j is testable at the output of a function G if and only if the number of terms containing A_j and not A_i , $i \neq j$ and $i = 0, 1, 2, \dots, k$ (the FALSE terms) in the Boolean polynomial equivalent to G is odd.

Proof

The theorem is proved by applying Theorem 1

Let

$$G(A_1, A_2, \dots, A_n) = C_0 \oplus C_1 A_1 \oplus \dots \oplus C_n A_n \\ + C_{n+1} A_1 A_2 \oplus \dots \\ \oplus C_{2n-1} A_1 A_2 \dots A_n$$

be the Boolean polynomial equivalent to G , where $C_i \in \{\text{TRUE, FALSE}\}$. Let X_0 equal the sum of terms in the polynomial equivalent to G that do not contain A_j and X_i be the product of $i - 1$ distinct variables $A_{i_k}, A_{i_k} \neq A_j$. The general Boolean polynomial equivalent to G may be rewritten as

$$G(A_1, A_2, \dots, A_n) = d_0 X_0 \oplus d_1 A_j \oplus d_2 A_j X_2 \\ \oplus d_n A_j X_n$$

The Boolean difference of G with respect to A_j is

$$\Delta_{A_j} G = d_1 \oplus d_2 X_2 \oplus \dots \oplus d_m X_m \oplus \dots \oplus d_n X_n$$

All X_m 's which contain A_i , $i = 0, 1, \dots, k$ such that A_i is FALSE are FALSE. Therefore, since the condition of testability of A_j for a pattern p is by Theorem 1

$$\Delta_{A_j} \Big|_p = \text{TRUE}$$

the EXCLUSIVE OR of all d_m 's for X 's not containing FALSE A_i 's along with d_1 must be TRUE. Therefore, the parity of terms containing A_j and not FALSE A_i 's must be odd.

The previous two theorems indicate methods for determining the testability of the input space of a given function. It remains to be shown how to realize totally self-checking morphic functions.

Reference 2 presents a universal morphic logic set of totally self-checking building blocks. This set consists of morphic AND, NOT and EXCLUSIVE OR functions (see Fig 1). Not all combinations of these elements are self-checking. The following theorem states the necessary connection conditions.

Theorem 3

A totally self-checking morphic circuit can be realized if and only if the implementation does not prohibit the application of all necessary test vectors to any of its morphic building blocks.

Proof

Fault security is assured since any invalid input code to any of the morphic building blocks will result in an invalid output codeword. The effect of the invalid input propagates to the output.

Self-testing can be shown as follows. The realization of the morphic function permits the application of all test vectors to each building block by assumption. Thus, any single fault in any building block will eventually result in the output of an invalid codeword from the faulty element. The invalid codeword again propagates to the output and is detected.

A construction algorithm is given in (Ref. 2) that guarantees totally self-checking realizations. The algorithm does not produce an optimal design either in performance or number of components. However, it is straightforward to implement and could easily be programmed.

III. Failure Model for an NMOS Custom LSI Structure

Figure 2 illustrates a structure for building custom NMOS integrated circuits. The structure and some of its properties have been reported on previously (Refs. 4 and 5). Logic gates are created and connected together in the structure by a simple mask-level programming scheme.

Due to the low-level implementation of this structure, certain failure mechanisms become more or less likely than other implementations. One of the primary motivations for the structure was to limit the types of defects that might occur to a well-defined set.

In addition to defects that are created in the manufacturing process, there is a set of so-called wear-out flaws and several random failures that determine chip reliability. These flaws are traceable to specification, environment, or fabrication but are not present until some time after the chip is in use. Wear-out ultimately determines the actual useful lifetime of all integrated circuits, however, random failures often occur well before wear-out, although with very low probability.

In well-established processes and technologies, little or no correlation exists between the location of processing defects found on chips of the same wafer or run. There is virtually no correlation of location of defects between wafers of different processing lots. If strong correlations did exist, they would be an indication of a fundamental fabrication failure that would easily be detected. Additionally, fabrication houses have a strong financial interest in correcting the fabrication process.

Integrated circuit defects that determine the infant mortality rate and, if undetected, cause some failures during the useful chip life are considered first. Since fabrication flaws tend to be randomly distributed over the surface of a wafer, a reasonably accurate and mathematically tractable model of their presence is the Poisson distribution,

$$P_k = (DA)^k e^{-DA} / k!$$

where P_k is the probability of k flaws occurring on a chip of area A , and D is the flaw density. The probability of no flaws, therefore, is

$$P_0 = e^{-DA}$$

and the probability of at least one flaw is

$$P_{k \geq 1} = 1 - e^{-DA}$$

Only flaws on active circuit areas need to be considered so A should be scaled by r where r is the ratio of active to total circuit area. For the structure in Fig. 2, r has been estimated at 0.7. Flaw density for a typical MOS process is approximately 13.5 flaws/cm² (Ref. 6).

In practice, various processing, electrical, and logical tests are performed on wafers and chips to detect the presence of defects.

Definition 7

Measured functional yield, ym , is the percentage of chips that pass the manufacturer's screening tests.

Measured functional yield is the sum of two yield terms.

Definition 8

Actual function yield, y , is the actual yield of good chips.

Definition 9

Define y_{bg} as the yield of bad chips that test good.

Actual functional yield is computed by

$$y = e^{-Da}$$

where $a = Ar$. The yield of chips with k undetected circuit flaws under a test of coverage c is

$$y_{bg}(k) = P_{k,r} (1 - c)^k$$

So the yield of bad chips testing good is

$$y_{bg} = \sum_{k=1}^{\infty} P_{k,r} (1 - c)^k$$

Substituting for $P_{k,r}$

$$y_{bg} = \sum_{k=1}^{\infty} \frac{e^{-Da}}{k!} (Da)^k (1-c)^k$$

$$= e^{-Da} (e^{Da(1-c)} - 1)$$

Therefore, the measured functional yield is computed by

$$y_m = e^{-cDa}$$

Table 1 lists the predicted NMOS flaws that affect the yield of circuits built in the structure of Fig. 2. Two of the indicated defects result in classical stuck-at faults. The remainder can be classified either as bridging faults (shorts) or floating faults. A floating condition arises when (1) a pull-up resistor does not pull up a gate output for some reason, (2) the output contact is missing, or (3) a wire is broken. Capacitive coupling of floating wires to neighboring lines may cause the defective wire to drift between logic states.

The preceding discussion dealt only with processing-induced defects. In addition to those flaws, there is a pair of NMOS wear-out defects that may occur. Table 2 lists their mechanisms and their most probable effects on logic.

Metal migration is a current-induced movement of metal in a direction perpendicular to current flow. It can be slowed to very low levels by reducing the current density in metal wires. The situation is undetectable until the metal finally breaks.

Contamination of gate oxides by sodium ions in the fabrication process is unavoidable. These ions are mobile and tend to accumulate under active transistor gates at the substrate side of the gate oxide. In enhancement-mode pull-down transistors, the initial effect of these ions is to make the substrate appear doped, similar to depletion-mode transistors. This lowers the transistor's threshold voltage making it more difficult to turn off. In NOR logic, under certain circumstances, the result is an input stuck at one, or equivalently, an output stuck at zero. Eventually, a sufficient number of ions will collect in the gate oxide to cause a low impedance path between the gate and substrate. The application of a logical 1 to the gate of the transistor will now punch a pinhole through the gate oxide creating a gate-to-substrate short. The result is a stuck-at zero on the input wire.

Finally, random failures may be due to wire bond failure, ionizing radiation, excessive temperatures, moisture leakage and electrical overstressing. The effects of bond failure and

electrical overstressing are similar to those failures already discussed. The remaining mechanisms cause catastrophic failures which are easily detected.

Figure 3 shows a circuit that models the faults indicated in Tables 1 and 2. Gates labeled with an asterisk are susceptible to classical stuck-at faults. All other gates are assumed to be perfect. The transistor switch models the floating condition. When a 1 is applied to the transistor gate, it passes a signal from source to drain. A 0 at the transistor gate breaks the signal path.

IV. Effects of NMOS Defects on Morphic Self-Checking

It has been shown in Section II that totally self-checking morphic circuits can be designed under the assumption of single stuck-at faults. The NMOS defects listed in Tables 1 and 2, however, include nonclassical defects, i.e., bridging faults and floating faults. It will be shown that morphic remains self-checking even when these faults appear.

Bridging faults are easily detected in morphic circuits because they alter an output function in a deterministic manner. Suppose a bridging fault occurred between one line of an input pair, $A_{i,1}$, and one of the output wires, g_1 , of a function G . Let the undamaged morphic function be implemented as

$$g_1 = g_1(A_1, A_2, \dots, A_i, \dots, A_n)$$

$$g_2 = g_2(A_1, A_2, \dots, A_i, \dots, A_n)$$

The damaged function will be

$$g_1 = A_{i,1}$$

$$g_2 = g_2(A_1, A_2, \dots, A_{i-1}, g_1, A_{i+1}, \dots, A_n)$$

which is easily detected by input patterns sensitizing input A_i .

More generally, for at least one input pattern, any pair of wires in an undamaged morphic circuit must have different logic states. If this were not the case then the pair of wires could be replaced by a single wire, and a short between them would not cause an error. A short between wire pairs is detected by applying the pattern that would normally place the wires into complementary states.

Floating defects results in transient faults. These are always detectable when the wire has floated to the wrong state.

Should the wire be in the correct state, no error is detected, but neither is this an error condition

The above discussion leads to the following theorem

Theorem 4

The realization of any totally self-checking morphic function in the NMOS structure of Fig 2 remains totally self-checking in the presence of any single fault

References

- 1 Anderson, D A , G Metze, "Design of Totally Self-Checking Check Circuits for m out of n Codes," *IEEE Trans Comp* , Vol C-22, No 3, March 1973, pp 263-269
- 2 Carter, W C , A B Wadia, D C Jessep, "Implementation of Checkable Acyclic Automata by Morphic Boolean Functions," *Symp Comp and Automata*, Polytechnic Institute of Brooklyn, April 1971, pp 465-482
- 3 Carter, W C , A B Wadia, D C Jessep, "Computer Error Control By Testable Morphic Boolean Functions – A Way of Removing Hardcore," *Symp FTC* 1972, pp 154-159
- 4 Sievers, M W , "A General Logic Structure for Custom LSI," *The Deep Space Network Progress Report 42-50*, Jet Propulsion Laboratory, Pasadena, California, April 15, 1979, pp 97-105
- 5 Sievers, M W , "Density and Reliability Predictions for A General Logic Structure for Custom LSI," *The Deep Space Network Progress Report 42-53*, Pasadena, California, October 15, 1979, pp 66-73
- 6 Case, G R , "Analyses of Actual Fault Mechanisms in CMOS Logic Gates," *13th Design Auto Conf* , Palo Alto, California, June 27, 1976, pp 265-270

Table 1 Effects of various predicted NMOS defects on the structure of Figure 2

Defect	Comment
1 Missing or defective pull-up, broken wire to pull-up	Float
2 Missing pull-down transistor	Input stuck at 1
3 Missing output contact	Float
4 Gate oxide pinhole	Input stuck at 0
5 Broken wire	Float
6 Bridging	Replace shorted terms with their AND

Table 2 Wear out mechanisms

Mechanism	Comment
1 Metal Migration	Float
2 Sodium ion contamination	Initially, input stuck at 1 (equivalent to output stuck at 0) finally input stuck at zero signal from source to drain

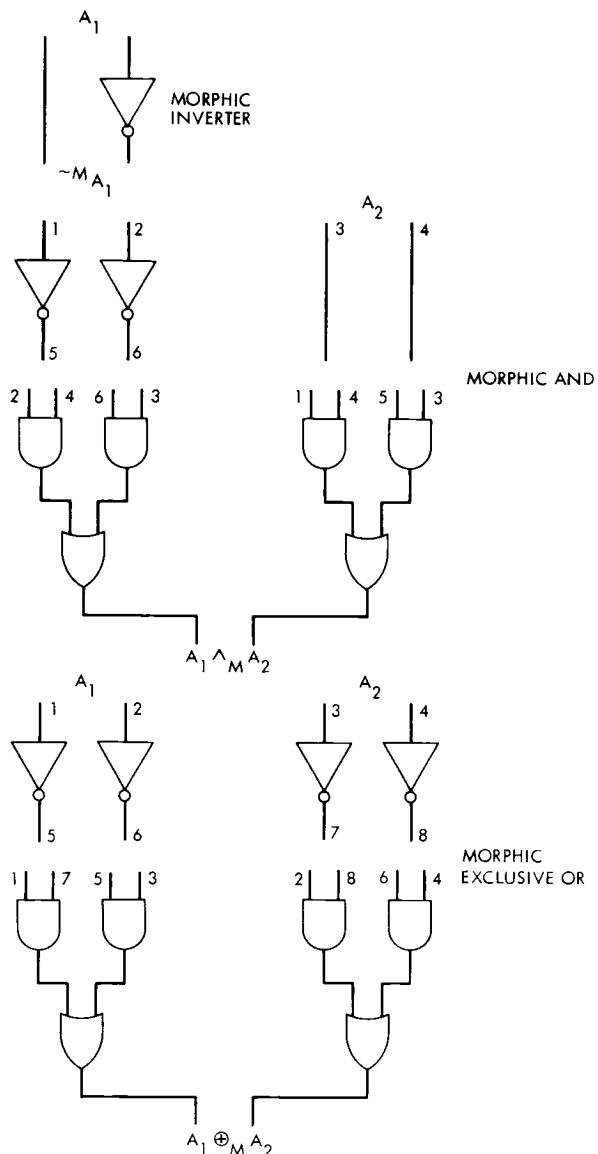
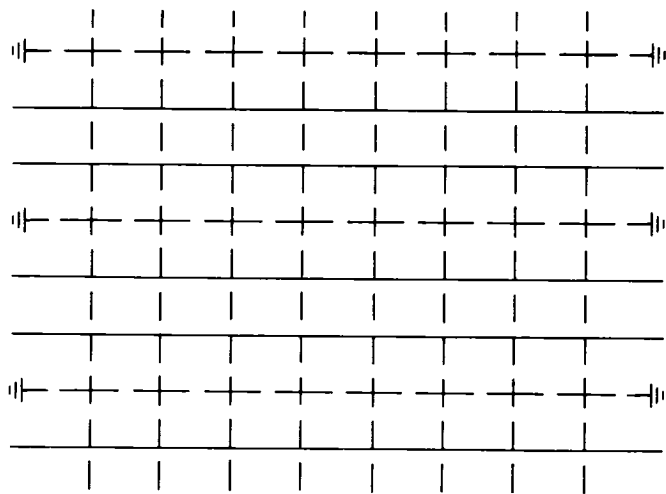


Fig. 1 Morphic building blocks



— METAL
— POLYSILICON
— DIFFUSION

Fig 2 NMOS general logic structure for integrated circuits

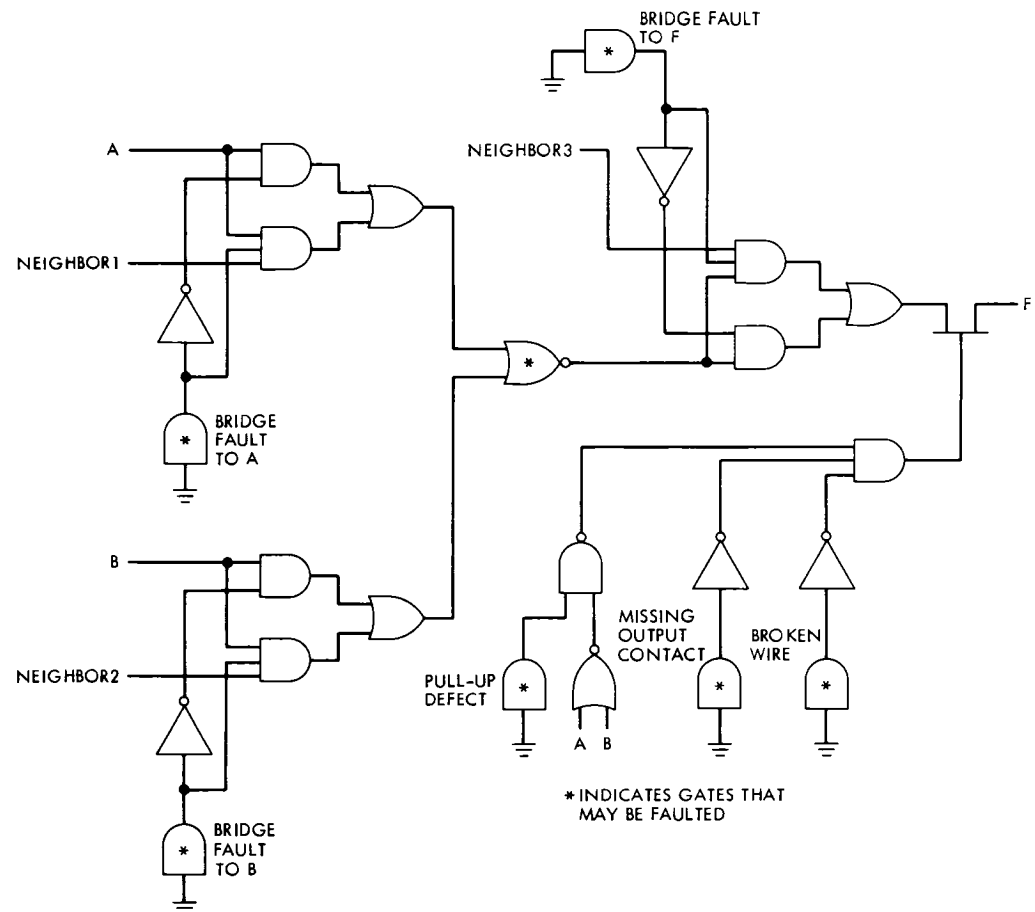


Fig 3 NMOS failure model for a two-input NOR gate

Pulse-Position-Modulation Coding as Near-Optimum Utilization of Photon Counting Channel with Bandwidth and Power Constraints

R G Lipes

Communications Systems Research Section

We show that the capacity, measured in nats per photon, of a pulse-position modulation (PPM) scheme involving Q uses of a channel that neglects thermal noise and makes binary decisions on the presence of photons (Z-channel) is very close to the optimum capacity for utilizing the Z-channel. For Q in excess of around 100, the differences in capacity are probably insignificant for any practical application. The PPM scheme capacity results as the optimum solution to a communication system design problem.

I. Introduction

In this article we bring together some of the results (Refs 1-3) on optical communications employing photon counting at the receiver that have been developed over the last couple of years. This will be done by showing that, for communication channels for which thermal noise can be neglected, a pulse-position-modulation (PPM) coding scheme has a capacity over the range of practical interest very close to optimum for reception which detects only the presence or absence of photons. The fact that this PPM scheme is convenient to analyze (Ref 2) and can be easily utilized in system design considerations enhances the significance of this result.

In the first section, the PPM scheme is explained. A design problem is formulated to obtain the maximum information rate subject to average power and bandwidth constraints. This procedure is equivalent to obtaining the minimum average power subject to information rate and bandwidth constraints, an approach closely related to the work described in Ref 3.

In the second section, the capacity of the Z-channel (Refs 1 and 4) is calculated so that a direct, meaningful comparison with the PPM capacity can be made. The Z-channel models the communication system which neglects thermal noise and for which binary decisions are made regarding the reception of photons. The capacity of the Z-channel upper bounds the information exchange per channel use through extension systems, such as the PPM scheme, composed of multiple uses of the Z-channel. Nevertheless, over a range of parameter values achievable by current or projected technology, the PPM capacity, measured in nats per photon, is only slightly inferior to that of the Z-channel.

In the third section, a design problem using PPM is formulated to obtain the maximum information rate subject to peak power and bandwidth constraints. It has been shown in Ref 5 that the ratio of peak-to-average power must increase exponentially with capacities greater than one nat per photon. Consequently, a different utilization of the PPM system for a

peak power constraint might be expected and is shown to be the case Presumably, the available technology and particular application will determine whether peak or average power constraints are appropriate for a given situation

In the fourth section, we discuss some areas that need to be investigated to improve our understanding of optical communication with photon counting reception

II. Optimized PPM Systems for Certain Optical Communications

In this and the remaining sections we will assume the Z-channel models the physical channel adequately If no photons are transmitted, none are received as thermal noise is being neglected If an expected value of λ photons reach the receiver, due to Poisson statistics the probability of none being detected is $e^{-\lambda}$ This Z-channel is depicted in Fig 1 Suppose a pulse position modulation scheme (Refs 1 and 2) is used over this channel in one of Q uses of the channel photons are transmitted with the decoder estimating in which one of the Q slots this transmission occurred The extended channel model for this system is seen in Fig 2, where the “0” output indicates all Q slots are estimated to have received zero photons A practical scheme for mitigating the effect of this “erasure” is to use a Reed-Solomon outer code on the Q -ary channel (Ref 2) The capacity for the Q -ary PPM channel, achieved when each of the Q codewords is equally likely, is

$$C = (1 - e^{-\lambda}) \log Q \text{ (nats/channel use)} \quad (1)$$

where all rates will be measured in nats unless otherwise stated

Now suppose we have the design problem of maximizing the information rate for this channel subject to average power and bandwidth constraints We will take the bandwidth constraint as requiring the duration of one of the Q time slots to be τ The average power constraint P_{av} (as measured at the receiver to avoid the important but, for this treatment, irrelevant problems of pointing, space loss, etc) can be expressed as

$$P_{av} = h\nu\lambda/(Q\tau) \quad (2)$$

where h is Planck’s constant, ν is the center frequency of the narrowband signal, and λ is the expected number of photons impinging on the receiver

The information or transmission rate R_T must be less than the channel capacity of Eq (1) divided by the time for a single channel use

$$R_T \leq (1 - e^{-\lambda}) \log Q/(Q\tau) \equiv (K/\tau) \rho \text{ (nats/sec)} \quad (3)$$

where, with the assumed constraints, $K \equiv P_{av} \tau/(h\nu)$ is constant and we have introduced ρ , the capacity per photon, a very important parameter for photon communication (Ref 1) For this channel, ρ has the value

$$\rho = (1 - e^{-\lambda}) \log Q/\lambda \text{ (nats/photon)} \quad (4)$$

Equation (3) shows that in this design problem, maximizing the information rate R_T subject to bandwidth and peak power constraints is equivalent to maximizing ρ Combining Eqs (2) and (3) gives

$$\rho = (1 - e^{-KQ}) \log Q/(KQ) \quad (5)$$

which is easily maximized as a function of Q numerically for different values of K

A related design problem is to minimize the average power (at the receiver) subject to bandwidth and information rate constraints Using the same notation of the previous design problem, we find the rate constraint implies

$$\lambda \geq -\log [1 - \pi Q/\log Q] \quad (6)$$

where the product $R_T\tau \equiv \pi$ Then, the inequality on the average power becomes

$$P_{av} \geq h\nu [-\log (1 - \pi Q/\log Q)]/Q\tau \quad (7)$$

Consequently, minimizing P_{av} is equivalent to maximizing the capacity per photon

$$\rho = \tau Q/[-\log (1 - \pi Q/\log Q)] \quad (8)$$

which is easily done numerically as a function of Q for different values of π Notice this design problem was addressed and solved in Ref 3, although the emphasis in that work is somewhat different from that presented here

These design problems are related in the following obvious way Assume the same bandwidth constraint is applied for each problem If the solution maximum rate of the first is used as the constraint value of the second, then the solution minimum average power of the second will be the same value as the constraint average power of the first Consequently, we can parameterize the optimizing solution by either K or π The results of numerical calculations are given in Table I and plotted in Fig 3 for values of π that might be expected for

current or projected values of available technologies. Notice that $\pi \equiv R_T\tau$ is exactly the inverse of what is called “bandwidth” expansion in Ref 5 and is there shown to increase exponentially with ρ for values of greater than one nat/photon. This behavior is quite apparent in Fig. 3.

III. Comparison of PPM Systems With Z-Channel Limit

As stated in the introduction, the capacity of the Z-channel upper bounds the information exchange per channel use through extension systems, such as the PPM scheme, which involve multiple uses of the Z-channel. To compare the PPM scheme with the Z-channel limit, we fixed the value of π as was done in generating Table 1. This parameter π can be viewed as the capacity of the channel per channel use divided by the number of component Z-channel uses. For example, for the Q -ary PPM channel the capacity per channel use is $(1 - e^{-\lambda}) \log Q$ and there are Q Z-channel uses, so $\pi = [(1 - e^{-\lambda}) \log Q]/Q$. For the Z-channel itself, π becomes simply the capacity per channel use, since the component Z-channel is used only once. The problem of computing the capacity of the Z-channel subject to an average power constraint is solved in Ref 4. The solution capacity satisfies

$$\begin{aligned} C = & -q(1 - e^{-\lambda}) - \lambda q e^{-\lambda} \\ & - [1 - q(1 - e^{-\lambda})] \log [1 - q(1 - e^{-\lambda})] \\ & (\text{nats/channel use}) \end{aligned} \quad (9)$$

where λ is the expected number of photons arriving at the receiver, and q is the probability that any photons are transmitted. Maximizing the mutual information subject to the average power constraint requires λ and q to satisfy

$$\log(q^{-1} + e^{-\lambda} - 1) = \lambda(\lambda + 1)/(e^\lambda - \lambda - 1) \quad (10)$$

In the “Z-channel” columns of Table 1, we have given the values of q and λ obtained when the capacity of Eq. (9) is fixed at the values of π and the constraint of Eq. (10) is applied. To compare with the PPM channel, notice that Q^{-1} plays the role of q since it corresponds to the probability of any photons being transmitted in a single use of the Z-channel. The capacity per photon for the Z-channel is given by

$$\rho = C/(q\lambda) \quad (11)$$

and upper bounds that for extension channels involving multiple uses of the Z-channel. From the table and Fig. 3, we

see the ρ values for PPM are only 5.8 percent and 2.5 percent lower than those for the Z-channel at $Q = 100$ and $Q = 1000$, respectively, with any essential difference disappearing for Q much greater than 1000. Consequently, for Q 's as low as 100, the PPM scheme could represent a practical, efficient use of the underlying Z-channel in many applications.

IV. PPM System Optimized With Peak Power Constraint

Consider the design problem of maximizing the information rate for the PPM channel subject to bandwidth and peak power constraints. The peak power seen at the receiver is

$$P_{pk} = h\nu\lambda/\tau \quad (12)$$

since all λ photons arrive in one time slot of duration τ . These constraints fix the expected number of photons, so the information rate satisfying

$$R_T \leq (1 - e^{-\lambda}) \log Q/(Q\tau) \quad (13)$$

can be maximized for Q that maximizes $(\log Q)/Q$, or $Q = e$. In this case the capacity per photon given by Eq. (4) is clearly not maximized for fixed λ at $Q = e$. The problem of maximizing information rate subject to bandwidth and peak power constraints is *not* equivalent to maximizing ρ subject to the same constraints. In fact, at the optimizing value of $Q = e$ for the rate maximization, $\rho = (1 - e^{-\lambda})/\lambda$, which is upper bounded by 1 nat/photon for all $\lambda \geq 0$. For Q -ary PPM, the rates of peak to average power grow as Q . Presumably the available technology and particular application will determine whether the peak or average power constraint is more appropriate, although current laser technology would indicate that peak power constraints are unnecessary for systems with Q less than tens of millions.

V. Areas For Further Study

In this article, we have shown numerically how close the capacity per photon for Q -ary PPM is to the upper bound for optimum use of the Z-channel. For Q in excess of 100 or so, it may be effectively indistinguishable for some applications. Furthermore, the PPM scheme is easy to analyze and we have indicated how it might be utilized in system design considerations. We have compared the PPM system to the Z-channel optimum because both systems make binary decisions regarding the presence of photons at the receiver. It would be very

interesting to determine how good is the practice of making binary decisions in photon counting reception. We know systems with average power constraints that transmit multiple amplitudes in a time slot to communicate more than one bit

are more efficient in the nats per photon measure. Work should be carried out to determine how much better they perform, although the bounds of Ref 5 show no dramatic improvement can be expected.

References

- 1 Pierce, J R , "Optical Channels Practical Limits with Photon Counting," *IEEE Trans Communications*, COM-26, 1978, pp 1819-1821
- 2 McEliece, R J , and Welch, L R , "Coding for Optical Channels with Photon Counting," in *The Deep Space Network Progress Report 42-54*, pp 61-66, Jet Propulsion Laboratory, Pasadena, Calif , Dec 15, 1979
- 3 Butman, S A , Katz, J , and Lesh, J R , "Practical Limitations on Noiseless Optical Channel Capacity," in *The Deep Space Network Progress Report 42-55*, pp 12-14, Jet Propulsion Laboratory, Pasadena, Calif , Feb 15, 1980
- 4 Gordon J P , "Quantum Effects in Communications Systems," *Proc Inst Radio Eng* , 50, 1962, pp 1898-1908
- 5 McEliece, R J , Rodemich, E R , and Rubin, A L , "The Practical Limits of Photon Communication," in *The Deep Space Network Progress Report 42-55*, pp 63-67, Jet Propulsion Laboratory, Pasadena, Calif , Feb 15, 1980

Table 1 Comparison of parameters of Q-ary PPM and Z channels as a function of capacity per channel use per number of slots

π	Q	Q-ary PPM channel		Z-channel		
		λ (expected no of photons)	ρ (nats/photon)	q (prob of photons)	λ (expected no of photons)	ρ (nats/photon)
0 26340	5	1 7054	0 77224	$1 3463 \times 10^{-1}$	1 4981	1 3053
0 14957	10	1 0486	1 4264	$7 3963 \times 10^{-2}$	1 1006	1 8374
$8 0013 \times 10^{-2}$	20	0 76396	2 0947	$3 8934 \times 10^{-2}$	0 84638	2 4281
$3 3726 \times 10^{-2}$	50	0 56398	2 9900	$1 6279 \times 10^{-2}$	0 63671	3 2538
$1 7303 \times 10^{-2}$	100	0 47116	3 6723	$8 3392 \times 10^{-3}$	0 53220	3 8987
$8 8170 \times 10^{-3}$	200	0 40470	4 3573	$4 2506 \times 10^{-3}$	0 45542	4 5548
$3 5930 \times 10^{-3}$	500	0 34119	5 2654	$1 7348 \times 10^{-3}$	0 38116	5 4339
$1 8159 \times 10^{-3}$	10^3	0 30500	5 9537	$8 7805 \times 10^{-4}$	0 33874	6 1052
$1 8603 \times 10^{-4}$	10^4	0 22562	8 2452	$9 0413 \times 10^{-5}$	0 24617	8 3582
$1 8875 \times 10^{-5}$	10^5	0 17906	10 541	$9 2119 \times 10^{-6}$	0 19273	10 631
$1 9058 \times 10^{-6}$	10^6	0 14844	12 839	$9 3316 \times 10^{-7}$	0 15815	12 914
$1 9190 \times 10^{-7}$	10^7	0 12677	15 138	$9 4194 \times 10^{-8}$	0 13400	15 202
$1 9289 \times 10^{-8}$	10^8	0 11061	17 438	$9 4871 \times 10^{-9}$	0 11621	17 493
$1 9367 \times 10^{-9}$	10^9	$9 9154 \times 10^{-2}$	19 739	$9 5419 \times 10^{-10}$	0 10257	19 788
$1 9429 \times 10^{-10}$	10^{10}	$8 8153 \times 10^{-2}$	22 040	$9 5846 \times 10^{-11}$	$9 1783 \times 10^{-2}$	22 084

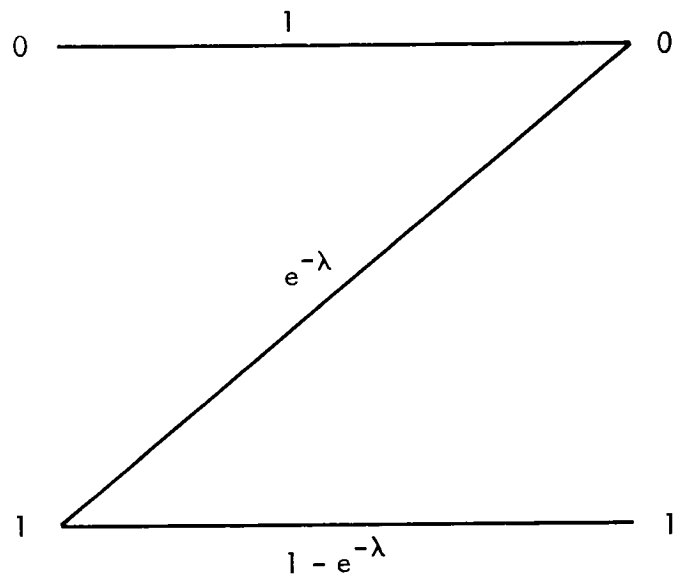


Fig 1 Z-channel with transition probabilities

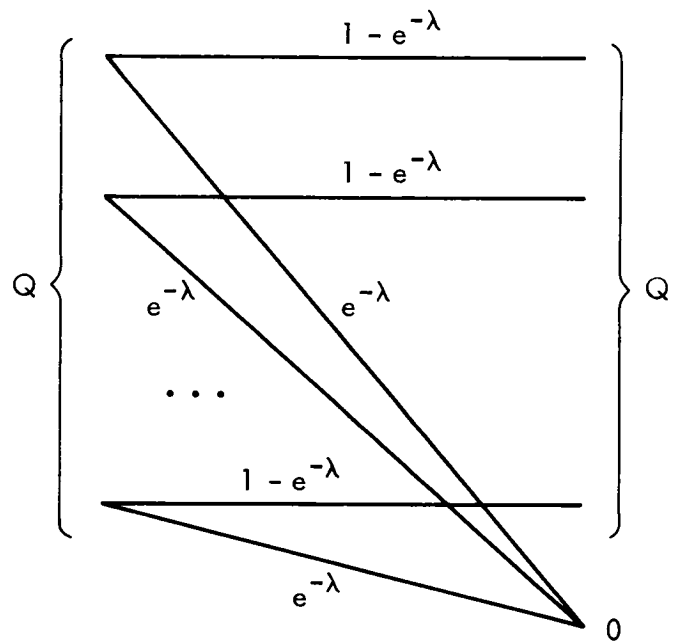


Fig 2 Q-ary pulse-position-modulation channel with transition probabilities

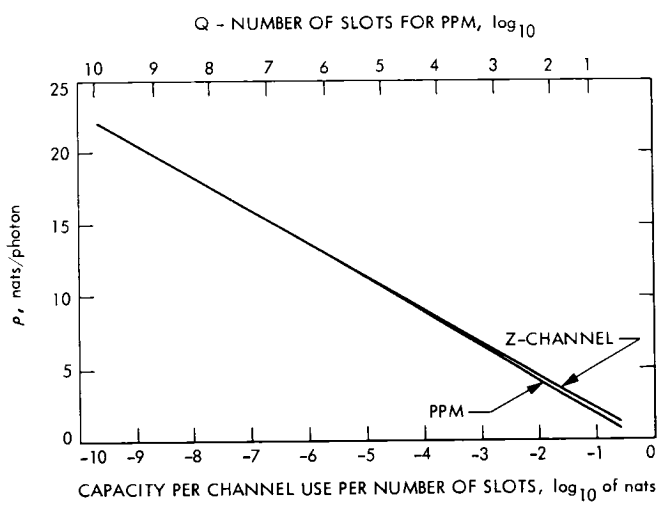


Fig 3 Variation of ρ for Q-ary PPM and Z-channels with capacity per channel use per number of slots

Deep Space Network Control Room Noise and Vibration Study

J C Rayburn

Deep Space Network Support Section

Vibration and noise levels in two of the DSN Deep Space Station (DSS) Operations Rooms have been an annoyance to personnel and are the suspected cause of tracking equipment failures. Measured noise levels were compared to Standard Noise Level Criteria curves. Precision instrumentation was used to measure noise and vibration levels in the rooms and equipment racks. Findings resulting from analysis of the measured data coupled with on-site noise reduction tests are discussed.

I. Introduction

At Deep Space Stations (DSSs) 11 and 61/63, existing vibration and noise levels have been an annoyance to personnel and are the suspected cause of tracking equipment failures. This study included on-site inspection and measurements to identify the noise and vibration sources and the related sound pressure levels, data analysis, and recommendations to reduce noise and vibration levels.

II. Measurement Criteria

Noise Criteria (NC) curves are commonly used to evaluate noise in buildings and are plotted against a background of measured sound pressure level vs frequency coordinates. A maximum noise criteria value of 55 (NC-55) is recommended for the Station Monitor and Control area in the Operations Room. At levels above NC-55, it is difficult to conduct telephone conversations and for operators to talk directly to each other if they are separated by a distance of more than a few feet. For comparison, in a typical private office, NC-35 or less is recommended.

A specified criteria for measuring vibration levels was not considered for rack and cabinet-mounted equipment in the Operations area. The goal was to reduce the vibration to an acceptable level by straightforward means, i.e. vibration damping and isolation.

III. Noise and Vibration Measurements

Airborne noise levels were compared to Standard NC curves to evaluate noise levels measured in the plenum space. Measured vibration levels radiated from fan enclosures were also converted to sound pressure levels and plotted vs NC curves. Additionally, a single sound meter reading in dBA was determined for each spectrum, the sound meter reading describes the response of the human ear. The sound meter readings were also used to compare the impact of fan noise with noise from other equipment in the Operations area where speech communication is important.

Figure 1, Curve No 1, shows the range of noise (sound pressure levels), measured one meter from the discharge of

three Westinghouse draw-through-type Air Handling Units (AHU-2, AHU-3, and AHU-4) located in the plenum at DSS 61/63 Two of the three units, AHU-2 and AHU-3, operate continuously Presently, AHU-4 is not used (except during adverse conditions when maximum cooling is required) because of its location directly beneath the Station Monitor and Control area Figure 1, Curve No 2, shows the range of noise levels radiated from the three fan enclosures Figure 2 compared dBA sound meter readings in the Station Monitor and Control area of the Operations Room with AHU-3 and AHU-4 operating together and with AHU-2 and AHU-4 operating together The difference in sound level measurements ranged between 2 and 7 dBA at various operator positions

As an on-site experiment, AHU-2 fan noise was considerably reduced when an experimental plywood duct lined with 25-mm, semirigid glass fiberboard was placed in front of the air handler output The noise reduction achieved by this experiment (10 dBA sound meter reading) is compared with existing conditions in Fig 1, Curve No 3

At DSS 11, precision sound level instruments were utilized to measure vibration acceleration levels in the equipment racks For example, muffin fan measurements were taken at the top of Telemetry Processor Assembly No 2 This was the worst-case unit that could be located by inspection Measurements with the fan on and the fan off confirmed that the muffin fan generated the most significant vibration in this particular rack

Figure 3 compares vibration measurements of upper and lower Wangco Tape Recorders at DSS 61/63 These units are supported only at the front of the cabinet with the entire casing cantilevered All measurements were made in the middle of the rear panels where vibration acceleration levels were greatest

For the Diablo Disk Units, measurements for vibration were made at the rear of the horizontal sliding support tracks Figure 4 shows the levels measured for the Diablo Disk Drive Unit at the top rear panel

Figure 4 also displays the average vibration levels measured on the Wangco vacuum pump housing and its integrally attached hardware at DSS 61/63 This entire unit is supported by three rubber mounts at the rear of the cabinet This allows the cantilevered front left corner to be relatively free to move and is the location where the measurements were made

DSS 61/63 Operations Room Lobby floor is also impacted by vibrating mechanical equipment and associated piping in the Mechanical Room below Piping that leads to compressors

is rigidly hung from the concrete floor slab above and this produces a condition that is particularly annoying to people standing in the lobby area

IV. Findings

Analysis of the measured data, coupled with on-site noise reduction tests, indicated that prefabricated sound attenuators or silencers in conjunction with duct work lined with a glass-fiber duct liner attached at the fan discharge should be installed on the three air handlers located in the Operations Room plenum at DSS 61/63

Because of the air distribution and total volume requirements, silencers with low static pressure drops are required It is estimated that the static pressure drop for each AHU, due to silencers only, will be about 5 mm to 8 mm for a 1-m-long silencer The existing AHUs' capacities can compensate for these static pressure drops

The estimated values of noise reduction at the AHU-3 duct output (29-dBA sound meter reading) for these improvements are shown on Fig 1, Curve No 4

Vibration acceleration levels in the equipment racks indicated improper isolation of vibrating cabinet-mounted instruments and cooling fans Contributing paths were established Measurements with the fan on and fan off confirmed that the muffin fan generated the most significant vibration in the racks

V. Action Planned

A. Air Handling Units

A design concept developed jointly by DSN support and station personnel for implementing the plenum air handler noise and vibration suppression technique described in Section IV was detailed Requests for implementation bids have been solicited from local Spanish heating and venting contractors It is expected the modifications will be completed during the second quarter of FY 80

B Muffin Fans

To reduce vibration, a 5-mm heavy metal ring will be mounted between the fan and the cabinet and securely fastened This should provide additional stiffness and add mass to dampen fan vibration To reduce airborne noise levels, a commercially available preformed glass fiber cylindrical duct will be placed over the fan This device will be located in the line of sight between the fan and operator positions and should provide some fan noise reduction due to absorption

C. Diablo Disk Units

All rack supports and associated connections will be stiffened All tracks will be aligned vertically and any horizontal adjustments will be made at the cabinet mounts to ensure proper tolerance between tracks Connections and mounting hardware joining the tracks to the angles which support the Diablo Disk Unit are to be made as tight as possible

D. Wangco Tape Recorder Drive

Consideration will be given to mounting a horizontal angle support spanning the entire cabinet width near the rear of the unit This will provide significant additional stiffness to these recorders and reduce the vibration levels associated with these units

E. Wangco Vacuum Pump

Attaching horizontal angle supports to the existing front metal flange, just above the fan, and an anchor to each cabinet sidewall should provide maximum vibration reduction for the vacuum pump Alternately, adding a support similar to the

existing hard rubber mounts between the cantilevered front left corner of the pump and the cabinet sidewall would reduce vibration

F. Pipe Hangers

To isolate existing compressor vibrations from the lobby floor at DSS 61/63 Operations Building, a series of spring hangers with 2 54-cm static deflection located as close to the underside of the floor slab as possible should be attached to the overhead pipe hangers (recommended Type PC-30 by Mason Industries, or equivalent by Amber/Booth or CalDyn)

V. Conclusion

By using precision instrumentation, equipment generating excessive noise and vibration in a DSS Control Room can be identified and measured Corrective engineering action then can be taken to reduce the noise and vibration to acceptable levels The air handler, muffin fans, Diablo Disk Unit, Wangco Tape Recorder Drive, and Wangco Vacuum Pump were identified as the sources of annoyance and corrective actions have been initiated

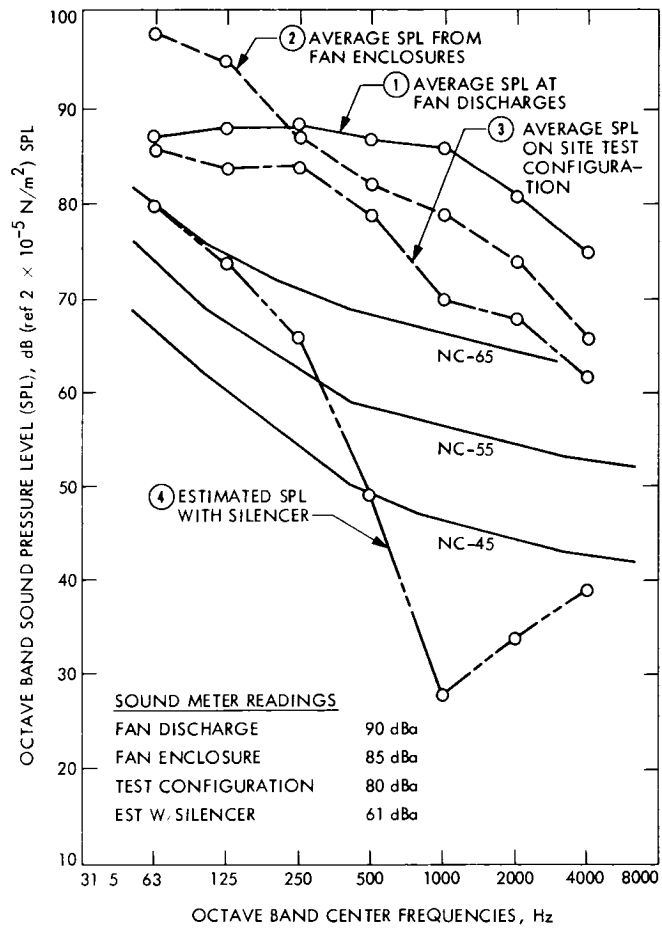


Fig. 1 Fan noise levels in plenum

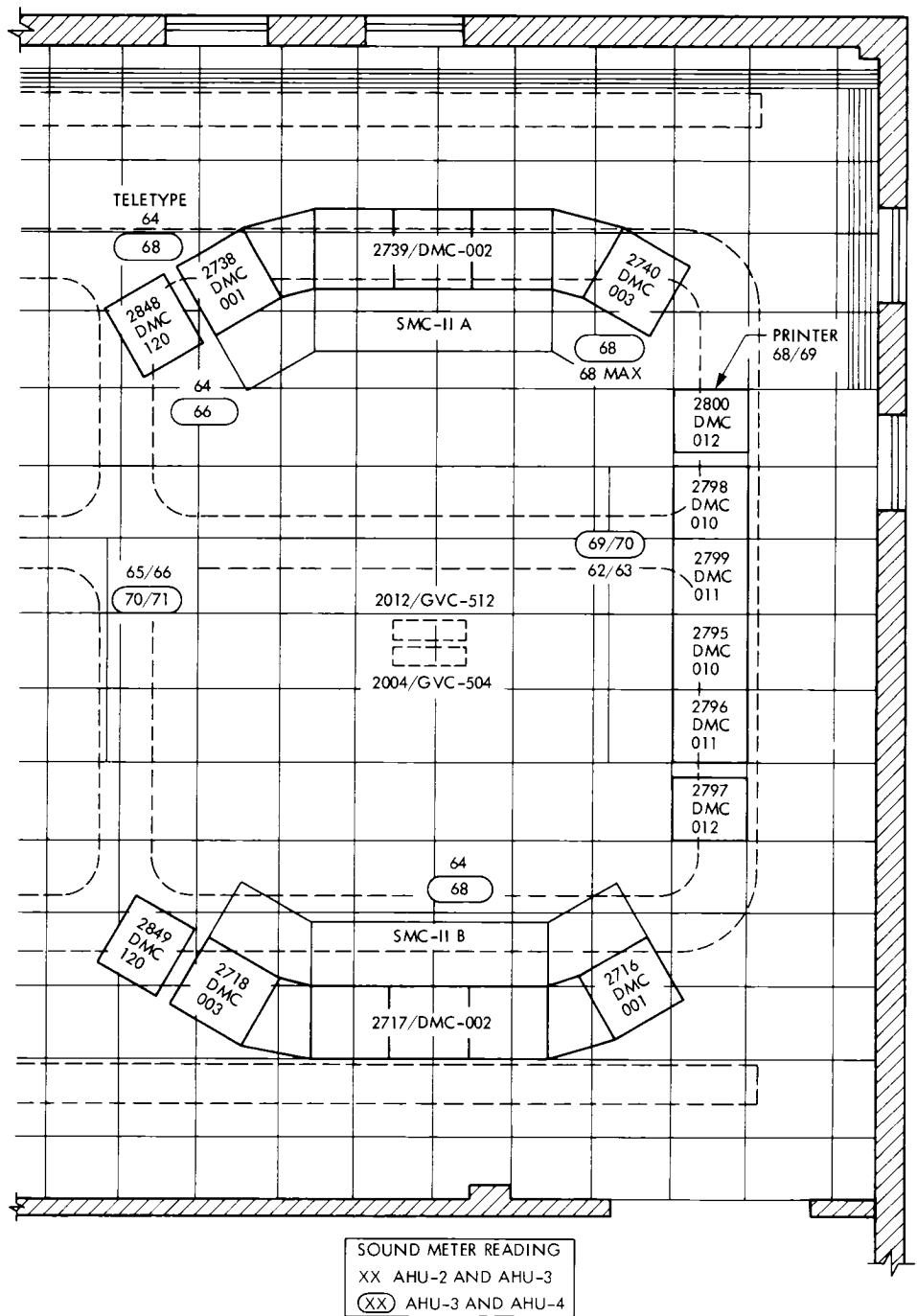
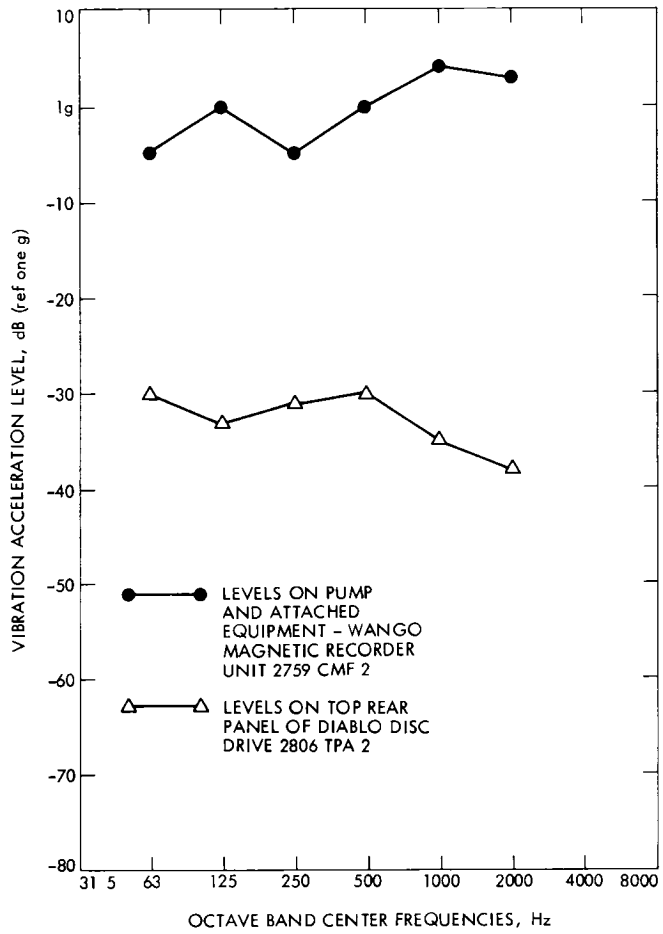
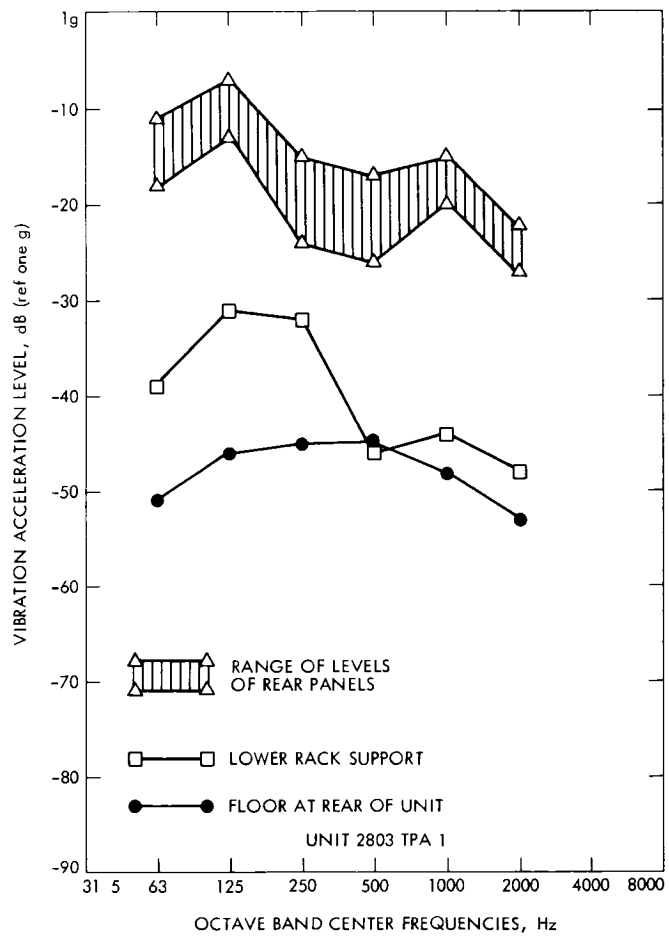


Fig 2 Noise levels (dBA) in Monitor and Control area



A Fast Algorithm for Encoding the (255,223) Reed-Solomon Code Over GF(2⁸)

R L Miller and T K Truong

Communications Systems Research Section

I S Reed

University of Southern California

A new scheme for reducing the numerical complexity of the standard Reed-Solomon (R-S) encoding algorithm is developed. As an example, the encoding of a (255,223) R-S code (NASA standard for concatenation with convolutional codes) is shown to require 75 percent fewer multiplications and 61 percent fewer additions than the conventional method of computation.

I. Introduction

In this article, the fast syndrome method developed in Ref 1 and Lagrange interpolation are used to develop a fast algorithm for encoding R-S codes. It is shown that both the number of multiplications and additions of this new scheme is substantially fewer than is required by the conventional encoding techniques.

An advantage of this new algorithm aside from speed is that its first step consists of performing a syndrome-like calculation, which can be implemented by using the existing syndrome algorithm used in the decoder. This fact can be used to lower the total hardware cost of the encoder-decoder system.

II. Encoding Procedure

Let $n = 2^m - 1$ be the block length of an R-S code of designed distance d in $GF(2^m)$. The number of m -bit message symbols is $k = n - d + 1$.

To encode the k information symbols into an $n = 2^m - 1$ symbol R-S code word, one first defines the generator polynomial

$$G(x) = \prod_{i=1}^{d-1} (x - \alpha^i)$$

when α is a primitive n th root of unity. The code consists of all multiples of $G(x)$, subject to the constraint that $x^n = 1$.

Let a_i for $d - 1 \leq i \leq n - 1$ be the message symbols, and define

$$I(x) = \sum_{i=d-1}^{n-1} a_i x^i$$

In order to generate the code word with information symbols corresponding to $I(x)$, proceed as follows: let

$$I(x) = Q(x)G(x) + R(x) \quad (1)$$

where $Q(x)$ is a quotient polynomial, $G(x)$ is the generator polynomials, and $R(x)$ is the remainder upon dividing $I(x)$ by $G(x)$. Finally, $I(x)$ is encoded into

$$C(x) = I(x) - R(x) \quad (2)$$

The new encoding procedure of an R-S code is composed of the following two steps

- (1) Compute $I(\alpha^i)$ for $1 \leq i \leq d-1$ by the technique which is used to compute syndromes in the decoder
Note that by Eq (2), $I(\alpha^i) = R(\alpha^i)$ for $1 \leq i \leq d-1$
- (2) Compute $R(x)$ from $R(\alpha^i)$ using Lagrange interpolation

$$R(x) = \sum_{i=1}^{d-1} R(\alpha^i) E_i(x)$$

where $E_i(x)$ is defined by

$$E_i(x) = \frac{\prod_{j \neq i} (x - \alpha^j)}{\prod_{j \neq i} (\alpha^i - \alpha^j)} \text{ for } 1 \leq i \leq d-1 \quad (3)$$

The degree of $E_i(x)$ is $d-2$, hence, the degree of $R(x)$ is at most $d-2$. Thus, the parity symbols consist of the $d-1$ coefficients of $R(x)$, as desired. Note that a direct computation of $R(x)$ in Eq (1) involves $(d-1) \cdot (n-d+1)$ multiplications and $(d-1) \cdot (n-d+1)$ additions. If one uses a fast

syndrome calculation, say, for the case $n = 255$, $k = 233$, it is shown in the following example that the encoder requires only 1812 multiplications and 2764 additions instead of the 7136 multiplications and 7136 additions required by a more conventional computation. This results in a significantly faster encoding scheme.

Example

Let $n = 255$ be the block length of an R-S code of designed distance $d = 33$ over $GF(2^8)$. This code will correct any combination of 16 or fewer symbol errors. The first step of the encoding process is to compute $I(\alpha^i)$ for $1 \leq i \leq 32$. That is,

$$I(\alpha^i) = \sum_{j=0}^{255-1} a_j \alpha^{ij} \text{ for } 1 \leq j \leq 32 \quad (4)$$

where α is an element of order 255 in $GF(2^8)$, and $a_j = 0$ for $0 \leq j \leq 31$. Note that Eq (4) is the same formula as Eq (1) in Ref 1. Thus, using the same computing procedure, one obtains $I(\alpha^i)$ for $1 \leq i \leq 32$. It follows from Ref 1 that the total number of multiplications and additions needed to compute the $I(\alpha^i)$ for $1 \leq i \leq 32$ is 852 and 1804, respectively. The second step of the encoding process is to compute $R(x)$ defined in Eq 3, i.e.,

$$R(x) = \sum_{i=1}^{32} R(\alpha^i) E_i(x) \quad (5)$$

Since $E_i(x)$ can be pre-computed, $32 \times 30 = 960$ multiplications and 960 additions are needed to compute $R(x)$. Hence, the total number of multiplications and additions required for encoding is $852 + 960 = 1812$ and $1804 + 960 = 2764$, respectively. In contrast, the total number of multiplications and additions for encoding by conventional methods is $223 \times 32 = 7136$ each.

Acknowledgment

The authors wish to thank Prof J. Massey of the Electrical Engineering Department, University of California, Los Angeles, for suggesting the possibility of a fast encoding algorithm of the type presented in this paper.

Reference

- 1 Truong, T. K., Miller, R. L., and Reed, I. S., "A Fast Technique for Computing Syndromes of BCH and R-S Codes," *Electronics Letters*, Vol. 15, No. 22, pp. 720-721, October 25, 1979

Maximum CW RFI Power Levels for Linear Operation of the DSN Block IV Receiver at S-Band Frequencies

D R Hersey and M K Sue
Telecommunications Systems Section

This article describes the results of a study performed to determine the maximum allowable CW RFI power into the DSN S-band maser to ensure linear amplification of the desired signal by the maser and Block IV receiver

I. Introduction

The power levels of CW signals that result in gain compression of the S-band maser at various frequencies has been well defined (Ref 1) It has been generally assumed that the maser will saturate at weaker power levels than stages in the receiver, and, consequently, the criterion for avoiding receiver saturation by CW radio frequency interference (RFI) was the maser saturation curve of Fig 1

In this study the most sensitive points within the Block IV receiver were considered along with the maser saturation characteristics A curve was developed to show maximum allowable CW interference power into the maser versus signal frequency to ensure linear operation of the receiver

It should be pointed out that many circuit parameter specifications which adequately ensure that the receiver meets its design requirements (i.e., properly receives the desired signal) do not provide sufficient information for determining the worst-case parameter values for RFI analyses For example, the minimum gain of an amplifier is specified but the maximum gain of the amplifier, which causes the worst case RFI effect, is not Because the worst-case values of many parameters could not be determined, it was necessary to use

typical and minimum specified values in this study As a result, the actual levels required to cause nonlinear operation of the receiver may vary from receiver to receiver and from the curve developed herein It is estimated that the magnitude of this variation is typically 3 dB

II. Model Description

The model for maximum allowable CW RFI at S-band is given in Appendix A and shown graphically by Fig 5 This analytic model is based upon the following assumed receiver settings and conditions

- (1) The design point tracking loop noise bandwidth ($2B_{Lo}$) is 10 Hz
- (2) The predetection bandwidth is 20 kHz
- (3) The system noise temperature is 23 K
- (4) The signal level control is set at 20 dB
- (5) The receiver is locked to a desired signal having a power level of -165 dBm (-195 dBW) at the maser input (this signal level corresponds to the minimum 10-dB SNR in $2B_{Lo}$ recommended by the DSN)

Shown in Fig 2 is a simplified block diagram of the Block IV receiver. The circled numerals denote circuit points where signal power must not exceed certain limits to ensure linear operation. The maximum allowable power levels at these points are determined by module characteristics, and by the overall gain and frequency response of the receiver stages preceding the circuit point (see Appendix B). These values are given in Table 1. The first row of Table 1 contains the module limits that are power levels which, if exceeded, will cause the stage associated with the point to operate in a nonlinear region. The subsequent entries in the table show the corresponding power at each preceding point when the most sensitive circuit points are consecutively set to their module limits.

As an example of the use of the table, consider the case when point 7 is set to its module limit. From the table it is seen that the maser input signal necessary to cause the limit value (+20 dBm) at point 7 is -90 dBm. From Fig 1, it is found that the maser limit value at frequencies within ± 4 MHz of the desired signal is -90 dBm, and, therefore, it is seen that the telemetry output (point 7) and maser will saturate at the same receiver input power.

To present the analytical model graphically, first, the maximum allowable power at the preselector input (from Table 1) was plotted versus interfering signal frequency in Fig 3. The points enclosed in circles and triangles are measured saturation values which are discussed in the following section.

Since the receiver preselector has a much wider bandwidth (140 MHz) than the maser (30 MHz), Fig 3 must be corrected for the maser frequency response. This plot is shown in Fig 4.

Next, the maser saturation characteristics curve (Fig 1) is combined with Fig 4 to obtain the overall receiver saturation curve shown in Fig 5. Figures 3, 4, and 5 are all drawn showing the receiver locked to a single desired carrier signal, as it would be at any given time. To define the susceptibility, taking into account that the receiver can be tuned to any frequency within the DSN S-band downlink receive band (2290 to 2300 MHz), the most sensitive region of the curve would be drawn 10 MHz wide (from 2290 to 2300 MHz).

III. Verification Tests

Verification of the model was accomplished by testing the Block IV receiver without the maser and combining the results with empirical maser saturation data obtained from the reference. Identical tests were performed in CTA 21, using an operational receiver, and in the Telecommunications Development Laboratory (TDL), which has the Engineering Model Block IV receiver.

The test configuration is shown in Fig 6. The spectrum analyzer is used to measure the suppression of the desired signal caused by the interfering signal applied at the preselector input. This analyzer provides a 1-Hz resolution bandwidth, which allows accurate measurement of the signal power at low signal-to-noise ratios. Because the instrument (HP Model 3580) is limited to frequencies of 50 kHz or less, down conversion of the 10-MHz and 100-kHz outputs was necessary. The attenuator used before the mixer is required to prevent the test mixer from being saturated by the interfering signal power at the 10-MHz distribution amplifier and 100-kHz IF amplifier outputs. The test accuracy is estimated to be ± 4 dB.

The results of these tests are shown in Fig 3. The TDL test results, shown by circled points, show good agreement with the model from 2260 to 2310 MHz. Deviations from the model outside this range were caused by the TDL's 325-MHz IF amplifier, which is of a different design than the DSN operational amplifier.

The CTA 21 points show good agreement with the model, except the points at 2330 and 2340 MHz show that the preselector bandwidth of CTA 21's receiver is approximately 4 MHz wider than assumed by the model.

Saturation characteristics of the 100-kHz IF amplifier at frequencies within the predetection bandwidth could not be measured directly. In this region, severe tracking performance degradation will occur before saturation takes place (tracking loop performance in the presence of a CW RFI will be discussed in future reports). Instead, the gain and output 1-dB compression point of the 100-kHz IF amplifier were measured and found to agree with the model assumed values (42 dB and +7 dBm, respectively).

IV. Conclusions

The test results show that the receiver only saturation model (Fig 3) is sufficiently accurate to use in developing the overall receiver saturation curve (Fig 5). This model predicts that the 10-MHz outputs to telemetry and ranging will saturate at nearly the same power level as the maser when the interfering signal frequency is within ± 4 MHz of the desired signal frequency. Outside of this region the maser saturation characteristics will predominate.

Within ± 10 kHz of the desired signal, it is known that severe carrier tracking degradation will occur at much lower levels of interfering signal power than that which will produce

saturation of the 100-kHz IF amplifier linear output. Modeling of the carrier tracking degradation produced by CW interfer-

ence is currently underway. This model and verification test results will be the subject of a future article.

Reference

- 1 Clauss, R. C., "X- and K-Band Maser Development Effects of Interfering Signals," *Deep Space Network Progress Report 42-42*, pp. 85-87, Jet Propulsion Laboratory, Pasadena, CA, Dec 15, 1977

Table 1 Maximum CW power levels to ensure linear receiver operation

Condition	Maximum CW power, dBm								
	Circuit point								
	1	2	3	4	5	6	7	8	9
Module limit See Fig 1		-	-7	-39	+10	-18	+20	-5	+7
For limit value at circuit point 9 for interfering frequencies within ± 10 kHz of desired signal frequency	-133	-85	-87	-94	-39	-68	-23	-35	+7
For limit value at circuit point 7 for interfering frequencies within ± 4 MHz of desired signal frequency	-90	-42	-44	-51	+4	-25	+20	-	-
For limit value at circuit point 6 for interference signals within ± 15 MHz of desired signal frequency	-83	-35	-37	-44	+11	-18	-	-	-
For limit value at circuit point 5 for interfering frequencies within ± 36 MHz of desired signal frequency	-84	-36	-38	-45	+10	-	-	-	-
For limit value at circuit point 4 for interfering frequencies between 2182 and 2322 MHz	-78	-30	-32	-39	-	-	-	-	-

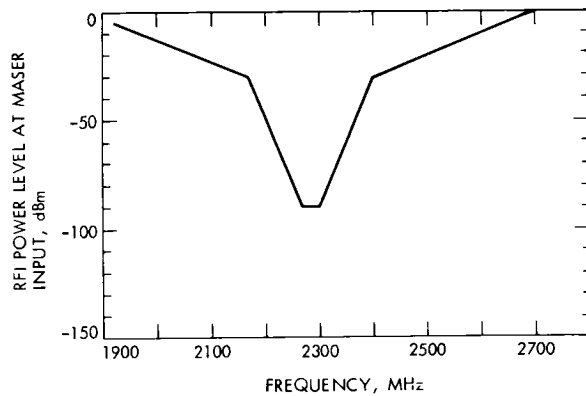
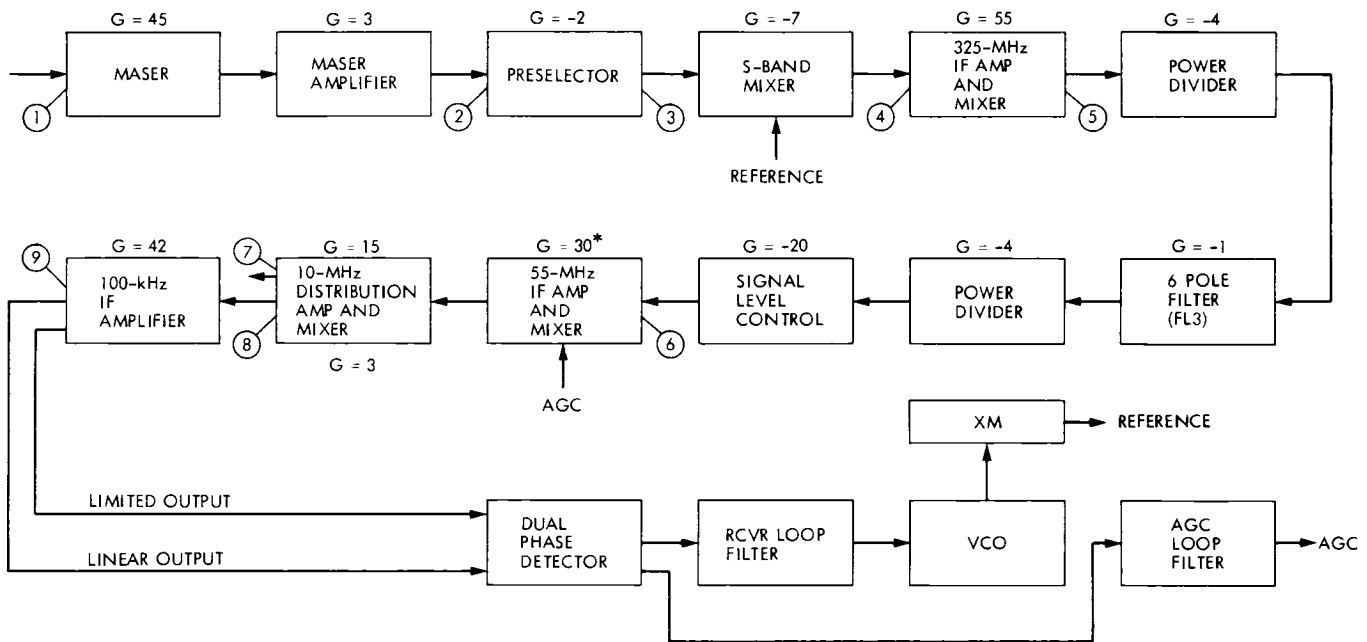


Fig 1 Maximum allowable CW RFI power to prevent S-band maser saturation (1 dB or less gain compression)



* FOR -165 dBm DESIRED SIGNAL INTO MASER

Fig 2 Simplified Block IV receiver block diagram, S-band

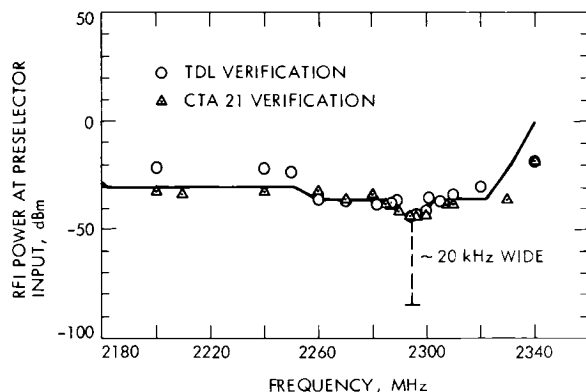


Fig 3 Maximum CW RFI power into Block IV receiver (only) for 1 dB or less gain compression (receiver locked to S-band channel 14)

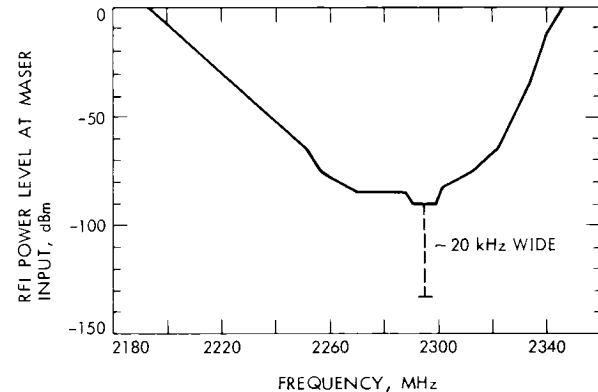


Fig 4 Maximum allowable CW RFI power into maser to prevent saturation of Block IV receiver (only) operating at S-Band channel 14

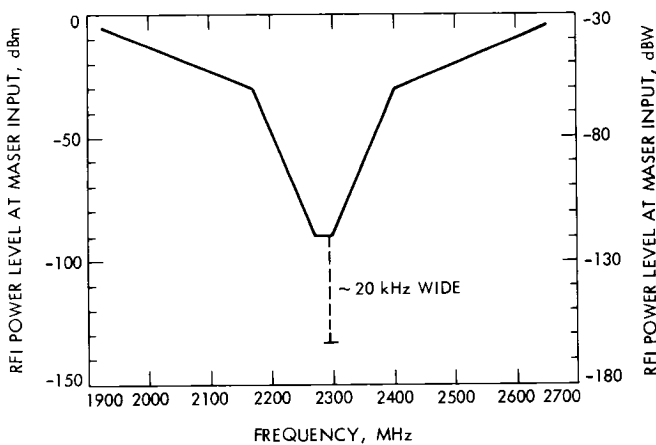


Fig 5 Maximum allowable CW RFI power into S-band maser for 1 dB or less gain compression of maser or Block IV receiver operating at channel 14

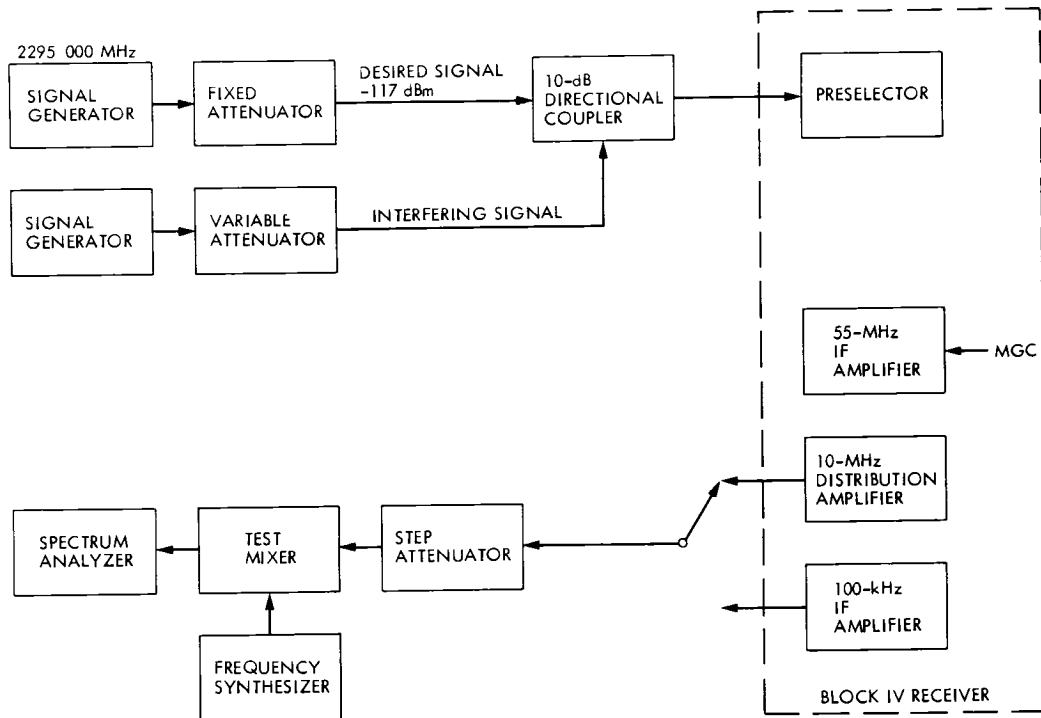


Fig 6 Test configuration for Block IV receiver S-band saturation test

Appendix A

Equations for Maximum Allowable CW Interference Power

The equations for each segment of the graph shown in Fig 5 are given below. In the following equations, P is the maximum allowable RFI power at the maser input in dBm, and f is the frequency of the RFI. The region of carrier tracking loop degradation is approximately 20 kHz wide with lower and upper frequency bounds of f_1 and f_2 , respectively. It follows then that f_1 is $f_c - 10$ kHz and f_2 is $f_c + 10$ kHz. If it is desired to use these equations to protect the entire DSN receive band (2290-2300 MHz), set f_1 and f_2 to 2290 and 2300 MHz, respectively.

$$P = \text{TBD} \text{ for } f_1 \leq f \leq f_2 \text{ (tracking degradation region)}$$

$$P = -90 \text{ for } 2270 \leq f < f_1 \text{ or } f_2 \leq f < 2300$$

$$P = -90 + 0.6(2270-f) \text{ for } 2170 < f \leq 2270$$

$$P = -90 + 0.6(f-2300) \text{ for } 2300 \leq f \leq 2400$$

$$P = -30 + 0.1(2170-f) \text{ for } 1870 \leq f \leq 2170$$

$$P = -30 + 0.1(f-2400) \text{ for } 2400 \leq f < 2700$$

$$P = 0 \quad \text{for } f < 1870 \text{ or } f \geq 2700$$

Appendix B

Model Assumptions

Gain Values to Circuit Points

Circuit point	From preselector input, dB	From maser input, dB
2	—	48
3	-2	46
4	-9	39
5	46	94
6	17	65
7	62	110
8	50	98
9	92	140

Conditions

- (1) Signal level control set to obtain 17 dB gain from circuit point 2 to circuit point 6
- (2) Gain of 55-MHz IF amplifier = 30 dB

Assembly Bandwidths*

Maser 30 MHz
 Preselector 140 MHz
 325-MHz IF amplifier 72 MHz (-3 dB bandwidth)
 FL3 30 MHz
 55-MHz IF amplifier 8 MHz
 10-MHz IF amplifier
 telemetry port (J6) 8 MHz
 100-kHz output (J2) 20 kHz (noise bandwidth)

*All bandwidths are -1 dB bandwidths unless specified otherwise. Roll-off asymptote slopes are available from authors.

General Sensitivity Analysis of Solar Thermal-Electric Plants

F L Lansing, E W Hayes, and C S Yung
DSN Engineering Section

Performance optimization of solar thermal-electric power systems depends on a number of major parameters, each affecting the specific power output and the overall conversion efficiency differently in magnitude and direction. This first-phase study presents analytically a unified and generalized treatment in predicting the technical performance of many present or future system designs and configurations. In an effort to screen the major design parameters whose effect on performance is high and to assess the system improvement or deficiency resulting from their change, the sensitivity analysis is performed. The sensitivity, defined as the percentage change of output divided by the percentage change in input, is evaluated analytically for seven major system design parameters. These design parameters are the solar radiation intensity, the ambient temperature, the optical-thermal characteristics of the collector subsystem (concentrator-receiver), the relative thermal efficiency for the energy conversion subsystem, the working fluid operating temperature, and the rate of fluid heat capacity. General performance sensitivity expressions are derived and numerically evaluated for the range of possible operating conditions. Furthermore, the effect of these major parameters on the system performance optimization is presented to identify future improvement areas and to pave the way for the second-phase study in the economic sensitivity analysis on bus bar energy costs.

I. Introduction

To satisfy the NASA goals of facilities energy conservation and the nationwide energy self-independence program, the Deep Space Network (DSN) is studying, among others, the concept of installing a 1-10 MW(e) solar thermal-electric power plant at one of its three deep space communications complexes.

Of major concern in the design of such a solar-powered plant is the need for insolation data, load profiles, weather data and the specification of some minimum, average or peak

values for the major design parameters. These design parameters, and environment data, will have errors either small or large when first estimated or measured. Moreover, it is expected that the actual operation of the power plant will be fluctuating and intermittent with interruptions depending on solar energy fluctuations, load variations, storage capacities, and its automatic control strategy, and, therefore, the actual plant operation will be different from what is designed. The deviation or discrepancy between design and actual operation could result in either serious or negligible effects (depending on the design parameter) on the overall plant performance. The serious effects will affect the estimated cost of the electrical energy produced at the bus bar.

An interesting attempt to investigate the sensitivity of solar thermal-electric output to the dynamics of the solar radiation was presented in Refs 1 and 2. In this dynamic model, sinusoids of different wavelength and frequency are imposed to simulate the solar transients on two different types of energy collection subsystems – a slow response and a fast response type, coupled with a reversible power conversion cycle. The results of Refs 1 and 2 are later discussed and verified in this work. However, since they are focused only on the variations of solar intensities, more work is felt needed to evaluate the sensitivity to other major design parameters.

This article presents, in a generalized way, the first part of the study which is to assess the consequences of the errors or design differences on the technical performance of the whole system. The objectives are to give an indication of the levels of tolerance which are acceptable, to shed some light onto the weight of each design parameter, and to seek ways to optimize the performance.

Some parts of the present study are described in simple and unsophisticated fashion in order to be transmitted to a wide range of reader backgrounds including those with limited experience in solar energy. Numerous papers in the literature have addressed in more detail the performance of various subsystems or components of many possible solar-plant configurations. The present study is not intended to review the technical performance of the individual component but, rather, cover the whole system behavior to enable the sensitivity analysis to be made.

One of the most important parameters that needs to be considered in the sensitivity analysis is the bus bar energy cost. This cost, besides its dependence on average annual performance and the total electrical energy produced over the lifetime of the plant, depends on the life cycle costs, including the installation costs, inflation rates, interest rates, taxes, depreciation, maintenance costs, etc., which require continuous updating from existing solar plants.

Although the present first-phase study gives the consequences of only the design parameters of differences on performance, the methodology followed can and will be extended in the future to cover the economic parameters as well as the design parameters. The temporary elimination of the bus bar energy cost from the technical analysis is assumed in this study not to cause a change of the point at which the overall system economics are optimum.

II. General Analysis

All conceivable present and future solar thermal power plants could be treated as a combination of the following

subsystems (1) an energy collection subsystem including the reflecting and absorbing surfaces, concentrators, and receivers through which the sun's light energy is converted into thermal energy as a sensible or latent heat carried away by a working fluid, (2) an energy conversion subsystem which is following an advanced power cycle including heat exchangers for heat addition, rejection, and regeneration, (3) an energy storage subsystem which matches the supply (solar energy) with the demand (electrical connected loads), and (4) an energy transmission subsystem to transmit the energy (in either thermal, chemical, or electrical form) from one subsystem to another.

The present sensitivity study is performed with the above solar system under consideration treated as a sequence of steady rate processes in subsystems held at a steady or quasi-steady state, i.e., no transient dynamics or intermittent operation is allowed. To illustrate this condition further, consider as in Fig 1 a solar thermal-electric power plant which is supplying an electrical load only at night time through an energy storage subsystem. The storage subsystem is charged in the sunny hours and is discharged at night. If the instantaneous plant efficiency is defined as the ratio between the electrical-connected loads and the incident solar energy, then the efficiency sensitivity to diurnal solar flux variations will be zero in the sunny period and infinity during the night period. The study, therefore, will have no value if intermittent or transient conditions prevail, since the term "efficiency" becomes meaningless. Therefore, we will proceed only under the conditions of steady or "quasi"-steady state. The treatment of storage systems and transient dynamics requires integrating or time-averaging techniques which require more information about the solar load profiles.

The installation cost of a solar-electric power plant and the bus bar unit energy cost are greatly influenced by the overall conversion efficiency. When the energy conversion is done via thermal power cycles, the overall efficiency becomes the product of collection efficiency, power cycle thermal efficiency, energy through storage efficiency, and energy transmission efficiencies.

The efficiency trends pertain to all collectors, and power cycles could, in general, be formulated as follows. The collection efficiency always decreases with increasing fluid operating temperature due to higher thermal losses and could reach zero when the incident solar radiation equals these losses. The power cycle efficiency, on the other hand, increases monotonically with the operating temperature and starts from zero at ambient temperature, as shown in Fig 2. The overall conversion efficiency will be zero at both ends I and II of Fig 2, and always possesses a maximum value in between them. For a good design, the optimum operating

temperature T_c^* corresponding to the maximum overall conversion efficiency, η_0^* , should be the system design point. Although a minimization of the bus bar energy cost may or may not require the operation at the peak plant efficiency, we will assume, for the present discussion, that the peak conversion efficiency is the desired goal.

The performance of solar collectors is generally the same whether they are focusing or nonfocusing types. The instantaneous efficiency of the collection subsystem could be, in general, approximated by a linear form similar to the Bliss, Whillier, and Hottel form

$$\eta_c = A - B(T_c - T_a)/I \quad (1)$$

where A and B are characteristic constants which depend on the material optical properties, collector geometry, heat losses, and fluid flow characteristics, T_c is the inlet fluid temperature, T_a is the ambient temperature, and I is the total solar flux. This linear form can be used as a piecewise approximation in the range of interest in the performance of high concentration collectors operating at high temperatures. For these cases, the efficiency trends are concave bending downward due to the effect of IR radiation losses, which are proportional to temperatures to the power 4. By proper choice of the constants A and B , the linear expression could provide a good approximation over the working range.

From an energy balance viewpoint, the collection efficiency, η_c , can also be expressed equivalently as

$$\eta_c = G_f C_f (T_H - T_c)/I \quad (2)$$

where G_f and C_f are the fluid mass flux and specific heat, respectively, and T_H is the exit fluid temperature. Equation (1) contains two collector-specific constants which are derived using the physical and optical properties through either theoretical analyses or by experiment. The exit fluid temperature, T_H , is completely omitted from Eq (1), but could be obtained from Eq (2). The constant A is proportional to the product of optical transmissivity or reflectivity and receiver absorptivity. The second term in Eq (1) represents approximately how much heat is lost to the atmosphere, and the difference represents the net solar energy fraction collected by the transfer fluid. The collector efficiency, therefore, can be negative or positive depending on the fluid temperature at the collector entrance. Equation (1) is selected for the present general sensitivity analysis because the variables it contains are independent of each other and, in general, is a simple representation of many conceivable collectors (Refs 3-14).

The second step is to determine an efficiency expression for the energy conversion subsystem. To treat the problem, also in a general way, let us assume that the power cycle under consideration performs as a percentage of the efficiency of a reversible Carnot cycle operating between the hot finite heat reservoir (fluid) and the cold infinite heat reservoir (ambient).

Using the laws of available and unavailable work in thermodynamics when working between these two heat reservoirs, the reversible work obtainable can be written for a constant specific heat fluid as

$$W_{rev} = G_f C_f (T_H - T_c) - G_f C_f T_a \ln (T_H/T_c)$$

The expression for the reversible cycle efficiency becomes

$$\eta_e = 1 - \frac{T_a \ln (T_H/T_c)}{(T_H - T_c)} \quad (3)$$

The efficiency in Eq (3) is more adequate than the Carnot's expression for two infinite heat reservoirs ($1 - T_a/T_H$), besides that, it is applicable to any thermodynamic cycle operating between the above temperature limits (T_c , T_H , and T_a).

The third step in the general analysis is to develop an expression for the overall solar-electric efficiency to be entirely made of independent system variables. The fraction λ , the efficiency ratio of a real power cycle as compared with a reversible one, is a design characteristic of the energy conversion subsystem. For simplicity, the fraction λ could be assumed to embody the energy storage and transmission efficiencies as well. The outlet temperature of the collector fluid, as required in solving Eq (3), could be expressed in terms of independent variables by setting Eqs (1) and (2) equal when assuming negligible temperature drop in the energy transmission lines. Hence,

$$T_H = T_c + \left[A - B \left(\frac{T_c - T_a}{I} \right) \right] \frac{I}{G_f C_f} \quad (4)$$

The final expression for the system overall efficiency (η_0) is the product of collection and conversion efficiencies, which is written as

$$\eta_0 = \eta_c \eta_e \lambda \quad (5)$$

The expressions in Eqs (1) through (5) simplify the performance of all solar thermal-electric power plants and lead to the general sensitivity analysis presented next.

III. Sensitivity Relations

The sensitivity concept is beneficial to the designer in allowing to sense in both magnitude and direction the effect of small or large deviations occurring in the various design parameters on the performance of the solar power plant. The sensitivity is the measure of the dependency of system characteristics on variations occurring in a particular element or parameter, as shown in Fig. 3. The sensitivity(s) is expressed analytically as

$$S = \left(\frac{\Delta Y/Y}{\Delta X/X} \right)_r$$

or

$$S = \left(\frac{dY}{dX} \cdot \frac{X}{Y} \right)_r \quad (6)$$

or

$$S = \left(\frac{d \ln Y}{d \ln X} \right)_r$$

where X is an arbitrary input element, Y is the system output, Δ represents a differential change in either X or Y , and the subscript (r) denotes conditions at a reference point. Equation (6) states that the differential sensitivity of Y with respect to X is the percentage change in Y divided by that percentage change in X which caused the change in Y to occur, keeping all other input elements unchanged. The definition is suitable only for small changes. Any system operating at an optimum value of one of its elements should have zero sensitivity with respect to this element.

The concept of sensitivity has been widely used in studying automatic controls, electric circuits, and many physical systems, and its present application to solar power plants represents a useful tool in the performance optimization.

In solar power plants, the input element X could be any one of the following

- (1) Inlet fluid temperature to the energy collection subsystem (T_c)
- (2) Collector optical characteristic constant, A
- (3) Collector thermal characteristic constant, B
- (4) Ambient temperature, T_a
- (5) Incident solar flux, I
- (6) Heat capacity of collector fluid, $G_f C_f$
- (7) Relative efficiency of energy conversion and transmission subsystems, λ

Note that the exit fluid temperature T_H could be expressed in terms of the other independent parameters in Eq. (4)

The system output, Y , on the other hand, could be (1) the overall solar-electric conversion efficiency, η_0 , (2) the net electrical (or mechanical) work output per unit collector W , where

$$W = \eta_0 I \quad (7)$$

or (3) the unit energy cost at the bus bar. Only the first two output variables are selected in this study. The sensitivity of the overall conversion efficiency to any input parameter X is denoted by S_x and that of the net electrical (or mechanical) work output to the input parameter X by \bar{S}_x . It can be easily proven from Eqs. (5), (6), and (7) that at a reference state (r),

$$S_x = \left[\frac{X}{\eta_0} \left(\frac{\partial \eta_0}{\partial X} \right) \right]_r, \quad (8)$$

or

$$S_x = \left[\frac{X}{\eta_c} \left(\frac{\partial \eta_c}{\partial X} \right) + \frac{X}{\eta_e} \left(\frac{\partial \eta_e}{\partial X} \right) + \frac{X}{\lambda} \left(\frac{\partial \lambda}{\partial X} \right) \right]_r,$$

and

$$\bar{S}_x = \left[\frac{X}{W} \left(\frac{\partial W}{\partial X} \right) \right]_r, \quad (9a)$$

and using Eqs. (7) and (8),

$$\bar{S}_x = S_x + \left[\frac{X}{I} \left(\frac{\partial I}{\partial X} \right) \right]_r, \quad (9b)$$

Also, it can be seen that if the overall efficiency (η_0) is written as $\eta_0(X_1, X_2, \dots)$, then

$$\left(\frac{\Delta \eta_0}{\eta_0} \right) = S_{X_1} \left(\frac{\Delta X_1}{X_1} \right) + S_{X_2} \left(\frac{\Delta X_2}{X_2} \right) + \dots \quad (10)$$

where X_1, X_2 are input parameters. Equation (10) is very important in determining the total effect of all input parameters of the system when each varies in magnitude and direction differently throughout the operating time.

The sensitivity expressions for each parameter have been derived following Eqs. (8) and (9) and simplified by algebraic manipulations of Eqs. (1) through (4). The results are discussed next.

IV. Results of Parameter Variations

All parameters used in the sensitivity analysis are given in standard international (SI) units. The values and ranges for each parameter were chosen from the practice gained in operating 12 different collector types (Refs 3-14). Each solar collector has, as an approximate representation, two identifying design parameters, namely, A and B , as shown in Fig 4. For low concentration collectors, with a concentration ratio of 1.5, the B values range from 0.0030 to 0.0060 kW/m²°C and the A values range from 0.4 to 0.8; for high concentration collectors, with a concentration ratio above 100, ¹ the value of A ranges from 0.6 to 0.9 and B ranges from 0.0001 to 0.0010 kW/m²°C (Ref 12). The fluid heat capacity ($G_f C_f$) may range from 0.01 to 0.05 kW/m²°C depending on the required temperature rise and the trade-off between pumping power and system efficiency. A nominal flow heat flux of 0.04 kW/m²°C is selected as a reference point only for the next discussion. As a reference weather, the ambient temperature is taken as 25°C (77°F), and the nominal solar flux is taken as 1 kW/m² (1 sun).

The relative efficiency of the energy conversion-transmission subsystem compared to the reversible path usually ranges from 40 to 60 percent and a value of 50 percent was chosen arbitrarily in the reference operating conditions.

A. Sensitivity to Inlet Fluid Temperature

The sensitivity of the overall efficiency to changes in the collector's inlet fluid temperature can be derived from Eqs (8) and (9). After performing the differentiation, the sensitivity expression is reduced to

$$\bar{S}_{T_c} = S_{T_c} = \frac{T_a(AI + BT_a) - B T_c T_H}{\eta_e \eta_c I T_H} \quad (11)$$

The sensitivity S_{T_c} could be negative, zero or positive, depending on whether the inlet fluid temperature T_c is smaller than, equal to, or larger than the optimum temperature T_c^* , respectively. The optimum inlet fluid temperature, T_c^* , is the temperature at which the overall efficiency is a maximum, or at which the sensitivity S_{T_c} is zero. In the special case where the flow rate is such that the temperature difference across the collector (between inlet and exit fluid temperatures) is small, i.e., $T_c \sim T_H$, then the optimum fluid temperature T_c^* can be given from Eq (11) approximately as

$$T_c^* \approx \sqrt{T_a^2 + \frac{AIT_a}{B}} \quad (12a)$$

¹Concentration ratio of parabolic dishes could range from 1500 to 2000

Accordingly, the reversible cycle efficiency in Eq (3) becomes

$$\eta_e^* \cong 1 - \frac{T_a}{T_c^*} \quad (12b)$$

In general, a more accurate, but somewhat complex, expression for T_c^* could be derived from Eq (11) by substituting the exit fluid temperature, T_H , using Eq (4). By solving the final quadratic equation, the expression for T_c^* in terms of the independent input parameters A , B , I , T_a and $G_f C_f$ becomes

$$T_c^* = \frac{(AI + BT_a)}{2(G_f C_f - B)} \left\{ \sqrt{1 + \frac{4 G_f C_f T_a (G_f C_f - B)}{B (AI + BT_a)}} - 1 \right\} \quad (13)$$

It is interesting to know that Eq (13) is independent of λ . The difference between the approximate expression of T_c^* in Eq (12a) and the accurate one in Eq (13) could be assessed by the following example. Suppose that the characteristic constants A and B for a given collector are 0.8 and 0.0057 kW/m²°C, respectively, and that the fluid heat capacity $G_f C_f$ is 0.04 kW/m²°C. With an ambient temperature of 25°C (298.15 K) and a solar intensity of 1 kW/m², the optimum temperature T_c^* from Eq (12a) is 88.43°C (371.58 K) and that from Eq (13) is 82.58°C (355.73 K), which shows their small difference. At the optimum inlet fluid temperature of 82.58°C, the optimum collector and reversible cycle efficiencies become 47.18 and 17.55 percent, respectively. Accordingly, if a real engine with a 50 percent relative efficiency is used, the maximum overall conversion efficiency for the system will be 4.14 percent, which is typical of high performance flat-plate collectors.

Hereafter, the above optimum inlet fluid temperature T_c^* , as determined from Eq (13), which is assumed as the design point, will be adopted in our analysis as a fixed reference state at which the performance sensitivity is evaluated. This condition was imposed since solar-power plants should operate at their "best" conditions, and deviations from this optimum performance are what the sensitivity analysis is, in the first place, seeking to evaluate. Operation at any inlet fluid temperature other than T_c^* (either higher or lower) will always result in lower overall efficiency. In the above numerical example, for instance, if the operating inlet fluid temperature is lower than the optimum 82.58°C, by 10°C, say, the sensitivity S_{T_c} becomes 1.2972 and the overall efficiency becomes 4.06 percent. Therefore, operating at temperatures other than the optimum T_c^* will change the sensitivity S_{T_c} , as determined from Eq (11), to be either positive or negative depending on whether $T_c < T_c^*$ or $T_c > T_c^*$, respectively. The maximum positive value of S_{T_c} occurs when the reversible cycle efficiency approaches zero, that is, when the temperatures T_c and T_H are close to the ambient T_a (see Fig 2), thus

making S_{T_c} approaching infinity On the other hand, the minimum value of S_{T_c} will be $-\infty$ when the temperature T_c theoretically reaches its limiting value \bar{T}_c . The latter is given from Eq (1) by equating the collector efficiency to zero

$$\bar{T}_c = T_a + \frac{AI}{B} \quad (14a)$$

Using the approximation made in Eq (12a), then

$$\bar{T}_c \cong T_c^* / T_a \quad (14b)$$

Figure 5 shows the variation of the optimum fluid temperature (T_c^*) with the major collector parameters A and B . It varies from about 50°C (122°F) for low performance flat-plate collectors to around 1400°C (2550°F) for high performance concentrators at the given ambient conditions. The optimum temperature is highly sensitive to the heat loss parameter B when B is small (e.g., for high performance collectors), but with less sensitivity as B tends to be larger (e.g., for low performance collectors).

Another interesting result could be reached for the relationship between η_c^* and η_e^* at the optimum fluid temperature T_c^* at large fluid flow rates. The approximate expressions given by Eqs (12) would yield

$$\eta_c^* \cong \left(A + \frac{BT_a}{I} \right) \eta_e^* \quad (15)$$

which means that the maximum overall conversion efficiency will only occur at the intersection point between the collector and reversible engine efficiency curves provided that the quantity $(A + (BT_a/I))$ is approximately unity. The location of the optimum temperature will be lower than the intersection temperature or higher depending on whether the value of $(A + (BT_a/I))$ is larger or smaller than 1, respectively.

The optimum fluid temperature, as shown in Fig 5, depends on the slope, B , and intersect, A , of the collector efficiency line. Smaller slopes and larger intersections achieve higher overall conversion efficiency and higher optimum temperatures. This explains why high concentration focusing collectors are offering a superior performance compared to low performance non-focusing types.

In the limit, as the parameter A approaches unity and B approaches zero, hypothetically, the optimum temperature T_c^* approaches infinity, the collector efficiency approaches unity, and the overall conversion efficiency approaches the relative efficiency λ as a limiting factor that will never be reached, otherwise, it violates the thermodynamics laws.

B. Sensitivity to the Collector Characteristic Intercept A

Similar procedures can be followed, and it can be shown from Eqs (8) and (9) that for the parameter A , the overall efficiency sensitivity S_A is

$$S_A = \bar{S}_A = \frac{A}{\eta_c \eta_e} \left(\frac{T_H - T_a}{T_H} \right) \quad (16)$$

Equation (16) also shows that the sensitivity S_A is independent of the relative engine efficiency (λ), and it is always a positive quantity. From thermodynamics principles, it can be proven that the reversible cycle efficiency η_e given by Eq (3) for a high temperature finite source (varying between T_c and T_H) is always less than the Carnot's expression with the high temperature infinite source (T_H) when both are working with the low temperature infinite sink (T_a). In other words, the quantity $(T_H - T_a)/T_H \eta_e$ is always greater than one. Since the quantity A/η_c is always greater than unity, as evidenced from Eq (1), the final result is that S_A is always larger than unity at all operating conditions and for any collector type. This gives the collector optical performance a major role in determining the plant overall efficiency. Figure 6 gives a plot of the sensitivity S_A for various collector types. The sensitivity S_A decreases as A increases and/or as B decreases. In the practical region of collector constants where A varies between a minimum of 0.4 to 0.85 maximum, and B varies between, say, a minimum of 0.0001 to 0.0060 kW/m²°C maximum, the sensitivity S_A varies between 1.2 for high performance collectors to 1.9 for low-performance types. In the hypothetical case, where $A \rightarrow 1$ and $B \rightarrow 0$, the sensitivity S_A approaches 1.

C. Sensitivity to the Collector Characteristic Slope B

The overall efficiency sensitivity S_B can be written using Eqs (8) and (9) as

$$S_B = \bar{S}_B = \frac{-B(T_c - T_a)(T_H - T_a)}{\eta_c I \cdot \eta_e T_H} \quad (17)$$

Equation (17) shows clearly that S_B is always a negative quantity independent of the power conversion system parameter λ . The negative sign is expected and in agreement with the intuition that the larger the slope of a solar collector, the larger the thermal losses and the lower the overall efficiency will be. No decisive conclusion can be made about whether S_B is larger than one or smaller than one, although the quantity $(T_H - T_a)/T_H \eta_e$ is always larger than one as discussed before,

but the quantity $B(T_c - T_a)/\eta_c$ can be either less than or larger than one from Eq (1) However, the sum (which may have no physical interpretation) of S_A and S_B from Eqs (16) and (17) is found to be always positive and greater than one

$$S_A + S_B = \bar{S}_A + \bar{S}_B = \frac{T_H - T_a}{\eta_e T_H} \quad (18)$$

In practice, the quantity $((T_H - T_a)/\eta_e T_H)$ is slightly larger than unity and the sensitivity S_B could be approximated as $(1 - S_A)$

As a numerical example for the relative magnitudes of S_A and S_B , take the collector constants A and B as 0.8 and 0.0057 kW/m²°C, respectively, a fluid heat capacity $G_f C_f$ of 0.04 kW/m²°C, and an optimum inlet fluid temperature of 82.58°C (355.73 K) as given before The exit fluid temperature T_H^* (from Eq (4)) will be 94.37°C (367.52 K), the optimum collector and reversible cycle efficiencies become 47.18 and 17.55 percent, respectively, and the sensitivities S_A and S_B are calculated as 1.824 and -0.748 The above shows how the effects of A and B can be quite significant on the overall efficiency, and the designer should always be seeking higher values for A and smaller values for B to improve the performance

In Fig 7, a plot is made for the sensitivity S_B at different values of A and B The absolute value of sensitivity S_B becomes smaller as A increases or B decreases The limits of S_B for current collectors range from -0.2 (for high performance types) to -0.8 (for low performance types)

D. Sensitivity to Ambient Temperature Variations

The overall efficiency sensitivity, S_{T_a} , to the ambient temperature variations can be derived from Eqs (8) and (9) using Eqs (1), (3), (4), (11), and (16) as follows

$$S_{T_a} = \bar{S}_{T_a} = 1 - S_a - S_{T_c} \quad (19)$$

or at the optimum temperature T_c^* ,

$$S_{T_a}^* = \bar{S}_{T_a}^* = 1 - S_a^*$$

Once more, the sensitivity S_{T_a} is independent of the engine parameter λ To determine the relative magnitude of S_{T_a} , the numerical values assigned in the last example would yield S_{T_a} equal to -0.824 The negative sign indicates that lowering the ambient temperature will yield an increase in the overall conversion efficiency in spite of the resulting decrease in the

collector's efficiency Figure 8 shows a plot of the sensitivity S_{T_a} at different values of A and B Numerically, the sensitivities S_{T_a} , $(1 - S_a)$ and S_b are found to be of the same order when Figs 7 and 8 are compared Different reference ambient temperatures were found to cause minor changes in S_{T_a} as shown in Fig 8

E. Sensitivity to Solar Radiation Intensity

Using Eq (8), the overall efficiency sensitivity to the solar radiation, I , can be written after some reductions as

$$S_I = \frac{A (T_H - T_a)}{\eta_c \eta_e T_H} - 1 \quad (20)$$

It has been shown in Eq (16) that the quantity $[A(T_H - T_a)/\eta_c \eta_e T_H]$ is always greater than unity, therefore, S_I is always a positive quantity and, in most cases, is less than unity From Eqs (16) and (20),

$$S_I = S_A - 1 \quad (21)$$

At this point, it is advantageous to determine the sensitivity (\bar{S}_I) for the net mechanical (or electrical) work generated subject to solar intensity variations The net work output per unit collector area and the sensitivity, \bar{S}_I , can be written using Eqs (7) and (9) as

$$\bar{S}_I = S_I + 1 = S_A \quad (22)$$

\bar{S}_I is always a positive quantity larger than unity For instance, in the last numerical example, a 1 percent increase in the solar intensity will cause an increase in the mechanical work output by 1.824 percent and an increase in the overall conversion efficiency by 0.824 percent Note that for parameters other than solar flux, I , the overall efficiency sensitivity, S , is identical to the net work sensitivity, \bar{S}

Figure 9 is a plot of the sensitivity S_I at different values of A and B Two reference values for I were tried (1 kW/m² and 0.5 kW/m²), and the results show that the larger the solar flux variation, the larger the sensitivity S_I and \bar{S}_I will be However, larger values of A and smaller values of B tend to reduce the sensitivity S_I

The results obtained from the above steady state analysis are in agreement with the results obtained in Refs 1 and 2, using a dynamic radiation model composed of sinusoids Values of \bar{S}_I between 1.62 and 1.9 at one sun (1 kW/m² peak) were obtained in Ref 1 for the fast-response NASA-Honeywell collector ($A = 0.713$, $B = 0.0029$ kW/m²°C to 0.0036

$\text{kW/m}^2\text{C}$, Ref 7) and \bar{S}_I between 1.61 and 1.70 for the slow response Owens-Illinois collector ($A = 0.45$ and $B = 0.0014 \text{ kW/m}^2\text{C}$, Ref 7) A comparison with Fig 9 shows the close behavior of the system response to the solar flux radiation between the present quasi-steady state and the dynamic transient model

F. Sensitivity to the Collector Fluid Heat Capacity

The heat capacity of the collector fluid, $G_f C_f$, is one of the parameters that can alter the exit fluid temperature, which in turn affects the engine's performance. The sensitivity S_G is determined from Eqs (8) and (9) at the reference state as

$$\bar{S}_G = S_G = \frac{G_f C_f}{\eta_c} \frac{\partial \eta_c}{\partial (G_f C_f)} + \frac{G_f C_f}{\eta_e} \frac{\partial \eta_e}{\partial (G_f C_f)} \quad (23)$$

For almost all solar collectors, the constants A and B in the efficiency expression, Eq (1), can be subdivided to be in the form

$$\eta_c = F \left[A' - B' \left(\frac{T_c - T_a}{I} \right) \right] \quad (24)$$

where F is a dimensionless flow factor dependent on the flow characteristics and

$$\begin{aligned} A &= A' F \\ B &= B' F \end{aligned} \quad \left. \right\} \quad (25)$$

Usually, the constants A and B have, at most, a very weak dependence on the flow characteristics. The first term in the right-hand side of Eq (23), namely, $(G_f C_f / \eta_c) (\partial \eta_c / \partial G_f C_f)$ will then be reduced to $G_f C_f / F \cdot \partial F / \partial G_f C_f$. The latter is always positive since increasing the flow rate improves the collector's efficiency in turn. On the other hand, the second term in the right-hand side of Eq (23) can be written using Eqs (3) and (4) as

$$\frac{G_f C_f}{\eta_e} \frac{\partial \eta_e}{\partial G_f C_f} = 1 - \frac{T_H - T_a}{\eta_e T_H} = 1 - (S_A + S_B) \quad (26)$$

which is usually a very small negative quantity as shown by Eq (18). If the variations of the flow factor F with the heat capacity $G_f C_f$ is small, such that it can be neglected, then Eq (26) can be used as a first approximation to the sensitivity S_G in comparison with other sensitivity expressions. In reality, S_G will be somewhat smaller than the approximate form given by

Eq (26) due to the opposing presence of F variations. Figure 10 is a plot of the sensitivity S_G as approximated by Eq (26) at different values of A , B , and reference fluid heat flux $G_f C_f$. The effect of the parameter A is negligible, but the effect of B is quite significant. At the reference value of $G_f C_f$ of 0.04 $\text{kW/m}^2\text{C}$, the sensitivity S_G varies between -0.001 (high performance collectors, $B \approx 0.0001$) to -0.08 (for low performance collectors, $B = 0.0060 \text{ kW/m}^2\text{C}$). Changing the flow heat capacity has caused a proportional change in the sensitivity S_G as shown in Fig 10. Although the sensitivity S_G tails the list of the whole parameters discussed above, it could have a significant degradation effect on the overall performance. In practice, the choice of the operating flow rate is based on a trade-off between the system efficiency and pumping power. Reference 15 gives a practical range of $G_f C_f$ for flat plate collectors to be from $24.4 \text{ kg/h} \cdot \text{m}^2$ ($\sim 5 \text{ lb/h} \cdot \text{ft}^2$) to $97.7 \text{ kg/h} \cdot \text{m}^2$ ($\sim 20 \text{ lb/h} \cdot \text{ft}^2$) with a recommended value of about $48.8 \text{ kg/h} \cdot \text{m}^2$ ($\sim 10 \text{ lb/h} \cdot \text{ft}^2$). These flow values, however, could be used for other solar power plants as a starting point in the design.

G. Sensitivity to the Conversion Relative Efficiency

The engine-transmission parameter λ has a direct one-to-one correspondence effect on the overall plant efficiency and work output. The sensitivity S_λ (or \bar{S}_λ), as deduced from Eq (9), is equal to 1 keeping all other parameters unchanged.

V. Summary

Discrepancies between design data and actual performance are expected to take place in the design and operation of future solar thermal-electric power systems, as in the case of any other system. Seven major design parameters were identified and their weight on performance variations were analyzed and estimated as a first phase of the study excluding the economic factors. The parameters studied were (1) fluid temperature entering the energy collection subsystem, (2) optical characteristics of the energy collection subsystem, (3) thermal loss characteristics of the energy collection subsystem, (4) ambient temperature, (5) incident solar flux, (6) heat capacity of working fluid, and (7) relative efficiency of energy conversion-transmission subsystems. An analytical model for all solar thermal-electric plants was laid out to enable the sensitivity expressions to be derived and evaluated in a general manner. The total effect on the plant performance is summed, as given in Eq (10). The performance sensitivity to the inlet fluid temperature was found changing from $+\infty$ at the ambient temperature to $-\infty$ at the collector's limiting temperature T_c^* , with a zero sensitivity at the optimum fluid temperature T_c^* . The temperature T_c^* is usually taken as the plant design point since it corresponds to the maximum overall conversion efficiency.

Second, the sensitivity S_A to the optical characteristic parameter A was found to always be positive, greater than unity (1.2-1.9), and independent of the relative power cycle efficiency, λ . Third, the sensitivity S_B to the thermal losses parameter (B) was found to always be negative (-0.2 → -0.8) independent of λ and have the same order of magnitude as the sensitivity to ambient temperature (S_{T_a}). Fourth, the sensitivity S_{T_a} was found to always be negative, independent of λ , and, in all present systems, less than one. Fifth, the variations of the solar flux I will result in sensitivities always larger than one (between 1.2-1.9) for the net work output. Finally, the least sensitivity of performance resulted from the fluid heat flux variations. Although increasing the fluid rate in the collection subsystem would improve the heat transfer coefficients and increase the harnessed energy, the negative impact

of reducing the exit temperature from the collection subsystem and the resulting decrease of the power cycle efficiency outweigh the benefit. All of the sensitivity expressions need to be substituted in Eq. (10) to determine the dynamic analysis of the system when it operates at off-design conditions.

This first-phase parameterization study has not only helped in shedding some light onto some major design variables which need to be accurately evaluated and closely adhered to during operation, but the effect of the probabilistic weather changes on performance is also quantified by some limiting values. The results would be most helpful in guiding the preliminary design stages, the future plant specifications, and the second phase of the study indicating the effects on unit energy costs at the bus bar.

Acknowledgment

The authors would like to acknowledge Phillip Moynihan, Manager of the Systems Engineering and Development Task, and Toshio Fujita, Manager of the Advanced Systems Identification Task, and both of the Solar Power System Projects in the Energy Technology and Application office (ET&A), who provided a number of invaluable suggestions in the present study.

References

- 1 Hamilton, C L , "Dynamic Modeling and Sensitivity Analysis of Solar Thermal Energy Conversion Systems," *Deep Space Network Progress Report 42-41*, pp 226-232, Jet Propulsion Laboratory, Pasadena, CA, Oct 1977
- 2 Reid, M S , Hamilton, C L , and Hester, O V , "The Engineering Analysis of Solar Radiation," *International Journal of Policy Analysis and Information Systems*, Vol 2, No 1, pp 187-217, July 1978
- 3 Simon, F , *Solar Collector Performance Evaluation with the NASA-Lewis Solar-Simulator Results for an All-Glass-Evacuated Tubular Selectively-Coated Collector with a Diffuse Reflector*, NASA TMX-71695, NASA-Lewis Research Center, Cleveland, Ohio, April 1, 1975
- 4 Ari Rabl, *Optical and Thermal Properties of Compound Parabolic Concentrators*, Argonne National Lab, Argonne, Illinois, February 1975
- 5 *Performance Study of the Compound Parabolic Concentrator Solar Collector*, report prepared by Environmental Consulting Services, Inc , Boulder, Colorado, for the Argonne National Laboratory, September 1974
- 6 *Corning Tubular Evacuated Collector*, Corning Glass Works, Lighting Products Division, Corning, New York, January 1975
- 7 Simon, F , *Flat-Plate Solar-Collector Performance Evaluation with a Solar Simulator as a Basis for Collector Selection and Performance Prediction*, NASA TMX-71793, NASA-Lewis Research Center, Cleveland, Ohio
- 8 Kleinkauf, W , Kohne, R , Lindner, F , and Simon, M , "A Solar Power Plant in the 10 KWe Range with Focusing Collectors," *International Aerospace Abstracts*, Technical Information Service of AIAA, paper No A76-45995, American Institute of Astronautics and Aeronautics, New York, New York, March 1976
- 9 Ramsey, J W , Sparrow, E M , and Ecker, R R G , "Solar Thermal Electric Power Generation Using a System of Distributed Parabolic Through Collectors," *International Aerospace Abstracts*, Technical Information Service AIAA, paper No A75-47511, American Institute of Astronautics and Aeronautics, New York, New York, August 1975
- 10 *Solar Energy Program Semiannual Review Report*, Sandia Laboratories, Albuquerque, New Mexico, July 1976
- 11 *Northrop Collector*, Northrup Incorporated, Hutchins, Texas, 1975
- 12 Shimada, K , and Swerling, M , *Terrestrial Solar Thermonic Energy Conversion Systems Concept*, Technical Memorandum 33-744, Jet Propulsion Laboratory, Pasadena, CA, November 1975
- 13 Lansing, F L , and Dorman, J , "High Efficiency Solar Concentrator," *Deep Space Network Progress Report 42-35*, pp 99-109, Jet Propulsion Laboratory, Pasadena, CA, October 1976
- 14 Anderson, D E , and Stickley, R A , "A Line Focus Segmented Mirror Concentrator," *Optics in Solar Energy Utilization II, SPIE*, Vol 85, pp 121-127, 1976
- 15 Hewitt H C , and Griggs, E I , "Optimal Mass Flow Rates Through Flat Plate Solar Collector Panels," ASME publication 76-WA/Sol-19, presented at ASME winter annual meeting, New York, N Y , Dec 1976

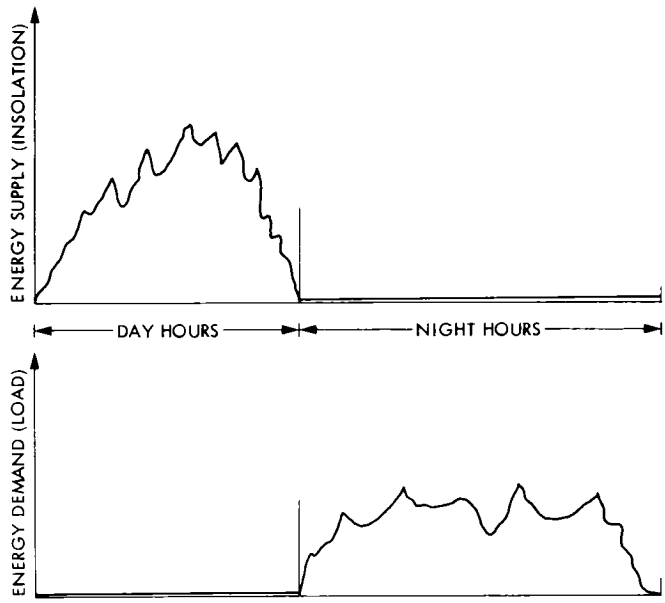


Fig. 1 Insolation and load profile

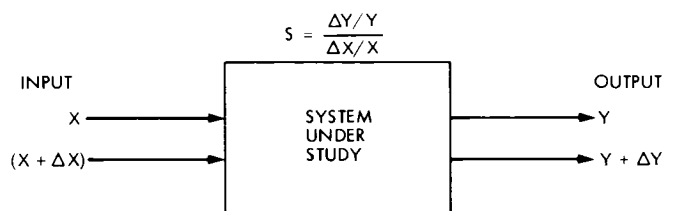


Fig. 3 Sensitivity definition

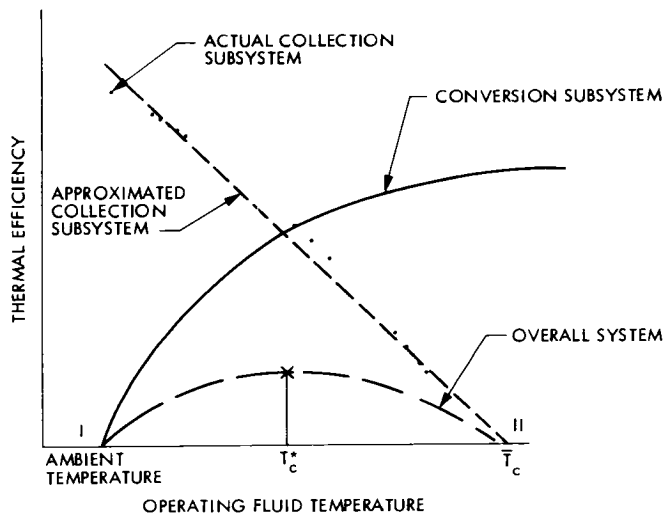


Fig. 2 Efficiency trends for collection and conversion subsystems

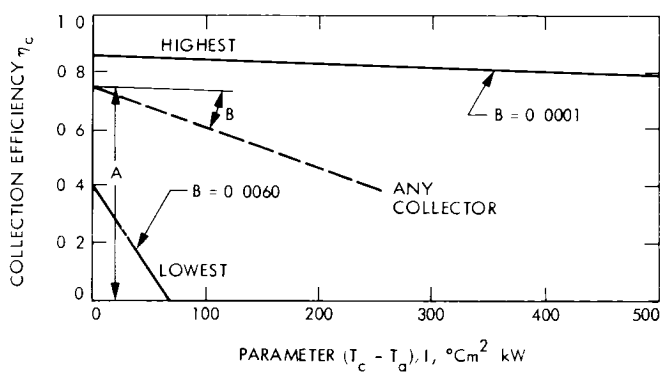


Fig. 4 Lowest and highest performance of current solar collector designs

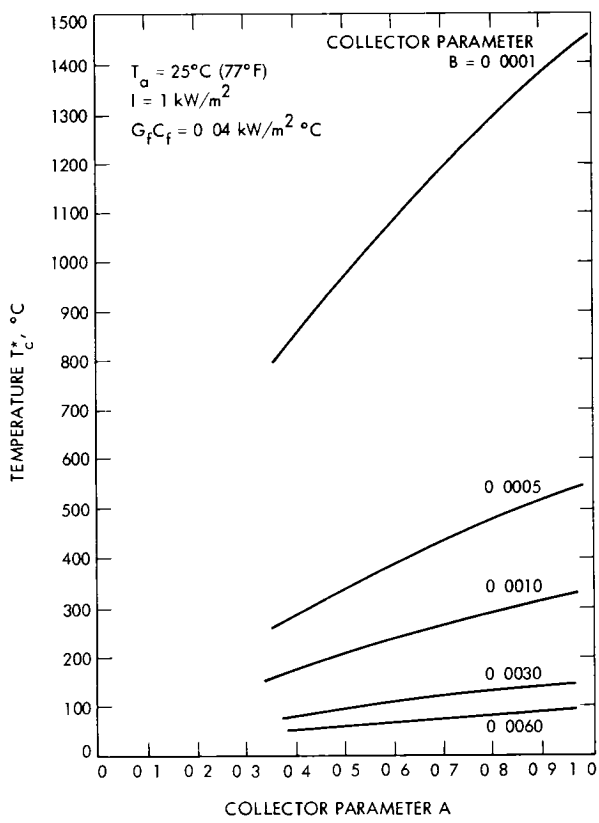


Fig. 5 Optimum inlet fluid temperature to collector for various designs

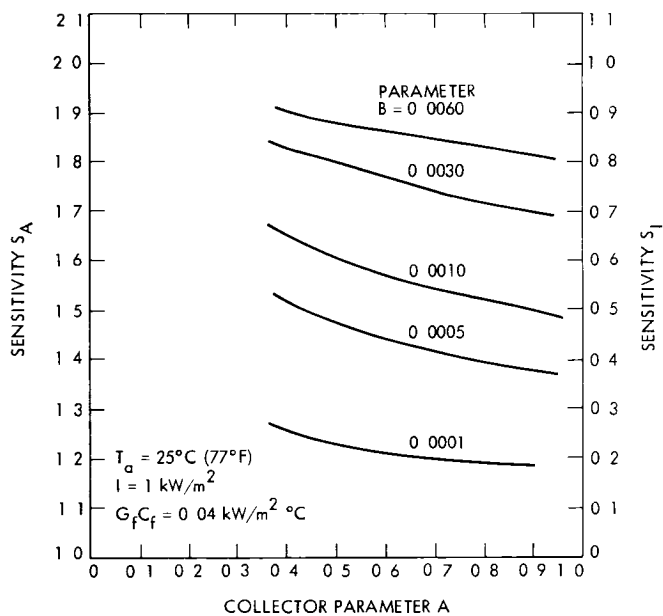


Fig. 6 Efficiency sensitivity S_A at optimum fluid temperature

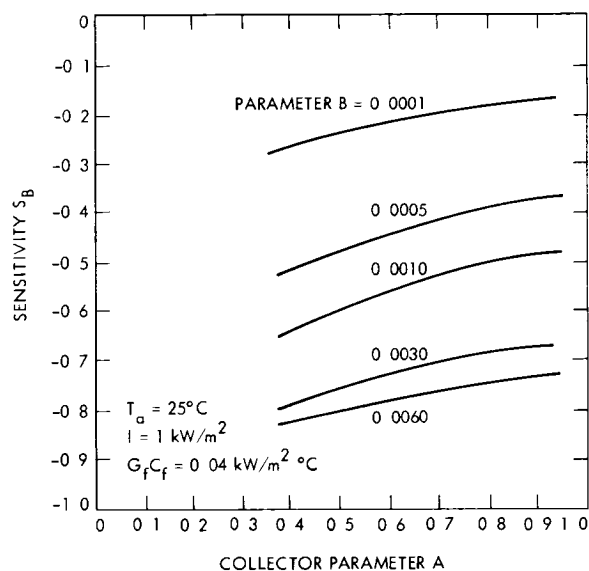


Fig. 7 Sensitivity S_B at optimum design point of various collector designs

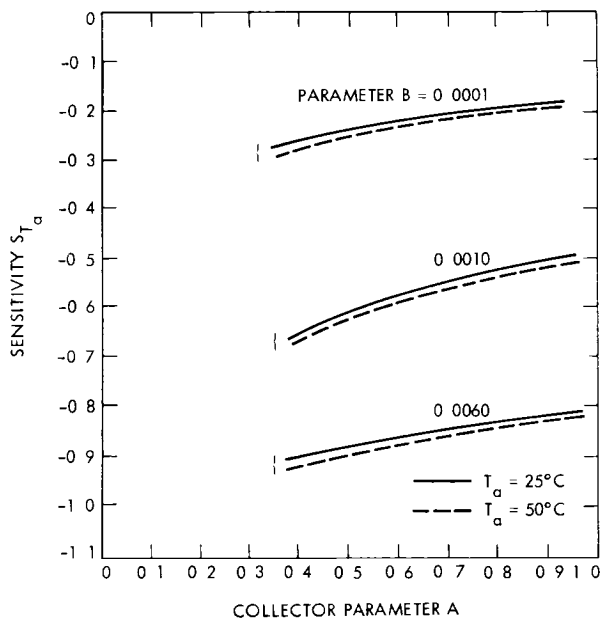


Fig 8 Sensitivity S_{T_a} at different temperature and optimum design point

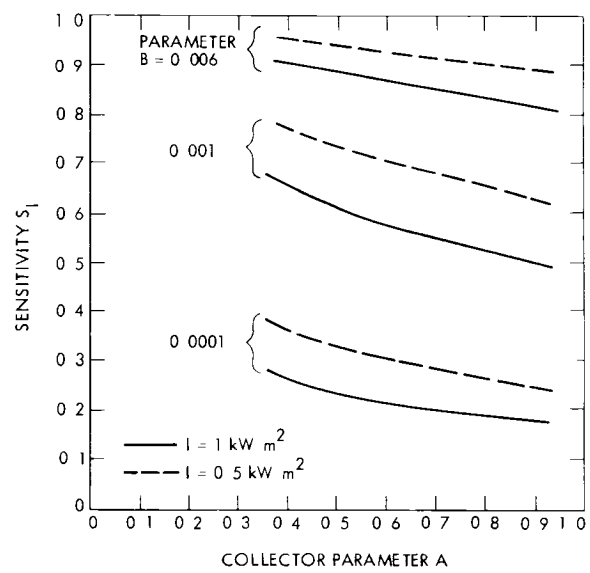


Fig 9 Sensitivity S_I at various solar intensities and for different designs

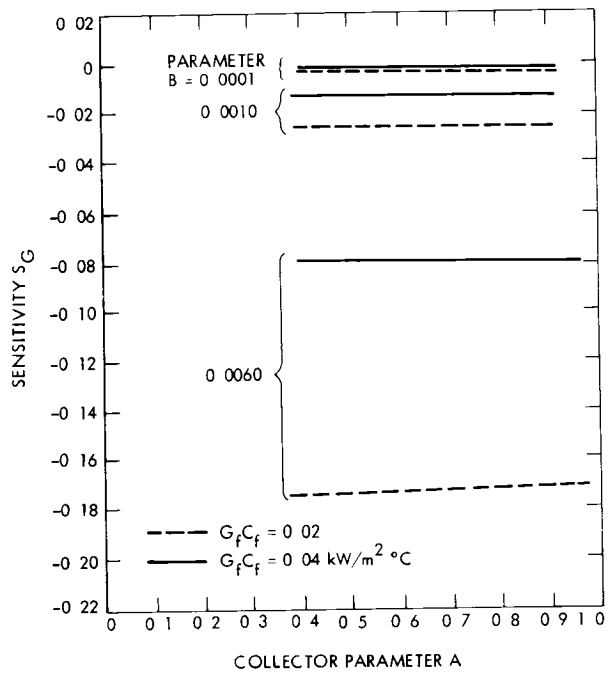


Fig 10 Sensitivity S_G at different fluid heat flux and for different optimum designs

Experimental Investigation of the Effects of Antenna Pointing Errors on Range Delays (Part II)

T Y Otoshi

Radio Frequency and Microwave Subsystems Section

This article presents new S-band test data obtained from an experimental study of the effects of antenna pointing error on range delays. The tests involved the use of the 26-m antenna at DSS 42, the collimation tower, and the Mu-2 Ranging System.

The results showed that when the antenna offset angles from boresight were less than the 3-dB points on the main beam, the worst case range changes were less than ± 7 cm with a measurement precision of about ± 1.5 cm. These results represent an improvement factor of 2 over previously reported results.

I. Introduction

A possible source of error on the measurement of time delays for ranging and VLBI is the change in time delays occurring when the antenna pointing changes from boresight (on target) to an angle offset from boresight. An offset from boresight can occur if the antenna pointing system is inaccurate, or when an error has been made in locating the target boresight position, or when using conical scanning.

An experiment involving a collimation tower and Mu-2 Ranging System was previously performed at DSS 42 (Ref 1). The results indicated that the change in range could be as large as ± 13 cm when the 26-m antenna was purposely pointed off target but the offset angle was within the 3-dB points of the main beam. The error bars associated with that test indicated that some of the changes could be due to residual calibration errors, drift, and noise.

This article presents new results of the antenna pointing experiment involving the collimation tower and Mu-2 Ranging

System at DSS 42. Very little theoretical or experimental data currently exists on the effects of antenna pointing errors on time delays. The new test data represents an improvement factor of 2 over the previously reported test data and therefore should be documented.

II. Test Setup and Procedure

The test setup consisted primarily of (1) a 244-m (8-ft) diameter parabolic antenna with a zero delay device installed on top of the DSS 42 collimation tower and (2) a 20-kW transmitter, a 26-m antenna, the Mu-2 Ranging System, and all of the tracking hardware and software normally used for station delay calibration and spacecraft tracking.

Significant parameters to note for this test were Channel 18 test frequencies (2114.676 MHz uplink and 2296.481 MHz downlink), 15-kW transmitted power, RCP polarization, and the Mu-2 Ranging System set for 1-MHz ranging code, 30-sec DRVID integration, and 3-dB carrier suppression.

The basic test procedure was described in detail in Ref 1 and will not be repeated here. The improvements in test procedure to obtain data for this article were as follows

- (1) Increase the number of closures back to boresight so that an accurate drift curve could be established and more accurate corrections could be made for drift
- (2) Insert a calibrated attenuator into the 182-MHz line at the collimation tower. The attenuator was adjusted at each offset angle to maintain a fairly constant downlink signal level. This procedure resulted in a smaller and less significant correction needed to account for range delay changes as a function of received signal levels
- (3) Increase the integration times for the DRVID¹ data at weaker signal levels so that standard deviations were nearly the same at all boresight offset angles

III. Test Results

Figure 1 shows the improved test results that were obtained with the new test procedures. The test results were corrected for changes in range delays due to signal level changes and also for drift in range delays with time. The data reduction procedure was to (1) obtain a signal level versus range correction curve by a weighted least squares method (see Ref 1), (2) correct range data for signal level changes, (3) perform a weighted second order least square curve fit to the boresight (zero offset angle) data versus time to obtain a drift curve and (4) make corrections for drift. The one-sigma error limits shown in Fig 1 are standard deviations of the mean (or standard error) which include errors due to measurement dispersion, errors in the signal level calibration curve, and errors in the drift correction curve. It can be seen that the total standard error is typically about 1.5 cm over the entire curve. In the previously reported experiment, the standard error was typically larger than 10 cm for offset angles greater than 0.16 degrees.

A more careful measurement involving the use of a calibrated attenuator at the collimation tower led to the result that the 3-dB points for the 26-m antenna were closer to 0.18 degree than the 0.15 degree reported in Ref 1. The value of

0.18 degree agrees well with a 0.19 degree calculated average value for uplink and downlink frequencies of 2114.676 MHz and 2296.481 MHz, respectively. The new power pattern or boresight curve shown in Fig 1 was obtained by taking one-half of the total measured signal level changes versus offset angles. The factor of one-half accounts for the fact that a signal level change on the uplink signal occurs due to offset angle and approximately the same change occurs on the downlink signal when it returns from the collimation tower back to the 26-m antenna.

Examination of the range change data in Fig 1 reveals that the maximum changes in range occurring within the 3-dB points are ± 3 cm for elevation angle offsets and ± 7 cm for azimuth angle offsets. The differences in azimuth and elevation range change curves are believed to be due to differences in ground multipath. It was previously thought that the difference in the two curves could be due to the quadripod support multipath. However, a further study showed that the quadripods are oriented close to 45 degrees with respect to the DSS 42 collimation tower vertical. Since the quadripod geometry is nearly the same for the two offset scan planes, quadripod multipath does not provide an explanation for the differences in the two scan plane results.

The test data has been analyzed for measurement error, but no further corrections have been made on the data. If the normal DSN procedure for correcting for declination angle changes were made for this test, the corrections would have been less than ± 1 cm.

Further analytical work needs to be done to confirm that antenna pointing errors are as small as was observed in these tests. Experimental work using VLBI techniques also needs to be done to determine if antenna pointing errors have negligible effects on VLBI measurements.

IV. Conclusions

An improved experiment was performed at DSS 42 to determine the effects of antenna pointing errors on range delays. It was found that when the 26-m antenna was scanned off target for antenna angle offsets within the 3-dB points of the main beam, the worst case range changes were less than ± 7 cm with measurement uncertainties of about ± 1.5 cm. These results represent an improvement factor of 2 over previously reported results.

¹DRVID is an acronym for Differentiated Range versus Integrated Doppler. When doppler is disabled as was the case for this test, the DRVID data becomes group delay change only.

Acknowledgments

The experimental results presented in this article are a tribute not only to the Mu-2 Ranging System, with its 1-MHz range code, but also a tribute to personnel at DSS 42 who obtained the test data. It should be mentioned that the author of this article contributed suggestions for the improved test procedures and performed the measurement error analysis of the experimental data, but the initiative, testing, and much of the primary data reduction were provided and accomplished by Alan Robinson and other personnel at DSS 42.

Reference

- 1 Otoshi T Y , and Taylor, T T , "An Experimental Investigation of the Effects of Antenna Pointing Errors on Range Delays," in *DSN Progress Report 42-53*, Jet Propulsion Laboratory, Pasadena, Calif , Sep 15, 1979, pp 141-147

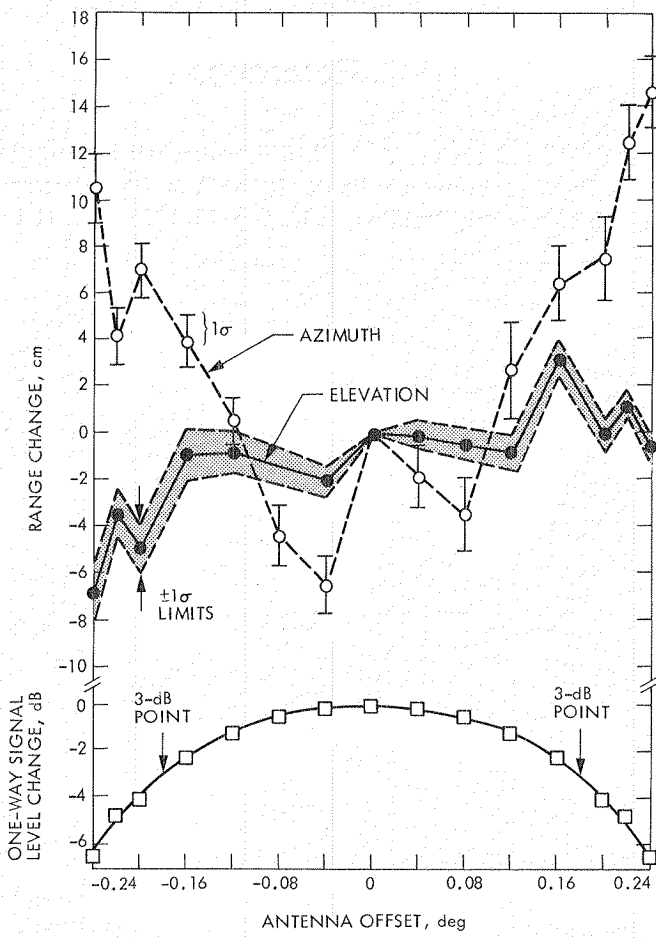


Fig. 1. Range delay changes versus elevation and azimuth angle offsets from boresight (tests performed at DSS 42 on 26-m antenna on 1979 Day of Year 225)

Network Operations Control Center (NOCC) Implementation Status Report

E A Garcia
DSN Data Systems Section

This article provides information regarding the implementation of changes to the Network Operations Control Center (NOCC) required to support the Voyager Jupiter and Saturn Encounters and DSN enhancements designed to reduce maintenance and operations costs

I. Voyager Jupiter

The Network Operations Control Center (NOCC) underwent various modifications to its distributed data processing network's hardware and software to support the Voyager Jupiter Encounters and the planned Voyager Saturn Encounters

The hardware and software modifications in support of the Jupiter Encounter were primarily to increase the telemetry data handling capability and Intermediate Data Records production as required to support the two spacecraft operating at 115.2 kbps. The modifications to the Network in support of high-rate telemetry resulted in the addition of the third Network Log Processor (NLP), along with four additional magnetic tape drives supporting two additional wideband channels from the Deep Space Network.

Interfacing with the third NLP, the Network Data Processing Area (NDPA) was implemented with the third Network Communications Equipment (NCE), which served to route the real-time high-rate telemetry data to a third Telemetry Real-Time Monitor (RTM). In addition to the real-time high-rate telemetry upgrade, the NOCC was implemented with an additional Data Records Processor obtained from MIL-71 on temporary loan, along with four magnetic tape drives and a

high-speed line printer to support the production of high-rate telemetry and radio science radio metric Intermediate Data Records (IDR) required to be delivered within twenty-four hours to project scientists (Several thousand reels of magnetic tape IDR's were delivered to project users at the completion of the two Voyager Jupiter Encounters.)

Also, supporting the Voyager Jupiter Encounter real-time radio-science experiments, the NOCC was augmented with hardware and software for a second Video Assembly Processor with a high-resolution Digital Video Generator Assembly, video hardcopy device, and a second Tracking Real-Time Monitor supporting real-time graphical displays of closed-loop receiver radiometry parameters.

Thus, in support of the Voyager Jupiter Encounter, the NOCC was augmented with a total of six processors with their corresponding operational peripherals and software programs.

II. Voyager Saturn

At the completion of the Voyager Jupiter Encounter support, the NOCC continues the development and implementation of additional operational capabilities needed to

support the Voyager Saturn Encounters in late 1980 and 1981

In support of the Voyager Saturn Encounter and DSN Operations, the NOCC is being augmented with the Radio Science Real-Time Monitor Processor (NRS-RTM) and supporting software. Also included will be the upgrade of the Video Assembly Processor (VAP) to provide two additional channels of high-resolution graphics.

The NRS-RTM, in conjunction with the upgraded VAP, will support the processing and generation of Real-Time Open-Loop Receiver Frequency Spectrum Graphical plots. These will be used by DSN operations and radio scientists during the encounter period. Another task of the NRS-RTM is the processing of Very Long Baseline Interferometry (VLBI) monitor data from the Deep Space Stations as required to coordinate the simultaneous data gathering of two Deep Space Stations. The two stations scheduled for a VLBI pass gather star source signals for non-real-time play-back to the Pasadena VLBI processing center. VLBI-processed data will be used in support of Voyager navigation to Saturn and beyond as well as to provide the DSN with accurate time-sync parameters.

Also, in support of Voyager 2 spacecraft up-link frequency tuning, various software programs in the Network's Support Subsystem and Tracking RTM were updated to support the generation and monitoring of up-link frequency tuning predictions transmission to the Deep Space Stations equipped with the up-link Programmable Oscillator Control Assembly (POCA).

III. DSN Enhancements

In addition to the Voyager Jupiter and Saturn Encounter preparations and implementations, the NOCC was upgraded to support DSN operations and improve the Network's reliability and sustaining engineering costs through the following implementations:

- (1) All NOCC processors are being upgraded to the DSN Standard Hardware Revision level as required to maintain the same configuration with the rest of the DSN processors deployed at each of the Deep Space Stations and at the Central Communications Terminal in Pasadena. This effort allows for sharing of DSN spares, test

equipment and documentation, and minimizes the amount of special training required for the DSN maintenance personnel.

- (2) All NOCC Software Operational Programs were modified for automatic Software Turn ON/OFF of the processor's Terminate I/O device. This modification is expected to reduce the high failure rate experienced in the Terminate bearings, ribbon control, and electronics.
- (3) The NOCC Display Subsystem Software was modified to eliminate the original interface design which interlocked the Display Processor Software with the Real-Time Monitor (RTM) Processor Software. With the new Display-RTM interface design, displays may be added, modified, or subtracted from the RTMs without requiring simultaneous releases of RTM/Display Software programs.
- (4) The NOCC Display Subsystem Varian Printer-Plotters were replaced with High-Speed Data-Products Line Printers. This modification eliminated a high failure rate assembly from the Network as well as providing the capability for a high-quality hardcopy print-out supporting DSN operations.
- (5) The NOCC Display Subsystem Video Assembly Processor's RAMTEK Video Generator will be replaced with a high-resolution 21-channel Video Generator from Grinnell Corp. This upgrade was required to eliminate from the Network the RAMTEK Video Generator which did not have the capability to add the required five DTV Graphics channels in support of real-time radio science graphics. The RAMTEK assembly being deleted from the Network is no longer supported by the factory and spare parts could only be obtained at very high costs.

The replacement of the RAMTEK with Grinnell DTV assembly also allows the NOCC to reconfigure the radio science graphics and Alphanumerics Display Systems into full prime/backup systems not previously available.

- (6) All NOCC Software program documentation (Software Operator's Manual (SOM), Software Specifications Document (SSD), and Software Test and Transfer (STT)) was updated and released to the new DSN Standard Practice requirements. This effort should minimize future NOCC software maintenance and sustaining costs.

End of Document